Characterization and longitudinal study of aerosol particles using a synergy of lidar techniques and passive remote sensing methods in the Mediterranean basin

Ourania Soupiona

Graduated from:

School of Applied Mathematics & Physical Sciences,
National Technical University of Athens, Greece

MSc Degree in Environmental Physics
Physics Department,
National and Kapodistrian University of Athens, Greece

Supervisor:
Prof. Alexandros Papayannis

Submitted in fulfilment of the requirements for the *Degree of Doctor of Philosophy*

Physics Department, School of Applied Mathematics & Physical Sciences,
National Technical University of Athens, Greece

Athens, 16 November 2020

H.F.R.I. Hellenic Foundation for Research & Innovation

GSRT GENERAL SECRETARIAT FOR RESEARCH AND TECHNOLOGY

This research project has been financed through a scholarship from the General Secretariat for Research and Technology (GSRT) and the Hellenic Foundation for Research and Innovation (HFRI), Greece (No 61/5039, 2017-2019).

Characterization and longitudinal study of aerosol particles using a synergy of lidar techniques and passive remote sensing methods in the Mediterranean basin

Ourania Soupiona

Graduated from:

School of Applied Mathematics & Physical Sciences,
National Technical University of Athens, Greece

MSc Degree in Environmental Physics
Physics Department,
National and Kapodistrian University of Athens, Greece

Supervisor:
Prof. Alexandros Papayannis

Submitted in fulfilment of the requirements for the *Degree of Doctor of Philosophy*

Physics Department, School of Applied Mathematics & Physical Sciences,
National Technical University of Athens, Greece

Athens, 16 November 2020

Supervisors: Prof. Alexandros Papayannis, PhD

Physics Department
National Technical University of Athens, Greece
email: apdlidar@mail.ntua.gr

Research Director Vassilis Amiridis, PhD

National Observatory of Athens, Greece
email: vamoir@noa.gr

Lecturer Eleni Giannakaki, Ph.D.

Environmental Physics and Meteorology Department
National and Kapodistrian University of Athens, Greece
email: elina@phys.uoa.gr

Examination Committee: Professor Alexandros Papayannis (NTUA)

Research Director Vassilis Amiridis (NOA)

Lecturer Eleni Giannakaki (UOA)

Professor Dimitrios Balis (AUTH)

Professor Maria Tombrou (UOA)

Professor Christine Böckmann (Univ. of Potsdam)

Assist. Professor Panagiotis Kokkalis (Univ. of Kuwait)

Τα μέλη της Επταμελούς Εξεταστικής Επιτροπής:

Α. Παπαγιάννης, Καθηγητής ΣΕΜΦΕ., Ε.Μ.Π.

Μ. Τόμπρου, Καθηγήτρια ΕΚΠΑ

MARIA TZELLA
Digitally signed by MARIA TZELLA
Date: 2020.12.04 13:22:53 +02'00'

Β. Αμοιρίδης, Ερευνητής Α΄ Ε.Α.Α.

Ε. Γιαννακάκη, Λέκτορας ΕΚΠΑ

ELENI GIANNAKAKI
Digitally signed by ELENI GIANNAKAKI
Date: 2020.12.04 15:15:11 +02'00'

Π. Κόκκαλης, Επίκουρος Καθηγητής (Univ. of Kuwait, Kuwait)

Δ. Μπαλής, Καθηγητής ΑΠΘ

Dimitrios Balis
Dimitrios Balis
06.12.2020 13:16

C. Bockmann, Καθηγήτρια (Univ. of Potsdam, Germany)

16.11.2020

ABSTRACT

The aim of this Doctoral Thesis is the study of the tropospheric aerosols by means ground based remote sensing and space-borne techniques, through statistical analysis of the retrieved aerosol optical properties. At the same time, advanced mathematical algorithms are applied to retrieve the aerosol microphysical properties while predictive models are used to obtain additional information, such as the source regions of the transported aerosols and their radiative forcing effect.

In the opening chapter, Chapter 1, a theoretical background on atmospheric aerosols, their role in atmospheric physics and the different types of aerosols are presented, giving an overall view of the studied field. There is a variety of aerosol sources and particle sizes and therefore, aerosols can be found at different heights in the atmosphere. All atmospheric aerosols scatter incoming solar radiation, while a few ones can also absorb it. In the atmosphere, there is a mixture of both scattering and absorbing aerosols, and their net effect on Earth's energy budget depends on surface and cloud characteristics. All these aspects are shortly presented in this Chapter.

In Chapter 2, except the vertical atmospheric structure, the fundamental aspects of atmospheric physic and optics are mentioned, focusing on the mechanisms of the atmospheric substances (aerosols and molecules) and their interactions with light. Absorption, transition, scattering, extinction, depolarization and fluorescence of light are the basic phenomena discussed here as a brief outline of the fundamental laws governing the transmission of light in the atmosphere centred around the Beer-Lambert law.

The aerosol remote sensing techniques are included in Chapter 3, along with the available instrumentation used to obtain our results. Firstly, the lidar technique is schematically analysed and a full description of the lidar equation is presented. The relevant detection modes of the lidar signals and the different types of lidar instruments are presented as well as the instrumentation that is available at the Laser remote sensing unit of NTUA. Additionally, the lidar pre-processing methods along with aerosol data products are mentioned. Finally, a brief description of the Aerosol Robotic Network (AERONET) of sun photometer measurements is presented.

Tools and modelling that exploit lidar satellite measurements which were used to enhance our findings are introduced and shortly presented in Chapter 4. The EARLINET Single Calculus Chain (SCC) is the tool used for retrieving the aerosol optical properties and the Spheroidal Inversion eXperiments (SphInX) software tool, developed at the University of Potsdam, provided the microphysical retrievals from lidar data inputs. Useful information about the HYSPLIT model which simulates the backward trajectory analysis, the Dust Regional Atmospheric Model (BSC-DREAM8b v2.0), the Library for radiative transfer (Libradtran) tool and satellite data is also provided.

Our results and a comprehensive analysis are presented in Chapter 5. Firstly, we present a comprehensive analysis of the seasonal variability of the vertical profiles of the optical and geometrical properties of Saharan dust aerosols, observed in the height region between 1000 and 6000 m, over Athens, Greece, from February 2000 to September 2017. These nighttime observations were performed by the EOLE Raman lidar system under cloud-free conditions. Moreover, 4 years of lidar measurements of Saharan dust intrusions over the Mediterranean basin (2014-2017), obtained from 4 selected EARLINET stations (Granada, Potenza, Athens, Limassol) are studied in terms of aerosol optical, geometrical, mixing state and microphysical properties. Specific case studies are further analysed. Finally, simulations of the regional radiative forcing of dust events over Mediterranean are presented.

The concluding remarks are given in Chapter 6, which is the final chapter of this Thesis.

ACKNOWLEDGEMENTS

I would honestly like to thank my supervisor Prof. Alexandros Papayannis for giving me the opportunity to work on this Thesis as a member of the Laser Remote Sensing Unit of the National Technical University of Athens. I could not imagine any better supervisor all these years. I am feeling glad and thankful for his trust and support and also for giving me the chance to make my own decisions and initiatives in research.

I also express my gratitude to my other two supervisors: Dr. Vassilis Amiridis, researcher in the National Observatory of Athens and Dr. Elina Giannakaki of the National and Kapodistrian University of Athens for their help and support whenever I was in their need.

I am especially grateful to Prof. Christine Böckmann for the very fruitful co-operation we had at the Institute of Mathematics, University of Potsdam, in Potsdam, Germany. This co-operation took place in the frame of the Erasmus+ Programme of the European Union which is also acknowledged for my 2-month training at the University of Potsdam. I would also like to thank Dr. Stefanos Samaras for answering all my scientific questions since despite his lack of free time, he was always willing to help me.

I have to admit that this Thesis would have been poorer without the contribution of Assist. Prof Panagiotis Kokkalis. His suggestions, ideas and scientific point of view were always innovative and he was always willing to work with me on the publications to peer reviewed journals.

Many thanks to the team from of the Department of Applied Physics of the University of Granada, and especially to Dr. Pablo-Ortiz-Amezcua, Dr. Guadalupe Sánchez Hernández and their supervisor Prof. Lucas Alados-Arboledas for their help and co-operation.

Spatial thanks also to Dr. Stergios Vratolis from the NCSR Demokritos, Athens and Dr. Nikolaos Papagiannopoulos from the CNR-IMAA of Potenza, Italy for their contribution so that this Thesis could be completed. The team of the National and Kapodistrian University of Athens, namely: Dr. Elissavet Bosioli, PhD candidate Georgia Methymaki and Prof. Maria Tombrou also contributed to my Thesis by providing modelling simulations.

Last but not least, I personally thank my colleagues Maria Mylonaki, Christianna Papanikolaou and Romanos Foskinis for their help and support both scientifically and psychologically. Except from great colleagues, they have been also great friends and co-travelers through these years.

This research project has been financed through a scholarship from the General Secretariat for Research and Technology (GSRT) and the Hellenic Foundation for Research and Innovation (HFRI), Greece (No 61/5039, period 2017-2019).

ΠΕΡΙΛΗΨΗ

Η παρούσα Διδακτορική Διατριβή έχει ως αντικείμενο τη μελέτη των τροποσφαιρικών αερολυμάτων με τη χρήση επίγειων και δορυφορικών τεχνικών, για την ανάκτηση των οπτικών ιδιοτήτων των αιωρούμενων σωματιδίων και την στατιστική ανάλυσή τους. Παράλληλα, εφαρμόζονται μαθηματικοί αλγόριθμοι για την ανάκτηση των μικροφυσικών τους ιδιοτήτων, καθώς και γίνεται χρήση προγνωστικών μοντέλων για ανάκτηση επιπλέον πληροφοριών, όπως ο προσδιορισμός της πηγής προέλευσης των αιωρούμενων σωματιδίων, αλλά και η επίδρασή τους στο ατμοσφαιρικό ενεργειακό ισοζύγιο.

Στο πρώτο κεφάλαιο (Κεφάλαιο 1) περιλαμβάνεται το θεωρητικό υπόβαθρο των ατμοσφαιρικών αερολυμάτων, ο ρόλος τους στην ατμοσφαιρική Φυσική, καθώς και οι διάφοροι τύποι αερολυμάτων, δίνοντας τη συνολική εικόνα του πεδίου μελέτης. Στο Κεφάλαιο 2 αναφέρονται οι θεμελιώδεις πτυχές της ατμοσφαιρικής Φυσικής και της Οπτικής, με έμφαση στους μηχανισμούς αλληλεπίδρασης του φωτός με τα ατμοσφαιρικά στοιχεία (αερολύματα και μόρια). Οι τεχνικές τηλεπισκόπησης αερολυμάτων που έχουν χρησιμοποιηθεί ευρέως σε αυτή τη διατριβή παρουσιάζονται στο Κεφάλαιο 3, μαζί με λοιπά διαθέσιμα όργανα που χρησιμοποιήθηκαν για τη λήψη δεδομένων των προς εξαγωγή αποτελεσμάτων. Συγκεκριμένα παρουσιάζεται η τεχνική light detection and ranging (lidar), καθώς και τα διάφορα στάδια επεξεργασίας των σημάτων lidar. Τα ατμοσφαιρικά προγνωστικά μοντέλα αλλά και εργαλεία που αξιοποιούν δορυφορικές μετρήσεις και χρησιμοποιήθηκαν για την ενίσχυση των αποτελεσμάτων μας παρουσιάζονται εν συντομία στο Κεφάλαιο 4. Η περιεκτική ανάλυση των αποτελεσμάτων παρουσιάζεται στο Κεφάλαιο 5, ενώ τα συμπεράσματα παρατίθενται στο Κεφάλαιο 6, που αποτελεί το τελευταίο κεφάλαιο αυτής της Διατριβής.

Στην παρούσα περίληψη περιλαμβάνονται τα κυριότερα αποτελέσματα: i) της συστηματικής μελέτης των 18 συνολικά ετών μετρήσεων (2000-2017) από τη βάση δεδομένων του Εργαστηρίου Τηλεπισκόπησης laser του ΕΜΠ, για το σταθμό της Αθήνας, ii) της τετραετούς μελέτης μετρήσεων lidar στην περιοχή της Μεσογείου (4 επιλεγμένοι σταθμοί του δικτύου EARLINET: Γρανάδα, Ποτένζα, Αθήνα, Λεμεσός), αναφορικά με τις οπτικές, γεωμετρικές, μικροφυσικές ιδιότητες σωματιδίων ερημικής προέλευσης από την περιοχή της Σαχάρας, καθώς και της πιθανή ανάμειξή τους με σωματίδια από διαφορετικές πηγές προέλευσης και τέλος, iii) των προσομοιώσεων ατμοσφαιρικού μοντέλου για τη μελέτη της επίδρασης των αιωρούμενων σωματιδίων στο ατμοσφαιρικό ενεργειακό ισοζύγιο, στην περιοχή της Μεσογείου. Για το σκοπό της μελέτης προσμείξεων εντός των παρατηρούμενων στρωματώσεων ερημικής προέλευσης, ο όρος «mixing» εισάγεται, αναφερόμενος στο χρονικό διάστημα κατά το οποίο οι αέριες μάζες ταξιδεύουν, μετά την έξοδο από την Αφρικανική ήπειρο ώσπου να φθάσουν στον εκάστοτε σταθμό παρατήρησης.

Η έρημος Σαχάρα είναι μια από τις σημαντικότερες πηγές αιωρούμενων σωματιδίων σκόνης παγκοσμίως. Η εναέρια μεταφορά των σωματιδίων αυτών προς στις μεσογειακές χώρες καθορίζεται από τις εκάστοτε επικρατούσες μετεωρολογικές συνθήκες στη Λεκάνη της Μεσογείου (Mona et al., 2012). Για παράδειγμα, στην περιοχή της Δυτικής Μεσογείου, τα επεισόδια μεταφοράς αφρικανικής σκόνης είναι συχνότερα το καλοκαίρι (Salvador et al., 2014), ενώ στην περιοχή της κεντρικής Μεσογείου, η άνοιξη και το καλοκαίρι, συνήθως, σχετίζονται με μεγάλο φορτίο σωματιδιακής σκόνης που εκτείνεται σε ύψη 3-4 χλμ (Barnaba and Gobbi, 2004). Στην Ανατολική Μεσόγειο, η κύρια μεταφορά Αφρικανικής σκόνης λαμβάνει χώρα από την άνοιξη έως το φθινόπωρο (Papayannis et al., 2009; Nisantzi et al., 2015; Soupiona et al., 2018) σαν αποτέλεσμα της υψηλής κυκλονικής δραστηριότητας στη βόρεια Αφρική κατά τη διάρκεια αυτών των εποχών (Flaounas et al., 2015). Λαμβάνοντας επίσης υπόψιν ότι η Λεκάνη της Μεσογείου είναι μια περιοχή με αξιοσημείωτη ηλιακή δραστηριότητα και επομένως, σημαντική εξάτμιση, αλλά και χαμηλά ποσοστά βροχόπτωσης, η αερομεταφορά σωματιδίων σκόνης που συνοδεύεται από διαδικασίες γήρανσης και ανάμειξης

καθιστούν αυτήν την περιοχή σημείο ενδιαφέροντος για τις παρούσες και μελλοντικές επιπτώσεις της κλιματικής αλλαγής (Michaelides et al., 2018).

Παρόλο που έχουν γίνει πολλές μεμονωμένες μελέτες σχετικά με τις οπτικές ιδιότητες της Σαχαριανής σκόνης βασιζόμενες στην τεχνική lidar (Landulfo et al., 2003; Ansmann et al., 2009; Papayannis et al., 2009; Tesche et al., 2011; Mona et al. ., 2012; Groß et al., 2013; Navas-Guzmán et al., 2013; Rittmeister et al., 2017; Soupiona et al., 2018), οι συστηματικές και μακροπρόθεσμες στατιστικές μελέτες είναι λίγες, όπως ολιγάριθμες είναι και οι διαθέσιμες μετρήσεις με δεδομένα με τη χρήση της τεχνικής αποπόλωσης, σε έγκριτες βάσεις δεδομένων. Για παράδειγμα, οι Saidou Chaibou et al. (2020) πρόσφατα μελέτησαν τη σημασία των επιπτώσεων της σκόνης στις κλιματικές μελέτες προκειμένου να βελτιωθεί η ακρίβεια των κλιματικών προβλέψεων. Όπως αναφέρουν, ακόμη και εαν η εκτίμηση της επίδρασης σκόνης στο κλίμα απαιτεί συνεχείς παρατηρήσεις, τόσο από δορυφόρους όσο και από επίγεια δίκτυα οργάνων, η χρήση κλιματικών μοντέλων είναι, επίσης, ζωτικής σημασίας για τη βελτίωση της κατανόησης της κατανομής των σωματιδίων σκόνης, των ιδιοτήτων τους και των επιπτώσεών τους στο ισοζύγιο ακτινοβολιών. Σε μια προηγούμενη μελέτη, οι Pérez et al. (2006) πρότειναν ότι ένα περιφερειακό μοντέλο ατμοσφαιρικής σκόνης, με ενσωματωμένες πληροφορίες επίδρασης της σκόνης στην ακτινοβολία, είναι μια πολλά υποσχόμενη προσέγγιση για περαιτέρω βελτιώσεις στην αριθμητική πρόγνωση καιρού και την εκτίμηση των ακτινοβολικών επιπτώσεων σε περιοχές που επηρεάζονται από σωματίδια σκόνης, όπως είναι η περιοχή της Μεσογείου. Ως εκ τούτου, παρόλο που η συνέργεια των επίγειων και δορυφορικών μετρήσεων είναι πολύ ελπιδοφόρα για την εις βάθος μελέτη των ιδιοτήτων των αιωρούμενων σωματιδίων σε παγκόσμια κλίμακα, η χρήση προγνωστικών περιφερειακών μοντέλων μπορεί, επίσης, να συμβάλει σημαντικά σε τέτοιες εκτιμήσεις, ειδικά σε περιοχές όπου οι μετρήσεις δεν είναι διαθέσιμες.

Το European Aerosol Research Lidar Network (EARLINET, https://www.earlinet.org/, Pappalardo et al., 2014) που ιδρύθηκε το 2000, παρέχει μια μεγάλη συλλογή από έγκυρα επίγεια δεδομένα συστημάτων lidar, σχετικά με μελέτη των οπτικών ιδιοτήτων των αερολυμάτων στην Ευρώπη. Επί του παρόντος, το δίκτυο περιλαμβάνει 31 ενεργούς σταθμούς lidar κατανεμημένους σε ολόκληρη την Ευρώπη, παρέχοντας πληροφορίες για κατακόρυφες κατανομές αερολυμάτων σε ηπειρωτική κλίμακα. Στην παρούσα Διατριβή, δεδομένα (level 2) τεσσάρων σταθμών από τη βάση δεδομένων EARLINET (https://data.earlinet.org/), έχουν αξιοποιηθεί: της Γρανάδας (Ισπανία), της Ποτέντζα (Ιταλία) της Αθήνας (Ελλάδα) και της Λεμεσού (Κύπρος). Οι κατακόρυφες κατανομές των συντελεστών οπισθοσκέδασης (β_{aer}), εξασθένησης (α_{aer}) λόγου αποπόλωσης (δ_{aer}) συλλέχθηκαν και αξιοποιήθηκαν, ως συνάρτηση του ύψους πάνω από τη μέση στάθμη της θάλασσας (a.s.l.) και αναλύθηκαν περαιτέρω, προς εξαγωγή συμπερασμάτων για τις οπτικές και μικροφυσικές τους ιδιότητες καθώς και για το ρόλο τους στο ισοζύγιο ακτινοβολιών στην περιοχή της Μεσογείου.

Το σύστημα πολλαπλών μηκών κύματος και αποπόλωσης Raman EOLE (aErosol και Ozone Lidar systEm) του Εθνικού Μετσόβιου Πολυτεχνείου (ΕΜΠ, 37.97 ° B, 23.79 ° A, 212 m a.sl.) βρίσκεται στο Εργαστήριο Τηλεπισκόπησης laser (Laser Remote Sensing Unit) του ΕΜΠ. Η πηγή εκπομπής είναι ένα παλμικό laser στερεάς κατάστασης, Nd:YAG, με παλμούς υψηλής ενέργειας laser στα 355, 532 και 1064 nm και ρυθμό επανάληψης 10 Hz. Η χωρική και χρονική ανάλυση είναι 7.5 m και 100 s, αντίστοιχα. Το σύστημα λήψης, που βασίζεται σε ένα τηλεσκόπιο τύπου Cassegranian 300 mm και διχρωικά κάτοπτρα, είναι σε θέση να ανιχνεύσει και να διακρίνει τα ελαστικά οπισθοσκεδαζόμενα σήματα στα 355, 532 και 1064 nm, καθώς και τα οπισθοσκεδαζόμενα κατά Raman στα 387, 607 και 407 nm αντίστοιχα (Papayannis et al., 2020). Ένα επιπλέον κανάλι αποπόλωσης στα 355 nm συμβάλλει στο να ληφθούν οι κατακόρυφες κατανομές της γραμμικής αποπόλωσης σωματιδίων κατακόρυφα στην ατμόσφαιρα. Για τη βαθμονόμησή του συστήματος αποπόλωσης εφαρμόζεται η μέθοδος βαθμονόμησης ± 45° (Freudenthaler et al., 2009).

i)Αρχικά, παρουσιάζουμε μια ολοκληρωμένη ανάλυση της εποχικής μεταβλητότητας των κατακόρυφων κατανομών των οπτικών και γεωμετρικών ιδιοτήτων των αερολυμάτων Σαχαριανής σκόνης, που παρατηρήθηκαν στην περιοχή ύψους μεταξύ 1000 και 6000 m (a.s.l.), πάνω από το σταθμό της Αθήνας, για τη χρονική περίοδο Φεβρουάριος του 2000 – Δεκέμβριος 2017. Οι νυχτερινές αυτές μετρήσεις πραγματοποιήθηκαν από το σύστημα EOLE, υπό ανέφελες συνθήκες. Η στατιστική ανάλυση αναφέρεται σε μηνιαίες μέσες τιμές και βασίζεται στις κατακόρυφες κατανομές των οπτικών ιδιοτήτων των αερολυμάτων (β_{aer}, α_{aer}, LR, AE) στα 355 nm (59 περιπτώσεις μεταφοράς σκόνης με περισσότερες από 80 ώρες μετρήσεων).

Στην Εικόνα 1α παρουσιάζεται η μηνιαία κατανομή του αριθμού των περιπτώσεων σκόνης όπως παρατηρήθηκαν από το σύστημα EOLE του ΕΜΠ (μόνο υπό ανέφελες συνθήκες) και προβλέφθηκαν από την BSC-DREAM8b, για την περίοδο 2000-2017. Ο μέγιστος αριθμός εμφάνισης των επεισοδίων σκόνης παρουσιάζεται το μήνα Μάϊο, τόσο στις προβλέψεις του μοντέλου (~30 περιπτώσεις), όσο και στις μετρήσεις από το σύστημα EOLE (~16 περιπτώσεις), ενώ η πλειονότητα των περιπτώσεων επεισοδίων μεταφοράς Αφρικανικής σκόνης παρατηρείται μεταξύ αρχές της άνοιξης (Μάρτιος) και μέσα φθινοπώρου (Οκτώβριος). Συγκεκριμένα, το 81% των προσομοιώσεων και το 95% των μετρήσεων εμπίπτουν σε αυτήν τη χρονική περίοδο. Ένα μικρό ποσοστό επεισοδίων εμφανίζεται κατά τους χειμερινούς μήνες, δεδομένου ότι κατά την περίοδο αυτή επικρατεί βορειοανατολική ροή ανέμων στον Ελλαδικό χώρο και κατά συνέπεια και στην Αθήνα (Kassomenos et al., 1995; Papayannis et al., 2009; Banks et al., 2016). Ωστόσο, το γεγονός ότι ο αριθμός των μετρήσεων του συστήματος EOLE είναι πάντα μικρότερος από τις αντίστοιχες προβλέψεις του μοντέλου BSC-DREAM8b, μπορεί να αποδοθεί στην αδυναμία της τεχνικής lidar να πραγματοποιεί μετρήσεις σε ατμοσφαιρικές συνθήκες νεφοκάλυψης.

Επιπλέον, κατά τη μελέτη μας βρήκαμε μια αρκετά ισχυρή συσχέτιση (συντελεστής συσχέτισης: R^2=0.81) μεταξύ των προβλέψεων και των μετρήσεων των μέσων μηνιαίων περιπτώσεων, φανερώνοντας έτσι τη γραμμική τους σχέση (Εικόνα 1β). Περίπου οι μισές των περιπτώσεις των προβλέψεων παρατηρούνται τελικά από το σύστημα lidar για τη χρονική περίοδο 2000-2017. Αυτό συνεπάγεται ότι στη χειρότερη περίπτωση, τουλάχιστον το 50% των προβλεπόμενων από το μοντέλο επεισοδίων σκόνης θα παρατηρηθεί τελικά από το σύστημα EOLE, υπό ανέφελες συνθήκες στην ελεύθερη τροπόσφαιρα της Αθήνας.

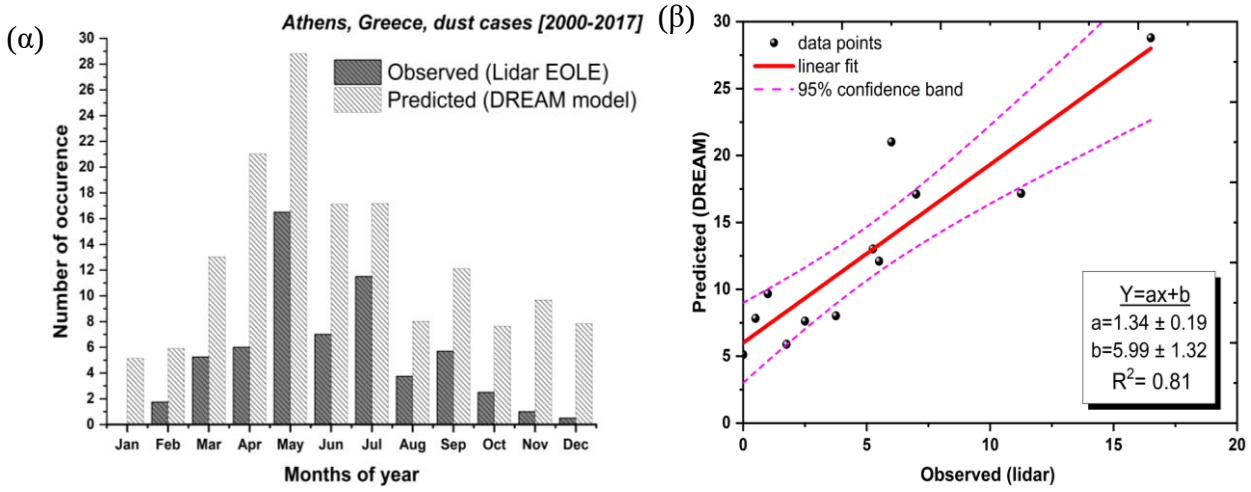

Εικόνα 1: α) Μηνιαία κατανομή και β) γραμμική συσχέτιση του μέσου αριθμού επεισοδίων σκόνης που παρατηρήθηκαν (EOLE) και προβλέφθηκαν (BSC-DREAM8b) για την χρονική περίοδο 2000-2017.

Η εποχιακή διακύμανση (από την άνοιξη έως το χειμώνα) των κατακόρυφων κατανομών (μαύρες γραμμές) των συνιστωσών β_{355}, α_{355} και LR_{355}, καθώς και οι μέσες τιμές τους (κόκκινες γραμμές) μαζί με την αντίστοιχη τυπική απόκλιση (SD) (μωβ οριζόντιες γραμμές σφάλματος) παρουσιάζονται στην Εικόνα 2(α, β, γ). Οι τιμές των LR_{355} (Εικόνα 2γ) έχουν υπολογισθεί για εύρος

ύψους μεταξύ 2000 και 4000 m, όπου συνήθως εντοπίζονται τα αερομεταφερόμενα στρώματα σκόνης Αφρικανικής προέλευσης (Papayannis et al., 2009). Συνολικά, οι κατακόρυφες αυτές κατανομές εμφανίζουν μια αρκετά μεγάλη μεταβλητότητα, λόγω της διαφορετικής έντασης και των διαφορετικών τροχιών των αερίων μαζών που φτάνουν στο σταθμό παρατήρησης (Αθήνα), όπως έχει προηγουμένως συζητηθεί και από τους Papayannis et al. (2009).

Συμπερασματικά, οι εποχιακές μέσες τιμές LR_{355} εντός των στρωματώσεων σκόνης (άνοιξη: 58 ± 9 sr, καλοκαίρι: 54 ± 9 sr, φθινόπωρο: 38 ± 6 sr, χειμώνας: 45 ± 6 sr) ποικίλλουν από εποχή σε εποχή, λαμβάνοντας μικρότερες τιμές κατά τους ψυχρότερους μήνες, κυρίως λόγω του μεγαλύτερου ποσοστού ανάμειξης με άλλους τύπους σωματιδίων. Η μέση τιμή LR_{355} για ολόκληρη την περίοδο μελέτης (2000-2017), ανεξαρτήτως εποχικότητας, υπολογίζεται ίση με 52 ± 13 sr, με ελάχιστο στα 22 sr και μέγιστο στα 77 sr.

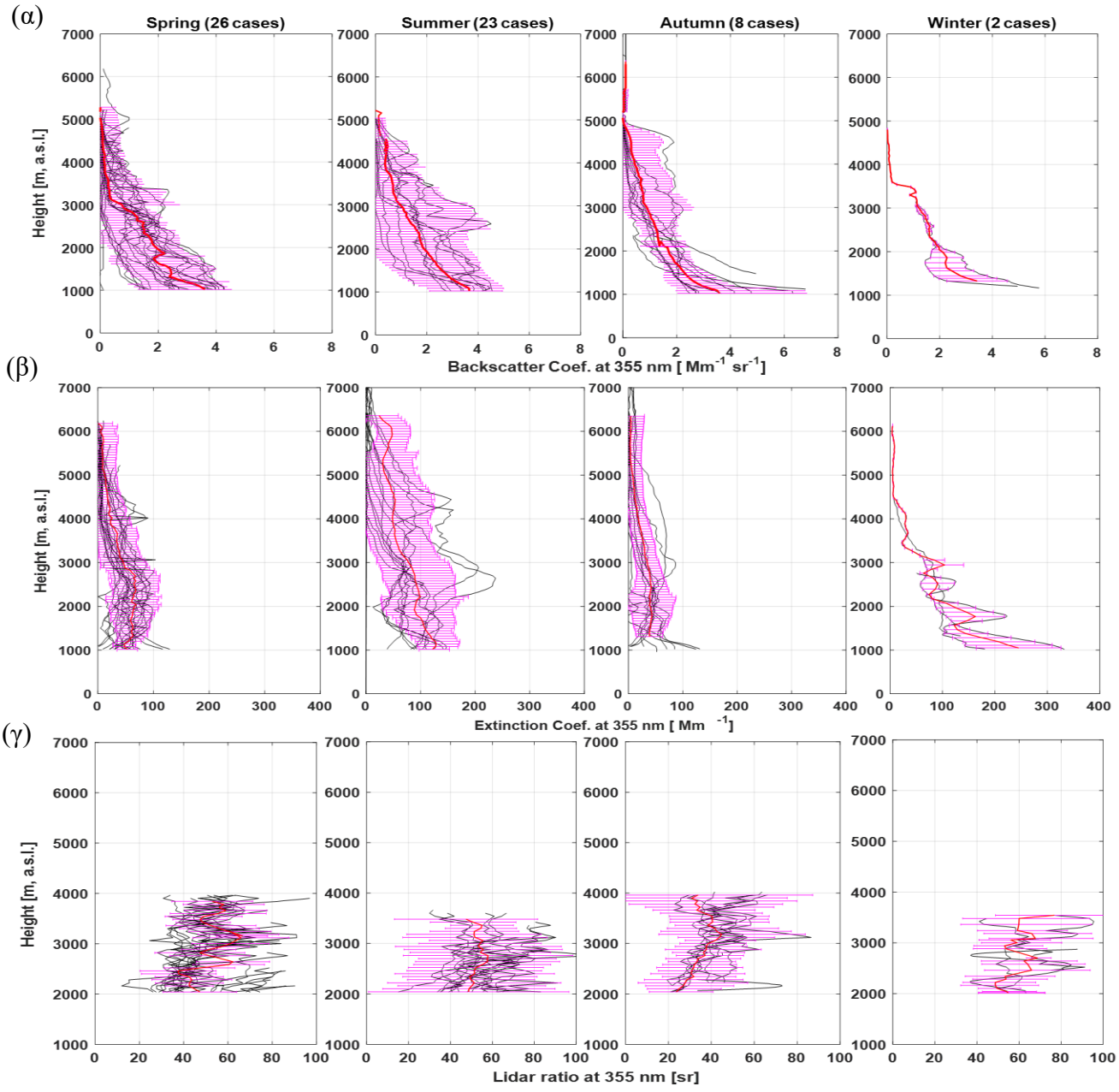

Εικόνα 2: Εποχιακή διακύμανση των κατακόρυφων κατανομών των οπτικών ιδιοτήτων: α) β_{355}, β) α_{355} και γ) LR_{355}, αερολυμάτων σκόνης, μαζί με τις μέσες τιμές τους (κόκκινες γραμμές) και την αντίστοιχη τυπική απόκλιση (μωβ οριζόντιες γραμμές σφάλματος) για τα 59 περιπτώσεις μεταφοράς σωματιδίων Αφρικανικής σκόνης (2000–2017).

Η εποχιακή μεταβλητότητα της οπτικής παραμέτρου AOD_{355}, όπως παρουσιάζεται στην Εικόνα 3α, με boxplots, είναι σημαντική, σημειώνοντας ελάχιστες μέσες τιμές (τετράγωνο σύμβολο εντός του boxplot) κατά τη διάρκεια του Φθινοπώρου και μέγιστες την άνοιξη και το καλοκαίρι. Επιπλέον, οι διάμεσοι (οριζόντιες γραμμές εντός του boxplot) κατά την άνοιξη και το καλοκαίρι είναι χαμηλότερες από τις αντίστοιχες μέσες τιμές, υποδηλώνοντας ότι, ενώ η κατανομή είναι μετατοπισμένη σε χαμηλότερες τιμές AOD_{355}, υπάρχουν μερικές εξαιρετικά μεγάλες τιμές AOD, που αντιπροσωπεύουν ακραία επεισόδια μεταφοράς σκόνης, τα οποία λαμβάνουν χώρα τη συγκεκριμένη περίοδο. Από την άλλη πλευρά, κατά τη διάρκεια του φθινοπώρου και του χειμώνα, η κατανομή των τιμών του AOD φαίνεται να είναι πιο ομαλή, καθώς οι αντίστοιχες μέσες και διάμεσες τιμές είναι σχεδόν ταυτόσημες. Η μέση τιμή AOD_{355} για ολόκληρη την περίοδο μελέτης (2000-2017), ανεξαρτήτως εποχικότητας, υπολογίζεται ίση με 0.25 ± 0.16.

Αντίστοιχα, η εποχιακή μεταβλητότητα της παραμέτρου LR_{355}, εκφρασμένη σε μέσες τιμές (και τυπική απόκλιση) φαίνεται στην Εικόνα 3β. Οι μέσες τιμές που σημειώνονται για την άνοιξη και το καλοκαίρι (58 ± 9 και 54 ± 9 sr, αντίστοιχα) είναι πολύ κοντά στις τιμές που μετρήθηκαν κατά τη διάρκεια του πειράματος SAMUM (53 ± 5 sr, στα 355 nm), όπως αναφέρεται από τους Groß et al., (2015), που αφορούν έντονα στρώματα σκόνης χωρίς σημαντική παρουσία προσμείξεων. Στην περίπτωσή μας, παρατηρείται μια αρκετά γρήγορη (1-2 ημέρες) μεταφορά από την Αφρικανική ήπειρο στην περιοχή της Αθήνας, γεγονός που υποδηλώνει χαμηλή πιθανότητα ανάμειξης σωματιδίων σκόνης με άλλους τύπους αιωρούμενων σωματιδίων κατά της διάρκεια τη μεταφορά τους. Οι μέσες τιμές LR_{355} το φθινόπωρο και το χειμώνα (38 ± 6 και 45 ± 6 sr, αντίστοιχα) είναι μικρότερες σε σύγκριση με τις προαναφερθείσες και είναι κοντά σε αυτές (40-45 sr) που παρατηρήθηκαν από τους Amiridis et al. (2005), Müller et al. (2007) και Papayannis et al. (2009), υποδηλώνοντας μια πιθανή ανάμιξη με αέριες μάζες ηπειρωτικής προέλευσης και «σύνθετες» διαδρομές εναέριας μεταφοράς μεγαλύτερης χρονικής διάρκειας.

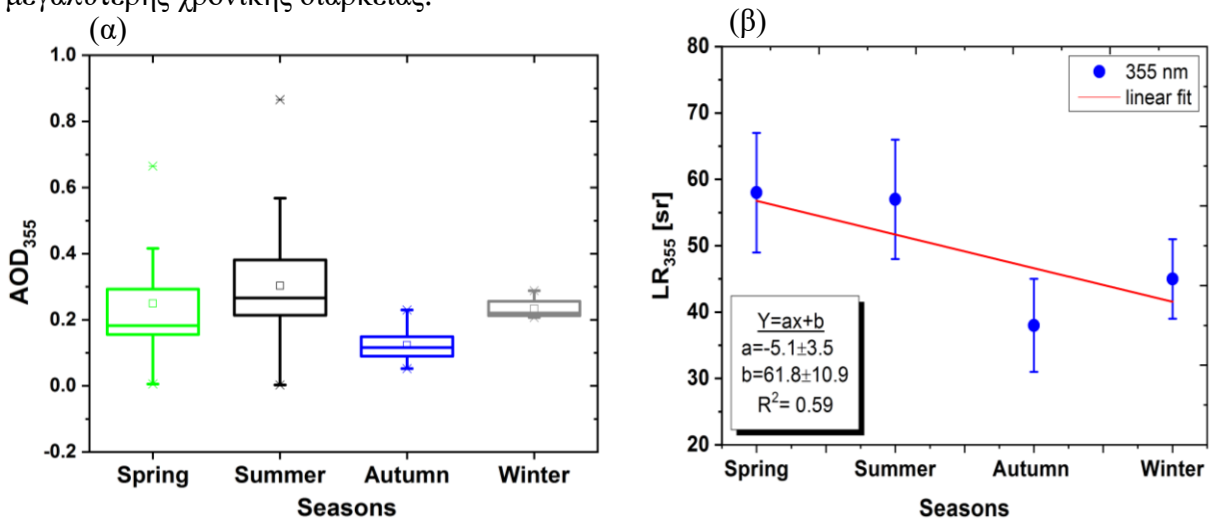

Εικόνα 3: Εποχιακή μεταβλητότητα των μέσων τιμών α) AOD και β) LR ταυτόχρονα με γραμμική συσχέτιση των μέσων τιμών (κόκκινη γραμμή), όπως υπολογίστηκε στα 355 nm κατά την περίοδο 2000-2017, για τα ύψη μεταξύ 2000 και 4000 m (a.s.l.).

Προκειμένου υπολογισθούν οι γεωμετρικές ιδιότητες (βάση, κορυφή, πάχος και κέντρο μάζας (z_{COM})) των στρωματώσεων σωματιδίων σκόνης στην ατμόσφαιρα, ακολουθήθηκε η διαδικασία που προτείνεται από τους Mona et al. (2006). Στον Πίνακα 1 παρουσιάζουμε την κατακόρυφη κατανομή (σε m) των μέσων, ελάχιστων και μέγιστων τιμών των προαναφερόμενων παραμέτρων που σχετίζονται με το υψόμετρο της στρωμάτωσης ερημικής σκόνης, όπως ανακτήθηκαν άμεσα από τη συνιστώσα β_{355}, από τις μετρήσεις του EOLE, κατά την περίοδο Φεβρουάριος 2000 - Δεκέμβριος 2017. Συγκεκριμένα, παρατηρήθηκαν πολλαπλά στρώματα αερολυμάτων σκόνης μεταβλητού πάχους (609-6199 m). Το z_{COM} αυτών των στρωμάτων εντοπίσθηκε σε υψόμετρα μεταξύ 1270 και 5738 m, λαμβάνοντας μέση τιμή 2508 ± 1109 m. Η βάση των στρωμάτων σκόνης κυμαίνεται από 926 m έως

5094 m, λαμβάνοντας μέση τιμή 1793 ± 1098 m. Αντίστοιχα, η κορυφή των στρωμάτων σκόνης κυμαίνεται από 2005 έως 8014 m, με μέση τιμή 3540 ±892 m.

Πίνακας 1: Κύρια γεωμετρικά χαρακτηριστικά (βάση, κορυφή, πάχος και κέντρο μάζας) στρωματώσεων σωματιδίων σκόνης με βάση τη συνιστώσα β_{355} των σημάτων lidar.

Έτη: 2000-2017	Μέση τιμή	Ελάχιστο	Μέγιστο
Βάση z_B (m)	1793±1098	5094	926
Κορυφή z_T (m)	3540±892	8014	2005
Πάχος *th* (m)	1747±785	6199	609
Κέντρο μάζας z_{com} (m)	2508±1109	5738	1270

Με βάση τις οπισθοτροχιές των αερίων μαζών που φθάνουν στην Αθήνα και υποδεικνύουν την πηγής προέλευσης και τη διανυθείσα διαδρομή τους, για κάθε μια απο τις 59 υπό μελέτη περιπτώσεις, πραγματοποιήθηκε ομαδοποίηση κατά συστάδες. Η ομαδοποίηση αυτή υλοποιήθηκε, χρησιμοποιώντας έναν αλγόριθμο που βασίζεται στους Dorling et al. (1992). Έτσι, προέκυψαν δύο μεγάλα συμπλέγματα: Σύμπλεγα Α και Σύμπλεγμα Β. Τα δύο αυτά συμπλέγματα διαφέρουν ως προς την πορεία που διένυσαν οι αέριες μάζες και το χρόνο παραμονής τους πάνω από συγκεκριμένες περιοχες: την Αφρικανική ήπειρο και τη Μεσόγειο Θάλασσα. Όπως φαίνεται και στην Εικόνα 4, οι αέριες μάζες αέρα που περιλαμβάνονται στο σύμπλεγμα Α παραμένουν, κατά μέσο όρο, 12 ώρες περισσότερο (εμπλουτισμός με σωματίδια σκόνης) πάνω από την Αφρικανική ήπειρο (75 ώρες) συγκριτικά με αυτές που ανήκουν στο σύμπλεγμα Β (63 ώρες). Επιπλέον, φθάνουν στην Αθήνα γρηγορότερα (πιθανώς έχοντας υποστεί μικρότερες αναμείξεις κατά τη μεταφορά τους), μετά από συνολικό χρόνο ταξιδιού 126 ωρών. Όσον αφορά το χρονικό διάστημα που παρέμειναν στη Μεσόγειο Θάλασσα, οι αέριες μάζες του συμπλέγματος Α παραμένουν κατά μέσο όρο 51 ώρες επάνω από αυτήν την περιοχή, πολύ λιγότερο από τις αντίστοιχες του συμπλέγματος Β, οι οποίες υπολογίζεται ότι παραμένουν για περίπου 78 ώρες, γεγονός που βοηθά στην επιπλέον ανάμειξή τους με σωματίδια διαφορετικής προέλευσης που λαμβάνουν χώρα στην περιοχή αυτή.

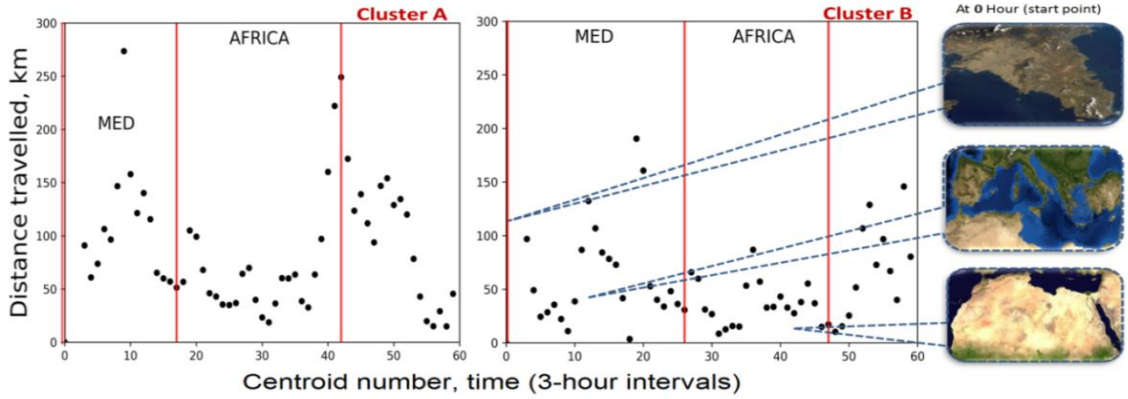

Εικόνα 4: Διανυθείσα απόσταση (σε χιλιόμετρα) ανά διάστημα 3 ωρών (μαύρες κουκίδες), για την 7-ήμερη οπίσθια πορεία του κεντροειδούς κάθε Συμπλέγματος: Σύμπλεγμα Α (αριστερά) και Σύμπλεγμα Β (δεξιά). Ο χρόνος παραμονής τους πάνω από τη Μεσόγειο (MED) και την Αφρικανική ήπειρο (AFRICA), φαίνεται με κόκκινα πλαίσια και αντιστοιχεί σε ώρες στον άξονα x.

ii)Εξετάζοντας τα επεισόδια μεταφοράς σκόνης στους 4 επιλεγμένους σταθμούς του δικτύου EARLINET (Γρανάδα, Ποτένζα, Αθήνα και Λεμεσός) ένα προς ένα, υπολογίσαμε, ακολούθως, τη βάση, την κορυφή και το πάχος κάθε ανιχνευόμενου στρώματος καθώς και τις μέσες τιμές των οπτικών ιδιοτήτων δp_{532}, LR_{532} και AOD_{532} εντός του κάθε στρώματος σκόνης όπως φαίνεται στην Εικόνα 5 (α-δ). Οι αντίστοιχες τιμές τυπικής απόκλισης δίνουν μια ένδειξη της μεταβλητότητας αυτών των παραμέτρων από τη βάση έως την κορυφή κάθε στρωμάτωσης. Κάθε υπο-σχήμα παρουσιάζει τα γεωμετρικά ή οπτικά χαρακτηριστικά των ανιχνευόμενων στρωματώσεων, ένα προς ένα, ανά σταθμό και ανά έτος.

Για αυτούς τους τέσσερις σταθμούς (από αριστερά προς τα δεξιά: Γρανάδα, Ποτέντζα, Αθήνα και Λεμεσός) υπολογίσθηκαν τα ακόλουθα πάχη στρώσης 3392 ± 1458 m, 2150 ± 1082 m, 1872 ± 816 m και 1716 ± 567 m αντίστοιχα. Αναφέρουμε, επίσης, τις μέσες τιμές των δ_{p532} 0.24 ± 0.05, 0.26 ± 0.06, 0.28 ± 0.05 και 0.28 ± 0.04 (Εικόνα 5β) και μέσες τιμές του AOD_{532} 0.40 ± 0.31, 0.11 ± 0.07, 0.12 ± 0.10 και 0.32 ± 0.17 (Εικόνα 5δ), αντίστοιχα. Όσον αφορά τη μέση τιμή της παραμέτρου LR_{532}, αυτή λαμβάνει σχεδόν την ίδια τιμή και για τους 4 σταθμούς,~51 sr (Εικόνα 5γ) σε συμφωνία με άλλες βιβλιογραφικές μελέτες που εξετάζουν παρόμοια επεισόδια μεταφοράς αφρικανικής σκόνης (Tesche et al., 2009; Ansmann et al., 2012; Groß et al., 2011; 2013). Αξίζει να σημειωθεί εδώ ότι ο σταθμός της Γρανάδας κατέχει την ελάχιστη μέση τιμή για τη βάση των στρωμάτων (1567 ± 788 m) και τη μέγιστη για την κορυφή (4960 ± 975 m) και το πάχος (καθ'ύψος) των στρωματώσεων. Η μεγαλύτερη όμως μέση τιμή του AOD_{532}, ίση με 0.40 ± 0.31, παρατηρείται, επίσης, για τις μετρήσεις που καταγράφηκαν στον ίδιο σταθμό, γεγονός που υποδεικνύει πυκνά στρώματα σκόνης στις περισσότερες περιπτώσεις που εξετάσθηκαν.

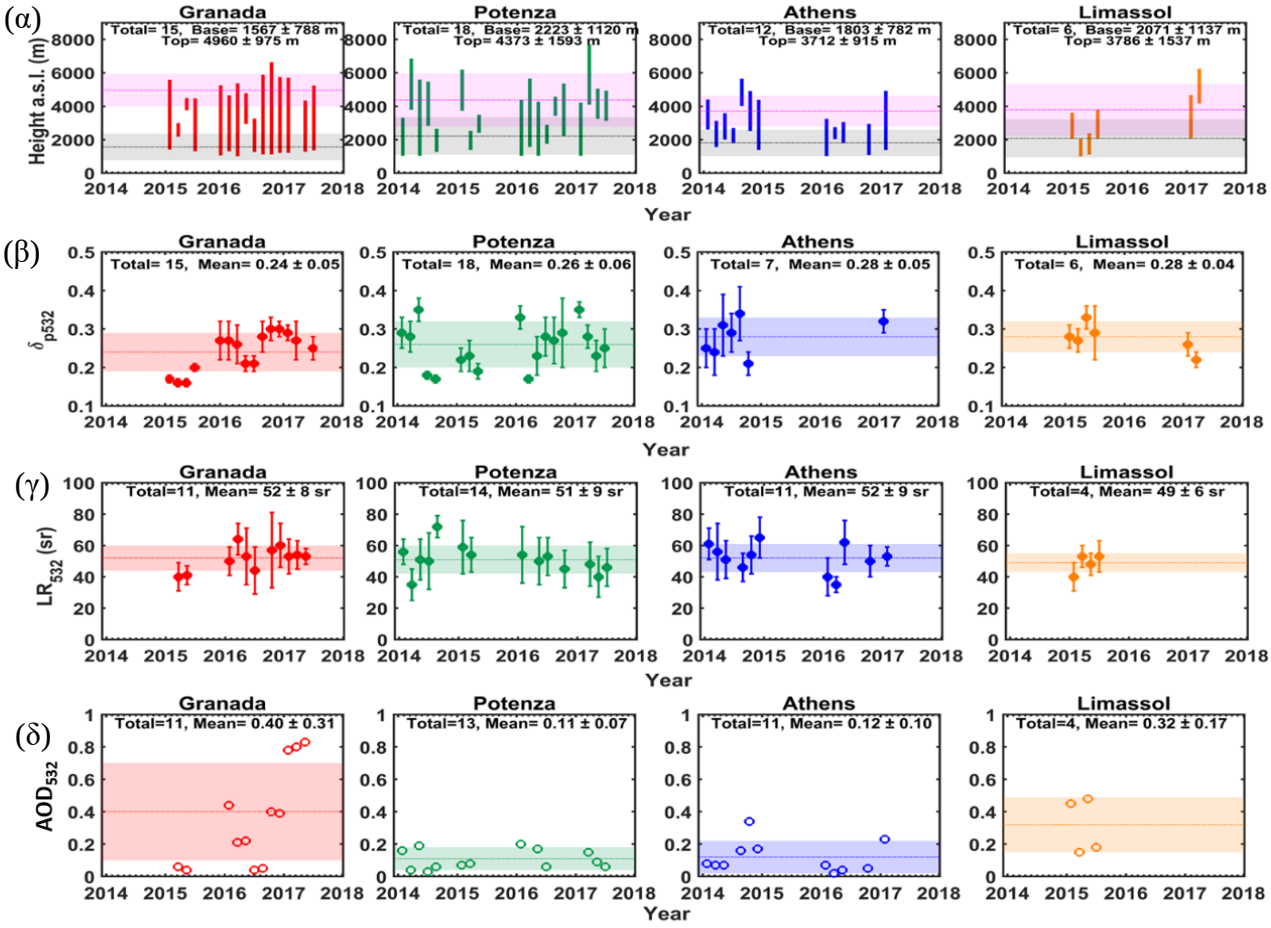

Εικόνα 5: Μέσες τιμές και τυπική απόκλιση α) βάσης και κορυφής, β) δ_{p532}, γ) LR_{532} και d) AOD_{532}, ανά μελετούμενο σταθμό (οριζόντιες γραμμές και ζώνες) και ανά περίπτωση (σύμβολα και γραμμές σφάλματος) στρωματώσεων από επεισόδια μεταφοράς σκόνης ερημικής προέλευσης.

Έχοντας ως αφετηρία την κατηγοριοποίηση που προηγήθηκε βασιζόμενη σε ένα αερομεταφερόμενο σύστημα High Spectral Resolution Lidar (HSRL) που προτάθηκε από τους Groß et al. (2013), αναπαραστήσαμε γραφικά τις παραμέτρους LR_{532} και δ_{p532} και εντοπίσαμε τρεις από τις έξι συνολικά υπάρχουσες κατηγορίες στα δεδομένα μας (Εικόνα 6). Η πρώτη κατηγορία (πράσινα σημεία-ρόμβοι) αντιπροσωπεύει μια κατάσταση ανάμιξης σκόνης Σαχάρας και σωματιδίων καύσης βιομάζας (BB & Saharan dust) και χαρακτηρίζεται από μεγάλη διασπορά μέσων τιμών LR_{532} και μικρές μέσες τιμές δ_{p532} (40 sr ≤ LR_{532} ≤ 75 sr, 0.15 ≤ δp_{532} ≤ 0.19). Η δεύτερη κατηγορία, (κόκκινα σημεία-ρόμβοι) αποδίδεται σε μια κατάσταση ανάμειξης, όπου κυριαρχούν τα σωματίδια σκόνης,

αλλά πιθανώς υπάρχουν και αερολύματα αστικής/ηπειρωτικής ή και θαλάσσιας προέλευσης (mixed Saharan dust), (40 sr ≤ LR_{532} ≤ 65 sr, 0,20 ≤ δp_{532} ≤0.29). Τέλος, η τρίτη κατηγορία (πορτοκαλί σημεία-ρόμβοι) αποδίδεται σε στρωματώσεις με σωματίδια σχεδόν αποκλειστικά Σαχαριανής σκόνης (Saharan dust), (45 sr ≤ LR_{532} ≤60 sr, 0.30 ≤ δp_{532} ≤ 0.36). Η πολυπληθέστερη και κατά συνέπεια, η πιο κοινή, μεταξύ των τριών κατηγοριών είναι αυτή που αντιπροσωπεύεται με κόκκινο χρώμα, όπως είναι αναμενόμενο, λόγω της συχνής ανάμειξης αερολυμάτων σκόνης με άλλα ηπειρωτικής προέλευσης (Papayannis et al, 2009). Τα όρια των κατηγοριών όσον αφορά, κυρίως, την παράμετρο αποπόλωσης δ_{p532}, συμπεριλαμβανομένης της τυπικής απόκλισης, δεν είναι σαφώς καθορισμένα και διακριτά αλλά αλληλεπικαλύπτεται δείχνοντας μια ρεαλιστική μετάβαση από τη μία κατηγορία στην άλλη, γεφυρώνοντας τα κενά της HSRL κατηγοριοποίησης.

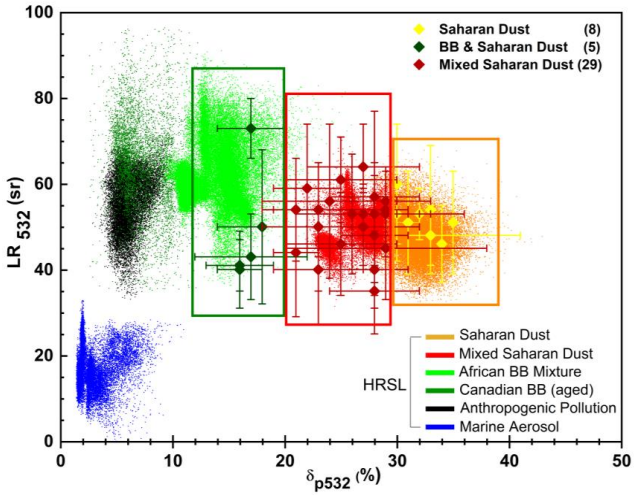

Εικόνα 6: Ζεύγος τιμών LR_{532} και δ_{p532} από μετρήσεις HSRL όπως παρουσιάσθηκαν από τους Groß et al. (2013), (χρωματιστές κουκκίδες) παράλληλα με τις επιλεγμένες μετρήσεις των τεσσάρων σταθμών του δικτύου EARLINET (σύμβολα ρόμβου και γραμμές σφάλματος).

Ο Πίνακας 2 συνοψίζει τις μέσες τιμές και την τυπική απόκλιση των γεωμετρικών, οπτικών και μικροφυσικών ιδιοτήτων των αερολυμάτων των τριών κατηγοριών, όπως προέκυψαν από την ομαδοποίηση του Εικόνας 6. Συνολικά, 5 από τις 42 περιπτώσεις μετρήσεων τοποθετούνται στην κατηγορία «BB & Saharan dust», 8 στην κατηγορία «Saharan dust» και 29 στην κατηγορία «mixed Saharan dust». Μια συνεργιστική προσέγγιση του HYSPLIT (οπισθοτροχιές διάρκειας 120 ωρών για κάθε περίπτωση) και του Google Earth (υπολογιστής γεωμετρικής απόστασης) μας επέτρεψε να εκτιμήσουμε την απόσταση που διάνυσαν (σε km) οι αέριες μάζες μέχρι να φθάσουν σε κάθε σταθμό παρατήρησης και τη διάρκεια ανάμειξης (mixing) των αερίων μαζών, ανά κατηγορία.

Από τις υπολογιζόμενες τιμές των προαναφερθεισών οπτικών παραμέτρων αερολυμάτων, παρατηρούμε ότι οι περιπτώσεις αερίων μαζών που ανήκουν κατηγορία «Saharan dust» παρουσιάζουν τη χαμηλότερη πιθανή διάρκεια ανάμειξης με άλλες αέριες μάζες (26 ± 13 ώρες), σε σύγκριση με τις άλλες δύο κατηγορίες (41 ± 26 ώρες για «BB & Saharan dust» και 31 ± 13 ώρες για «mixed Saharan dust»). Επιπλέον, οι αέριες μάζες της κατηγορίας αυτής φαίνεται να ταξιδεύουν γρηγορότερα από εκείνες των άλλων δύο, καλύπτοντας ταυτόχρονα τη μεγαλύτερη απόσταση κατά μέσο όρο (4845 ± 2825 km, εντός 120 ωρών). Η κύρια διαφορά μεταξύ των δύο υπολειπόμενων κατηγοριών (BB & Saharan dust / Mixed Saharan Dust) αποδίδεται κυρίως στο χρόνο ανάμειξης. Οι μάζες αέρα της τελευταίας κατηγορίας παραμένουν 15 ώρες περισσότερο, κατά μέσο όρο, κυκλοφορώντας πάνω από τη Μεσόγειο και την Ευρώπη, οπότε είναι αρκετά πιθανό να εμπλουτίζονται με αερολύματα διαφορετικών πηγών προέλευσης.

Όσον αφορά τις οπτικές ιδιότητες των αερολυμάτων, οι συνιστώσες β_{532} και α_{532} λαμβάνουν χαμηλότερες τιμές για τις κατηγορίες «BB & Saharan dust» και «mixed Saharan dust» (1.10 ± 0.15 x10^{-3} km^{-1} sr^{-1}, 0.47 ± 0.28 km^{-1} και 1.24 ± 0.80 x10^{-3} km^{-1} sr^{-1}, 0.74 ± 0.48 km^{-1} (αντίστοιχα) και

μεγαλύτερες τιμές (1.54 ± 1.05 x10^{-3} km^{-1} sr^{-1}, $0{,}80 \pm 0.27$ km^{-1} sr^{-1}) για την κατηγορία «Saharan dust». Κατά συνέπεια, παρατηρούνται μεγαλύτερες τιμές AOD_{532} (0.32 ± 0.25) για την τελευταία κατηγορία σε σύγκριση με τις άλλες δύο, λόγω του υψηλότερου σωματιδιακού φόρτου. Οι μεγαλύτερες τιμές των δ_{p532} (0.32 ± 0.02), υποδεικνύουν το μη σφαιρικό σχήμα των καθαρών στρωμάτων Σαχαριανής σκόνης (Freudenthaler et al., 2009) της αντίστοιχης κατηγορίας. Παρόμοιες τιμές του LR_{532} παρατηρούνται και στις τρεις κατηγορίες και, επομένως, δεν μπορούν να εξαχθούν συμπεράσματα σχετικά με την κατάσταση ανάμειξης των στρωματώσεων από αυτήν την παράμετρο, εκτός από ότι το εύρος της τυπικής απόκλισης αυτής της παραμέτρου, μειώνεται καθώς μειώνεται και το ποσοστό ανάμειξης. Επιπλέον, για τις περιπτώσεις που υπήρχαν επιπλέον διαθέσιμες μετρήσεις στο υπεριώδες μήκος κύματος (355 nm), παρατηρείται ότι η αναλογία του λογού lidar στα δύο μήκη κύματος (δηλαδή το κλάσμα LR_{355}/LR_{532}) συγκλίνει στη μονάδα για την κατηγορία «Saharan dust», υποδεικνύοντας έτσι την απουσία φασματικής εξάρτησης από την περίπτωση στρωματώσεων με σωματίδια σκόνης χωρίς επιπρόσθετη ανάμειξη (Müller et al., 2007; Veselovskii et al., 2020). Για αυτές τις περιπτώσεις, επίσης, η παράμετρος $AE_{\beta 355/532}$ τείνει στο μηδέν λαμβάνοντας μια μέση τιμή ίση με 0.35 ± 0.45.

Στο πλαίσιο αυτής τη εργασίας υπολογίσαμε, επίσης, τις μέσες τιμές και την τυπική απόκλιση των μικροφυσικών ιδιοτήτων των αερολυμάτων για κάθε μελετούμενη περίπτωση, όπως εκτιμήθηκαν από τον αλγόριθμο αντιστροφής του υπολογιστικού πακέτου SphInX για όλες τις περιπτώσεις καθεμιάς από τις τρεις κατηγορίες. Έτσι, η κατηγορία «BB & Saharan dust» λαμβάνει τη μικρότερη μέση τιμή ενεργούς ακτίνας($R_{eff} = 0.293 \pm 0.074$ μm) λόγω του εκ φύσεως μικρότερου μεγέθους των αερολυμάτων καύσης βιομάζας, ενώ ελαφρώς μεγαλύτερες τιμές παρουσιάζονται για τις άλλες δύο κατηγορίες αερολυμάτων. Οι τιμές του πραγματικού (RRI) και φανταστικού μέρους του δείκτη διάθλασης (IRI) καθώς και του συντελεστή λευκαύγειας (SSA) στα 532 nm ήταν παρόμοιες και για τις δύο κατηγορίες που δεν περιλάμβαναν αερολύματα καύσης βιομάζας, ενώ η παρουσία αυτού του είδους αερολυμάτων στην αντίστοιχη κατηγορία οδηγεί σε μεγαλύτερες τιμές RRI και IRI και χαμηλότερη τιμή SSA. Τα αποτελέσματα των μικροφυσικών ιδιοτήτων είναι σε συμφωνία με αυτά που αναφέρονται στη μελέτη των Petzold et al. (2011) στην ελεύθερη τροπόσφαιρα πάνω από το Ντακάρ (Σενεγάλη, Αφρική), για ερημική σκόνη, αλλά και για σκόνη αναμεμειγμένη με σωματίδια ανθρωπογενούς προέλευσης.

Πίνακας 2: Μέσες τιμές οπτικών, γεωμετρικών και μικροφυσικών ιδιοτήτων των τριών κατηγοριών μαζί με την τυπική απόκλιση (SD). Μηδενική τιμή SD δείχνει μη-μεταβλητότητα στην αντίστοιχη ανακτημένη παράμετρο. Ο όρος ανάμειξης (mixing) αναφέρεται στις ώρες που ταξίδεψαν οι αέριες μάζες μετά την έξοδο τους από την Αφρικανική ήπειρο.

Παράμετροι		**Κατηγορίες**		
		BB & Saharan Dust	**Mixed Saharan Dust**	**Saharan Dust**
Οπτικές ιδιότητες	**β_{532} (km^{-1}sr^{-1})**	1.10±0.15 [x10^{-3}]	1.24±0.80 [x10^{-3}]	1.54±1.05 [x10^{-3}]
	α_{532} (km^{-1})	0.47±0.28	0.74±0.48	0.80±0.27
	LR_{532} (sr)	51 ± 15	50 ± 7	52 ± 5
	δ_{p532}	0.17 ± 0.01	0.26 ± 0.03	0.32 ± 0.02
	LR_{355}/LR_{532}	0.69 ± 0.24	0.84 ± 0.16	0.98 ± 0.16
	$AE_{\beta 355/532}$	0.44 ± 0.59	0.52 ± 0.61	0.35 ± 0.45
	AOT_{532}	0.03 ± 0.02	0.15 ± 0.10	0.32 ± 0.25
Γεωμετρία και ανάμειξη	**Thickness (km)**	0.79 ± 0.21	2.08 ± 0.76	3.10 ± 1.72
	Distance (km)	3496 ± 1185	3662 ± 1617	4845 ± 2825
	Mixing (hours)	41 ± 26	66 ± 41	26 ± 13
Μικροφυσικές ιδιότητες	**R_{eff} (μm)**	0.293 ± 0.074	0.360 ± 0.081	0.387 ± 0.070
	RRI	1.50 ± 0.00	1.47 ± 0.05	1.47 ± 0.05
	IRI	0.005 ± 0.000	0.0046 ± 0.0045	0.0041 ± 0.0018
	SSA_{532}	0.9482 ± 0.0019	0.9644± 0.0181	0.9638± 0.0219
	SSA_{355}	0.9372 ±0.0070	0.9579 ± 0.022	0.9517 ±0.0264

iii) Για την ανάκτηση προσομοιώσεων της ηλιακής ακτινοβολίας αξιοποιήσαμε το μοντέλο LibRadtran version 2.0.2. (Emde et al., 2016) σε συνθήκες μέσων γεωγραφικών πλατών. Εφαρμόσαμε ένα σύνολο τεσσάρων προσομοιώσεων ανά καταγεγραμμένο επεισόδιο. Οι δύο πρώτες προσομοιώσεις αναφέρονται σε ατμοσφαιρικές συνθήκες καθαρού ουρανού με αερολύματα υποβάθρου, η μια για τη μικρού μήκους (shortwave, SW) και η δεύτερη για τη μεγάλου μήκους κύματος (longwave, LW) ακτινοβολία, αντίστοιχα, καθώς αυτές οι δύο φασματικές περιοχές αντιμετωπίζονται ξεχωριστά από το μοντέλο LibRadtran. Οι εναπομένουσες δύο προσομοιώσεις αντιστοιχούν σε ατμόσφαιρα που είναι επιπρόσθετα επιβαρυμένη με σωματίδια ερημικής σκόνης και προσμείξεις σωματιδίων, και πάλι, για τις φασματικές περιοχές SW και LW ξεχωριστά. Εδώ, οι κατακόρυφες κατανομές των στρωματώσεων για κάθε μία από τις υπό μελέτη περιπτώσεις, χρησιμοποιήθηκαν ως πρόσθετη πληροφορία εισόδου στο μοντέλο αυτό, στο οποίο επιπλέον, έγινε η παραδοχή ότι τα σωματίδια είναι μη-σφαιρικά. Οι κατακόρυφες αυτές κατανομές παρουσιάσθηκαν με 3 διαφορετικές προσεγγίσεις και συνεπώς, με τρία διαφορετικά σχήματα εισόδου στο LibRadtran: A) κατακόρυφη κατανομή συγκέντρωσης μάζας όπως προσομοιώνεται από το προγνωστικό μοντέλο BCS-DREAM8b, B) κατακόρυφη κατανομή συγκέντρωσης μάζας, μόνο για τη συνιστώσα της σκόνης, όπως υπολογίζεται μαθηματικά από το συντελεστή β_{532} και C) κατακόρυφη κατανομή του συντελεστή α_{532} μαζί με τις αντίστοιχες μέσες τιμές του AOD_{532} για κάθε μια περίπτωση. Στο τελικό στάδιο, από τις τιμές εξόδου του μοντέλου, υπολογίσαμε τις παραμέτρους ΔF, ARF, ARF_{NET} και ARF_{ATM} όπως αυτές προκύπτουν από αντίστοιχες μαθηματικές εξισώσεις.

Για τις 3 αυτές προσεγγίσεις, έχουν χρησιμοποιηθεί 30 κατακόρυφα επίπεδα μεταξύ εδάφους και ύψους 120 km, με χωρική κατακόρυφη ανάλυση 500 m ξεκινώντας από το επίπεδο εδάφους (BOA) έως 2000 m και από 5000 έως 10000 m. Ακολούθως, μεγαλύτερη ανάλυση 200 m από 2000 έως 5000 m, λόγω της παρουσίας των στρωμάτων σκόνης σε αυτό το εύρος ύψους και, επιπλέον, στα ύψη 20 km και 120 km (TOA). Όλες οι προσομοιώσεις πραγματοποιήθηκαν για τρεις διαφορετικές ζενίθιες ηλιακές γωνίες (SZA): 25^o, 45^o και 65^o, καλύπτοντας έναν τυπικό ημερήσιο κύκλο για εκτιμήσεις της ηλιακής ακτινοβολίας στα μέσα γεωγραφικά πλάτη που εξετάζουμε. Όλες οι περιπτώσεις αντιμετωπίσθηκαν για ατμοσφαιρική κατάσταση υπό ανέφελες συνθήκες. Εκτός από το υψόμετρο σε km (z_{out}), τα επιπλέον αποτελέσματα εξόδου με το τέλος των προσομοιώσεων είναι: η συνιστώσα της άμεσης ηλιακής ακτινοβολίας (e_{dir}), η ολική ακτινοβολία (e_{glo}) η διάχυτη καθοδική ακτινοβολία (e_{dn}), η αντίστοιχη διάχυτη ανοδική ακτινοβολία (e_{up}), και ο ρυθμός θέρμανσης (θερμότητα, σε K/ημέρα), όπως περιγράφεται από τους Mayer et al. (2017).

Η Εικόνα 7 απεικονίζει τα αποτελέσματα υπολογισμού του ισοζυγίου ακτινοβολιών (ARF, Aerosol Radiative Forcing) για κάθε μια από τις τρεις προαναφερόμενες κατηγορίες: «BB & Saharan dust», «Mixed Saharan dust» και «Saharan dust». Το ARF στην περιοχή ακτινοβολίας μικρού κύματος (280-2500 nm) είναι αρνητικό, τόσο στην επιφάνεια (Bottom of the Atmosphere, BOA), όσο και στην κορυφή της ατμόσφαιρας (Top of the Atmosphere, TOA) και για τις 3 κατηγορίες, ενώ η κατηγορία που περιλαμβάνει σωματίδια καύσης βιομάζας έχει σημαντικά μικρότερη επίδραση ψύξης και για τις 3 προσεγγίσεις. Το ARF φαίνεται να είναι αντιστρόφως ανάλογο με την αναλογία ανάμειξης, καθώς εκτιμώνται μεγαλύτερες μέσες απόλυτες τιμές για τη λιγότερο αναμειγμένη κατηγορία.

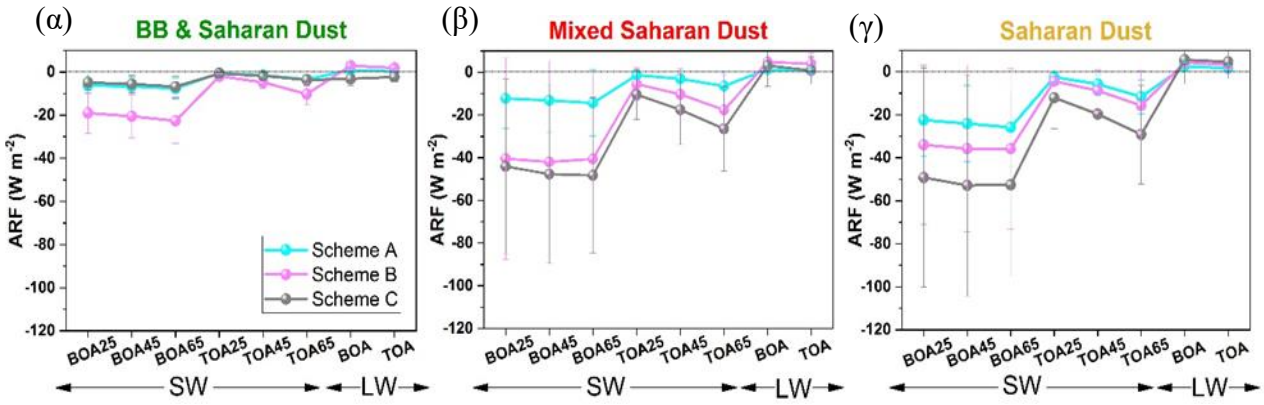

Εικόνα 7: Μέσες τιμές ARF σε SW και LW, στην επιφάνεια (BOA) και στην κορυφή (TOA) της ατμόσφαιρας μαζί με την σχετική τυπική απόκλιση για τις τρεις κατηγορίες που σχετίζονται με την κατάσταση ανάμειξης αερίων μαζών. Συγκεκριμένα α) «BB & Saharan dust»ω,β) «Mixed Saharan dust» και γ) «Saharan dust». Η διακεκομμένη γραμμή αντιπροσωπεύει την τιμή μηδέν του ARF.

Λαμβάνοντας υπόψη ότι η επίδραση του καθαρού ρυθμού θέρμανσης από τα επεισόδια μεταφοράς σκόνης, είναι πιο έντονη κοντά στην επιφάνεια για μικρές ηλιακές ζενίθιες γωνίες (SZA), οι εκτιμήσεις αυτής της παραμέτρου στην επιφάνεια (BOA) στις 25^{o} SZA για όλες τις υπό μελέτη περιπτώσεις, παρουσιάζονται στην Εικόνα 8. Καθίσταται έτσι σαφές ότι το πρόσημο του καθαρού ρυθμού θέρμανσης στο κατώτερο όριο της ατμόσφαιρας (BOA) εξαρτάται από την κατακόρυφη κατανομή των σωματιδίων σκόνης και το οπτικό πάχος (AOD). Πιο συγκεκριμένα, η πλειονότητα των περιπτώσεων με χαμηλές τιμές AOD_{532} (≤0.2) και μικρή έκταση κατακόρυφα (πάχος στρωμάτωσης ≤2 km) δίνει αρνητικές τιμές καθαρού ρυθμού θέρμανσης.

Επιπλέον, όσο υψηλότερη είναι η τιμή του AOD τόσο μεγαλύτερη είναι η απόλυτη τιμή του καθαρού ρυθμού θέρμανσης. Όσον αφορά το ύψος της βάσης της στρωμάτωσης, αυτό παίζει βασικό ρόλο στον απόλυτο καθαρό ρυθμό θέρμανσης κάθε περίπτωσης, καθώς τα στρώματα ερημικής σκόνης που ευρίσκονται κοντύτερα στο έδαφος, λαμβάνουν μεγαλύτερες τιμές απόλυτου καθαρού θέρμανσης. Για παράδειγμα, μια στρωμάτωση με βάση 2800 m, πάχος 730 m και AOD_{532} ίσο με 0.01 έχει καθαρό ρυθμό θέρμανσης -0.17 K/ημέρα, ενώ μια στρωμάτωση με βάση 3800 m, πάχος 660 m και AOD_{532} ίσο με 0.02 έχει σχεδόν μηδενικό ρυθμό θέρμανσης (-0.03 K/ημέρα). Και τα δύο αυτά επεισόδια που μελετήσαμε, συνέβησαν τον ίδιο μήνα (Αύγουστος). Σε μια άλλη σύγκριση, οι τιμές καθαρού ρυθμού θέρμανσης -0,02 K/ημέρα και +0,09 K/ημέρα αναφέρονται για δύο στρωματώσεις, κατά τη διάρκεια του καλοκαιριού που έχουν σχεδόν το ίδιο ύψος βάσης (2600 m και 2500 m) και πάχος (2300 m και 2400 m) αλλά διαφορετικές τιμές AOD_{532} (0.08 και 0.34 αντίστοιχα). Τέλος, ένας συνδυασμός μεγάλων τιμών AOD_{532} (0.21-0.83) και μεγάλου πάχους (2100-5500 m), δύο παράμετροι που συνήθως εξαρτώνται άμεσα, σε συνδυασμό με χαμηλό ύψος βάσης (1000-1500 m), δίνουν μεγάλες τιμές του καθαρού ρυθμού θέρμανσης με θετικό πρόσημο που κυμαίνεται από +0.06 έως +0.26 K/ημέρα.

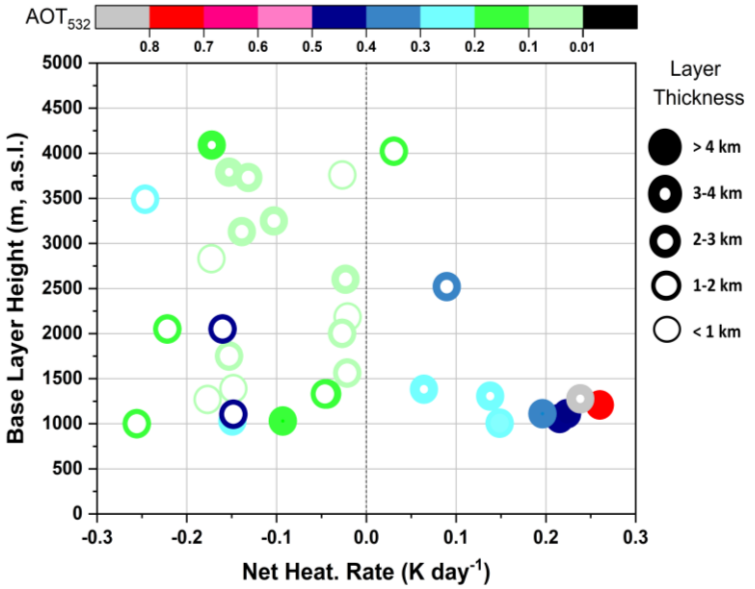

Εικόνα 8: Εκτιμώμενες τιμές καθαρού ρυθμού θέρμανσης ανά περίπτωση του Σχήματος C στο κατώτερο τμήμα της ατμόσφαιρας (BOA), στις 25° SZA, συναρτήσει του ύψους βάσης των στρωματώσεων αιωρούμενων σωματιδίων ερημικής προέλευσης. Η έγχρωμη οριζόντια κλίμακα υποδεικνύει τις τιμές $AOD_{532,}$ ενώ το πάχος συμβόλου υποδεικνύει το πάχος στρωμάτωσης.

Τέλος, στην Εικόνα 9 αναπαρίστανται οι κατακόρυφες κατανομές ARF από το έδαφος έως τα 10 km, όπως προέκυψαν από την προσέγγιση C στις 45° SZA, ανά σταθμό. Ταυτόχρονα παρουσιάζονται και οι κατακόρυφες κατανομές του συντελεστή a_{532} για το ίδιο εύρος ύψους, όπως καταγράφηκαν από τις μετρήσεις του lidar. Οι κατακόρυφες αυτές κατανομές, αμφιμονοσήμαντα, ακολουθούν την ίδια κατακόρυφη δομή, ενώ οι τιμές ARF κοντά στο έδαφος είναι αρκετά υψηλές, κατ' απόλυτη τιμή, προκαλώντας ψύξη και μειώνονται με την αύξηση του ύψους. Πιο συγκεκριμένα, το ARF κυμαίνεται από -150.0 έως -1.9 W m^{-2} για τη Γρανάδα, από -38.1 έως -3.7 W m^{-2} για την Ποτένζα, από -64.8 έως -13.2 W m^{-2} για την Αθήνα και από -90.3 έως -28.4 W m^{-2} για τη Λεμεσό, ανάλογα με την ένταση του κάθε επεισοδίου. Οι αντίστοιχες διακυμάνσεις του α_{532} είναι 0.286–0.029 km^{-1}, 0.268–0.088 km^{-1}, 0.135–0.078 km^{-1} και 0.547–0.214 km^{-1}. Οι μέγιστες τιμές α_{532} παρατηρούνται συνήθως μεταξύ 2000 και 6000 m a.s.l., υποδεικνύοντας την παρουσίας στρωμάτων σκόνης, που αποτυπώνεται σαν μια μείωση της ηλιακής ακτινοβολίας που φθάνει στη γήινη επιφάνεια, στο ισοζύγιο ακτινοβολιών.

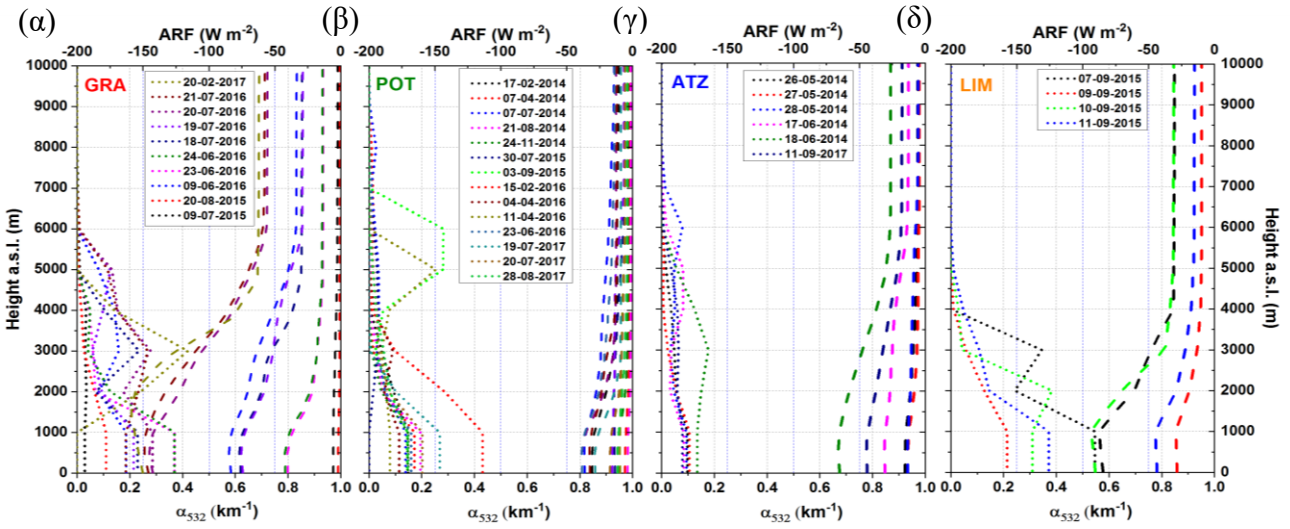

Εικόνα 9: Κατακόρυφες κατανομές του α_{532} (διακεκομμένες κουκίδες) όπως υπολογίσθηκαν από μετρήσεις του Raman lidar (EOLE) μαζί με αυτές του ARF (SW, διακεκομμένες παύλες) που υπολογίστηκαν από προσομοιώσεις LibRadtran από την προσέγγοση C για τις τοποθεσίες: α) Γρανάδα, β) Ποτένζα, γ) Αθήνα και δ) Λεμεσού, στις 45° SZA .

Συμπερασματικά, στο πλαίσιο της παρούσας διδακτορικής Διατριβής, μελετήσαμε ένα σύνολο μετρήσεων lidar, σε βάθος χρόνου 18ετίας (2000-2017), εξετάζοντας τις γεωμετρικές και οπτικές ιδιότητες των σωματιδίων ερημικής προέλευσης, από μεταφορά (έρημος Σαχάρα), στην περιοχή της Αθήνας (τοπική κλίμακα). Σε περιφερειακή κλίμακα, μελέτη τετραετούς σειράς μετρήσεων (2014-2017), από επιλεγμένους σταθμούς του δικτύου EARLINET (Γρανάδα, Ποτέντζα, Αθήνα, Λεμεσός), οδήγησε σε εξαγωγή αξιόλογων συμπερασμάτων ως προς τις γεωμετρικές, οπτικές και μικροφυσικές ιδιότητες σωματιδίων ερημικής προέλευσης, καθώς και ως προς το βαθμό ανάμειξής τους, κατά τη μεταφορά τους από την πηγή προέλευσης, στον εκάστοτε σταθμό παρατήρησης.

Επιπλέον, η σημασία της συστηματικής χρήσης μετρήσεων τηλεπισκόπησης lidar ως δεδομένα εισόδου σε μοντέλα μεταφοράς ακτινοβολίας τονίζεται στην παρούσα Διδακτορική Διατριβή, δημιουργώντας ένα βασικό εργαλείο που επιτρέπει την εκτίμηση των ακτινοβολικών επιδράσεων από διαφορετικούς τύπους αερολύματος, όπως η ερημική σκόνη και οι προσμείξεις αυτής, σε ηπειρωτική κλίμακα. Συνίσταται, επίσης, η περαιτέρω διερεύνηση της κατάστασης ανάμειξης των αερολυμάτων καθώς, όχι μόνο οι οπτικές τους αλλά και οι μικροφυσικές τους ιδιότητες και η ακτινοβολητική δράση τους μπορεί να ποικίλλουν σε μεγάλο βαθμό, ανάλογα με τους τύπους ανάμιξης και έτσι, να επιδρούν με διαφορετικό τρόπο στο ενεργειακό ισοζύγιο της γήινης ατμόσφαιρας.

TABLE OF CONTENTS

LIST OF SYMBOLS

Symbol	Description	Units
AE	Ångström Exponent	-
a_{eff}	effective aspect ratio	-
a_t	surface-area concentration	$\mu m^2 cm^{-3}$
a_{width}	aspect ratio width	-
F	fluxe	$W\ m^{-2}$
LR (λ)	Lidar ratio	sr
O(r)	Overlap function	-
r	range	m
r_{eff}	effective radius	μm
u_t	total volume concentration	$\mu m^3 cm^{-3}$
Z_{COM}	centre of mass	m
$\alpha_{aer}(\lambda)$	aerosol extinction coefficient	m^{-1}
$\alpha_{mol}(\lambda)$	molecular extinction coefficient	m^{-1}
$\beta_{aer}(\lambda)$	aerosol backscatter coefficient	$m^{-1}sr^{-1}$
$\beta_{mol}(\lambda)$	molecular backscatter coefficient	$m^{-1}sr^{-1}$
$\delta_p(\lambda)$	linear particle depolarization ratio	-
$\delta_v(\lambda)$	linear volume depolarization ratio	-
λ	wavelength	nm
$\sigma(\lambda, r)$	scattering coefficient	-
ρ	particle mass density	gm^{-3}

LIST OF ABBREVIATIONS

Abbreviation	Description
a.g.l.	Above ground level
a.s.l.	Above sea level
ABL	Aerosol Boundary Layer
AD	Analog Detection mode
AERONET	AErosol RObotic NETwork
AOD	Aerosol Optical Depth
AR	Assessment Report
ARF	Aerosol radiative Forcing
BB	Biomass Burning
BC	Black Carbon
BE	Beam Expander
BOA	Bottom of Atmosphere
CALIPSO	Cloud-Aerosol Lidar and Infrared Pathfinder Satellite Observation
CCN	Cloud Condensation Nuclei
CRI	Complex Refractive Index
EARLINET	European Aerosol Research Lidar Network
EOLE	aErosol and Ozone Lidar systEm
FIRMS	Fire Information for Resource Management System
FWHM	Full Width at Half Maximum
GUI	Graphical User Interface
HSRL	High Spectral Resolution Lidar
IFF	Interference Filters
IN	Ice Nuclei
IPCC	Intergovernmental Panel on Climate Change
IRI	Imaginary (part of) Refractive Index
Laser	Light Amplification by Stimulated Emission of Radiation
LibRadtran	Library for Radiative transfer
Lidar	Light Detection and Ranging
LRSU	Laser Remote Sensing Unit
LW	Longwave
MODIS	Moderate Resolution Imaging Spectroradiometer
NTUA	National Technical University of Athens
OPAC	Optical Properties of Aerosol and Clouds
PANACEA	PANhellenic infrastructure for Atmospheric Composition and climatE change
PBL	Planetary Boundary Layer

PC	Photon-counting detection mode
PM	Particulate Matter
PMT	Photon-multiplier
PSD	Particle Size Distribution
RF	Radiative Forcing
rMBE	relative Mean Bias Error
RRI	Real (part of) Refractive Index
rRMSE	relative Root Mean Square Error
SCC	Single Calculus Chain
SD	Standard Deviation
SphInX	Spheroidal Inversion eXperiments
SSA	Single-Scattering Albedo
SW	Shortwave
SZA	Solar Zenith Angle
TOA	Top of Atmosphere
TR	Transient Recorder
UTC	Universal Time Coordinated

Chapter 1: Introduction on atmospheric aerosols

The main objective of the present Ph.D. Thesis is to improve and enrich the knowledge on atmospheric aerosol research, focusing on issues with high scientific interest and huge impact on atmospheric and climate studies. For this purpose, many aspects have been approached: retrievals of the optical, geometrical, microphysical properties and simulations of the radiative effects of dust aerosol particles are some of these aspects of the present Thesis. Specifically, we focus on desert dust which is a major component of atmospheric aerosol, especially near desert areas.

Mineral dust particles are originated by wind erosion of the land surface in arid and semiarid regions and can be transported in long ranges from a place to another altering, not only the local, but also the regional and global climate. Consequently, dust particles play an important role in the Earth system and energy budget with impacts on climate, meteorology, ecosystems or even human health. Despite the importance of dust there are still large uncertainties related to dust and resulting effects on the radiation budget and therefore their role is still under study. The present Thesis aims to fill some of the aforementioned gaps by combining remote sensing measurements, tools, modelling and radiative transfer estimations.

1.1 Atmospheric aerosols: a historical background

The atmospheric aerosol science was first approached by physicists, chemists, and meteorologists, in a more concise way, since the 19th century. In 1930, long before the laser invention, Edward. H. Synge proposed measuring the upper air density profiles by determining the scattering intensity using an array of searchlight beams (Synge, 1930; Tuve et al., 1935). The first observations were made seven years later by Hulburt, (1937) where traces of the searchlight beams were captured using a sensitive photographic film after long exposure. Despite the innovative idea of using searchlight beams, it was not before the early 1960s and the invention of the laser (Light Amplification by Stimulated Emission of Radiation) and Q-switching techniques (Maiman, 1960; McClung, F.J. & Hellwarth, 1962) until lidar technology started to rapidly develop, together with technological advancements in lasers, optical components and photodetectors. The first atmospheric research using laser radars is attributed to Fiocco & Smullin (1963) where scattered light, presumably from dust particles, was detected along the beam pathway in the upper atmosphere. Since then, important knowledge has been added in the theory of the existence and the role of these suspended particles while new instruments have been developed.

Over the last 50 years, major aerosol types have been identified and categorized, whereas a significant amount of studies concerning the spatio-temporal distribution of aerosols to be found in different seasons and locations has been published. On the other hand, the laser remote sensing aerosol retrievals have been an area of active research for more than 40 years now. Lidar's first applications came in meteorology, where the National Center for Atmospheric Research used it to measure clouds and pollution. Nowadays, ground-based and satellite atmospheric lidars in synergy with other instruments and models are widely used in studying all the major atmospheric components such as, aerosols, gases, temperature, wind and clouds.

1.2 The importance of studying aerosols

First of all, what is the definition of aerosols? Aerosols are minute solid or/and liquid particles suspended in the air (Hinds, 1998). Their origin, anthropogenic or natural, determines their initial physicochemical properties such as the size, the chemical composition (type) and the shape. Dispersed aerosol particles always undergo changes caused by collisions and other effects such as interaction

with other components, altering their physical properties and chemical composition. The term of diameter is usually mentioned when referring to their size, however, in reality, aerosols can be found in many different shapes and morphologies depending on their origin. For instance, we can notice their presence as they scatter and absorb sunlight. Their scattering of sunlight can reduce visibility (haze) and redden sunrises and sunsets.

Aerosols interact both directly and indirectly with the Earth's radiation budget and climate. As a direct effect, the aerosols scatter sunlight. An aerosol's effect on light depends primarily on the composition and the colour of the particles. As an indirect effect, they can modify the size of cloud particles, changing the clouds' reflection and absorption of sunlight, the life-time and, thereby affecting the Earth's energy budget. The radiative effects of atmospheric aerosols have been strongly indicated by the Fifth Assessment Report (AR5) of the IPCC (2014), while their effect in visibility, vegetation and humans' health and other living species is existing too.

Depending on the season and the weather conditions, aerosol layers can make their way into the atmosphere almost anywhere on Earth, both in the troposphere and the stratosphere. Although most aerosols remain suspended in the atmosphere for short periods –typically between four days and a week– they can travel over vast distances. For example, dust plumes from the Sahara desert frequently cross the Atlantic and reach the Caribbean) (Tesche et al., 2011; Rittmeister et al., 2017) or in our case, they cross the Mediterranean Sea and find their way to Europe (Balis et al., 2006; Wiegner et al., 2011; Valenzuela et al., 2014; Nisantzi et al., 2015; Mandija et al., 2017; Soupiona et al., 2018; 2019; Fernández et al., 2019). In another example smoke plumes from wildfires in Siberia and Canada can find their way to the Arctic ice cap and Europe (Mattis et al., 2008; Baars et al., 2019; Papanikolaou et al., 2020). It is also important to mention here that over time, as urbanization and industrialization has proceeded, aerosol emissions have changed significantly. Key aerosol groups include sulfates, organic carbon, black carbon, nitrates, mineral dust, and sea salt.

1.3 Aerosols' role in climate change

Once in the atmosphere, aerosols can have a variety of impacts. All aerosols scatter and some of them also absorb the sun radiation. As a result, when found in large concentrations, they tend to scatter sunlight back to space, preventing the direct sun beam reaching the Earth's surface. This can lead to a cooling of the Earth's surface, a change in the latent heat and sensible heat fluxes, and an alteration in the distribution of heating in the atmosphere. Whilst the direct sun beam is prevented from reaching the surface, more scattered light is available and this may affect the photosynthesis. On the other hand, strongly absorbing aerosols, such as black carbon, have a warming effect. Aerosols are also indirectly linked to the climate system by changing cloud formation, characteristics, lifetime and rainfall acting as cloud condensation nuclei (CCN) or ice nuclei (IN). Lohmann and Feichter, (2005), Seinfeld et al., (2016) as well as Weinzierl et al., (2017) are some of the scientists that have extensively studied the relationship between aerosol and cloud interactions.

The term of Radiative forcing (RF) is often used to quantify and compare the potential climate impact of the various aerosol effects. RF is defined as a change in the Earth's radiation balance due to a perturbation of anthropogenic or natural origin. Global average RF estimates in 2011 relative to 1750 and aggregated uncertainties for the main drivers of the Earth's climate, from the IPCC AR5 (2014), are presented in Fig. 1.1 while the error bars represent 90% confidence intervals of the RF. The numerical values are provided on the right part of the figure, together with the column of the confidence level in the net forcing (VH – very high, H – high, M – medium, L – low, VL – very low). The RF of the total aerosol effect in the atmosphere, which includes cloud adjustments due to aerosols, is calculated to be of –0.9 [–1.9 to −0.1] W m^{-2} (medium confidence). This results from a negative forcing contribution from most aerosols and a positive one from black carbon absorption of solar radiation. Furthermore, there is a high confidence that aerosols and their interactions with clouds have

offset a substantial portion of the global mean forcing from well-mixed greenhouse gases. However, they continue to contribute to the largest uncertainty in total RF calculation.

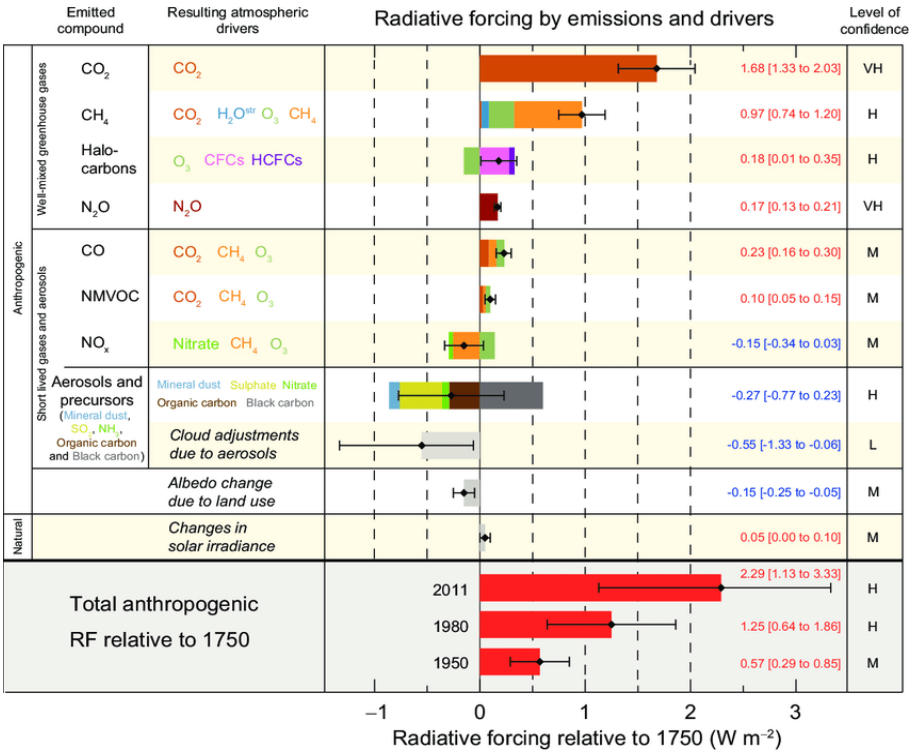

Figure 1.1: Global mean positive and negative radiative forcing and ranges since 1750 for anthropogenic carbon dioxide (CO_2), methane (CH_4), nitrous oxide (N_2O), aerosols and other important agents and mechanisms. The net anthropogenic radiative forcing and its range are also shown (IPCC, 2014).

1.4 Particle Size Distribution (PSD)

Aerosols arising both from natural (dust, sea salt, volcanic ash and volcanic sulphates) and human activities (soot, ammonium sulphate and ammonium nitrate) are often mixed together, while uplifting and travelling long distances. Directly emitted (primary) particles are distinguished from secondary particles which are formed by transformations. Each atmospheric particle mode has its specific sources. Radius or diameter characterize size of one particle, but the particles may have complex shapes and radii vary by orders of magnitude. More specifically, the size range spans over 5 orders of magnitude (~1 nm – ~100 μm). Size affects both the lifetime and the physical and chemical properties. The atmospheric aerosols can be described rather well with a set of log-normal distribution functions (normally distributed in logarithmic scale) (Seinfeld and Pandis, 2006).

As Fig. 1.2 depicts, nucleation particles form by condensation of super-saturated gases, Aitken particles from the nucleation mode or incomplete combustion (e.g. soot) processes, the accumulation mode particles from the Aitken particles or intensive mechanical processes and the coarse particles from the accumulation mode particles and moderate mechanical processes (e.g. abrasion of mineral dust, volcanic ash, sea spray). In most cases the aerosol modes are not monodisperse. Usually, the lowermost particle diameter is of the order of 1 nm because in terms of kinetics all particles with diameters smaller than 1 nm should be categorized as ion clusters (Laakso, 2004).

Depending on the different particle sizes, aerosols are fount at different heights in the atmosphere. A distinctive nucleation mode usually appears close to boundary layer aerosol sources and in the upper troposphere because the nucleation mode particles are converted into Aitken mode particles by coagulation. A considerable number of accumulation modes are always present in aged aerosol layers as they have been matured by aging of the nucleation mode and sedimentation takes

place slowly. On the other hand, the coarse mode aerosol particles feature efficient sedimentation activities. Therefore, these particles mainly can be found close to source regions of primary aerosols.

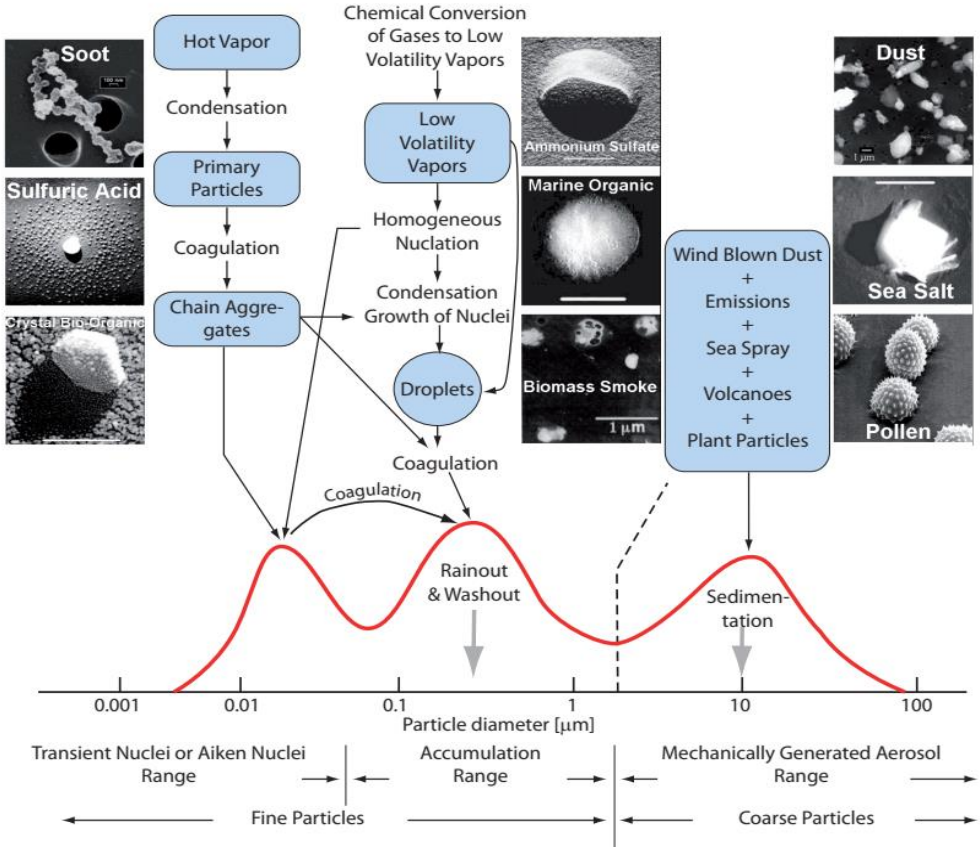

Figure 1.2: Schematic multi-modal particle size distribution with typical formations, sources and removal mechanisms. Example particle types included (Figure adapted from Zieger, (2011). Original source: Whitby, 1978; Seinfeld and Pandis, 2006).

1.5 Aerosol sources and typing

The majority of atmospheric aerosols that can be found suspended in the atmosphere (nearly 90%) originate from natural sources. Sea salt from ocean waves and dust from deserted regions are two of the most abundant aerosol types (Textor et al., 2006). However, volcanos eject huge columns of ash into the air during an eruption and the forest fires eject biomass burning aerosols and organic carbon aloft. Though less abundant, another portion of aerosols is considered of anthropogenic origin and can often dominate the air inside the Aerosol Boundary Layer (ABL) of urban and industrial areas.

There are two broad categories of aerosols: the *primary* aerosols which are generated or emitted as solid particles (e.g. Saharan dust, sea salt or soot) and the *secondary* aerosols that are formed from primary pollutants in the atmosphere through chemical reactions (e.g. ammonium sulphate aerosols are formed from the gases sulphur dioxide and ammonia, whilst organic aerosols are formed by chemical reactions acting on chemicals such as isoprene which is emitted by vegetation). However, aerosols are often classified according to their composition, origin, or size.

Table 1.1 summarizes these three large categories and what they include. Particle size is sometimes also classified according to "PM" (particulate matter) thresholds, particularly in characterizing the health effects of air pollution. $PM_{2.5}$ particles are those smaller than 2.5 µm in diameter, while PM_{10} includes all particles smaller than 10 µm.

Table 1.1: Aerosol classification according to their composition, origin and size.

AEROSOL CLASSIFICATION		
Composition	**Origin**	**Size**
• Soluble materials (sea salt, ammonium sulfate, or ammonium chloride, natural and anthropogenic • Mineral (e.g., dust; constituents of sand or soil) • Carbonaceous (black carbon and organics) – e.g. smoke • Biogenic (created by living organisms) • Volcanic (often sulfate aerosols from the oxidation of sulfur dioxide, ash) • Secondary organic aerosol (formed from condensed gases) • Mixtures of the above types	• Marine: arising mostly from the evaporation of sea spray • Continental: dust and the result of photochemical reactions • Biomass burning • Volcanic • Human-made: the result of combustion or photochemical reactions involving pollutants.	Fine mode (≤ 2 μm diameter): • Aitken particles (mostly < 0.2 μm in diameter); • Large or accumulation-mode particles (0.2 to 2 μm diameter). Coarse mode (> 2 μm diameter): • Giant particles (>2 μm diameter); • Ultragiant (> 20 μm diameter).

1.5.1 Mineral dust aerosols

Mineral dust aerosols originate as soil emitted loft particles loft into the atmosphere by wind erosion activities having radii ranging from about 0.1 to 50 μm (Duce, 1995) with non-spherical shapes. The soil is most vulnerable to erosion in dry regions, where particles are only loosely bound to the surface by the low soil moisture. Larger particles may fall out near the source region, but smaller particles can be transported thousands of kilometres (km) downwind. The radiative effect of each particle depends upon its cross-sectional area, so that the smallest particles, which have the longest atmospheric lifetimes, also have the largest radiative effect per unit mass (Miller and Tegen, 1998). Dust aerosols both reflect and absorb sunlight that would otherwise reach the surface (Lacis and Mishchenko, 1995; Tegen et al., 1996).

1.5.2 Sea salt - Marine aerosols

These aerosols are emitted into the atmosphere through the evaporation of sea surface spray mainly driven by wind. They can be formed both from primary and secondary processes. Spray droplets are regarded as the largest aerosols having radii of approximately 0.5-5 μm and a considerable mass and are readily deposited on the ground. The marine aerosol consists predominantly of chlorides (~88.7%) and sulphates (~10.8%), whereas other chemical substances make up a mere 0.5% of the total mass (Gustafsson and Franzén, 2000). Sea breezes are usually conducive to the transport of marine aerosols over land areas (Derimian et al., 2017). Atmospheric sea salt plays important role in marine cloud formation and atmospheric chemistry (Cochran et al., 2017).

1.5.3 Smoke and Biomass Burning aerosols

Biomass Burning (BB) aerosols are emitted into the atmosphere by intense forest or agricultural fires, savannah grass, and other types of vegetation, occurring most frequently in the tropical or subtropical regions during drought periods. Emissions from burning vegetation include elemental carbon (EC) and organic carbon (OC) as well as other particulate substances, together with gases such as CO_2, CO, NO_x, CH_4, and nonmethane hydrocarbons (NMHCs). Combustion processes generate particles varying in size (smaller than 0.2 μm up to a few microns, representing coarse-mode particles, ≥2 μm). BB particles are considered spherical to nearly-spherical while differentiations are observed between fresh and aged smoke aerosols (Nicolae et al., 2013; Baars et al., 2019). Black Carbon (BC) is produced primary from the incomplete high-temperature combustion of fuels (fossil

and bio-) and biomass. Naturally, as the combustion process is never complete (i.e., partial oxidization to CO_2), various gases, organic carbon (OC) and BC are released into the atmosphere. The amount of BC to OC depends on the burning material.

1.5.4 Volcanic ash

Volcanic aerosol emissions are a powerful natural driver of year-to-year and decade-to-decade variations in climate. Volcanoes emit fine ash and sulfur dioxide gas (SO_2), which reacts with water in the atmosphere to form sulfuric acid (H_2SO_4). Volcanic ash particles may be transported over large distances of several thousand kilometres while smaller particles of a few microns and below may even travel around the world (Papayannis et al., 2012; Kokkalis et al., 2013; Vernier et al., 2016). When volcanic plumes are emitted powerfully enough to reach the stratosphere, the H_2SO_4 can form a persistent haze of liquid droplets, reflecting away sunlight and cooling the earth. In other words, introduction of H_2SO_4 aerosols into the stratosphere will increase the albedo of the Earth, which is essentially the reflectivity for incoming solar radiation.

1.5.5 Urban aerosols

Urban aerosol layers are dominated by anthropogenic sources. Their origin may be either primary (direct emission into the atmosphere) or secondary (post-emission formation in the atmosphere). Aerosol mass concentrations in urban areas range from a few tens of $\mu g/m^3$ to 1 mg/m^3 during air pollution episodes in heavily polluted cities in developing countries (e.g. Jiang et al., 2015). Health impacts of particles in urban atmospheres have long been well documented (Harrison, 2004).The World Health Organization (WHO, 2005) has introduced the air quality guideline that is an annual mean concentration guideline for particulate matter. This guideline is intended for worldwide use but have been developed to support actions to achieve air quality that protects public health in different contexts. It stipulates that $PM_{2.5}$ should not exceed 10 $\mu g/m^3$ annual mean, or 25 $\mu g/m^3$ 24-hour mean and that PM_{10} cannot exceed 20 $\mu g/m^3$ annual mean, or 50 $\mu g/m^3$ 24-hour mean.

1.5.6 Bioaerosols

The bioaerosols are airborne particles of biogenic origin (e.g. bacteria, viruses, fungi, fungal spores), which are various fragments or sub-products released from living organisms (e.g. pollen) (Ariya et al., 2009). They are considered as coarse mode aerosols since they have sizes ranging from 10 nm to ~100 μm (depending on their origin). The bioaerosols have been under intense study during the last decades due to their impact on human health (diseases, allergies etc) and also as climate players (acting as CCN or IN) (Fröhlich-Nowoisky et al., 2016). Recent observations and studies indicate that there are significant emissions of bioaerosols not only from terrestrial ecosystems (Després et al., 2012; Fröhlich-Nowoisky et al., 2016) but also by the sea surface (Aller et al., 2005; Wilson et al., 2015).

Chapter 2: Atmospheric Optics - Interaction between light and matter

Several optical phenomena govern the propagation of light through the atmosphere. In this section, some of the basic interactions between light and atmosphere, such as the transmission, absorption, emission and scattering will be presented. Although all these interactions can be considered as part of an overall radiative transfer process within the Earths' atmosphere, we will treat them as distinct optical phenomena: molecular absorption, Rayleigh scattering, aerosol (Mie) scattering, Raman scattering, depolarization and fluorescence. Each of these basic phenomena will be discussed here as a brief outline of the fundamental laws governing the transmission of light in the atmosphere centred around the Beer-Lambert law.

Light interaction with particles

The Beer-Lambert law describes the exponential decay of the intensity of light propagating in an absorptive medium within a distance L:

$$I = I_0 e^{-\alpha(\lambda)L} \tag{2.1}$$

where I_0 is the incident light intensity, I is the light intensity transmitted through the medium in the forward direction (i.e. parallel to the incident light), and the $\alpha(\lambda)$ is the volumetric extinction coefficient.

This law, consequently, relates the attenuation of light to the properties of the atmospheric volume through which light is traveling. It describes also the relationship between the absorbance and the concentration of an absorbing species and implies that both the type and the concentration of the molecules are important in the process of the radiation absorption.

Let us describe now the Transmittance (T) of an atmospheric volume as follows:

$$T = \frac{I}{I_0}, \quad 0 < T < 1 \tag{2.2}$$

where I_0 is the intensity of the incidal light and I the intensity of the transmitted light. The absorbance (A) has a logarithmic relationship to the transmittance given by:

$$A = log_{10}\frac{I_0}{I} = -log_{10}T = \varepsilon c l \tag{2.3}$$

where ε is a constant called molar extinction coefficient of the attenuating species and is a measure of the probability of the electronic transition involved in the absorption process, c is the concentration of the attenuating species and l is the length of the light path.

2.1 Atmospheric structure and composition

The Earth's atmospheric layers are characterized by variations in temperature resulting primarily from the absorption of the incoming solar and outgoing Earths' radiation: Specifically, atmosphere has a series of 5 layers, each with its own specific characteristics: the troposphere (up to 8-15 km in altitude, depending on the latitude), the stratosphere (8-15 up to 50 km), the mesosphere (50-85 km), the thermosphere (85 to between 500 and 1000 km) and the exosphere (>500 or >1000 km). Our main interest is centered around the troposphere, which is the lowest layer of Earth's atmosphere and nearly all the weather phenomena occur. In the troposphere, mostly 99% of the water vapor in the atmosphere is found mixed in different layers. Tropospheric aerosols emitted in this layer can travel over long

distances in many different altitudes as wind favour their uplift and transport. Air pressure drops, and temperature gets lower, as you move vertically inside this layer.

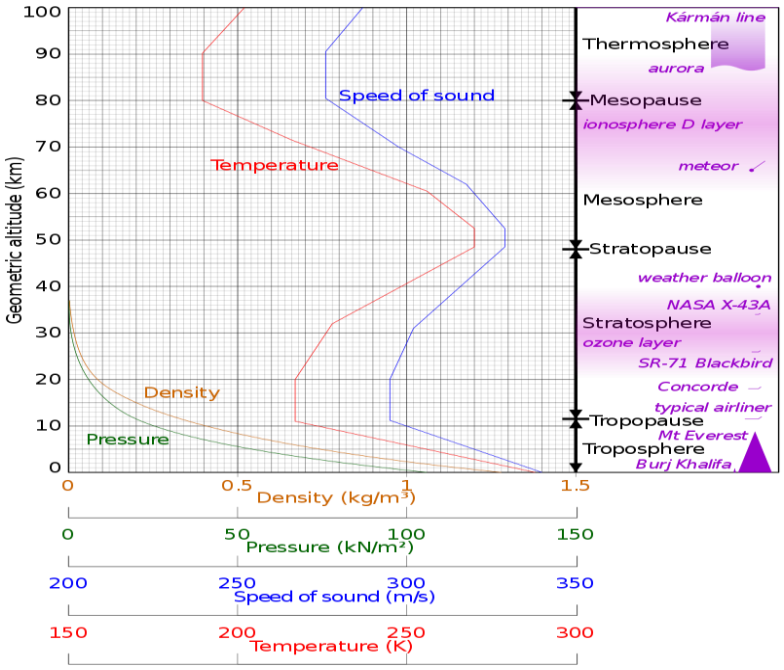

Figure 2.1: Atmosphere graph of geometric altitude versus air density, pressure, the speed of sound and temperature wit approximate altitudes of various objects (adapted from US Standard Atmosphere, 1962).

The *Planetary Boundary Layer* (*PBL*) is the lower part of the troposphere where the majority of the human activities take place and the air flow field is strongly and directly influenced by the interactions with the surface. The thickness (depth) of the PBL is not constant. The physical mechanisms which contribute to the diurnal variation of the PBL structure are mainly the evaporation and transpiration, the heat transfer, the frictional drag, the pollutants emission and the terrain-induced flow modifications. During daytime, there is a statically-unstable Mixed Layer (ML) which reaches its maximum depth in late afternoon (cf. Fig.2.2) due to the solar heating of the ground. At night, a statically Stable Boundary Layer (SBL) forms under the neutral Residual Layer (RL). The RL contains the pollutants and moisture from the previously developed ML, being not very turbulent. The layer close to the surface is the so-called surface layer (SL). The free troposphere is clearly separated from the ML by the so-called Entrainment Zone (EZ). During nighttime, the turbulence is diminished in the EZ but a nonturbulent separation layer, called capping inversion, remains. More details about the PBL structure and dynamics can be found in Stull (1988).

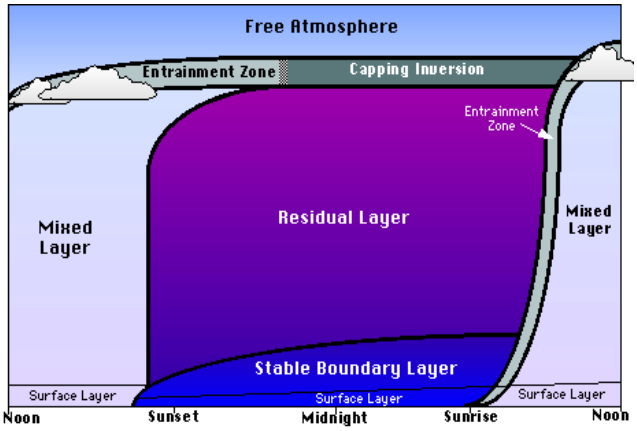

Figure 2.2: Structure of the Planetary Boundary Layer (Adapted from Stull, 1988).

2.2 Atmospheric optical phenomena measured by remote sensing techniques

2.2.1 Absorption of light

Absorption is one possible result of the interaction of electromagnetic radiation and matter. The process of absorption means that a substance captures and transforms energy. For a photon to be absorbed it has to be of a particular wavelength (λ) (or energy) and because of the principle of conservation of energy, the absorption of light induces a change in the energy state of the atom (or molecule) by either an electronic, vibrational, or rotational transition. The absorption lines of gases provide information on temperature and pressure. Figure 2.3 shows the absorption spectra of some of the most important trace gas molecules in the spectral region between 3 and 5 μm.

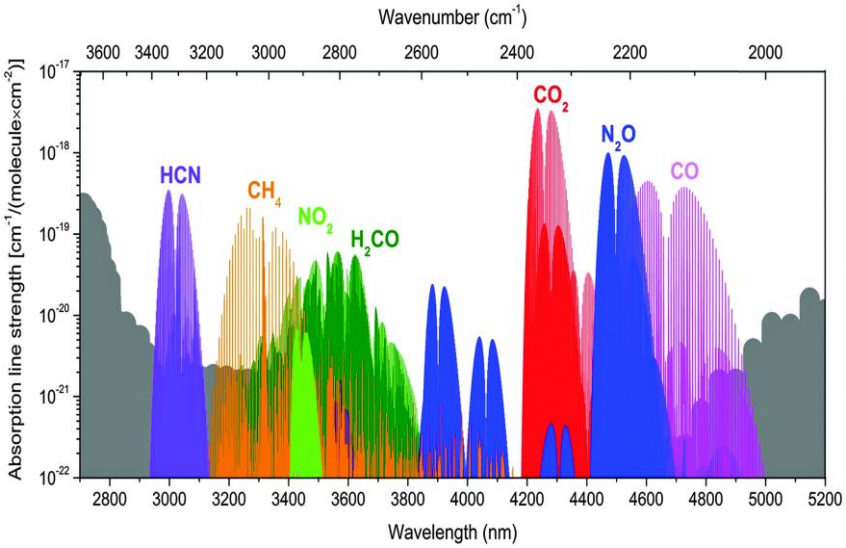

Figure 2.3: Absorption spectra of some important trace gases in the wavelength region 3-5 μm. The solid grey background shows the water vapour absorption. This figure shows only the absorption line strengths per molecule, without taking into account the abundances of the molecular species. The molecular line data are derived from the HITRAN 2012 database (Figure adapted by Vainio and Halonen, 2016).

2.2.2 Transmission of light

Transmission is the passage of electromagnetic radiation through a medium leaving the frequency of the radiation unchanged. The transmittance of a medium is defined, as shown previously, by the ratio of transmitted radiant to incident radiant light intensity. The total transmittance is further subdivided in regular transmittance and diffuse transmittance, which are given by the ratios of directly transmitted radiant power and diffusely transmitted radiant power to incident radiant power, respectively.

2.2.3 Scattering of light

In addition to being absorbed or transmitted, the propagating electromagnetic radiation in the atmospheric volume can also be scattered by the suspended particles in the atmosphere. The term scattering is mostly used for diffuse scattering, where light is sent into a wide range of directions. The amount scattered in any direction forms a pattern that is described by the single scattering phase function P(θ), where θ is the scattering angle that is the angle between the scattered light and the forward direction. The backscatter corresponds to θ = 180°, while forward scattering corresponds to θ = 0°. Details about the backscatter coefficient will further be presented in the Chapter 3 (Sect. 3.1 and 3.4).

The *elastic* scattering occurs when there is no loss of energy of the incident photon and thus, the λ of the scattered light is not changed. The elastically scattered photons can change direction but do not change their inner energy and λ. In other words, the oscillating electric field of a light wave acts on the charges of the "particle", causing them to oscillate at the same frequency. The "particles" (individual aerosol particles, atoms or molecules), therefore, become small radiating dipoles whose radiation we see as scattered light. *Mie* and *Rayleigh* scattering are the two elastic scattering processes. The first one occurs when the scattering "particles" have a similar size as the λ of light and is particularly relevant for meteorological optics. The second one occurs when the "particles" are much smaller (radius less than approximately 1/10) than the λ of the radiation.

The *Rayleigh* scattering results from the electric polarizability of the particles. The strong wavelength dependence of the scattering ($\sim\lambda^{-4}$) is the reason for the blue colour of the sky and for the redden sunrises and sunsets.

The *Inelastic* or *Raman scattering* occurs in molecules when the kinetic energy of an incident photon is increased (Stokes Raman scattering) or reduced (anti-Stokes Raman scattering) during the molecular interaction. By measuring the energy difference between the incident electromagnetic radiation and the scattered electromagnetic radiation, important information about the vibrational energy and frequencies can be obtained.

Figure 2.4 illustrates the rotational-vibrational Raman spectra of several atmospheric molecules such as oxygen (O_2), nitrogen (N_2) and water vapor (H_2O) in gas, liquid and solid phase. The incident light at 355 nm excites the atmospheric nitrogen molecules which emits light at the 1st Stokes line at 387 nm. When the incident beam is at 532 nm, the Raman scattered photon is detected at 607 nm. Therefore, a lidar system based on the Raman scattering can also detect Raman lines of the water vapor at 407 nm for an incident light beam at 355 nm. Thus, it appears that a spectrally resolved analysis of the backscattered radiation allows the measurement of various atmospheric species. Usually, the Raman scattering gases with well-known mixing ratios in the atmosphere (i.e. O_2, N_2) can be used as calibration values in this process.

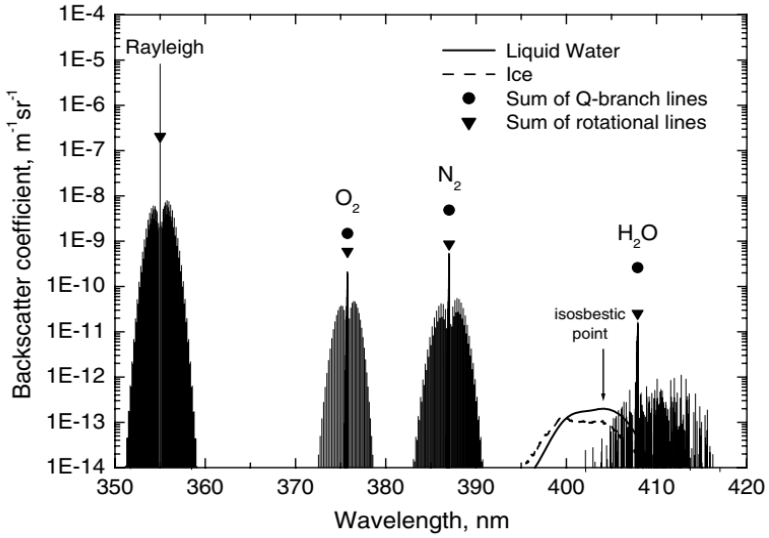

Figure 2.4: The Raman backscatter spectrum of the atmosphere for an incident laser wavelength at 355 nm (atmospheric pressure at the sea level, temperature 300 K, N_2 and O_2 content of 0.781 and 0.209, respectively, and water-vapor mixing ratio of 10 g/kg). The curves for liquid water and ice are arbitrarily scaled (Adapted from Wandinger, 2005).

2.2.1 Extinction (or Attenuation) of light

Atmospheric extinction is the sum of the scattering and absorption processes, so it represents total the effect of the light passing through a medium. In the atmosphere, aerosol particles can scatter and absorb solar and the Earths' radiation altering the air temperature and the rates of photochemical

reactions. The key parameters that govern the scattering and absorption of radiation by a particle are: i) the λ of the incident radiation, ii) the size of the particles, expressed as a dimensional size parameter x: $x\,{}^{\pi D}/_{\lambda}$, where D is the particle diameter, and iii) the complex refractive index (CRI) of the particle m: $m = n + ik$, where n is the real part, responsible for scattering and k the imaginary part of the refractive index, responsible for absorption. Both n and k depend on λ and the chemical composition of the particle. Therefore, the knowledge of the vertical profiles of the aerosol CRI is of primary importance when we study the energy equilibrium of the Earth through the attenuation of the atmospheric radiation by aerosols, gases and/or clouds. In order to solve the radiation transfer equation, one requires information of the optical properties of the gases and particulates (such as extinction coefficient, single scattering albedo, scattering phase function, asymmetry parameter etc.).

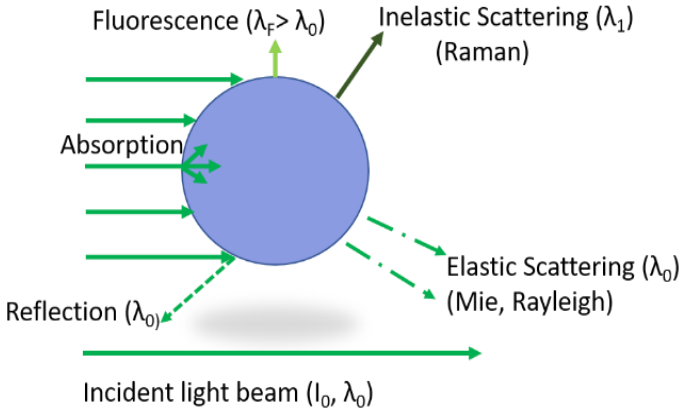

Figure 2.5: Interaction of light with a spherical aerosol.

2.2.2 Depolarization of light

It is well documented that atmospheric particles may have many different shapes. This can be studied by the light depolarization effect which provides information about the nature of the scattering particles, since the Mie scattering theory indicates that depolarization is caused by non-spherical scatterers. Therefore, the Mie scattering theory can often be a very rough approximation. As long as the particles are small compared to the wavelength of the incident radiation, the actual shape does not play a major role on the scattering properties as theories for non-spherical scatterers show (Pollack and Cuzzi, 1980). If the particles are large and non-spherical, like ice crystals, fluffy soot agglomerates, mineral dust, or sea-salt particles, we cannot use the Mie scattering theory any more, but we have to apply more elaborate non-spherical scattering theories (Heller and Nakagaki, 1974; Mishchenko et al., 1996). The presence of large non-spherical particles in the atmosphere can easily be detected by lidar techniques. Spherical scatterers do not change the polarization state of a linearly polarized laser light if scattered at 180°, whereas non-spherical scatterers lead to a depolarization of backscattered radiation. Therefore, the polarization-sensitive light detection is particularly useful in the investigation of cirrus clouds and dust layers (Freudenthaler et al., 2009). When the polarization state of the laser radiation emitted is well known, it is possible to measure how much radiation is backscattered in the same polarization and how much at the perpendicular.

2.2.3 Fluorescence of light

In *elastic scattering*, except that photons in the incident beam are redirected from their original path without a change in photon energy, absorption of light by the particle can also occur. In this case, the absorbed energy can be re-radiated as thermal emission or fluorescence. While the former is believed to be the dominant process, certain aerosol particles containing bio-agents have been found to be fluorescent (Immler et al., 2005; Pan et al., 2007; Richardson et al., 2019).

Chapter 3: Aerosol Remote Sensing

This section is dedicated to the basic aerosol remote-sensing techniques and associated instruments. We will discuss the active and passive remote sensing techniques. Light detection and ranging (lidar) is an active remote sensing technique which uses electromagnetic energy in the optical (Ultra Violet to mid-Infrared) range to detect an object (target). Firstly, the lidar technique will schematically analysed (Sect.3.1) , followed by a full description of the lidar equation (Sect. 3.1.1) and the relevant detection modes of the lidar signals. Different types of lidar instruments will be presented (Sect. 3.1.5) until we focus on the instrumentation that is available at the Laser Remote sensing unit of NTUA and which was extensively used for our study (Sect. 3.2). Additionally, the lidar pre-processing methods (Sect.3.3) along with aerosol data products (Sect. 3.4) will be presented. Finally, a brief description of the other EARLINET stations, used in this study (Sect. 3.5) and the Aerosol Robotic Network of sun photometer measurements (Sect. 3.6) will be presented at the end of this Chapter.

3.1 The lidar technique

The principle behind a lidar is quite simple, aiming to determine the distance between the target and the instrument (range), and deduce the physical properties of the object based on interaction of the radiation with the target through phenomena such as scattering, absorption, reflection, and fluorescence. A laser transmitter emits light pulses to the atmosphere under study: an optical assembly, usually a telescope, collects part of the scattered radiation, which, after being spectrally filtered, is fed into a photo-detector; the detected signal is then amplified, digitized and processed to retrieve atmospheric parameters of interest. The basic layout of a lidar system is shown in Fig. 3.1. The wavelengths used in lidar system depend on the application and extend from about 250 nm to 11 μm. High-power excimer and Nd:YAG lasers have been spreading out in the field since the 1980s (Ancellet et al., 1989). Excimer lasers produce ultraviolet radiation, whereas the Nd:YAG crystal emits in the infrared spectral region at a wavelength of 1064 nm. Frequency doubling and tripling with nonlinear crystals is widely used to convert the primary Nd:YAG radiation to 532 and 355 nm or even to quadrupling at 266 nm. Both laser types serve not only as direct lidar emitters, but also to pump secondary laser sources. The radiation can be shifted to longer wavelengths by stimulated Raman scattering in gases such as hydrogen and deuterium (Papayannis et al., 1990).

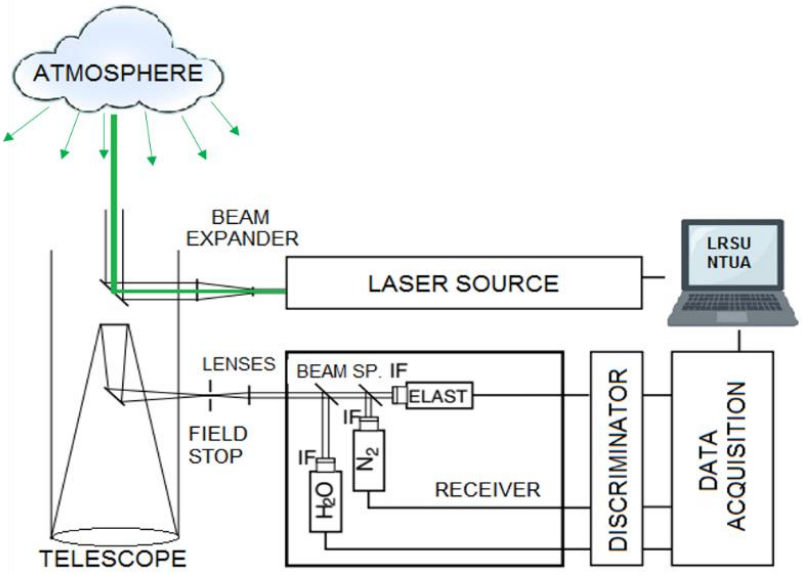

Figure 3.1: Typical illustration of a Raman lidar setup. (Original source: Wandinger, 2005).

3.1.1 The elastic lidar equation

The elastically backscattered lidar signal from a range r is given by the following equation (Weitkamp, 2005):

$$P(r,\lambda) = \frac{n\,P_0 O(r)[\beta_{mol}(r,\lambda)+\beta_{aer}(r,\lambda)]\times exp[-2\int_0^r \alpha_{mol}(r',\lambda)+\alpha_{aer}(r',\lambda)dr']}{r^2} + P_{bg} \quad (3.1)$$

P(r) is the received power from a distance r, n is an instrumental constant which contains lidar parameters describing the efficiencies of the optical and detection units [$n = \frac{Ec}{2}A_r$, where E is the energy (J), A_r is the effective telescope area (m^2) and c is the speed of light], O(r) describes the overlap between the outgoing laser beam and the receiver field of view (overlap function), $\beta = \beta_{mol}(r) + \beta_{aer}(r)$ [$m^{-1}sr^{-1}$] is the atmospheric backscatter coefficient and $\alpha = \alpha_{mol}(r) + \alpha_{aer}(r)$ [m^{-1}] is the atmospheric extinction coefficient. Both the α and β coefficients contain the molecular and the particulate contributions.

The backscatter coefficient $\beta(r)$ is the primary atmospheric parameter that determines the strength of the received lidar signal. It describes how much light is scattered into the backward direction, i.e., towards the lidar receiver. The molecular scattering (index mol) contribution, mainly occurring from nitrogen and oxygen molecules, primarily depends on the air density, thus decreases with distance (range) between the receiver and the scattering atmospheric volume. The particulate scattering (index aer for aerosol particles) is highly variable in the atmosphere on all spatial and temporal scales. Aerosol particles represent a great variety of scatterers: tiny liquid and solid air pollution particles consisting of, e.g., sulfates, soot and organic compounds, larger mineral-dust and sea-salt particles, pollen and other biogenic material, as well as comparably large hydrometeors such as cloud and rain droplets, ice crystals, hail etc.

The last term in the lidar equation, P_{bg}, includes the atmospheric background light at the detection wavelength λ, and any electronic (thermal noise and the dark current noise of the detectors used) background noise signal. The transmission term T(r) can take values between 0 and 1 and is given by

$$T(r) = exp[-2\int_0^r a(r',\lambda)dr' \text{ where, } a(r,\lambda) = \alpha_{mol}(r',\lambda) + \alpha_{aer}(r',\lambda) \quad (3.2)$$

This term results directly from the Lambert–Beer law applied on the laser light which is attenuated by aerosols and molecules. The integral considers the optical path from the lidar system to

distance r. The factor 2 stands for the two-way transmission path of the laser beam inside the probed atmospheric volume. The sum of all transmission losses represents the laser light extinction, during its propagation in an atmospheric volume within a range r from the lidar system. The atmospheric extinction is related to scattering and absorption of light by molecules (α_{mol}) and particles (α_{aer}). It is divided into scattering (index sca) and absorption (index abs) contributions and is written as:

$$\alpha(r,\lambda) = \alpha_{mol,sca}(r,\lambda) + \alpha_{mol,abs}(r,\lambda) + \alpha_{aer,sca}(r,\lambda) + \alpha_{aer,abs}(r,\lambda) \quad (3.3)$$

3.1.2 Solving the elastic lidar equation

In any form and for a specific wavelength λ, the elastic lidar equation has two unknown quantities (β and α) which is an intrinsic problem of an elastic backscatter lidar system since one has to retrieve two unknowns with only one equation. Several solutions (depending on different assumptions) have been proposed in the literature in order to solve the elastic lidar equation. Here we follow the Klett-Fernard method which is valid for highly turbid and moderately turbid atmospheres.

In order to apply it, the following assumptions have to be made: the molecular atmosphere scattering properties, $\beta_{mol}(r,\lambda)$ and $a_{mol}(r,\lambda)$ are considered known and determined from the best available nearby meteorological radiosonde data or approximated from a standard atmospheric model. Furthermore, we assume that the extinction-to-backscattering ratio (lidar ratio) for aerosols $LR(r,\lambda) = \frac{\alpha_{aer}(r,\lambda)}{\beta_{aer}(r,\lambda)}$, remains constant with range, meaning that the size distribution and composition of the aerosol scatterers are not changing with range and that the variations in the aerosol backscattering are only due to changes in their number density.

Furthermore, the lidar ratio for molecular scatterers is considered constant and equal to: $LR_{mol}(r) = \frac{\alpha_{mol}(r)}{\beta_{mol}(r)} = \frac{8\pi}{3}$.

The first step of the lidar signal processing is to subtract the background signal P_{bg} from the detected lidar signal P(r) at wavelength λ and then to define the Range Corrected Signal (RCS) as:

$$S(r,\lambda) = P(r,\lambda) - P_{bg} \quad (3.4)$$

Therefore, from eq. (3.1.):

$$RCS(r,\lambda) = S(r,\lambda) \times r^2 = n\,P_0 O(r)[\beta_{mol}(r,\lambda) + \beta_{aer}(r,\lambda)] \times exp[-2\int_0^r \alpha_{mol}(r',\lambda) + \alpha_{aer}(r',\lambda)dr' \quad (3.5)$$

Thus, the final solution is given by Klett (1981):

$$\beta(r,\lambda) = \frac{RCS(r,\lambda)\times exp\left[2(LR(\lambda)-LR_{mol})\int_r^{r_{ref}} \beta_{mol}(r',\lambda)dr'\right]}{\frac{RCS(r_{ref},\lambda)}{C\times\beta_{mol}(r_{ref},\lambda)} + 2LR(\lambda)\int_r^{r_{ref}} RCS(r',\lambda)\times exp\left[2(LR(\lambda)-LR_{mol})\int_{r'}^{r_{ref}} \beta_{mol}(r'',\lambda)dr''\right]dr'} \quad (3.6)$$

where

$$C = \frac{\beta_{mol}(r_{ref},\lambda)+\beta_{aer}(r_{ref},\lambda)}{\beta_{mol}(r_{ref},\lambda)} \quad (3.7)$$

and r_{ref} is a reference height. If at the r_{ref} there are no aerosols (aerosol free region) we can assume that $\beta_{aer}(r_{ref},\lambda) = 0$, and thus, $C = 1$.

According to Klett, the profile of the particle $\alpha(r,\lambda)$ can then be estimated from the solution $\beta_{aer}(r,\lambda)$ by $a_{aer}(r,\lambda) = LR(r,\lambda) \times \beta_{aer}(r,\lambda)$.

3.1.3 The Overlap function $O(r)$

The geometric factor $G(r) = \frac{O(r)}{r^2}$ includes the laser-beam receiver-field-of-view overlap function $O(r)$ described before and the term r^{-2}. The quadratic decrease of the signal intensity with distance is due to the fact that the receiver telescope area is part of a sphere's surface with radius R that encloses the scattering atmospheric volume (Weitkamp, 2005). The function $O(r)$ results from the combination of all geometric effects and its value starts from zero and becomes unity when the laser beam is completely imaged onto the detector through the field stop. Therefore, the effect of the overlap function on the backscattered lidar signal is eliminated above a certain altitude (called overlap height). For large telescopes the overlap function can affect the lidar return signal up to distances of several receiving kilometers (Wandinger, 2005). To minimize the distance of full overlap, the laser beam is transmitted to the atmosphere with a small tilted angle. Above that range, the backscattered light beam is totally captured by the receiver telescope. However, at any lower altitude from ground to this full overlap range, the backscattered signal is affected by the incomplete overlap function (i.e., $O(r) < 1$). Figure 3.2. graphically depicts this effect, where, at short ranges, the telescope does not "see" the laser beam. As the beam travels away from the lidar, more and more of the laser beam is "seen" by the telescope until, near the peak of the signal, the entire beam is inside the telescope's field of view ($O(r) = 1$).

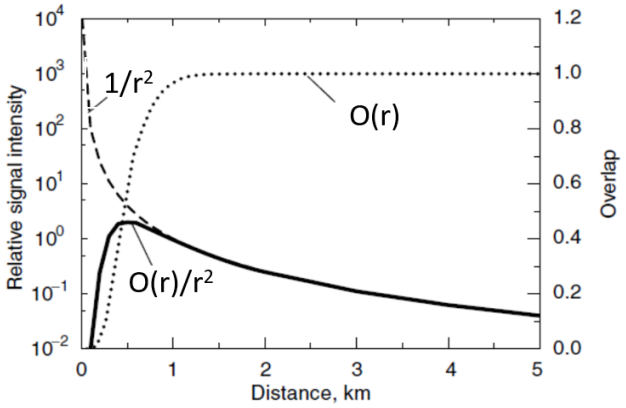

Figure 3.2: Influence of overlap function O(r), on a lidar signal (Wandinger, 2005).

3.1.4 Signal detection and gluing

For a ground-based lidar system, the backscattered light usually has large dynamic range, typically of 10-15 km. For this reason, there are two main techniques of measuring in detecting the backscattered lidar signal: Analog mode with high linearity, is efficient for measuring strong signal returns at low altitudes, typically up to 2-8 km, depending on the intensity of the laser pulse emitted and the parameter of the receiving telescope, whilst the Photon-counting mode has the capability to measure weak signals from high altitudes even up to 165 km (Du et al., 2018). In many lidar systems, the atmospheric return signal is measured in both Analog and Photon Counting modes and then combined into an entire profile by using a "gluing" algorithm before further signal processing.

i)Analog Detection mode (AD): A transient recorder operating in the AD mode is based on an analog-to-digital converter (ADC), which samples and digitizes the lidar signals with a sampling rate of 20-40 MHz (depending on the type of the Transient Recorder (TR) used) with a 12-16-bit resolution. A memory length up to 8192- or 16000-time bins, depending on the TR type, can be selected. Each time bin corresponds to a typical spatial resolution of a few meters depending on the sampling rate of the TR used. For instance, the 20 MHz sampling rate corresponds to a 7.5 m spatial resolution. Because the corresponding high time resolution is not meaningful, lidar signals are normally averaged over time intervals of a few seconds to minutes to reduce the amount of data that must be stored.

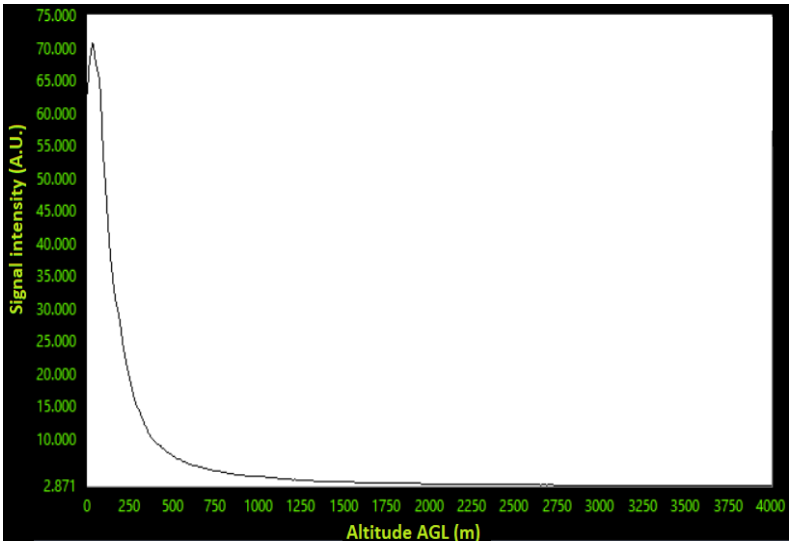

Figure 3.3: Typical lidar signal acquired in the AD mode at 532 nm.

ii)Photon-counting detection mode (PC): In this case, flux levels as low as a few tens of photons per second can be measured. In the photon counting mode the level of the incident flux is such that the cathode emits only single electrons. The individual anode charges due to single photons are integrated to produce proportional voltage pulses, which are passed through a discriminator to a pulse counter, the output of which over a pre-set time period is a measure of the incident flux. To obtain a satisfactory signal-to-noise ratio (SNR) of the lidar signal in the photon counting mode, a sufficiently large number of laser shots should be obtained (normally more than 1000). Photomultipliers (PMTs) in the PC mode are typically used in Raman lidar systems to detect signals in the UV-VIS spectral range. High quantum efficiency and low noise characteristics are required. However, the intensity of near-field signal can easily exceed the maximum counting rate of PC, which results in saturation of photon counting rate. In that case, nonlinear error introduced from pulse pile-up appears.

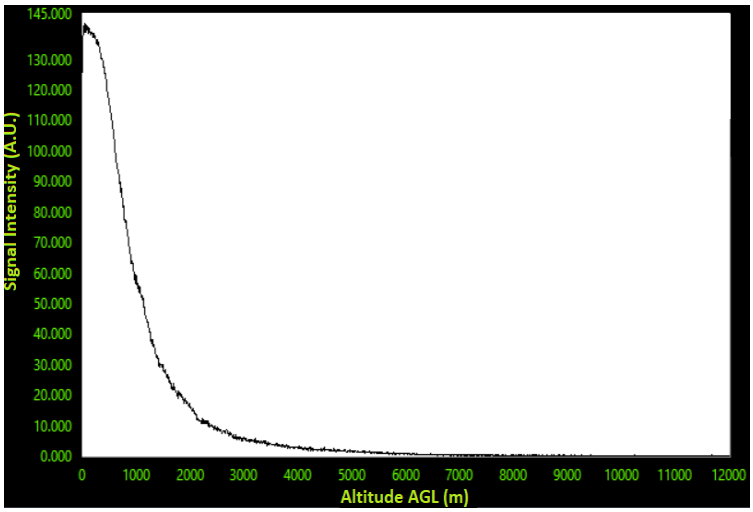

Figure 3.4: Typical lidar signal acquired in the PC mode at 532 nm.

iii) Gluing lidar signals: Although both the aforementioned methods can be used separately, the combination (gluing) of both techniques gives the advantage of generating one single lidar signal with a high linearity due to the AD conversion for high light-level signals (especially in the near range) and a high sensitivity due to the PC mode for low light-level signals (in the far range). Existing gluing algorithms solve the fitting coefficients by matching both AD and PC data over a predefined spatial range (or equivalently, over a predefined upper and lower counting rate) depending on the type of the photodetector (usually a PMT) used (D'Amico, 2016).

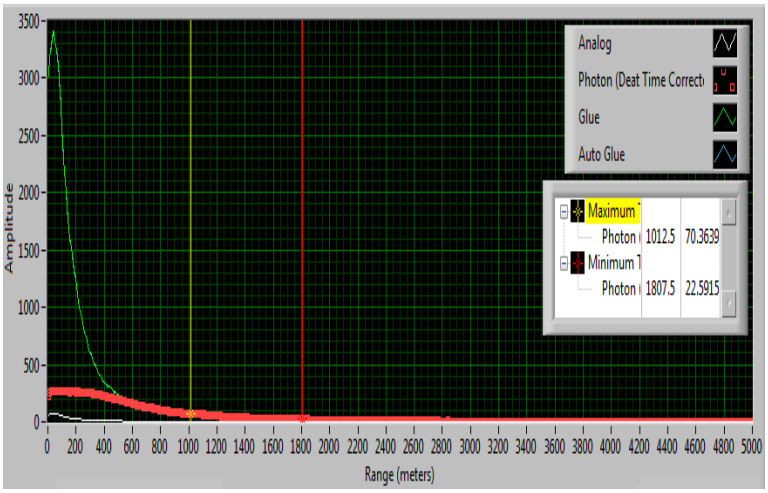

Figure 3.5: Gluing AD and PC signals within a specific height range (in meters).

3.1.5 Different atmospheric lidar types

As we have already mentioned, lidars are active optical remote sensing instruments with unique capabilities for atmospheric sounding. We will, now, shortly, focus on the most important atmospheric lidar techniques (cf. Table 3.1).

Table 3.1: Lidar types assosiated with various physical processes and the main atmospheric parameters retrieved.

Physical Process	Lidar type	Atmospheric parameter
Elastic backscatter from aerosols and clouds (Mie)	**Backscatter lidar**	Aerosols and clouds (geometrical and optical properties)
Elastic backscatter from molecules (Rayleigh)	**Rayleigh lidar**	Atmospheric density, stratospheric temperature
Absorption by atoms and molecules	**Differential-Absorption lidar (DIAL)**	Gaseous pollutants, ozone, water vapor
Absorption by atoms and molecules	**Raman Lidar**	Ozone
Scattering due to vibration and rotation of molecules	**Vibrational Raman lidar**	Water vapor, aerosols, clouds
Scattering due to rotation of molecules	**Rotational Raman lidar**	Aerosols, clouds, temperature in troposphere and low stratosphere
Fluorescence	**High-atmosphere Fluorescence lidar**	Fluorescence from atoms of metals, wind and temperature
Change in frequency due to Doppler effect (molecules and clouds)	**Doppler lidar**	Wind
Depolarization of light (aerosols and clouds)	**Depolarization lidar**	Non-sphericity and shape

3.2 Lidar instrumentation

The following section provides information on the instrumentation and the measurement techniques used to retrieve the vertical profiles of the aerosol physical, optical and microphysical properties. Special emphasis will be given to the lidar systems used to detect the mineral dust events observed over south European region. These measurements have den performed in the frame of the

European Aerosol Research Lidar Network (EARLINET) and other national/international research programs.

3.2.1 The European Aerosol Research Lidar Network (EARLINET)

EARLINET was established on May 2000 as a research project with the goal of creating a quantitative, comprehensive, and statistically significant database of the horizontal, vertical, and temporal distribution of aerosols on a continental scale. Since then, EARLINET has continued to provide the most extensive collection of ground-based data for the aerosol vertical distribution over Europe. It is undoubted that the aerosol vertical profiling in the atmosphere is particularly important and that lidar technique is the most appropriate tool for providing this information. For this purpose, long-term multiwavelength β_{aer} and α_{aer} vertical profiles are available from EARLINET (https://www.earlinet.org/) through an easily accessible database, covering the European continent.

We have to mention here that the EARLINET data must meet stringent stability and absolute accuracy standards in order to achieve the desired confidence level when used for aerosol radiative forcing needs; thus, the network has developed a rigorous quality assurance program addressing both instrument performance and evaluation of the algorithms. For the full harmonization of the data analysis and the data traceability, the EARLINET Single Calculus Chain (SCC), a tool for the automatic analysis of lidar measurements, has been developed (cf. Sect. 4.1) At present, 31 active stations distributed over Europe are part of this network (Fig. 3.6). Most of the lidar systems have been developed and run by research institutions.

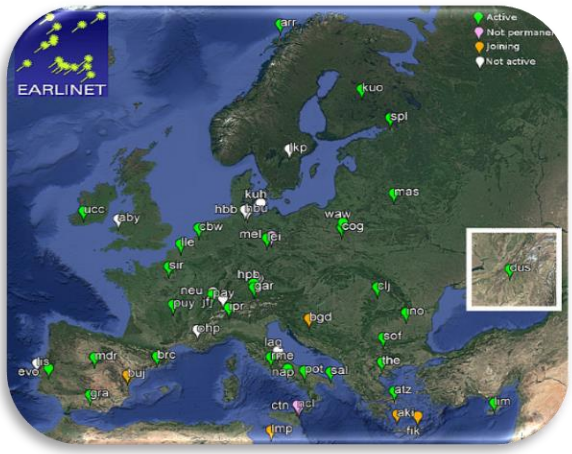

Figure 3.6: Map of the distribution of the EARLINET stations over EUROPE (last update: 06/12/2019, https://www.earlinet.org/).

The EARLINET institutional members are obliged to follow the rules as defined in the EARLINET constitution. This includes (among others) the performance of regular lidar measurements and standard quality assessment checks. Specifically, the EARLINET measurements are conducted three-times per week during preselected days (one daytime measurement and two night measurements per week) and during important special aerosol events like Saharan dust, forest fire smoke, volcanic events, photochemical smog episodes and also during CALIPSO overpasses (https://www-calipso.larc.nasa.gov/; Mattis et al., 2007; Pappalardo et al., 2010).

3.2.2 The Laser Remote Sensing Unit (LRSU) of the National Technical University of Athens (NTUA)

The Laser Remote Sensing Unit (LRSU) belongs to the Laboratory of Optoelectronics, Laser and their Applications" both at the Physics Department of the National Technical University of Athens (NTUA), Athens, Greece (37.96° N, -23.78° E, elev. 212 m a.s.l.). The mission of LRSU is to perform high-rated research on various topics of environmental sciences, such as Laser Remote Sensing of the

Atmosphere, Atmospheric Physics and Air Pollution, environmental Physics and Global Climate Change. Among others, LRSU is a founding member of EARLINET.

LRSU is equipped with i) an advanced six-wavelength elastic-Raman lidar system EOLE (aErosol and Ozone Lidar systEm) and ii) one aerosol depolarization system (DEPOLE) both members of EARLINET. Moreover, the EOLE system has been quality checked through two intercomparison campaigns, the latter of which was in 2016 against the EARLINET reference lidar system MUSA in the frame of the ATHens Lidar Intercomparison campaign (ATHLI16, Amodeo et al., 2018). MUSA stands for MUltiwavelength lidar System for Aerosol measurements, the lidar system operated by CNR-IMAA in Potenza, Italy.

3.2.3 The EOLE lidar system of NTUA

The EOLE lidar system is able to perform independent and simultaneous measurements of the vertical profiles of the aerosol backscatter β (at 355, 532, and 1064 nm) and extinction coefficient α (at 355 and 532 nm) with the use of the vibrational-Raman channels at 387 and 607 nm. Additionally, the mixing ratio of the water vapour (WVMR) is retrieved in the troposphere using the H_2O Raman channel at 407 nm. EOLE's laser source is a pulsed Nd:YAG laser system which emits, simultaneously, high energy pulses at 354.93, 532.0, and 1064.2 nm, with energies of 240, 310 and 260 mJ, respectively at 10 Hz repetition frequency. The system is designed following the optical setup of a typical EARLINET (European Aerosol Research Lidar Network) lidar system (Papayannis et al., 2020), and, as already mentioned, it meets all the quality assurance requirements of EARLINET(Amodeo et al. 2018).

The laser beam containing all three wavelengths is expanded by a Beam Expander Unit (BE) designed to provide a factory-set expansion of the laser beam to obtain a magnification factor (MF) of 3 (MF=3) and a reduction of the laser beam divergence by a factor equal to MF before being emitted, vertically, in the atmosphere. A 300 mm diameter Cassegrainian telescope (focal length f=600 mm, FOV=1.5 mrad) collects all elastically backscattered lidar signals (354.93, 532 and 1064.2 nm), as well as those generated by the spontaneous Raman effect (by atmospheric N_2 at 386.6 and 607.4 nm and by H_2O at 407.5 nm). At the entrance of the telescope a high-grade fused silica optical fiber (N.A.=0.22±0.02 and 1.5 mm core diameter) is used to transfer the lidar signals to the 6-wavelength spectrometer, which is equipped with achromatic collimating lenses, dichroic beam splitters, as well as doublets, eye pieces and interference filters (IFF) placed in front of the detectors (PMTs at 354.93-386.6-407.5-532-607.4 nm and APD -Avalanche Photo-Diode- at 1064.2 nm) (Kokkalis et al., 2012).

All optical components of the 6-wavelength spectrometer are mounted on micrometric positioners and rotators, fixed on an anti-vibrating optical table; therefore, they can be placed at an optimal position. The choice of the optical components, as well as their optimal position has been identified through advanced ray-tracing code (Zemax), by simulating the projection of the laser beam down to the PMTs' photocathodes (Kokkalis et al., 2012). Narrowband IFFs are used to suppress the atmospheric background noise at the detected wavelengths (354.93-386.6-407.5-532-607.4-1064.2 nm). In Table 3.2 the technical characteristics of the receiving system of EOLE are summarized.

The PMTs and APD output signals, are fed into fast transient recorders (Licel GmbH) working in both the analog (using 20 MHz ADCs-12-bits) and photon counting (250 MHz count rates) mode, at 8196 range bins. The 12-bit AD conversion system can store up to 4000 signal records of 8196-range bins each. However, in the case of a single acquisition only 1000 lidar returns were averaged, corresponding to a time resolution of 1.66 mins and a spatial resolution of 7.5 m. EOLE's overlap distance is of ~600 m above ground with a systems' elevation of 212 m a.s.l. The lidar signals are pre-processed and corrected for the electronic and atmospheric background noise (Sect. 3.3), prior to the retrieval of the RCS given in arbitrary units (a.u.).

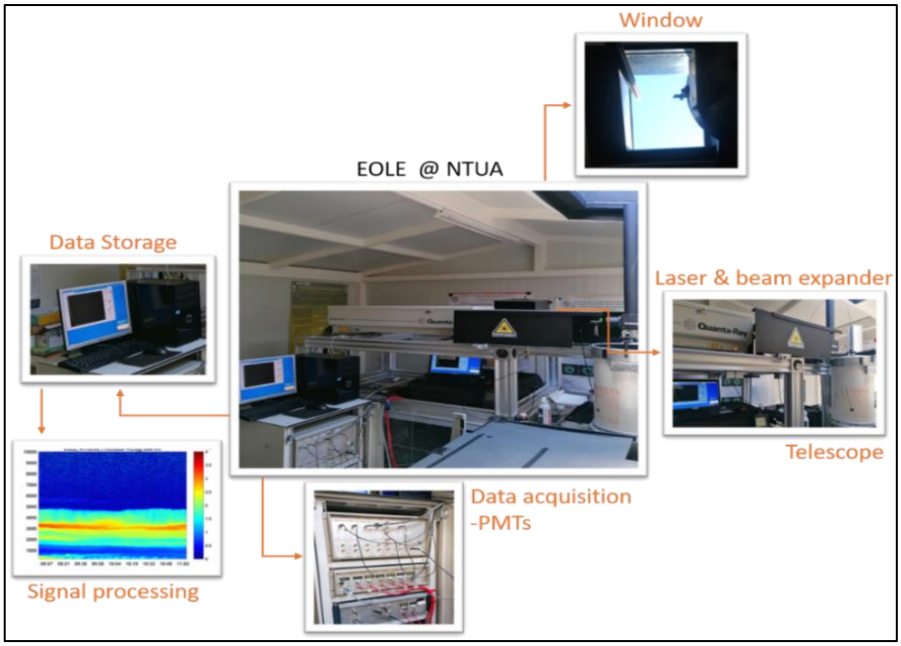

Figure 3.7: The EOLE lidar setup of NTUA.

In frame of the project "PANhellenic infrastructure for Atmospheric Composition and climatE change" (PANACEA, MIS 5021516) which is implemented under the Action "Reinforcement of the Research and Innovation Infrastructure", the EOLE lidar will be updated in order to be more automated adding also a sky camera for continuous cloud monitoring. The PANACEA project is funded by the Operational Programme "Competitiveness, Entrepreneurship and Innovation" (NSRF 2014-2020) and co-financed by Greece and the European Union (European Regional Development Fund) (https://panacea-ri.gr).

Table 3.2: Technical characteristics of the optical components of the wavelength separation system of EOLE.

TECHNICAL CHARACTERISTICS OF EOLE						
Optical components	**Channels**					
	354.9 nm	**386.6 nm**	**407.5 nm**	**532 nm**	**607.4 nm**	**1064.2 nm**
IFF bandwidth (nm, FWHM)	1.08	0.84	0.5	0.5	1.06	0.97
Transmission (%)	47.5	77.4	51	45	78.7	45.7
Out of band blocking (>OD)	6	8	10	4	6	4
Detector model-Hamamatsu	R7400P-03	R7400U-P06	R7400U-02	R7400-P02	R7400U-20	Si-APD-1.5
Eye-piece	YES	YES	YES	YES	YES	YES

3.2.4 The DEPOLE lidar of NTUA

The depolarization lidar technique consists of two receiving channels which detect the backscatter light of a linearly polarized laser beam: the backscatter beam contains two components: the perpendicular to the emitted laser beam and the parallel one. The detection of the two components allows the discrimination between different particle types in the atmosphere. At LRSU a second ND:YAG laser is used emitting a vertically polarized beam at 355 nm (> 99%), while an additional telescope (200 mm diameter, Dall-Kirkham Cassegrainian with focal length f=1000 mm) collects the elastically backscattered lidar signals at 355 nm at 2 the polarization planes (parallel and vertical) which are then optically separated by a polarizing beamsplitter cube (PBC) (Papayannis et al., 2020).

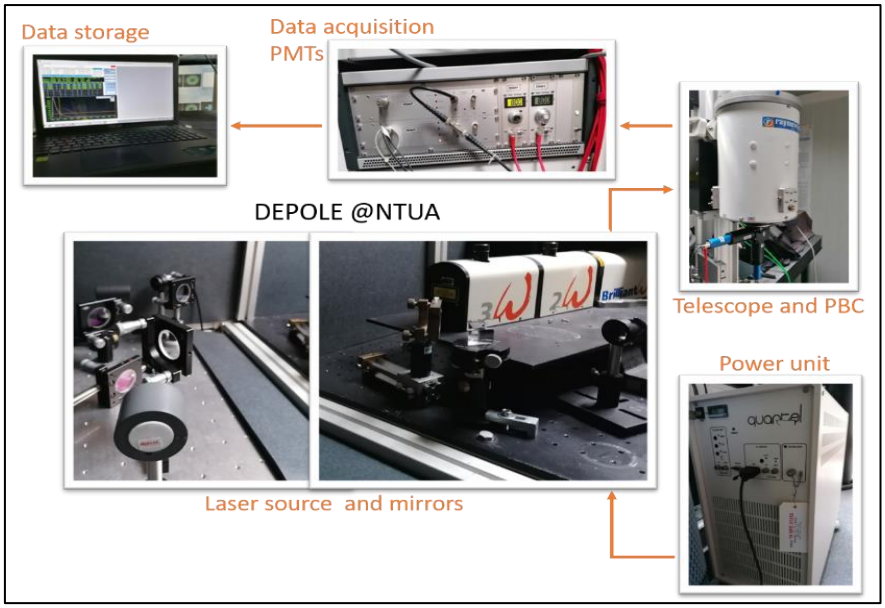

Figure 3.8: The DEPOLE lidar setup of NTUA

In frame of the PANACEA project an extra detection channel will be added to detect the vertical and parallel polarized lidar signals at 532 nm providing the vertical aerosol linear depolarization ratio at this wavelength.

3.2.5 AIAS mobile depolarization system

A van-mounted 532 nm elastic depolarization lidar (AIAS) is also available at LRSU, to provide the vertical aerosol linear depolarization ratio at 532 nm in the troposphere, thus estimating the sphericity of the probed aerosols. AIAS is based on a pulsed Nd:YAG laser system (Litron Nano SG 150-10 Series) which emits pulses at 532 nm, with energies of 95 mJ at 10 Hz. The laser beam at 532 nm is vertically polarized (>99%) using a λ/2 waveplate and expanded by a Galilean telescope (x4), before being emitted in the atmosphere (beam divergence <0.4 mrad). A 200 mm diameter Dall-Kirkham Cassegrainian telescope (focal length f=1000 mm) collects the elastically backscattered lidar signals at 532 nm (at 2 polarization planes: parallel and vertical). A secondary mirror is used to guide the backscattered light to the wavelength separation unit which is equipped with collimating lenses, dichroic beam splitters a polarizing cube, as well as doublets and very narrow IFF (0.6 nm at FWHM) placed in front of the detectors (PMTs). A PBC mounted in a rotating base, is used to separate the co-polarized and de-polarized light at 532 nm, and to calibrate the lidar signals.

Figure 3.9: The van-mounted 532 nm depolarization AIAS mobile lidar system.

In frame of the PANACEA project an extra detection channel will be added to detect the vertical and parallel polarized lidar signals at 1064 nm providing the vertical aerosol linear depolarization ratio at this wavelength.

3.3 Lidar data pre-processing steps

The lidar data pre-processing is performed on the so-called raw lidar signals. The following measurements and corrections are part of the data pre-processing and are necessary to be performed before retrieving the aerosol optical properties. They refer not only to the system itself and its electronic parts, but also to the atmospheric contribution.

3.3.1 Electronic noise correction-Dark measurements

Electronic signal background results from electronic effects (noise) of the signal detection and the data acquisition unit. Part of this noise is removed from the useful signal after subtraction of the so-called zero/dark measurements. A dark measurement is a normal measurement with sufficient time averaging, but with a fully covered telescope or with covered detectors. This signal shows all stray pick-ups and signal distortions which do not stem from the atmospheric backscatter, but only from the lidar system itself (e.g. laser flash-lamp pulse pick-ups, or system trigger pick-ups). All lidar system parameters (e.g. detector high voltage, must be set at the same value as for all normal measurements.

3.3.2 Trigger delay correction

The trigger delay is the time delay occurring between the start of the emitted lase pulse and the time in which the acquisition system starts to detect the lidar signal. This effect can cause critical errors in the near-range signal up to about 1 km range. Especially the Raman signals can be distorted dramatically, because the signal slope in the near range changes very much when the trigger delay for the range correction is varied. Therefore, the so-called trigger delay has to be measured.

3.3.3 Atmospheric background correction

When retrieving lidar profiles, it is necessary to take extra precautions to carefully remove not only outliers, spikes, and electronic contamination from each profile in the signal useful regions, but also in the background (very far) region. Any contamination of the signal in the background region has the same order of magnitude as the true signal and, thus, produces a disproportionate effect on the lidar profile. The atmospheric background noise including sunlight and cosmic noise is not range-dependent. Thus, it should be determined at the very far range of the lidar profile, where the transmitted laser beam has been totally attenuated and hence only atmospheric background and cosmic noise might be present.

3.3.4 Dead time correction

One of the main hardware limitations of the PC mode is that this acquisition mode presents a dead time, which means that there is a period of insensitivity after a photon detection during which arriving photons cannot be registered. The relationship between the true number of photons N′ and the observed ones N, from a single photon pulse is: $N' = \frac{N}{1-N\frac{\tau_d}{\tau_s}}$, where τ_s is the sampling time and τ_d is the dead time. At short ranges, where the backscatter lidar signal is strong, the number of uncounted photons is significant and can lead the system to saturation. Therefore, in this case, the number of the true photons has to be calculated.

3.3.5 Depolarization calibration (± 45º)

In a polarization lidar system, the two polarization components are separated in the receiver by means of a PBC. However, this separation is not perfect. Furthermore, the PBC might be misaligned with respect to the polarization plane of the emitted laser beam and the sensitivity for each channel can

be different (for example different filters and different High Voltages at the PMTs). Thus, the polarization system needs a careful calibration and the accurate measurements of the depolarization ratios strongly depend on the exact calculation of the system calibration constants including the calibration factor V* (Freudenthaler et al., 2009). This parameter includes the effects of different responsiveness for the two detection modules which are part of the depolarization channels but also the crosstalk of the PBC module and optics diattenuation after the calibrator. A reliable solution for calibrating the depolarization measurements is represented by the ±45° calibration techniques. This calibration implements a 45° rotation of the depolarization analyzer (PBC and the PMTs) with respect to the polarization plane of the laser in order to equalize the light intensity in the cross and parallel channels. When comparing the calibration signals, the ratio between the transmitted and reflected signals reflects the contribution of optics and electronics in the lidar receiving unit. Further details are provided in Freudenthaler et al. (2009).

3.4 Lidar data products

After the lidar signal pre-processing has been performed, the lidar signals can be directly used for the retrieving of the vertical profiles of the aerosol optical properties. A detailed analysis of the intensive and extensive aerosol properties will provide useful information about the aerosol characteristics. The available aerosol optical properties, also known as lidar products, will be presented below.

3.4.1 Extensive and intensive aerosol optical properties of EOLE and DEPOLE lidar systems

The extensive aerosol properties (α_{aer}, β_{aer}, δ_v) are proportional to the amount of aerosol present in the atmosphere while the intensive aerosol properties (*LR*, AE_σ, δ_p, *AOD*) indicate the characteristics of the aerosols:

- *Aerosol Backscatter coefficient (β_{aer})*: calculated from the elastic channels (355-532-1064 nm) by using the Fernald-Klett algorithm (Klett, 1981).
- *Aerosol Extinction coefficient (α_{aer})*: the aerosol extinction coefficient at 355 and 532 nm, retrieved from the Raman signals at 387 and 607 nm, by using the Raman algorithm (Papayannis et al., 1990; Ansmann et al., 1992).
- *Lidar ratio (LR)*: the extinction-to-backscatter ratio which is a proxy of the aerosols' absorption characteristics and size,

$$LR(\lambda, r) = \frac{\alpha_{aer}(\lambda, r)}{\beta_{aer}(\lambda, r)} \tag{3.8}$$

- *Ångström exponent (AE_σ)*: the wavelength dependence of the aerosol scattering intensity can be approximated by a power law (Ångström, 1929),

$$\sigma(\lambda, r) = \sigma(\lambda_0, r)(\lambda/\lambda_0)^{-AE_\sigma} \tag{3.9}$$

where $\sigma(\lambda_0, r)$ is the aerosol scattering coefficient at a given reference wavelength λ_0, and AE_σ is the dimensionless Ångström exponent. This exponent corresponds to the slope of a double-logarithmic plot of $\sigma(\lambda_0)$ versus λ and is calculated according to equation (3.9):

$$AE(\lambda_1/\lambda_2, r) = -\frac{\log\left(\sigma_{\lambda_1,r}/\sigma_{\lambda_2,r}\right)}{\lambda_1/\lambda_2} \tag{3.10}$$

The wavelength dependent Ångström exponent pairs of scattering that suggests the particle size, namely, the backscatter and extinction related Ångström exponents are: $AE_{\alpha 355/532}$, $AE_{\beta 355/532}$ and $AE_{\beta 532/1064}$.

For nighttime measurements, the Raman technique is applied as proposed by Papayannis et al., (1990) and Ansmann et al. (1992) to retrieve the β_{par} and α_{par} vertical profiles, with systematic uncertainties of ~5–15% and ~10–25% respectively (Ansmann et al., 1992; Mattis et al., 2002). Therefore, the corresponding systematic uncertainty of the retrieved lidar ratio values is of order ~11–30%, while the mean uncertainty for AE_{β} and AE_{α} ranges between 0.02-0.04 and 0.03-0.08, respectively, as estimated by propagation error calculations.

- *Water vapor mixing ratio profile WVMR*: is based on the simultaneous detection of the 355 nm Raman shifted laser beam by the atmospheric nitrogen N_2 (at 387 nm) and water vapor H_2O (at 407 nm). The Raman lidar technique has been widely used to provide the vertical profiles of WVMR (in g of H_2O/kg of dry air), in the troposphere.
- *Linear volume depolarization ratio δ_v*: is defined as the ratio of the total cross–polarized to the total parallel-polarized backscattered coefficient: $\delta_v = {\beta_{\perp}}/{\beta_{\parallel}} = {P_{\perp}}/{P_{\parallel}}$
- *Linear particle depolarization ratio δ_p*: o is defined as the ratio of the perpendicular polarization component to the parallel component of aerosol (without molecular part) scattering: $\delta_p = {\beta_{\perp}^{p}}/{\beta_{\parallel}^{p}} = \frac{(1+\delta_m)\delta_v R-(1+\delta_v)\delta_m}{(1+\delta_m)R-(1+\delta_v)}$, where the backscatter ratio R can be retrieved from the total lidar signal P (Freudenthaler et al., 2009).
- *Aerosol optical depth (AOD):* represents the aerosol load in an atmospheric path and is a measure of the total aerosol extinction (Liou, 2002). AOD is commonly used as an estimate of the amount of aerosol particles in the atmosphere, although it also depends on the optical properties of the aerosol. In the lidar technique, this parameter can be calculated by integrating the extinction coefficient profile from the surface up to the maximum possible measurement height range: $AOD = \int_0^r a(r')dr'$.

3.5 Data from other EARLINET stations

In our analysis of typical Saharan dust intrusions in the Mediterranean, except Athens (Greece), three other EARLINET stations were selected (listed from West to East): Granada (Spain), Potenza (Italy) and Limassol (Cyprus), for a four year (2014–2017) common period of aerosol depolarization Raman lidar data obtained at 532 nm. Table 3.3 summarizes the basic information about these lidar systems for each location. Except the Limassol station which provides data only at 532 nm, the three remaining stations are equipped with a depolarization Raman-lidar system able to provide extensive aerosol properties, namely three β_{aer} (355, 532, 1064 nm) and two α_{aer} (355, 532 nm) as well as aerosol intensive properties namely the backscatter and extinction related Ångström exponents ($AE_{\alpha 355/532}$, $AE_{\beta 355/532}$, $AE_{\beta 532/1064}$ nm), the lidar ratio (LR), and additionally the linear volume (δ_{v532}) and particle depolarization ratio (δ_{p532}) at 532 nm.

Table 3.3: Station name, location, lidar setup and relevant references of the four selected EARLINET stations.

Station	Abbreviation	Location	Lidar setup	References
Andalusian Institute for Earth System Research, University of Granada, Spain	IISTA-CEAMA, **Gr**	37.16° N, -3.61° E, elev. 680 m	MULHACEN $3\beta + 2\alpha + \delta_{p532}$ Overlap: 500 m a.g.l.	Guerrero-Rascado et al., 2008
Consiglio Nazionale delleRicerche – Istituto di Metodologie per l'AnalisiAmbientale, Potenza, Italy	CNR-IMAA, **Po**	40.60° N, 15.72° E, elev. 760 m	MUSA $3\beta + 2\alpha + \delta_{p532}$ Overlap: 405 m a.g.l.	Madonna et al., 2011
Laser Remote Sensing Unit, National Technical University of Athens, Athens, Greece	LRSU-NTUA, **At**	37.96° N, 23.78° E, elev. 212 m	EOLE/AIAS $3\beta + 2\alpha + \delta_{p532}$ Overlap: 800 m a.g.l.	Papayannis et al., 2020
Cyprus University of Technology, Limassol, Cyprus	CUT, Lm	34.67° N, 33.04° E, elev. 10 m	Polarisation Raman lidar, $1\beta + 1\alpha + \delta_p$ (532 nm) Overlap: 250 m a.g.l.	Nisantzi et al., 2015

3.6 The AErosol RObotic NETwork (AERONET)

The AErosol RObotic NETwork (AERONET, https://aeronet.gsfc.nasa.gov/, Holben et al., 1998) runs Sun/sky photometers (CIMEL) for direct sun and sky radiation measurements at hundreds of sites. For more than 25 years, the project has provided long-term, a continuous and readily accessible public domain database of aerosol optical, microphysical and radiative properties for aerosol research and characterization, validation of satellite retrievals, and synergism with other databases. The network imposes standardization of instruments, calibration, processing and data distribution. These photometers perform direct solar irradiance measurements at 340, 380, 440, 500, 675, 870, 940 and 1020 nm and diffuse sky radiance at 440, 675, 870 and 1020 nm. The uncertainty of the aerosol size distribution retrieved by the sky radiance measurements is based on the calibration uncertainty of each wavelength, which is assumed to be < ± 5%. More details can be found in Dubovik and King (2000) and Dubovik et al. (2006).

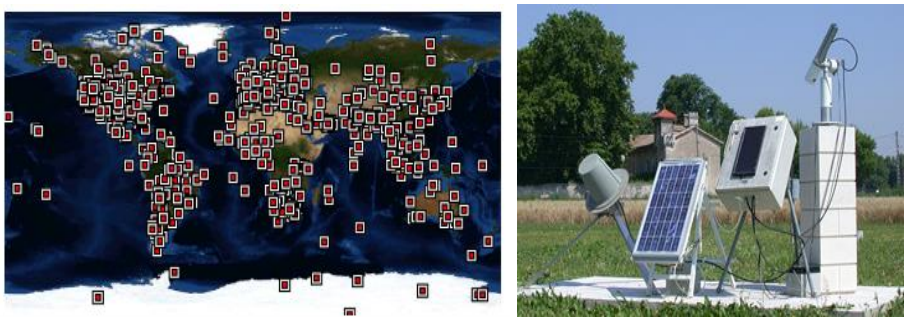

Figure 3.10: Left: Global distribution of AERONET stations, Right: Typical AERONET station with sun photometer. (https://aeronet.gsfc.nasa.gov/)

Thus, the AERONET collaboration provides globally distributed observations of spectral aerosol optical depth (AOD), inversion products, and precipitable water in diverse aerosol regimes. The processing algorithms have evolved from version 1.0 to version 2.0 and now version 3.0. Version 3 AOD data are computed for three data quality levels: Level 1.0 (unscreened), Level 1.5 (cloud-screened and quality controlled), and Level 2.0 (quality-assured). Inversions, precipitable water, and other AOD-dependent products are derived from these levels and may implement additional quality checks.

The AERONET sites to be considered in this study are located in Granada, Potenza Athens and Limassol, for the cases that were common in the EARLINET and AERONET database during the period 2014-2017 [Granada (37.164° N, 3.605° W), IMAA_Potenza (40.601° N, 15.724° E), ATHENS-NOA (37.972° N, 23.718° E) and CUT-TEPAK (34.675° N, 33.043° E)] . The available AERONET level 2.0 version 3 inversion products for the aforementioned sites were used under mineral dust transfer conditions over these sites.

Chapter 4: Tools and Modelling

In this chapter we will shortly present and describe the tools and models synergistically used with the lidar measurements for this study. By combining remote sensing measurements and other tools, a comprehensive and deep analysis can be performed covering all the aspects of a long-range transported event. Moreover, the benefits of aerosol lidar measurements can be highlighted by using them for calibration dust verification of various dust models.

4.1 The Single Calculus Chain (SCC)

The EARLINET Single Calculus Chain (SCC) is a tool for the automatic analysis of aerosol lidar measurements. The development of this tool started in the framework of EARLINET-ASOS (European Aerosol Research Lidar Network – Advanced Sustainable Observation System); it was extended and is continuing under the ACTRIS (Aerosol, Clouds and Trace gases Research InfraStructure Network) umbrella. The main aim of SCC is to provide a data processing chain that allows all EARLINET stations to retrieve, in a fully automatic way, the aerosol backscatter and extinction profiles starting from the raw lidar data of the lidar systems they operate. A general overview of the SCC is provided by D'Amico et al. (2015; 2016). All input parameters needed to perform the lidar analysis are stored in a database to keep track of all changes which may occur for any EARLINET lidar system over the time, assuring the traceability of the data. The end user can interact with the SCC via a user-friendly web interface (https://scc.imaa.cnr.it/). All SCC modules are developed using open-source and freely available software packages.

The structure of the SCC server is briefly presented in Fig. 4.1. The typical SCC analysis scheme comprises two steps: the pre-processing of raw data with EARLINET Lidar Pre-Processor (ELPP) and the subsequent optical processing of the pre-processed lidar data with EARLINET Lidar Data Analyzer (ELDA). By pre-processing we mean the set of operations, which must be applied to the raw lidar data before they can be processed by ELDA. Each single lidar system can be linked to several lidar configurations, which describe different lidar setups with specialized measurement capabilities (for example daytime or nighttime conditions).

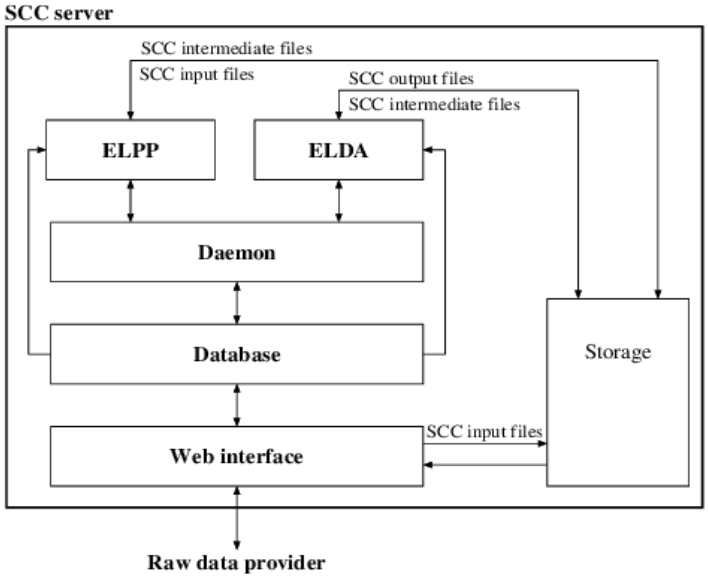

Figure 4.1: Block structure of the Single Calculus Chain (D'Amico, 2015).

The high-quality of the SCC products is proven by the good agreement between the SCC analysis, and the corresponding independent manual retrievals. The ability of the SCC to provide high-quality aerosol optical products is demonstrated for an EARLINET intense observation period. The current SCC version is the v.5.1.1, while all SCC products are compatible with Panoply (https://www.giss.nasa.gov/tools/panoply/) and an open Quicklook web interface is available (https://quicklooks.earlinet.org).

4.2 The Spheroidal Inversion eXperiments (SphInX) tool

The Spheroidal Inversion eXperiments (SphInX) software tool has been developed at the University of Potsdam (Samaras, 2016) within the Initial Training for atmospheric Remote Sensing (ITaRS) project (2012-2016). This software provides an automated process to carry out calculations from lidar data to obtain the aerosol microphysical properties and further to statistically evaluate the inversion outcomes. SphInX software was created to handle non-spherical particles using a two-dimensional (2D) generalization of the Mie model and considering the spheroid-particle approximation. A spheroid is geometrically obtained from a revolution of an ellipse about one of its principle axes. Denoting the semi-minor axis with n and the semi-major axis with b, the aspect ratio ($a = n/b$) can characterize three possible particle shapes: oblate ($a < 1$), sphere ($a = 1$), prolate ($a > 1$). Particle distributions are the main products of the regularized inversion but here depend not only on size (r) but also on shape (α), which is the reason they are referred to as shape-size distributions. There are several common microphysical parameters (redefined to suit the advanced model) and other new shape parameters introduced in SphInX, which can be calculated by knowing the volume shape-size distribution. For this study we will restrict to the following parameters:

the total volume concentration: $\mathrm{u_t} = \int_{a_{min}}^{a_{max}} \int_{\mathrm{r_{min}}}^{\mathrm{r_{max}}} \mathrm{u(r,a)dr}\, da$ [μm^{3}cm^{-3}] (4.1)

the surface-area concentration $\mathrm{a_t} = \int_{a_{min}}^{a_{max}} \int_{\mathrm{r_{min}}}^{\mathrm{r_{max}}} \frac{3}{\pi r^3} G(r,a)u(r,a)drda$ [μm^{2}cm^{-3}] (4.2)

where the function G(r,a) denotes the spheroidal geometrical cross section of the particle, which can be explicitly computed as follows:

$$G(r,a) = \begin{cases} 2\pi\left[n^2 + \frac{b^2}{e}\tanh^{-1}(e)\right], \text{ where } e = \sqrt{1 - b^2/n^2}, & \text{if } a < 1, \\ 4\pi r^2, & \text{if } a = 1, \\ 2\pi\left[n^2 + \frac{nb}{e}\sinh^{-1}(e)\right], \text{ where } e = \sqrt{1 - n^2/b^2}, & \text{if } a > 1. \end{cases} \quad (4.3)$$

the effective radius $\mathrm{r_{eff}} = 3\,{}^{\mathrm{u_t}}\!/_{\mathrm{a_t}}$ [μm] (4.4)

the effective aspect ratio $a_{eff} = \int_{a_{min}}^{a_{max}} \int_{\mathrm{r_{min}}}^{\mathrm{r_{max}}} \mathrm{u(r,a)dr}\, da \Big/ u_t$ (4.5)

the aspect ratio width $a_{width} = \int_{a_{min}}^{a_{max}} (a - a_{eff})^2 \int_{\mathrm{r_{min}}}^{\mathrm{r_{max}}} \mathrm{u(r,a)drda} \Big/ u_t$ (4.6)

Note that r here plays the role of a radius of a fictitious spherical particle with equal volume to the actual spheroidal one.

The software package consists of three (main) Graphical User Interfaces (GUI), serving different purposes:

SphInX Configurator: where all initial calculation parameters for the inversion are set [e.g. size distribution characteristics, lidar setup, mathematical parameter settings (methods, splines, interval partitions and simulation configurations)]. There is also the possibility of loading netcdf or ascii files

with the optical parameters from measurement cases. This GUI communicates all initializations to SphInX Main either directly or through user-stored configuration files.

SphInX Main: an independent GUI where the inversion takes place. This GUI is responsible for the retrieval of the resulting microphysical parameters, including visualizations (either real-time or on demand) of the shape-size distribution and the solution space. Owing to the structure of this gui with several mathematical parameters (e.g. regularization parameters), and illustrations of solution spaces, distributions and tabularized retrieval outcomes, here, occur all preliminary tests which are vital for the main runs. This gui communicates all inversion products to SphInX MPP either directly or through user-stored configuration files.

SphInX MPP: an independent GUI where all microphysical parameters are shown both individually and briefly in Tables with an error analysis, regarding accuracy (in case of simulations) and solution uncertainties. This GUI focuses mainly on an *a posteriori* filtering and analysis of the inversion results.

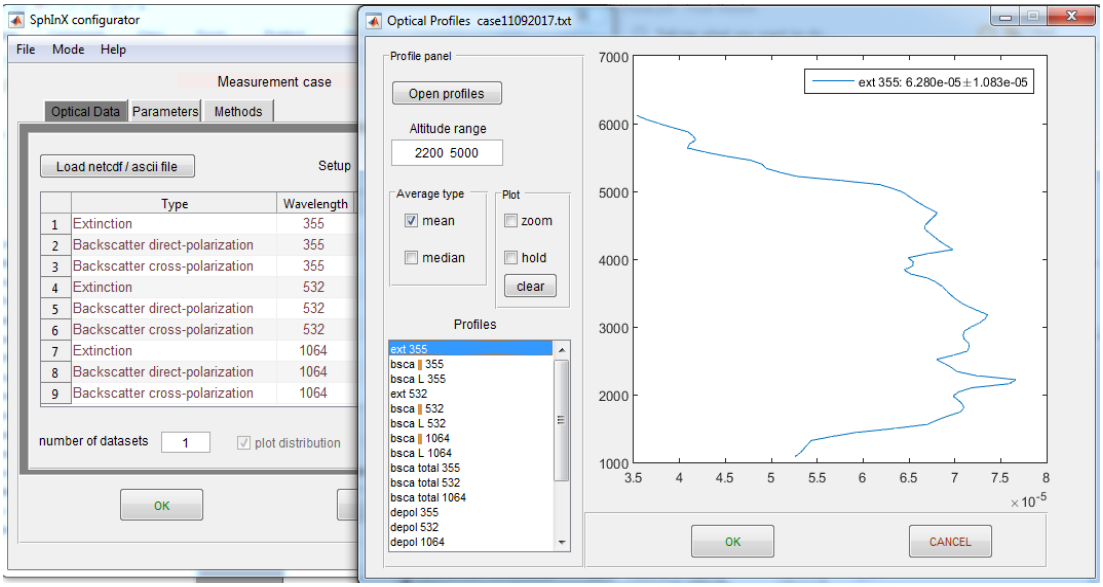

Figure 4.2: SphInX configurator.

SphInX operates with expendable pre-calculated discretization databases based on spline collocation and on look-up tables of scattering efficiencies using T-matrix theory (Rother and Kahnert, 2009). This is to avoid the computational cost which would otherwise limit the microphysical retrieval to an impractical point. When no information on the linear particle depolarization ratio (δ_{aer}) is given (usual setup "$3\beta_{aer} + 2a_{aer}$"), the software runs using Mie theory. The inversion is done by regularization combined with a parameter choice rule. The following combinations are available:

- Truncated singular value decomposition (TSVD) with the discrepancy principle (DP),
- Tikhonov regularization with the L-curve method (LC),
- Padé iteration with the discrepancy principle,
- Tikhonov regularization with the generalized cross validation method (GCV),
- Tikhonov regularization with the discrepancy principle, and
- Padé iteration with the L-curve

Details on the widely used methods TSVD and Tikhonov and the parameter choice rules DP, LC and GCV can be found in most books about regularization (for instance Hansen, 2010). Padé iteration,

in this context, is part of the so-called generalized Runge-Kutta regularization methods (cf. Böckmann and Kirsche, 2006).

The aerosol optical data profiles obtained from hourly-averaged vertical profiles of the aerosol optical properties retrieved from Raman lidar observations were used as inputs for our microphysical inversions. This was done by specifying certain layers of interest and then averaging to produce the 6-point dataset of the so-called $3\beta_{\mathrm{aer}} + 2a_{\mathrm{aer}} + 1\delta_{\mathrm{aer}}$ setup. These thin layers were selected in heights above the atmospheric boundary layer, where the LR and AE values were varying slowly showing homogeneity inside the plumes. The next step was to determine the initial parameters for the retrieval using physical knowledge and/or inversion stability tests.

Such preliminary numerical tests revealed an overall superior behaviour of the method Padé-DP as compared to the other built-in methods. This motivated us to choose the Padé iterative regularization method (Böckmann and Kirsche, 2006) for our measurement cases, in particular with a fixed number of 30 iterations. Moreover, a strong tendency to shape-bimodality led us to use 6 - 8 spline points and the spline degrees 2–4 among the maximum available ranges of 3-20 and 2-6 respectively. The CRI is fed to the software separately for the real and imaginary parts which then constitutes a grid combining the following default values: Real part (RRI) $[1.33, 1.4, 1.5, 1.6, 1.7, 1.8]$ and Imaginary part (IRI) $[0, 0.001, 0.005, 0.01, 0.03, 0.05, 0.1]$.

Ideally, this grid can be further confined either when there is sufficient knowledge on aerosol composition (or the exact CRI) and/or through numerical tests which indicate unstable or relatively improbable solutions. For our study the CRI grid was narrowed down to (RRI $[1.4, 1.5]$, IRI $[0, 0.001, 0.005, 0.01]$). Extreme absorption (RRI=0.05 or 0.03) was ruled out mostly for the following reasons.

First, it is expected to manifest itself much less often for dust particles. According to some reports on literature, such values can be found, for instance, directly on dust site (see e.g. Wagner et al., 2012) or when the dust concentration is lower so that a soot-type absorber prevails (see e.g. Schladitz et al., 2009). Therefore, while not improbable we consider those cases much less encountered and not relevant to the presented cases.

Second, preliminary runs with higher IRI and/or lower RRI have shown that the resulted shape-size distributions are less easily reconcilable physically, suggesting smoother representations and having undesired systematic behaviour. This is indeed an inherent issue of the inversion process since high IRI values and/or low RRI values are known to smooth out the involved scattering cross sections, see e.g. (Samaras, 2016; Rother and Kahnert, 2009) and lead to more severely ill-posed problems. Thus, the risk to compromise further the retrieval combined with the relatively small likelihood of high absorption outweighs the benefit here. Higher RRI values impose only a minute variation to the results according to preliminary runs and thus excluded too.

The determination of the CRI grid is known to have a severe impact even for less complicated schemes based on Mie theory and it is apparently applicable here since we add an additional dimension (shape information) and simultaneously we restrict to coarser radius- and aspect ratio ranges. However, massive simulations performed by Samaras (2016) for different atmospheric scenarios showed that microphysical retrievals with an initially known CRI keep high accuracy and small uncertainty levels. Furthermore, variations of the RRI have minor effects in the retrieved parameters at, $\mathrm{u_t}$, r_{eff} and variations of the IRI adds a relatively conservative percentage of 3-20% to the uncertainties compared to the fixed-RI retrievals when the imposed measurement error is reasonably contained. For the retrieval of the shape parameters, the situation is more complicated, and simulations suggest that the quality of the results depend additionally on particle size. Detailed implications of possible variations in shape (α), size (r), and composition (CRI) in the context of simulations exceed the scope of this Thesis. For more details one can see Samaras (2016).

4.3 The Hybrid Single-Particle Lagrangian Integrated Trajectory (HYSPLIT) model

The HYSPLIT model is a complete system for computing simple air parcel trajectories, as well as complex transport, dispersion, chemical transformation, and deposition simulations. HYSPLIT continues to be one of the most extensively used atmospheric transport and dispersion models in the atmospheric sciences community. A common application is a backward trajectory analysis to determine the origin of air masses and establish source-receptor relationships. HYSPLIT has also been used in a variety of simulations describing the atmospheric transport, dispersion, and deposition of pollutants and hazardous materials. The model calculation method is a hybrid between: i) the Lagrangian approach, using a moving frame of reference for the advection and diffusion calculations as the trajectories or air parcels move from their initial location, and ii) the Eulerian methodology, which uses a fixed three-dimensional grid as a frame of reference to compute pollutant air concentrations.

The model's default configuration assumes a 3-dimensional (3D) particle distribution (horizontal and vertical) and can be run interactively on the Web through the ARL READY system, or the code executable and meteorological data can be downloaded to a Windows or Mac PC. The web version has been configured with some limitations to avoid computational saturation of the ARL web server. The registered PC version is complete with no computational restrictions, except that users must obtain their own meteorological data files. For our analysis, the Web version of HYSPLIT was used. More details and information can be found in Stein et al. (2015).

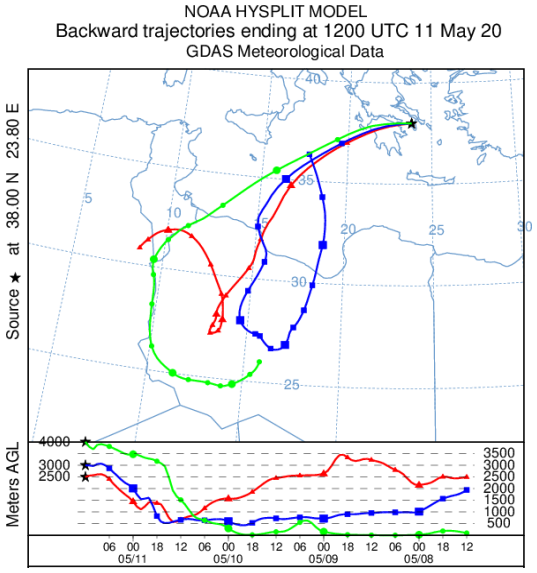

Figure 4.3: Example of Saharan dust intrusion over Athens as simulated by HYSPLIT backward trajectory model, on 11 May 2020, 18:00 UTC, at 2500, 3000 and 4000 m AGL.

4.4 The Flexible Particle Dispersion Model (FLEXPART)

The Flexible Particle Dispersion Model (FLEXPART, https://www.flexpart.eu/), is a Lagrangian transport and dispersion model suitable for the simulation of a large range of atmospheric transport processes. Apart from transport and turbulent diffusion, it is able to simulate dry and wet deposition, decay, linear chemistry; it can be used in forward or backward mode, with defined sources or in a domain-filling setting. It can be used from local to global scale. In this study, FLEXPART based on Global *Data* Assimilation System (GDAS) data, was used in order to provide sensitivity (residence time) plumes (Stohl et al., 1998b; Stohl et al., 1999; Stohl et al., 2005; Seibert and Frank, 2004). Specifically, 7-day backward runs for releases of 40000 air parcels every 3 hours at 2000 to 4000 m

a.s.l. were obtained by the FLEXPART model (see Sect. 4.4). Residence time (sensitivity) in grid cells above 4000 m a.s.l. is excluded, as the grid cells that might have pollutants in that height cannot be considered as aerosol source areas. FLEXPART takes into account not only grid scale wind (as simple trajectory models do) but also turbulent wind fluctuations and mesoscale wind fluctuations. It also incorporates drift correction (to prevent accumulation of computational particles released) and density correction (to account for the decrease of air density with height). FLEXPART model can be used to calculate with accuracy backward sensitivity plumes for periods as long as 30 days, in order to assess the impact of remote source areas.

4.5 The Weather Research and Forecasting (WRF/Chem) model

The fully coupled (on-line) atmospheric numerical model Weather Research and Forecasting (WRF/Chem, version 3.8, Grell et al., 2005) is able to simulate the chemical transformation of gaseous and particulate pollutants along with the meteorological parameters. It also has the ability to simulate the effect of chemistry on atmospheric processes. In the present work, WRF/Chem was used for selected cases. The simulations are performed by applying a 'two-way' nesting approach: the parent domain (D01) extends (8 º N-72º N, -18 º W -58 º E) having a resolution of 55 x 55 km. The first nested domain (D02) has a resolution of 18 x 18 km, the second nested covers Greece (D03) with 6 x 6 km resolution and the innermost one (D04) covers mainly the GAA area with 2 x 2 km resolution. The atmosphere is divided into 40 full vertical sigma levels; the first level is placed at approximately 10 m above ground level, while the isobar of 50 hPa comprises the simulated top of the model. Input data for the initial, lateral, and boundary conditions have been obtained from the National Centers for Environmental Prediction (NCEP) operational Global Final (FNL) Analyses. Gas phase chemistry is simulated by the RADM2 mechanism (Stockwell et al., 1990), while for the aerosols the Modal Aerosol Dynamics Model for Europe (MADE) (Ackermann et al., 1998) for inorganic species and the Secondary Organic Aerosol Model (SORGAM) (Schell et al., 2001) for secondary organic aerosols are used. The global emission inventory used in the study is the EDGAR-HTAP with a horizontal grid resolution of $0.1^o \times 0.1^o$ (Janssens-Maenhout et al., 2015). The inventory covers (anthropogenic) agriculture, energy, industry, residential and transport sectors and the reference year is 2010. The fire emissions inventory is based on the Fire Inventory from the National Center of Atmospheric Research (FINN), provided daily at 1 km horizontal resolution. Sea-salt and dust emissions are generated on-line using Gocart emissions. MEGAN scheme for biogenic emissions. Both direct and indirect aerosol-radiation-clouds interactions are considered.

4.6 The Dust Regional Atmospheric Model (BSC-DREAM8b v2.0)

The Earth Sciences Department from the BSC-CNS maintains a dust forecast operational system with the updated of the former Dust Regional Atmospheric Model (DREAM; Nickovic et al., 2001) called BSC-DREAM8b v2.0 (https://ess.bsc.es/bsc-dust-daily-forecast, Pérez et al., 2006; Basart et al., 2012) and conducts modelling research and developments. The model is designed to simulate and/or predict the atmospheric cycle of the eroded desert dust and was developed as a pluggable component of the Eta/NCEP (National Centers for Environmental Prediction) model. It solves the Euler-type partial differential nonlinear equation for dust mass continuity and it is fully inserted as one of the governing prognosis equations in the atmospheric Eta/NCEP atmospheric model equations. Its' configuration includes a 0.3º x 0.3º horizontal resolution (in the rotated semi-staggered Arakawa E grid), 24 vertical levels and 72-hour daily forecasts. The meteorological fields are initialized every 24h (at 12 UTC) with the NCEP global analysis (0.5ºx0.5º) and boundary conditions are updated every 6h with the NCEP GFS forecasts (0.5ºx0.5º). Since there are not yet satisfactory three-dimensional dust concentration observations, the initial state of dust concentration in the model is defined by the 24-hour forecast from the previous-day model run. The model at the starting day is run using "cold

start" conditions, i.e., the zero-concentration initial state. It provides Dust forecasts for: North Africa, Middle East and Europe, Sahara – Sahel, Spain, Canary Islands and Atlantic. For our analysis, the Middle East and Europe domain was used. More details and information about the updated BSC-DREAM8b and the new NMMB/BSC-Dust models can be found in Basart et al. (2012) and Pérez et al., (2011), respectively.

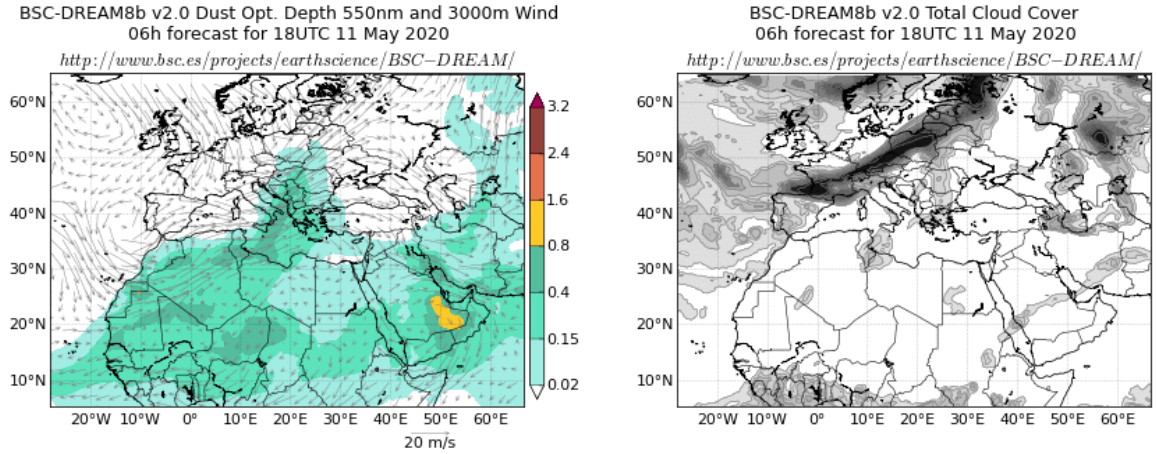

Figure 4.4: Example of Saharan dust intrusion over the Mediterranean and Balkans as estimated by the BSC-DREAM model, on 11 May 2020, 18:00 UTC. Left: Dust optical depth at 550 nm and 3000 m wind, Right: Total cloud cover.

4.7 The Library for radiative transfer (Libradtran) tool

The LibRadtran package (Mayer and Kylling, 2005) contains numerous tools to perform various aspects of atmospheric radiative transfer calculations. It is a library of radiative transfer routines and programs. The central program of the LibRadtran package is the radiative transfer tool *uvspec* that calculates the radiation field in the Earth's atmosphere. The structure of the *uvspec* model and other details can be found in Mayer et al. (2017). The *uvspec* model is invoked from the command line (similar both for UNIX-like and Windows types of operating systems):

uvspec < input file > output file

where the *input file* is a free format ASCII file that contains options and corresponding parameters specified by the user. A description of the numerous options (close to 200 for version 1.0) and respective parameters is provided in the LibRadtran User's Guide (Mayer et al., 2017).

A unique feature of *uvspec* is that the user has a choice of various radiative transfer equation solvers which are selected by the *rte_solver* option in the input file. This way, for the radiative transfer problem at hand an appropriate solver may be chosen, e.g. a fast two-stream code to calculate approximate irradiance or a discrete ordinate code to accurately simulate radiances, with or without polarization. The *uvspec* model includes the following three essential parts: (1) An atmospheric shell which converts atmospheric properties like ozone profile, surface pressure, or cloud microphysical parameters into optical properties required as input to (2) the radiative transfer equation solver which calculates radiances, irradiances, and actinic fluxes for the given optical properties; finally (3) post-processing of the solver output including multiplication with the extra-terrestrial solar irradiance, correction of Earth-Sun distance, convolution with a slit function, or integration over wavelength (depending on the choice of the user).

The Optical Properties of Aerosol and Clouds (OPAC) database (Hess et al., 1998) is widely used as a reference of aerosol optical properties in the solar and infrared spectral regions for the estimation of aerosol radiative effects (e.g. Gómez-Amo et al., 2014), as well as in the inversion of satellite observations (Klüser et al., 2012). The aerosol optical properties are the extinction, scattering,

and absorption coefficients, the single scattering albedo, the asymmetry parameter, and the phase function. They are calculated on the basis of the microphysical data (size distribution and spectral refractive index) under the assumption of spherical particles in case of aerosols and cloud droplets and assuming hexagonal columns in case of cirrus clouds. Thus, in a new version of the database OPAC (Koepke et al., 2015) the optical properties of the mineral particles are modelled describing the particles as spheroids with size dependent aspect ratio distributions, but with the size distributions and the spectral refractive indices not changed against the previous version of OPAC. Data are given for up to 61 wavelengths between 0.25 and 40 μm and up to eight values of the relative humidity. The software package also allows calculation of derived optical properties like mass extinction coefficients and Ångström coefficients.

4.7.1 Applied methodology for radiative simulations

In our study, the *uvspec* program which calculates the radiation field in the Earth's atmosphere was implemented for the disort radiative transfer equation (1-D geometry). Mid-latitude conditions (AFGL Atmospheric Constituent Profiles, 0–120 km) and a typical surface albedo value (0.16) for urban cities were taken into account based on visual observations. The OPAC data set (Koepke et al., 2015) was used for desert spheroids (T-matrix calculations).

A set of four simulations was carried out per case of the studied dust events. The first two simulations refer to clear-sky atmospheres with background/baseline aerosol conditions (default properties: rural type aerosol in the boundary layer, background aerosol above 2 km, spring-summer conditions and a visibility of 50 km, index "clear" in Eq. 4.7), the first for the SW and the second for LW range, since these ranges are treated separately by LibRadtran. The remaining two simulations correspond to dust loaded atmosphere, again, the one for the SW range and the other for the LW range, respectively, for which the vertical profiles of the dusty layers were used as additional inputs (index "dusty" in Eq. 4.7). These inputs have been obtained by three different Schemes: A) vertical mass concentration profiles simulated by the BCS-DREAM8b model, B) vertical mass concentration profiles of only the dust component ($mass_d$) as calculated from Eq. 5.2 (cf. Fig. 4.5; Sect. 5.3.1) utilizing the β_{532} coefficient and, C) vertical profiles of α_{532} along with the respective mean AOT_{532} value. In the final step, we calculated the parameters ΔF, ARF, ARF_{NET} and ARF_{ATM} applying Eqs. 4.7—4.10.

The flowchart in Fig. 4.5 depicts these three Schemes applied to create the input files for the dust-loaded atmospheric conditions used in LibRadtran software package (Emde et al., 2016). Scheme A refers to the dust mass concentration as estimated by BSC-DREAM8b over the studied sites. In Scheme B, only the dust vertical distribution is used as input, (based on the separation of the β_{532} into dust and non-dust components that led to the calculation of the vertical distribution of the dust-only mass concentration) in order to determine the Dust Radiative Forcing (DRF). On the other hand, in Scheme C both contributions of dust and non-dust aerosols (total α_{aer}) are taken into account. Additionally, for Scheme C conversion factors from OPAC were used in order to convert the α_{aer} and the corresponding AOT from 532 nm to 10 μm (peak, within the atmospheric window). The conversion was based on an adaptive inversion algorithm of Shang et al. (2018) who presented a way to convert extinction coefficients at different wavelengths by using Ångström exponent values derived from AOTs. It should be mentioned here that the Scheme B, even though it also includes many assumptions and uncertainties in its calculations, is the only one, compared to the rest two (Schemes A and C) that gives us the opportunity to calculate only the dust contribution in the radiative effect.

In this study 30 vertical levels have been used between ground and 120 km height with a resolution of 0.5 km starting from the bottom of the atmosphere (BOA) to 2 km and from 5 to 10 km, a resolution of 0.2 km from 2 km to 5 km, due to the presence of the dust layers within this height range and additionally at the heights of 20 and 120 km, where the latter is mentioned as top of the atmosphere (TOA). The aerosol radiative forcing (ARF) defined as the perturbation in flux in the

atmosphere caused by the presence of the dust aerosols in relation to that calculated under clear sky conditions, can be expressed as (Quijano et al., 2000; Sicard et al., 2014; Mishra et al., 2014):

$$ARF(z) = \Delta F^{dusty}(z) - \Delta F^{clear}(z) \quad (4.7)$$

where, the net flux, ΔF is the difference between the downwelling, and upwelling flux, F↓ and F↑, respectively:

$$\Delta F(z) = F\downarrow(z) - F\uparrow(z) \quad (4.8)$$

The fluxes (in W m^{-2}) are calculated separately for SW and LW radiation sources. The way the ARF is defined, at a given altitude will be positive when the aerosols cause a heating effect, and negative when they cause a cooling effect. The use of Eq. 4.7 assumes that the amount of the incoming solar radiation at the TOA is equal for both cases with and without the presence of dust aerosols. Therefore, the net ARF is expressed as:

$$ARF_{NET}(z) = ARF_{SW}(z) + ARF_{LW}(z) \quad (4.9)$$

Finally, the ARF within the atmosphere can be defined as the difference between ARF at the TOA and BOA:

$$ARF_{Atm} = ARF_{TOA} - ARF_{BOA} \quad (4.10)$$

All simulations were performed for three different Solar Zenith Angles (SZA), 25° 45° and 65° covering a typical diurnal cycle for radiative forcing estimates at mid-latitudes. All cases were treated for cloud-free conditions. Except the altitude in km (z_{out}), the additional outputs that have been implemented in our Schemes are: the direct horizontal irradiance (e_{dir}), the global irradiance (e_{glo}) the diffuse downward irradiance (e_{dn}), the diffuse upward irradiance (e_{up}), and the heating rates (heat) in K day^{-1}, as described by Mayer et al. (2017).

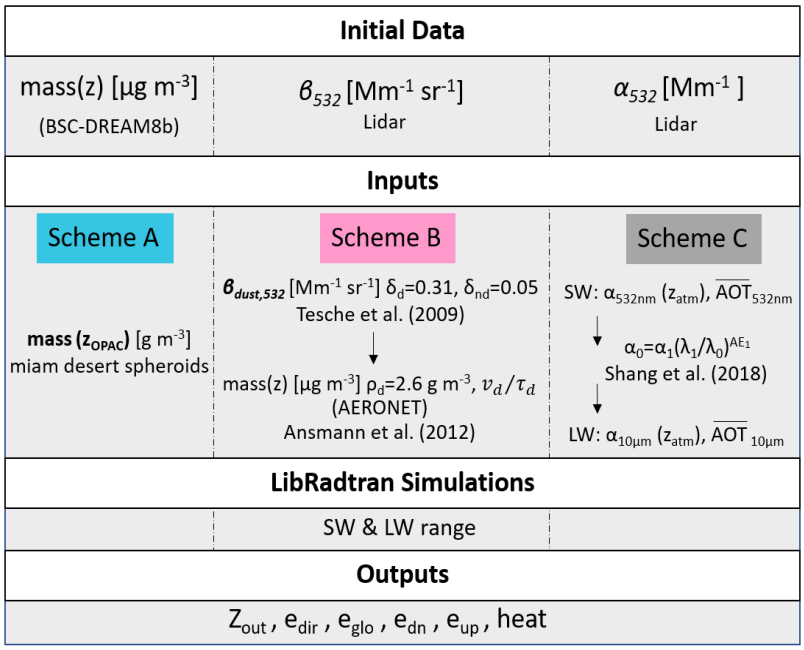

Figure 4.5: Flowchart of the three Schemes used to retrieve simulations of irradiances using the LibRadtran software package.

4.7.2 Radiation data set

LibRadtran irradiance outputs have been validated against reference solar irradiance pyranometer measurements at the Earth's surface (Kosmopoulos et al., 2018). For this study, solar radiation data measured by pyranometers were available only for the Granada and Athens stations. The reference solar radiation data set consists of one-minute simultaneous measurements of horizontal global and diffuse irradiance measured with two CMP11 pyranometers, at Granada, and two CMP21, at Athens (NOA's actinometric station in Penteli mountain). These pyranometer models, both manufactured by Kipp & Zonen, have a black-coated thermopile acting as a sensor which is protected against the meteorological conditions by two concentric hemi-spherical domes. They both comply with the International Organization for Standardization (ISO) 9060 (1990) criteria for an ISO secondary standard pyranometer, being classified as "high quality" according to the World Meteorological Organization (WMO) nomenclature (WMO, 2018). Additionally, the corresponding pyranometer measuring the diffuse component was mounted on a shading device to block the direct irradiance and prevent it from reaching the sensor.

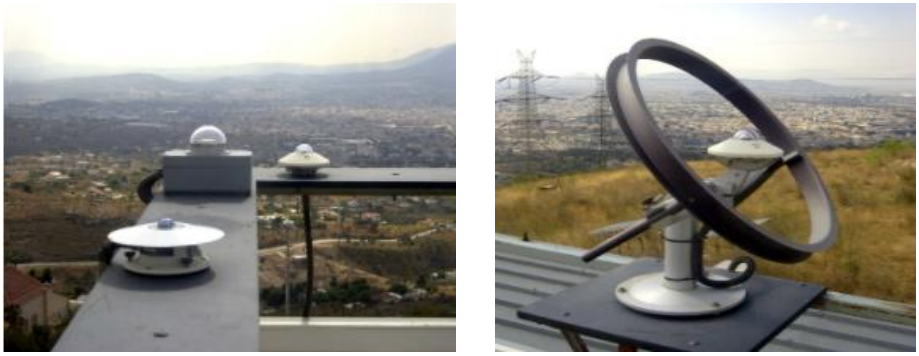

Figure 4.6: The pyranometers for providing solar radiation data measurements (Left: total irradiance, Right: diffuse irradiance), located at NOA's actinometric station in Penteli mountain, Attica (http://www.meteo.noa.gr/GR/iersd_station-images_gr.htm).

In this study, the shading devices employed were a Solys2 sun tracker and a CM121 shadow ring, at Granada and Athens respectively, both manufactured by Kipp & Zonen. For those diffuse irradiance measurements taken using a shadow ring, the model proposed by Drummond (1956) has been apply in order to correct for the diffuse radiation intercepted by the ring, as suggested the manufacturer (Kipp & Zonen, 2004).

4.8 Satellite data

Moderate Resolution Imaging Spectroradiometer (MODIS) observations, a key instrument aboard the Terra (originally known as EOS AM-1) and Aqua (originally known as EOS PM-1) satellites (https://worldview.earthdata.nasa.gov/). Terra MODIS and Aqua MODIS are viewing the entire Earth's surface every 1 to 2 days, acquiring data in 36 spectral bands, or groups of wavelengths (see MODIS Technical Specifications). The MODIS instrument provides high radiometric sensitivity (12 bit) in 36 spectral bands ranging in wavelength from 0.4 µm to 14.4 µm. The responses are custom tailored to the individual needs of the user community and provide exceptionally low out-of-band response. Two bands are imaged at a nominal resolution of 250 m at nadir, with five bands at 500 m, and the remaining 29 bands at 1 km. A ±55-degree scanning pattern at the EOS orbit of 705 km achieves a 2,330-km swath and provides global coverage every one to two days. The optical system consists of a two-mirror off-axis afocal telescope, which directs energy to four refractive objective assemblies; one for each of the VIS, NIR, SWIR/MWIR and LWIR spectral regions to cover a total spectral range of 0.4 to 14.4 µm.

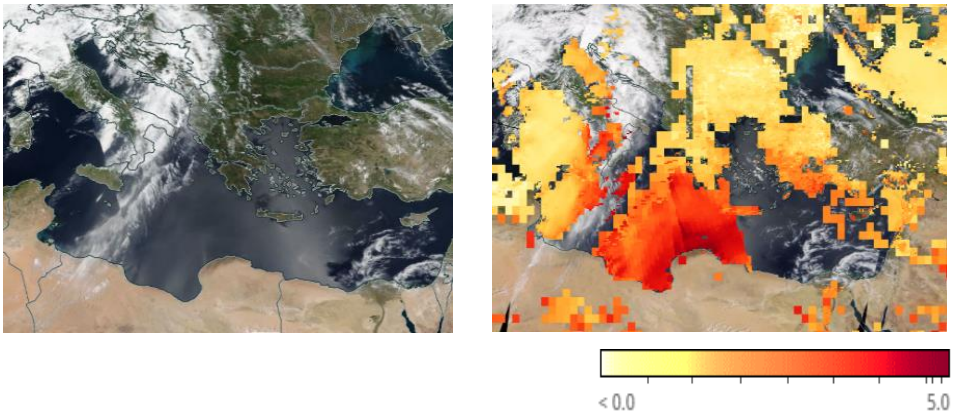

Figure 4.7: Left: MODIS true colour image, Right: Terra and Aqua MODIS combined value of Aerosol Optical Depth on 11 May 2020.

The Cloud-Aerosol Lidar and Infrared Pathfinder Satellite Observation (CALIPSO) satellite provides new insight into the role that clouds and atmospheric aerosols (airborne particles) play in regulating Earth's weather, climate, and air quality. CALIPSO combines an active lidar instrument with passive infrared and visible imagers to probe the vertical structure and properties of thin clouds and aerosols over the globe. CALIPSO was launched on April 28, 2006 with the cloud profiling radar system on the CloudSat satellite. CALIPSO and CloudSat are highly complementary and together provide new 3-D perspectives of how clouds and aerosols form, evolve, and affect weather and climate (https://www-calipso.larc.nasa.gov/). The former is equipped with the Cloud Aerosol Lidar with Orthogonal Polarization (CALIOP) instrument has been delivering aerosol and cloud profiles across the globe for more than 10 years (Winker et al., 2009). CALIOP measures aerosol backscatter profiles at 532 and 1064 nm, including parallel and perpendicular polarized components at 532 nm, at high horizontal and vertical resolution. The data are processed to Level 2 (L2) products, providing aerosol and cloud backscatter and extinction coefficients at 532 and 1064 nm as well as the linear particle depolarization ratio at 532 nm (Winker et al., 2009).

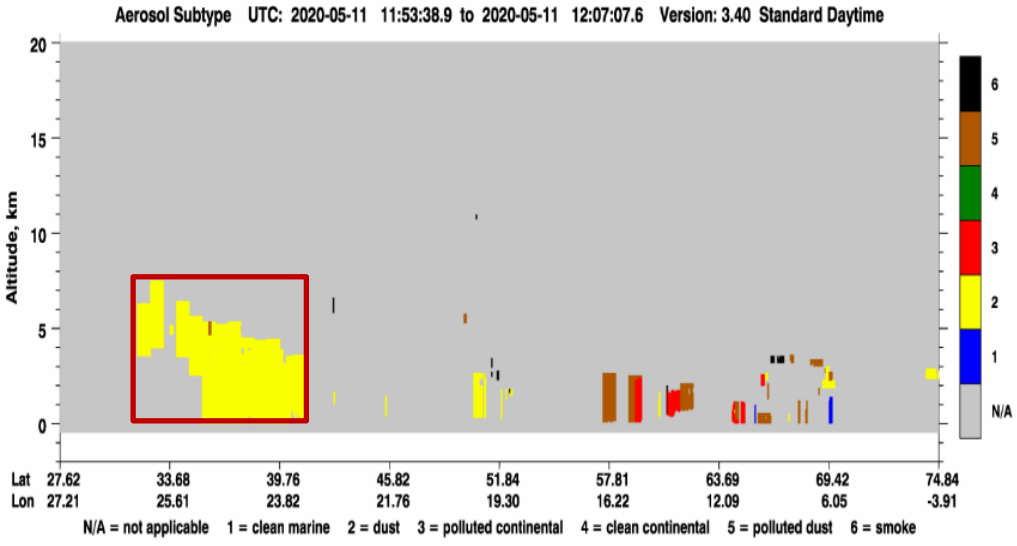

Figure 4.8: Example of Saharan dust intrusion over the Mediterranean and Balkans detected by CALIOP during an overpass on 11 May 2020. Position (altitude, latitude and longitude) and type of the detected dust aerosol layers over our region are contained within the red box.

Fire Information for Resource Management System (FIRMS), a NASA-funded application, distributes Near Real-Time (NRT) active fire data within 3 hours of satellite observation from NASA's Moderate Resolution Imaging Spectroradiometer (MODIS) and NASA's Visible Infrared Imaging

Radiometer Suite (VIIRS). For this study, information for fires and thermal anomalies were taken into account using this application (https://firms.modaps.eosdis.nasa.gov/).

Figure 4.9: FIRMS, Active fires and thermal anomalies from MODIS, AQUA, Corrected Reflectance (true color), on 11 May 2020, over Greece.

Each MODIS active fire/thermal hotspot location represents the center of a 1km pixel that is flagged by the algorithm as containing one or more fires within the pixel. Combined (Terra and Aqua) MODIS NRT active fire products (MCD14DL) are processed using the standard MOD14/MYD14 Fire and Thermal Anomalies algorithm.

Chapter 5: Results and Analysis

Chapter 5 contains a full discussion, interpretation and evaluation of the results with reference to other literature findings. All these results have been published online: Soupiona et al., 2018; Soupiona et al., 2019; Soupiona et al., 2020 (cf. Appendix A— Paper I, Paper II, Paper III). However, results from Soupiona et al. (2018) have been updated in this Thesis, in order to additionally include data from the year 2017.

5.1 18 years measurements of Saharan dust intrusions over Athens (2000-2017)

We present a comprehensive analysis of the seasonal variability of the vertical profiles of the optical and geometrical properties of Saharan dust aerosols, observed in the height region between 1000 and 6000 m, over Athens, Greece, from February 2000 to December 2017. These nighttime observations were performed by the EOLE Raman lidar system under cloud-free conditions. The statistical analysis (referring to aerosol monthly mean values) is based on nighttime vertical Raman measurements of range-resolved aerosol optical properties (β_{aer}, α_{aer}, LR) at 355 nm (59 dust events during more than 80 measurement hours).

5.1.1 Dust climatology: Observations versus Predictions

The schedule of the EOLE measurements during Saharan dust outbreaks (Papayannis et al., 2005, 2009) is based on early warnings, using forecasted data, provided by the BSC-DREAM8b model (Basart et al., 2012), (see Sect. 4.6). The identification of the dust cases is based mainly on AOD values derived from sun photometer data over Athens (https://aeronet.gsfc.nasa.gov) and MODIS observations (see Sec. 4.8).

In Fig. 5.1a we present the monthly evolution of the number of dust cases observed by EOLE (only under clear sky conditions) and predicted by BSC-DREAM8b, for the period 2000–2017. The maximum number of occurrence of the dust days occurs within May, in both predicted (~30 cases) and observed cases (~16 cases), while the majority of the dust cases is observed between early spring (March) to autumn (October). Specifically, 95% of the observed cases and 81% of the predicted ones, fall within this period. On the other hand, a minimum occurrence appears during the winter months, due to the prevailing north-eastern flow over Athens during this period (Kassomenos et al., 1995; Papayannis et al., 2009; Banks et al., 2016). However, the fact that the number of observed dust days is always fewer than the forecasted ones, can be attributed to the inability of the lidar technique to perform measurements under cloudy/rainy atmospheric conditions.

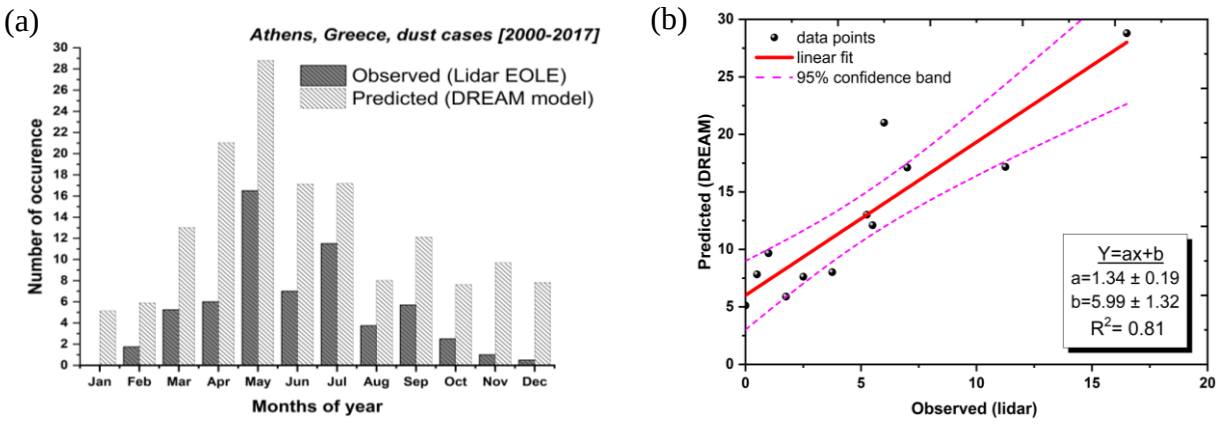

Figure 5.1: a) Monthly evolution and b) linear fit of the mean monthly number of dust cases observed (EOLE) and predicted (BSC-DREAM8b) for the period 2000–2017.

Moreover, we found a quite strong correlation (R^2=0.81) between the occurrences of the observed and forecasted number of monthly mean cases, denoting their linear association (Fig. 5.1b). Roughly, about half of the forecasted dust cases are finally observed by the lidar system during the studied time period (2000–2017). In the worst-case scenario, at least the 50% of the forecasted by the model dust events will be finally observed with EOLE, over the cloudless sky of Athens.

5.1.2 Dust optical properties

In Fig. 5. 2a and b we present the seasonal variation (from spring to winter) of the vertical profiles (black lines) of β_{aer} and α_{aer}, at 355 nm, as well as their mean values (red lines) and the corresponding statistical error expressed by the standard deviation (SD) of each mean seasonal vertical profile (magenta horizontal error bars). Similarly, the seasonal variation of the LRs and their corresponding mean values are presented in Fig. 5.2c in the height range between 2000 and 4000 m, where usually most of the Saharan dust layers are detected. All these profiles show a quite large variability due to the varying intensity and different air mass trajectories of the dust events occurring over Athens, as previously discussed in Papayannis et al. (2009). In our case, the mean LR_{355} values within the dust plumes (spring: 58 ± 9 sr, summer: 54 ± 9 sr, autumn: 38± 6 sr, winter: 45 ± 6 sr) vary from season to season, taking lower values during the colder months. Therefore, not only the time of the transport, but also the transport paths and the prevailing atmospheric conditions that vary among seasons, may affect a dust layer itself.

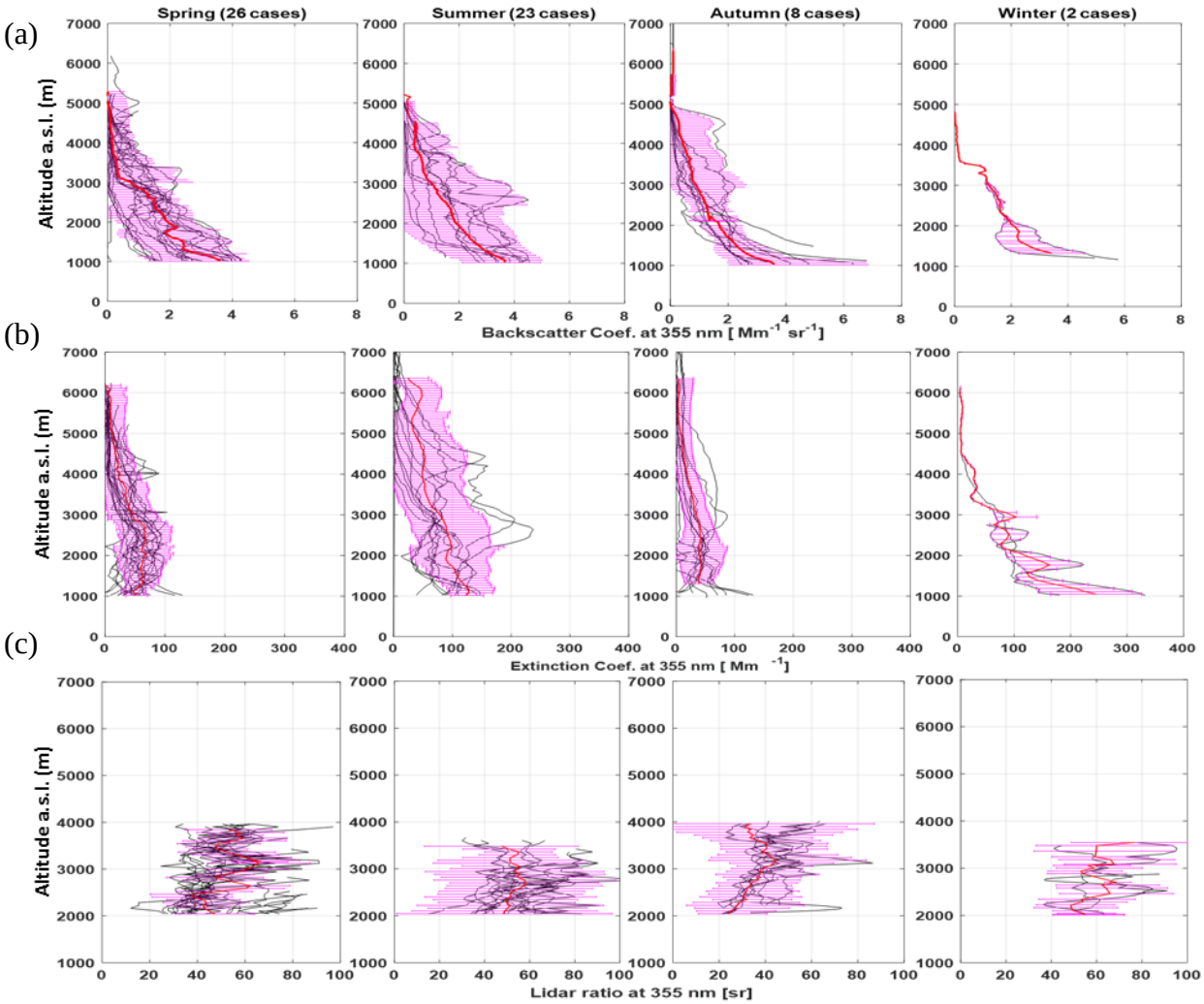

Figure 5.2: Seasonal variation of the vertical profiles of the aerosol optical properties: a) β_{355}, b) α_{355} and c) LR_{355}, along with their mean values (red lines) and the corresponding SD (red error bars) for the 59 dust cases (2000–2017).

The frequency distribution of the LR_{355} (61 cases), of the range 2000-4000 m (a.s.l.) is shown in Fig. 5.3. This distribution clearly shows a maximum occurrence at 40–50 sr (37% of cases) with the majority of cases lying between 42 and 62 sr (25%–75%), as shown in the inset boxplot of Fig. 5.3. The mean LR_{355} of all cases was found to equal to 52 ± 13 sr (with a min. of 22 sr and a max. of 77 sr) in the height range 2000–4000 m a.s.l. The quite large standard deviation values and the outliers of the boxplot indicate, for many cases, a possible mixture of dust with other aerosol types (e.g. marine, polluted continental, and/or biomass burning ones).

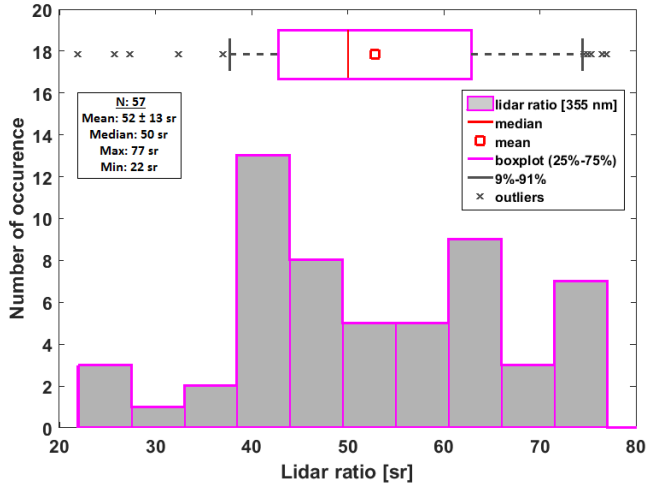

Figure 5.3: Histogram and boxplot of the occurrence of LR_{355} for the 59 dust cases during the period 2000-2017, as calculated for heights between 2000 and 4000 m.

The seasonal variability of the AOD at 355 nm is demonstrated in Fig.5.4a. In the box plot, the box spans the interquartile range (IQR) from 25% to 75% percentile including the median line and the whiskers are chosen maximally 1.5x IQR away from the box. In this way, we can discern outsiders, shown as asterisks. It is evident that the AOD_{355} shows a significant seasonal variability, with minimum mean values (squared symbols) during autumn and maximum mean values in spring and summer months. These minimum and maximum levels of AODs are consistent with the seasonal Saharan dust outbreaks, in accordance with the seasonal variation observed over Athens by Papayannis et al. (2009), but at 532 nm. Moreover, the medians (vertical lines) of spring and summer are lower than the corresponding mean values, indicating that the distribution is skewed to lower values, while there are some exceptionally large ones (extreme dust episodes occurring during the abovementioned period). On the other hand, during the autumn and winter months, the distribution of the AOD values seems to be more normal, as the corresponding mean and median values are almost equal. Regarding the AOD seasonal variability, the AOD values lay in a wide range during the hotter months (spring, summer), while during the colder months (autumn, winter) the variation is limited. The mean AOD_{355} over the entire period (2000-2017) was found equal to 0.25±0.16, ranging between a minimum of 0.03 and a maximum of 0.86.

The seasonal variability of the mean LR_{355}, along with their SD is shown in Fig. 5.4b. These values range within the dust plumes from 38 sr (in autumn) to 58 sr (in spring). In fact, the springtime and summertime values (58±9 and 54±9 sr, respectively) are very close to the ones (nearly pure dust) measured *in situ* during the SAMUM experiment (53±5 sr, at 355 nm, as shown by Groß et al., 2015), which indicates a very low mixing rate of dust (strong dust events with a very fast (1-2 days) transported from the African continent to Athens passing over the Mediterranean Sea) with other types of aerosols during their transport. The respective autumn and winter mean LR values (38±6 and 45±6 sr, respectively) are lower when compared to the aforementioned ones but remain within those (40-45 sr) reported by Amiridis et al. (2005), Müller et al. (2007) and Papayannis et al. (2009), indicating a possible mixing with continental air masses and different transport paths. Moreover, our data reveal a

seasonal downtrend (R^2=0.59) in dust episode occurrences originating from Saharan desert from spring to winter, according to Fig 5.4b with a minimum during autumn months.

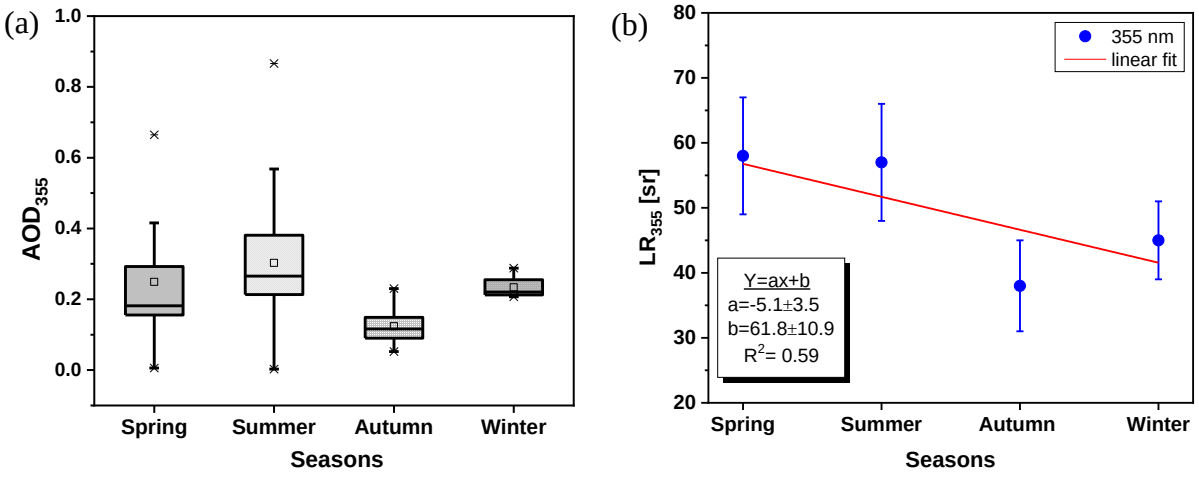

Figure 5.4: a) Box plot of the seasonal variability of the mean AOD values and b) Mean seasonal lidar ratio values along with the linear fit of the mean values (red line), as calculated at 355 nm during the period 2000–2017, between 2000 and 4000 m a.s.l.

No specific trends could be revealed during the reporting 18-year period, concerning the modification of dust pathways and dust quantities arriving over Athens based on the available air mass trajectory simulation data, except the aforementioned seasonal preference of the strongest dust transport during spring and summer. Therefore, it can be concluded that not only the time spent over the long-range transport areas, but also the transport path and the atmospheric conditions that vary among seasons, may affect the characteristics of the dust layer itself. A more comprehensive analysis about aging and mixing properties of dusty layers will be analyzed later on (cf. Sect. 5.2.3 – 5.2.4).

5.1.3 Dust geometrical properties

In order to characterise the probed dust layers, in terms of their geometrical properties (base, top, layer thickness and centre of mass (z_{COM})), as calculated from the lidar retrievals, one can follow the procedure proposed by Mona et al. (2006). In Table 5.1 we present the vertical distribution (in m) of the mean, minimum and maximum values of the aforementioned dust altitude-related parameters retrieved directly from the β_{355} over Athens, during the reported period (February 2000 - December 2017). Multiple aerosol dust layers of variable thickness (609-6199 m) were observed. The z_{COM} of these layers was located in altitudes between 1270 and 5738 m with a mean value of 2508 ± 1109 m. The variability of the z_{COM} values could be related to the mixing of the different air masses arriving over our measuring site (Matthias et al., 2004). The base of the dust layer ranged from 926 m to a maximum of 5094 m, with a mean value of 1793±1098 m. Additionally, the top of the dust layer ranged from 2005 to 8014 m, with a mean value of the order of 3540 m.

Table 5.1: Main characteristics of the Saharan dust retrieved from the b_{aer} profiles at 355 nm.

Years: 2000-2017	Mean±SD	Maximum	Minimum
Base z_B (m)	1793±1098	5094	926
Top z_T (m)	3540±892	8014	2005
Thickness *th* (m)	1747±785	6199	609
Centre of mass z_{com} (m)	2508±1109	5738	1270

According to the seasonal evolution of the base and top values, a mean minimum value during the autumn and winter months can be indicated, which is related to the lower temperatures of the free troposphere, leading to cooler ground surfaces. On the contrary, during the hot period (spring and

summer months) these geometrical parameters show higher values (Fig. 5.5). Therefore, we can observe a downward trend of the mean seasonal base and top values from spring (base: 2150 m, top: 4560 m) to winter (base:1800 m, top: 3980 m). Moreover, the mean seasonal thickness values present a relatively low SD equal to 9%, among the seasons. These observed trends could be related to: i) the different atmospheric conditions that prevail and characterize each season, ii) the occurrence of Saharan episodes over our area which is higher during spring and summer months, and iii) the convective activity which is strongest during the hot periods (mainly late spring and summer).

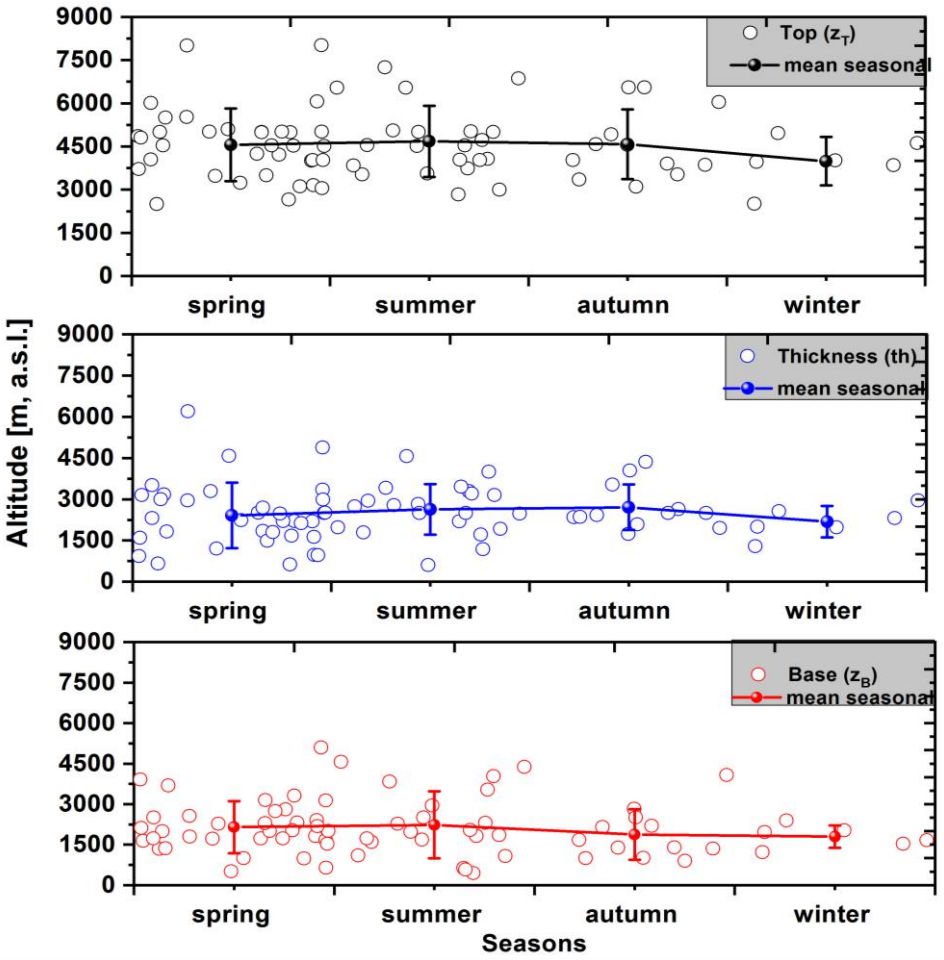

Figure 5.5: Annual evolution of the layer properties: base z_B (lower part), thickness th (middle part) and top z_T (upper part) and their corresponding seasonal means with standard deviations for the 18 year period studied.

5.1.4 Clustering analysis: origins of Saharan dust intrusions over Athens

A cluster analysis has been applied to all air mass trajectories arriving over Athens in order to identify their origin using an algorithm based on Dorling et al. (1992). The basic idea is that the non-hierarchical clustering algorithm generates a large number of "seed" trajectories, which cover the spread of the real trajectories used in the analysis and then, assigns each of the real trajectories to that seed which is closest in terms of the Euclidean distances between their corresponding 6-hourly coordinates. The user can define a percentage change in Root Mean Square Deviation (RMSD) which, when exceeded at some stage in the reduction of the number of clusters, signifies an optimum number of clusters to be retained in the analysis. The algorithm indicated these two optimum main clusters, with the corresponding average trajectories, called centroids (Toledano et al., 2009). Using these two "clusters" the FLEXPART transport model was implemented in order to provide dust plumes on the basis of their residence time (expressed in hours) called sensitivity plumes (Stohl et al., 1998; Stohl et al., 2005, see Sect. 4.4). Therefore, 7-day air mass backward trajectories were calculated from 0 to 500

m a.s.l. height over the source region, reaching over Athens between 2000-4000 m a.s.l., with a 3-hour interval.

In Fig. 5.6, our clustering analysis reveals these two main clusters: one pathway from south-west to north-east, with dust emission areas in Algeria, Tunisia, and Libya (Cluster A, linked with a low-pressure over Morroco and Algeria and a high-pressure over Libya-Egypt) and a second one from south, across the Mediterranean Sea with emission areas over Libya and the remaining part of Algeria and Tunisia (Cluster B, linked with a low-pressure over Spain and a high-pressure over Libya-Egypt) in accordance with Moulin et al. (1997). Actually, the second cluster has similar pattern with the first one, except that it is more shifted to the east and north and has contribution from Europe. Moreover, Cluster B has a bigger number of air mass trajectories (60% of the cases) with lower lidar ratio values compared to Cluster A (40% of the cases), while its centroid is shifted more to the Mediterranean Sea.

Regarding the aerosol optical properties we found higher mean AOD values within Cluster A (0.39±0.15) than within Cluster B (0.32±0.22), at 355 nm. For Cluster A, the mean LR_{355}value was also higher (52±15 sr), compared to Cluster B (44±15 sr). The difference in the values of these optical properties between the two clusters indicates that, although the origin does not differ much, the distance travellled and the residence time of the air masses, may differ.

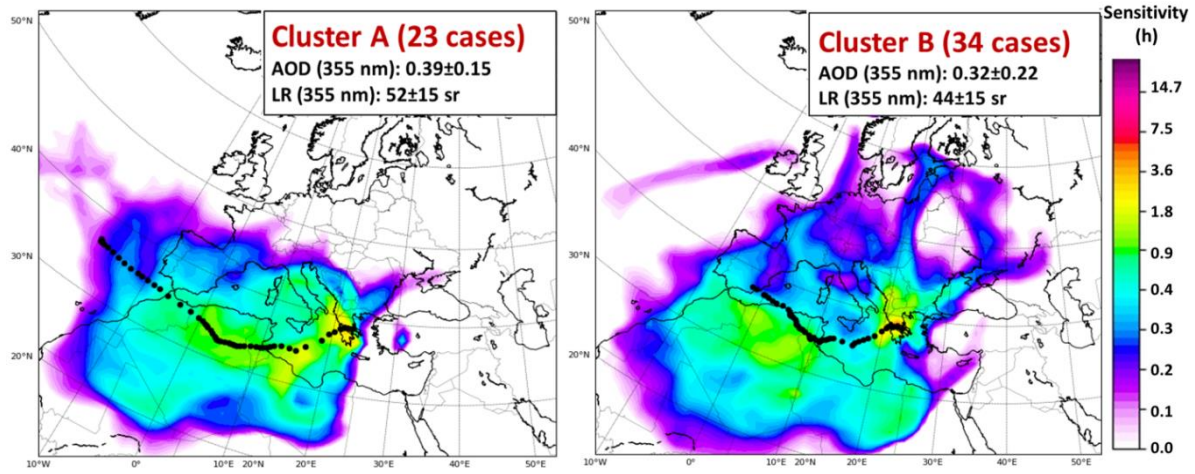

Figure 5.6: 7-day air mass backward FLEXPART clusters for 59 Saharan dust cases (2000-2017). Particles are released at a uniform rate during a 3-hour interval from 0 to 500 m a.s.l. height reaching over Athens between 2000-4000 m. Left: Cluster A, Right: Cluster B. For each cluster, the centroids are presented (black dots) and the mean optical properties are mentioned (inset legend). The air mass residence time along the centroids' trajectory over each site is shown in hours. The charts are plotted with X axis (longitude) and Y axis (latitude).

In order to verify this assumption, we calculated the air mass velocity within each cluster, correlating the distance travelled within 3-hour interval along the clusters' centroid. Therefore, it is evident that the distance travellled and the residence time are both directly related to the air mass aging processes.

Indeed, as shown in Fig. 5.7, the air masses of Cluster A remain 12 hours more (dust enriched) over the African continent (75 hours) than those of Cluster B (63 hours) and reach Athens faster (less mixing during transport) after a total travel time of 126 hours. Concerning the time period spent over the Mediterranean Sea, the air masses of Cluster A stay 51 hours over that area, much less than the air masses of Cluster B, which stay for about 78 hours. Obviously, he air masses of Cluster B circulate ~27 hours more over the Mediterranean Sea compared to those of Cluster A, thus, they mix more with marine aerosols within the first 500 m a.s.l.

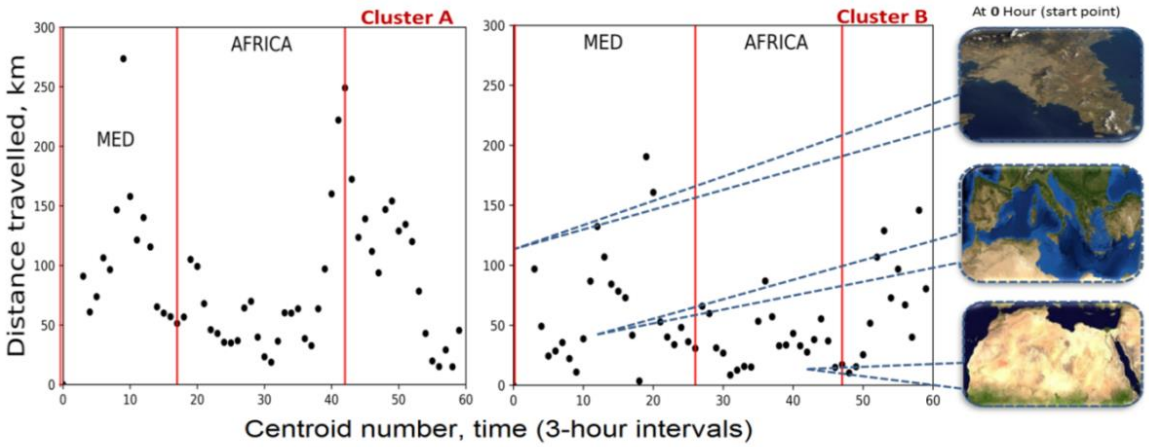

Figure 5.7: Distance travelled (in km) every 3-hour interval for the 7-day backward trajectory of each clusters' centroid: cluster A (left) and cluster B (right). Their residence time over Mediterranean and the African continent (red rectangulars) are mentioned by the black dots (each dot represents a 3-hour interval).

5.2 4 years of measurements of Saharan dust intrusions over the Mediterranean basin (2014-2017)

It is well documented that mineral dust may highly influence the atmospheric radiative balance through scattering and absorption processes (direct effect) as well as the cloud nucleation, formation and lifetime (indirect effects) as shown in IPCC (2014). Over the Mediterranean Basin, Saharan dust advections are modulated by meteorology along rather regular seasonal patterns (Mona et al., 2012). For instance, in the western Mediterranean region the African dust occurrence is higher in summer (Salvador et al., 2014), while in the central Mediterranean region, spring and summer are, usually, associated with dust aerosol loads extending up to altitudes of 3–4 km (Barnaba and Gobbi, 2004). Finally, in the Eastern Mediterranean the main dust transport occurs from spring to autumn (Papayannis et al., 2009; Nisantzi et al., 2015; Soupiona et al., 2018) as a result of the high cyclonic activity over the northern Africa during this period (Flaounas et al., 2015). Considering also that the Mediterranean is a region of high evaporation, low precipitation and remarkable solar activity, the transportation of dust aerosols accompanied with aging and mixing processes make this area a study of interest for present and future climate change effects (Michaelides et al., 2018).

5.2.1 Data selection and methodology

The selection of the discussed dust cases of the four EARLINET stations (Granada, Potenza, Athens and Limassol, see Sect. 3.5), was based on the values of the optical properties of δ_{p532} and LR_{532} measured by lidar (Groß et al., 2013). Since pure dust layers (δ_{p532}=0.31±0.02, Freudenthaler et al., 2009) rarely occur over the Mediterranean cities due to continental contamination by urban, pollution or even BB aerosols and other mixtures, a sufficiently lower δ_{p532} threshold value should be considered to characterize an aerosol layer as a dusty one over the studied area. Moreover, the respective LR_{532} values for long-range transported Saharan dust aerosols over the Mediterranean area are expected to range between 35-75 sr as previously reported (Mona et al., 2006; Papayannis et al., 2008; Tesche et al., 2009; Groß et al., 2011; Ansmann et al., 2012; Nisantzi et al., 2015; Soupiona et al., 2018).

Considering these aspects, from the total set of Saharan dust events per station listed in the EARLINET database for the common period 2014–2017, we considered for further analysis only the data meeting the following three basic criteria: a) $\delta_{p532} \geq 0.16$ in the free troposphere, b) 35 sr $\leq LR_{532} \leq$75 sr in the free troposphere and c) the thickness of the detected layer to be at least 500 m. The critical height (in meters a.s.l.) in which the first criteria was met, was considered to be the base of the dust layer. This assumption was deemed necessary to be made since usually, the lofted dust layers cannot

be distinguished from the top of the PBL, while the presence of urban haze and pollution decreases drastically the values of δ_p down to 0.03–0.10 (Gobbi et al., 2000; Groß et al., 2013). As top of the dust layer it was estimated the height where the lidar signals were well fitting the molecular scattering in the free troposphere (both δ_{p532} and β_{532} tending to zero). For some cases over Athens, where depolarization measurements were unavailable, the values of the base and top were calculated from the Raman lidar signals, following the procedure proposed by Mona et al. (2006).

A careful investigation of the air mass origin and long-range mineral dust transport by means of backward trajectory analysis was carried out using the HYSPLIT model (Sect. 4.3). The kinematic back-trajectories were calculated using the vertical velocity component given by the meteorological model with a 96–120 hours pathway (4–5 days backward). MODIS/Terra information (Sect. 4.8) was also taken into account for detecting the corresponding hot spots of possible fires and thermal anomalies along the trajectories (not shown here).

In our analysis for the cases over the Mediterranean area, e ended up to study 51 individual cases in total (15 for Granada, 18 for Potenza, 12 for Athens and 6 for Limassol). It should be mentioned here that for the region of Cyprus, the situation is more complex since except Saharan dust events, Middle East dust outbreaks occur frequently (Nisantzi et al., 2015; Kokkalis et al., 2018; Solomos et al., 2019). On top of that, dust particles originating from Middle East proved to have different lidar ratio values than the corresponding observations over Saharan desert (Mamouri et al., 2013; Kim et al., 2020). Considering this, dust events observed over the Limassol station originating from Middle East region were not included in our study issue.

Figure 5.8 reveals the air mass backward trajectories concerning the air mass origin as obtained by HYSPLIT per station and per observed layer. In the majority of cases, the air masses originate from the western and north-western Africa (Morocco, Mauritania, Algeria and Tunisia). Taking a quick look, one can observe two dominant occurrences: i) trajectories which travel directly from the source to the observation station and ii) trajectories that circulate over the Mediterranean or Atlantic Ocean (for the Granada and Potenza cases), Europe and Balkans or even Turkey (for the Limassol and Athens cases) before reaching the observation stations.

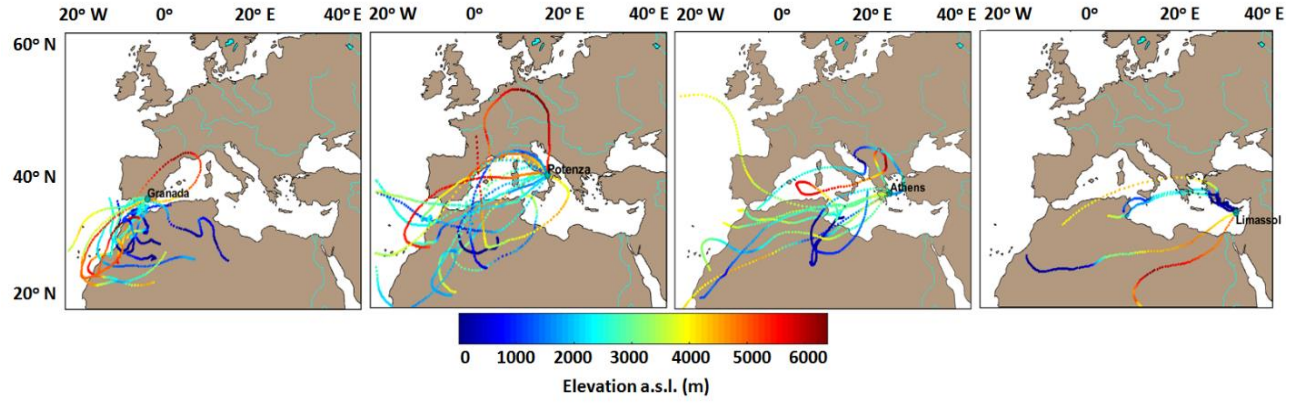

Figure 5.8: 96–120-hour backward trajectories over a) Granada, b) Potenza, c) Athens and d) Limassol, for arrival heights of approximately the center of each observed dust layer (51 cases, 2014–2017).

5.2.2 Aerosol geometrical and optical properties per site

Examining the dust events case by case, we calculated the base, top and thickness of each detected layer and the mean values of δ_{p532}, LR_{532} and AOD_{532} inside each dust plume as shown in Fig.5.9 (a-d). The corresponding SD values give an indication of the variability of these parameters from base to the top of each dust layer. Each sub-figure shows the geometrical or optical characteristics of the detected layers one by one, per station and per year. Figure 5.9a shows the aerosol geometrical properties per case including the mean values of the base and top height of the dust layers per station,

along with their SD (marked with horizontal bounded lines). For these four sites (from left to right hand: Granada, Potenza, Athens and Limassol) the mean layer thicknesses were calculated: 3392 ± 1458 m, 2150 ± 1082 m, 1872 ± 816 m and 1716 ± 567 m, respectively; we also report on the mean δ_{p532} values of 0.24 ± 0.05, 0.26 ± 0.06, 0.28 ± 0.05 and 0.28 ± 0.04 (Fig. 5.9b), and mean AOT_{532} values of 0.40 ± 0.31, 0.11 ± 0.07, 0.12 ± 0.10 and 0.32 ± 0.17 (Fig. 5.9d), respectively. Almost equal mean LR_{532} values of ~51 sr (Fig. 5.9c) were found for all stations in good agreement with literature findings (Tesche et al., 2009; Ansmann et al., 2012; Groß et al., 2011; 2013). It is worth mentioning that the Granada station holds the minimum mean value for layers' base (1567 ± 788 m) and the maximum for top (4960 ± 975 m) and layer's thickness. The largest mean AOD value, equal to 0.40 ± 0.31, is also observed over the Granada station depicting thick dust layers in the majority of cases.

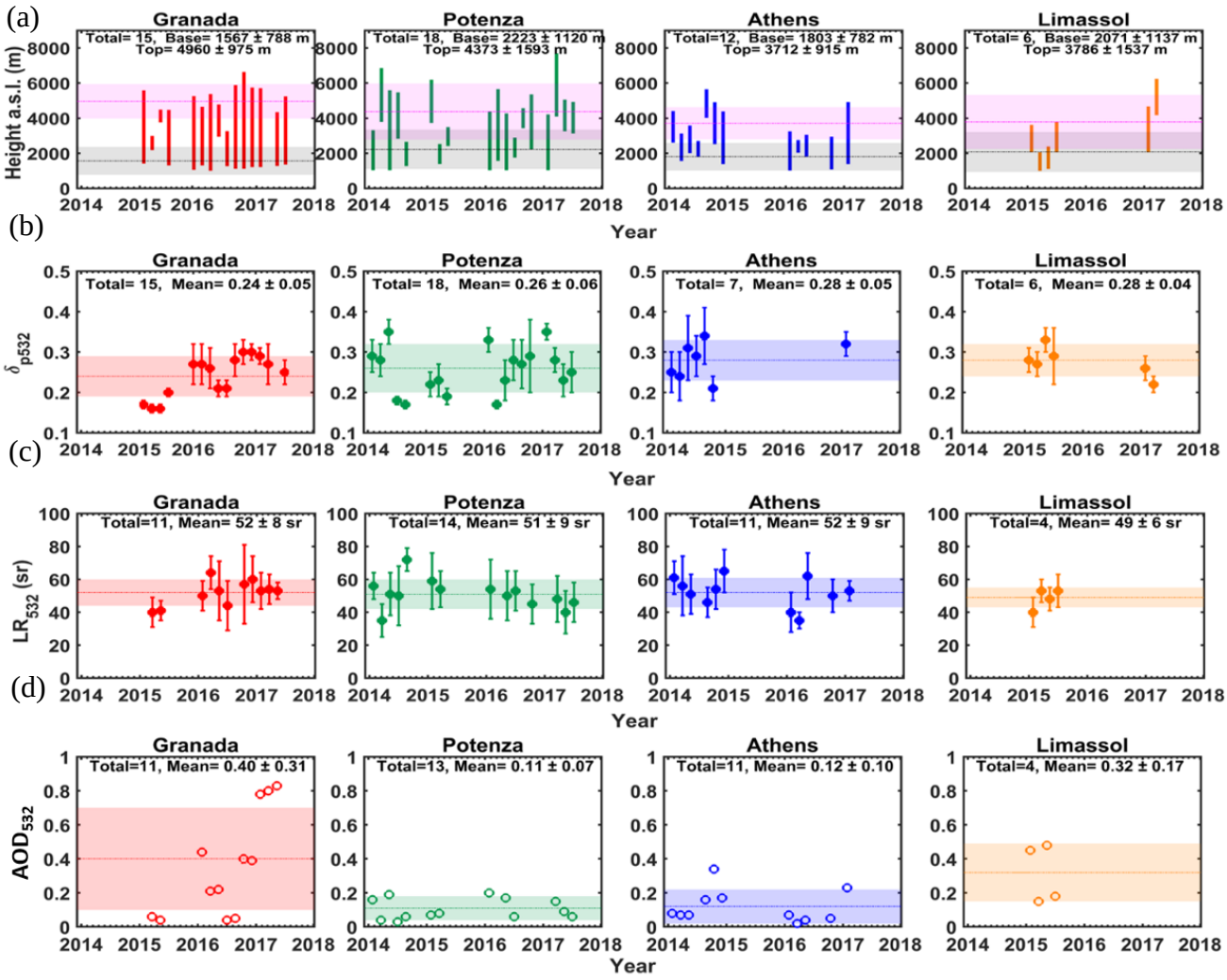

Figure 5.9: Mean values along with standard deviation of a) base and top, b) δ_{p532}, c) LR_{532} and d) AOD_{532}, per station (text and banded lines) and per case (symbols and error bars) inside the observed dust layers (2014-2017).

Considering Granada's station as representative of the west Mediterranean region, Potenza of the central Mediterranean region, Athens and Limassol stations of the eastern Mediterranean region, a dust aerosol mode classification per region can be performed. For this purpose, the mean AOD_{532} versus the $AE_{\beta 532/1064}$ giving an indication of the aerosol particle size in the atmospheric column relevant to the aerosol load for each region are shown in Fig. 5.10. A wide spread of the AOD values at moderate to low $AE_{\beta 532/1064}$ values (between 0 and 0.6) observed in the western Mediterranean region, demonstrates that the dust size distribution in this area is dominated by coarse mode particles

during dust events of different intensities. On the other hand, the presence of dust layers, in the central and eastern Mediterranean regions can be associated with higher $AE_{\beta 532/1064}$ values (even up to 1.5) and consequently, with the presence of fine mode particles and lower dust loads, probably due to mixing processes of dust particles with other aerosol types. Our findings verify that the longer the dust transport is, more likely it is for the dust aerosols to be mixed with background aerosols in the eastern Mediterranean (Groß et al., 2019).

In terms of the aerosol size distribution, the scatter plot of Fig. 5.10 allowed us to perform a k-means clustering (Arthur and Vassilvitskii, 2007) in order to define three physically interpretable aerosol size distributions: a) fine mode, with $AE_{\beta 532/1064} > 0.6$, b) coarse mode, with $AE_{\beta 532/1064} \leq 0.6$ and AOD_{532} between 0 and 0.2, c) whilst $AE_{\beta 532/1064}$ values smaller than 0.6 attributed to large AODs (between 0.2 and 0.8) are representative of extreme dust events. It seems that the majority of these extreme dust outbreaks occurs over the western Mediterranean region, more likely due to its location close to the African continent and the local atmospheric circulation. For example, Fernández et al. (2019) recently reported an unprecedented extreme winter time Saharan dust event (February 2017) over the whole Iberian Peninsula with AODs > 0.2 (675 nm) and AE values around 0. More studies referring to the occurrence of extreme dust events over the aforementioned area can be found in literature (Cachorro et al., 2008; Guerrero-Rascado et al., 2009).

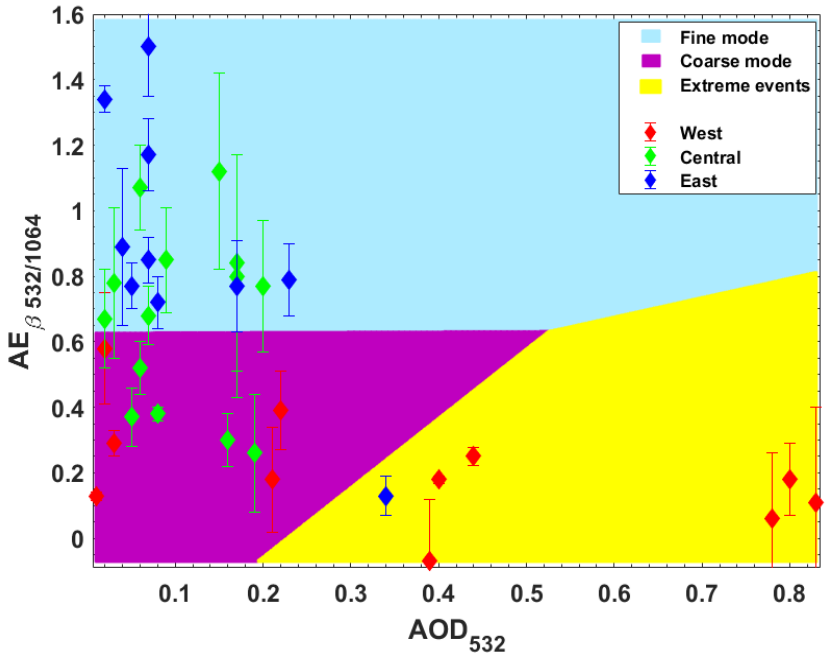

Figure 5.10: $AE_{\beta 532/1064}$ versus AOD_{532} per region: west (red marks and error bars), central (green marks and error bars) and east (blue marks and error bars) Mediterranean region. K-means clustering revealed three clusters: fine mode (ciel background), coarse mode (magenda background) and extreme dust events (yellow background).

5.2.3 Mixing state properties and microphysical properties of dusty layers

Based on the High Spectral Resolution Lidar (HSRL) classification presented by Groß et al. (2013), we plotted the intensive aerosol quantities LR_{532} versus δ_{p532} and we identified three of the six existing clusters in our data (Fig 5.11). The first cluster (green marks and error bars) represents a mixing state of Saharan dust and BB aerosols having a large spreading in the mean LR values and low mean δ_{p532} values (40 sr $\leq LR_{532} \leq$ 75 sr, 0.15 $\leq \delta_{p532} \leq$ 0.19). The second one, (red marks and error bars) is attributed to mixed Saharan dust, where dust aerosols are dominant, with urban/continental, marine or even pollen aerosols also possibly present (40 sr $\leq LR_{532} \leq$65 sr, 0.20 $\leq \delta_{p532} \leq$ 0.29). The third cluster (orange marks and error bars) is attributed to pure Saharan

dust aerosols ($45\ \text{sr} \leq LR_{532} \leq 60\ \text{sr}$, $0.30 \leq \delta_{p532} \leq 0.36$). The most populated and consequently, the most common, among those three clusters is the red one, as expected, due to the frequent mixing of dust aerosols with continental ones (Papayannis et al, 2009). The range of our measured δ_{p532} values as indicated with the horizontal error bars in Fig. 5.11, overlap between the three identified aerosol clusters, showing a more realistic transition from one cluster to the other, bridging the gap specifically between green and red clusters from the HSRL classification.

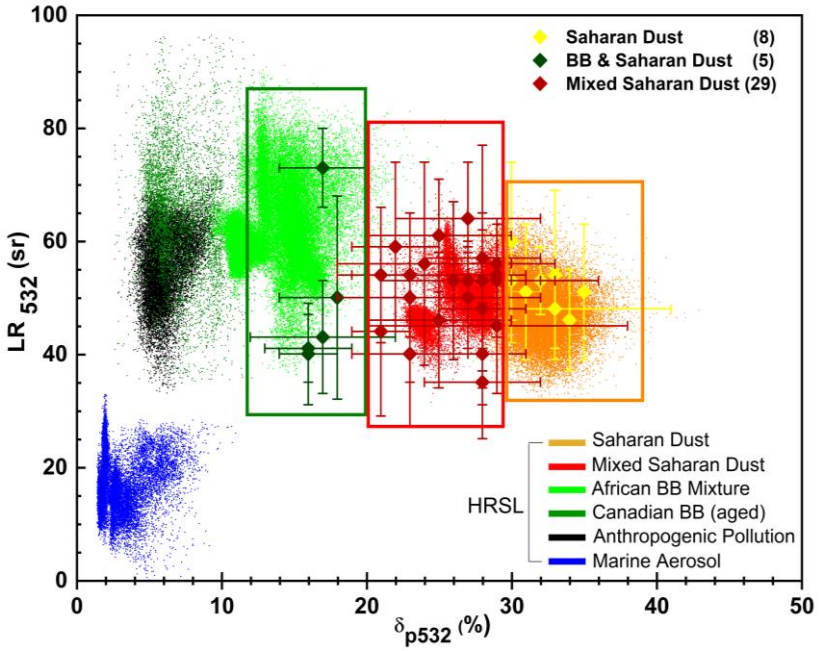

Figure 5.11: LR_{532} versus δ_{p532} values from HSRL observations presented by Groß et al. (2013), (colored dots) along with the selected datasets from the four EARLINET stations (symbols and error bars).

Table 5.2 summarizes the mean values of the aerosol geometrical, optical, and microphysical properties of the three identified clusters along with their SD (5 cases for BB & Saharan dust, 8 cases for Saharan dust, 29 cases for mixed Saharan dust). A synergistic approach of HYSPLIT (trajectories of 120 hours backward for each case) and Google Earth (distance calculator) tool allowed us to estimate the distance travelled (in km) to the respective sites and the mixing hours per cluster. Specifically, the term of mixing was introduced to refer to the hours the air masses travelled after leaving the African continent. We can see that the Saharan dust cluster of the air masses shows the lowest mixing with other air masses (26 ± 13 hours), compared to the other clusters (41 ± 26 hours for the BB & mixtures and 66 ± 41 hours for the mixed Saharan dust cluster). Moreover, the air masses from the Saharan dust cluster seem to travel faster than those of the other clusters, although covering a greater distance (4845 ± 2825 km) at the same time period (within 120 hours). Moreover, the main difference between the two remaining clusters (BB & mixtures/Mixed Saharan Dust) is attributed to the mixing hours. The air masses of the latter cluster (Mixed Saharan Dust) remain 15 hours longer and circulate over the Mediterranean and Europe, so they are probably enriched with other aerosol types.

Concerning the aerosol optical properties retrieved by lidar, the β_{532} and α_{532} show lower values for BB & dust and for mixed Saharan dust cases ($1.10 \pm 0.15\ x10^{-3}$km^{-1}sr^{-1}, 0.47 ± 0.28 km^{-1} and $1.24 \pm 0.80\ x10^{-3}$km^{-1}sr^{-1}, 0.74 ± 0.48 km^{-1} respectively) and higher values ($1.54 \pm 1.05\ x10^{-3}$ km^{-1}sr^{-1}, 0.80 ± 0.27 km^{-1}) for the Saharan dust cluster. Therefore, higher AOD values (0.32 ± 0.25) were found for the latter cluster compared to the others, due to the higher dust burden of these events over the affected sites. The highest δ_{p532} values (0.32 ± 0.02) indicate the arid origin and the coarse mode of pure Saharan dust layers (Freudenthaler et al., 2009) of the corresponding cluster. No direct

information can be extracted from the similar LR_{532} values about the mixing state of the aerosol layer, except that the range of the SD narrows as the mixing decreases. Additionally, for the cases that observations at 355 nm were available, it seems that LR color ratio (namely the LR_{355}/LR_{532}) converges to 1 for the Saharan dust cluster, indicating the absence of spectral dependence for the case of pure dust (Müller et al., 2007; Veselovskii et al., 2020). For these cases also, $AE_{\beta 355/532}$ becomes closer to zero taking mean value of 0.35 ± 0.45.

We also summarise the changes in the mean microphysical properties estimated with the SphInX tool for all cases of each of the three identified clusters. The BB & Saharan dust cluster takes the lower mean R_{eff} value (0.293 ± 0.074 μm) due to the fine structure of BB aerosols inside the layer, while a mean value of R_{eff} equal to 0.360 ± 0.081 μm corresponds to the cluster of mixed Saharan dust and a slightly larger value (0.387 ± 0.070 μm) corresponds to the Saharan dust cluster. The values for RRI, IRI and SSA at 532 nm were similar for these two clusters that do not include BB aerosols, whilst the presence of BB aerosols of the first cluster leads to higher RRI and IRI values and lower SSA ones, making these results to be in good agreement with the ones reported in Petzold et al. (2011) over Dakar, for mineral dust and dust mixed with anthropogenic pollution.

Table 5.2: Mean values of optical, geometrical and microphysical properties of the three identified clusters along with their SD. Zero SD indicates no variability in the corresponding retrieved parameter. The term of mixing refers to the hours the air masses travelled after leaving African continent.

Parameters		Clusters		
		BB & Saharan Dust	**Mixed Saharan Dust**	**Saharan Dust**
Optical Properties	**β_{532} ($km^{-1}sr^{-1}$)**	1.10±0.15 [x10^{-3}]	1.24±0.80 [x10^{-3}]	1.54±1.05 [x10^{-3}]
	α_{532} (km^{-1})	0.47±0.28	0.74±0.48	0.80±0.27
	LR_{532} (sr)	51 ± 15	50 ± 7	52 ± 5
	LR_{355} (sr)	35 ± 13	42 ± 7	51 ± 10
	LR_{355}/LR_{532}	0.69 ± 0.24	0.84 ± 0.16	0.98 ± 0.16
	δ_{p532}	0.17 ± 0.01	0.26 ± 0.03	0.32 ± 0.02
	$AE_{\beta 355/532}$	0.44 ± 0.59	0.52 ± 0.61	0.35 ± 0.45
	AOD_{532}	0.03 ± 0.02	0.15 ± 0.10	0.32 ± 0.25
	Thickness (km)	0.79 ± 0.21	2.08 ± 0.76	3.10 ± 1.72
Geometry & Mixing	**Distance (km)**	3496 ± 1185	3662 ± 1617	4845 ± 2825
	Mixing (hours)	41 ± 26	66 ± 41	26 ± 13
	R_{eff} (μm)	0.293 ± 0.074	0.360 ± 0.081	0.387 ± 0.070
Microphysical Properties	**RRI**	1.50 ± 0.00	1.47 ± 0.05	1.47 ± 0.05
	IRI	0.005 ± 0.000	0.0046 ± 0.0045	0.0041 ± 0.0018
	SSA_{532}	0.9482 ± 0.0019	0.9644± 0.0181	0.9638± 0.0219
	SSA_{355}	0.9372 ±0.0070	0.9579 ± 0.022	0.9517 ± 0.0264

5.2.4 Mixing processes and spheroid aerosol microphysical properties of 4 specific events (Athens and Granada)

In this section we will show the great potential of lidar stand-alone retrievals of non-spherical aerosol microphysical properties. We present the aerosol optical and microphysical properties during 4 selected Saharan dust events over Athens (Greece; NE Mediterranean) and Granada (Spain; NW Mediterranean) focusing on short-range to long-range dust processes. We selected specific dust transport cases taking into account their transport time and mixing process whose datasets allowed for stable microphysical inversions: 11 September 2017, Athens (case A), 16 June 2013, Granada (case B), 19 April 2018, Athens (case C) and 9 June 2016, Granada (case D).

At a first step, we verified that the source region of the air masses arriving over Athens and Granada, was originating from the African continent, again, by means of the HYSPLIT model for a period of 120 hours backward in time. The air mass trajectories were computed for arrival heights of approximately the bottom, center and top of each observed layer. Again, mixing time refers to the hours the air masses travelled after leaving the African continent until they were detected over the observation stations. Based on this transport time, the four selected dust cases reveal a pattern which allows us to separate them into two categories: (i) transport time ≤ 1 day, which indicates quite pure or less mixed particles within the dust layer (Fig. 5.5), (ii) transport time > 1 day, which indicates a combination of mineral dust, polluted mineral dust or even smoke arriving over the stations (Fig. 5.6).

i) Transport time (after African continent) ≤ 1 day: The air mass backward trajectories arriving over Athens on 11 September 2017 (case A), at 18:00 UTC, between 2-4 km (cf. Fig. 5.12 left), shows that ~18 hours of the total of 120 hours of the residence time are spent over the Mediterranean Sea and 60 (at 3000 m) to 100 hours (at 4000 m) over S. Morocco, Algeria and Libya, where Saharan desert areas spread out. Similarly, for the air mass backward trajectories arriving over Granada on 16 June 2013 (case B), at 22:00 UTC, between 2.5-4 km, (cf. Fig. 5.12 right), ~24 hours are spent over N. Morocco and Alboran Sea and 48 hours (at 2500 and 3000 m) over E. Morocco and Algeria, areas that belong to the Saharan region. Consequently, the aforementioned air masses in both cases are travelling quite fast (≤1day), probably favouring the direct transport of mineral dust aerosols.

ii) Transport time (after African continent) > 1 day: For the case of 19 April 2018 detected over Athens (case C), the air mass backward trajectories (calculated at 18:00 UTC), show that less than 30 of the total 120 hours are spent over Libya and Tunisia, while the rest 90 hours are spent circulating over the Mediterranean, Aegean Sea and Bulgaria (cf. Fig. 5.13 left). Analogously, for the case of 9 June 2016 detected over Granada (case D), the calculated air mass backward trajectories at 02:00 UTC show that ~48 of the total 120 hours are spent over the Atlantic Ocean and the Andalusian region while the other 72 hours over S. Morocco and Algeria (cf. Fig. 5.13 right). It is evident that in both events, there is no direct air mass flow from the source region to the lidar stations, but an alternative path above marine and urban areas. Therefore, the measured aerosol optical properties for these cases can be attributed to a mixing state where industrial/continental, marine or even biomass burning aerosols were possibly mixed with the desert dust aerosols.

In order to investigate the possible mixing with other aerosol particle types during the air masses transport we used the observations of the spaceborne lidar system CALIOP (on board the CALIPSO mission, cf. Sect. 4.8) to track the aerosol plumes for the cases of the second category. In this study we used the aerosol typing product of (Kim et al., 2018). We found CALIPSO overpasses intersecting the air mass backward trajectories as presented in Fig. 5.13 (red boxes). Using the aerosol typing mask tool (Omar et al., 2009), it was possible to determine the degree of mixing for these two cases. It is easily observed that the air masses that eventually arrived over Athens at 19 April 2018 contained not only pure mineral dust, but also polluted dust and even some smoke particles (yellow, brown and black colors respectively). Moreover, the case of 9 June 2016 shows that mainly pure dust (above 3 km) and polluted dust (below 3 km) was transported over Granada. Keeping this information in mind, one could expect different features in terms of the aerosol optical and microphysical properties for these two dust transport cases compared to the two abovementioned. It should be noted here that there were no CALIPSO data available for case A and no overpass over Spain for case B, consequently no such information is provided in Figs. 5.12a and 5.12b.

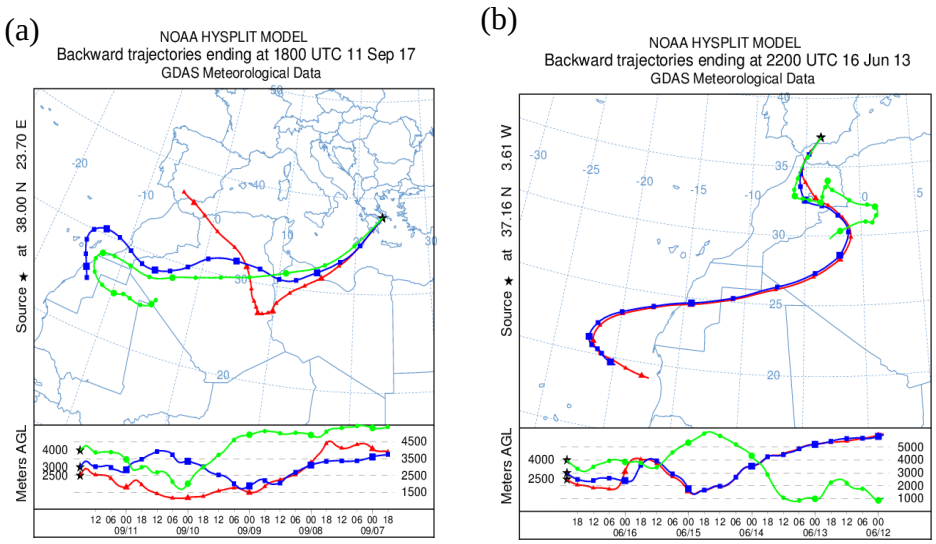

Figure 5.12: 120-hour air mass backward trajectories arriving over a) Athens on 11/09/2017, (case A, 18:00 UTC), between 2-4 km height and b) Granada on 16/06/2013, (case B, 22:00 UTC), between 2.5-4 km height.

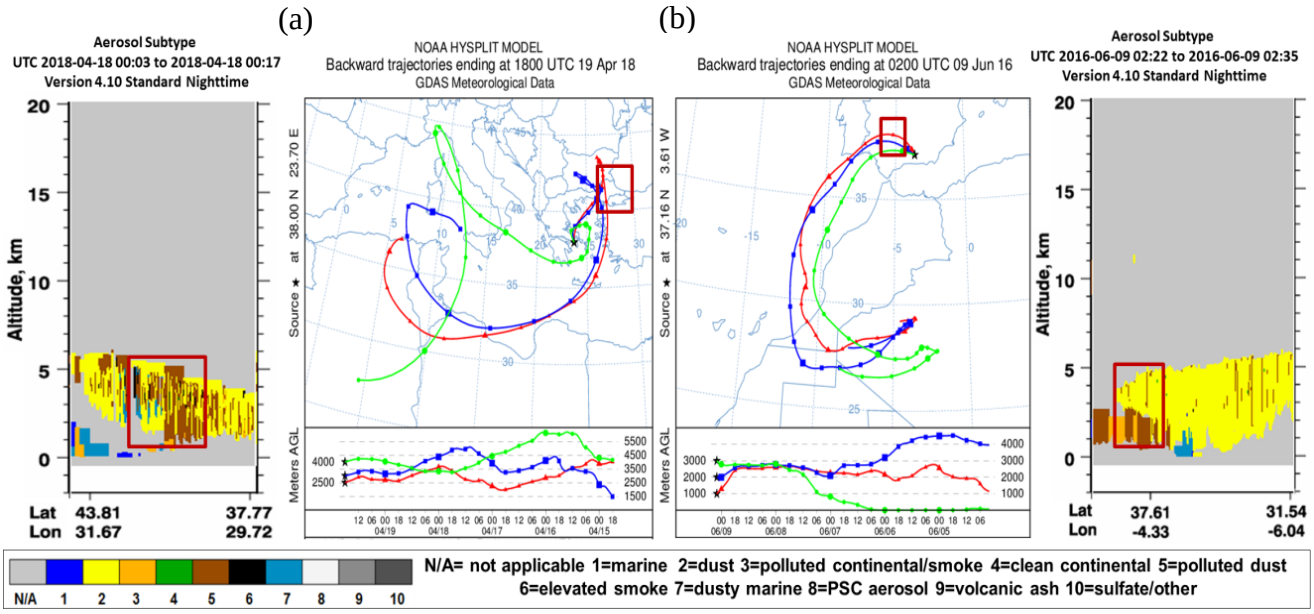

Figure 5.13: 120-hourair mass backward trajectories over a) Athens on 19/04/2018, (case C, 18:00 UTC), between 2.5-4.5 km and b) Granada on 09/06/2016, (case D, 02:00 UTC), between 1-3 km height, along with position (altitude, latitude and longitude) and type of the aerosol layers detected by CALIOP during one overpass tracking the air masses contained within the red boxes (extreme left and right). Yellow and brown colors stand for pure and polluted dust respectively, while black indicates smoke.

Apart the analysis of the lidar data, we also used AERONET data. The main direct AERONET products obtained for the relevant selected temporal windows are summarized in Table 5.3. The AOD at 500 nm was at least 0.27, with relatively low Fine Mode Fractions (FMF) values in all cases but C. In this case, the presence of polluted and smoke particles (Fig. 5.13a) makes the fine and coarse mode (related to mineral dust) share similar proportions with a FMF of 55%. The spectral dependent AOD's and the AE_{AOD}'s show values much lower than the usual ones over urban sites (e.g. Alados-Arboledas et al., 2003 and 2008; Lyamani et al., 2010; Gerasopoulos et al., 2011), again with the exception of case C, where the AE values are close to 1, a representative value for mixed biomass burning with desert dust aerosols (Giannakaki et al., 2016).

Table 5.3: Columnar aerosol properties retrieved from direct AEORNET measurements during the selected 4 dust cases.

Case	Time (UTC)	AOD (500 nm)	FMF (%)	AE_{AOD} (440/870 nm)
A) AT, 11/09/2017	15:36	0.34	22	0.22
B) GR, 16/06/2013	18:28	0.27	28	0.36
C) AT, 19/04/2018	15:20	0.27	55	0.94
D) GR, 09/06/2016	18:21	0.54	19	0.16

Additionally, in Fig. 5.14a, we can observe typical SSA values for dust particles increasing with wavelength, except case C, ranging from 0.85 to 0.98 as also observed by Dubovik et al. (2002), Valenzuela et al. (2012) and Benavent-Oltra et al. (2017). The IRI values (Fig. 5.14b), especially in case B, are slightly higher than the reported by Dubovik et al. (2002), in agreement with those from Benavent-Oltra et al. (2017). The analysis of the spectral behaviour of these two variables (SSA, IRI) yields further interesting information. The cases with shorter transport time (case A and B) have similar positive slope for SSA and negative for IRI, as also reported in the literature (Toledano et al., 2011; Valenzuela et al., 2012; Lopatin et al., 2013; Schuster et al., 2016; Benavent-Oltra et al., 2017). For case C, where the dust was transported during longer time with a strong possibility of mixing with biomass burning particles, we can observe no dependence on wavelength (zero slope), a feature related to the presence of black carbon from combustion (Bergstrom et al., 2007). In case D, where again the transport process last longer, the spectral dependence is more pronounced in the shorter wavelengths showing similarities with cases A and B. These results suggest that the higher the element of dust and the contribution of larger particles in the mixing, the more pronounced spectral difference for smaller wavelengths. Moreover, their absorption is lower and thus, their SSA values are higher in general for the cases with more aged or mixed particles (cases C and D). It should be noted here that, up to now, there have been numerous studies providing fundamental insights into the complex photochemistry of mineral dust aerosol in the atmosphere (Cwiertny et al., 2008). Liquid or adsorbed water and coatings can affect dust photochemistry as mineral dust particles are transported through the atmosphere, as well as the diurnal cycle can affect the mineral dust properties between daytime (AERONET) and nighttime (Raman-lidar) measurements.

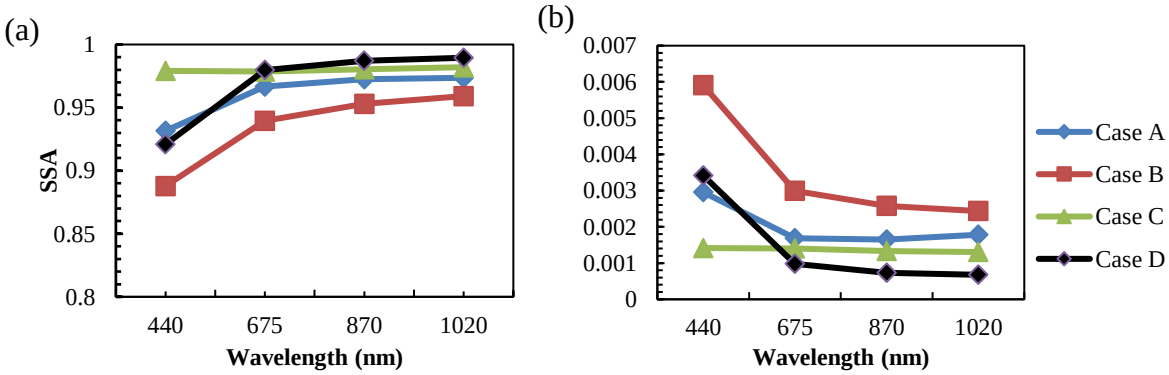

Figure 5.14: AERONET retrievals of a) SSA and b) IRI for cases A to D.

In all four studied dusty cases, the aerosol size distributions retrieved by the AERONET inversion code showed again that the fine mode particles do not have a significant contribution to the measured AOD values compared to the coarse mode particles that are dominant in the atmospheric column (Fig. 5.15). This means a contribution of larger particles that corroborates the desert origin of the probed aerosols. The dominance of the coarse mode particles is highlighted by the bimodal size distribution with separation radius ranging from 0.18 μm to 0.30 μm. For our first category (Cases A and B), the bimodal volume size distributions have almost similar structure with low fine mode concentration ($< 0.02\ \mu m^3/\mu m^2$). Specifically, for case B, the coarse mode is shifted to slightly larger

radii, while a small difference in maximum volume concentration equal to 0.06 $\mu m^3/\mu m^2$ indicates quite similar intensity of the events of cases A and B. For our second category (Cases C and D), a large difference in the size distributions between the two events is observed. A high peak of coarse mode for case D in comparison to the lower concentration of case C represents a more intense dust episode. The highest intensity differences among the dust episodes are mostly reflected by the associated magnitudes of the volume concentration. For instance, the highest coarse-mode peak, corresponding to Case D, represents a relatively more intense dust episode as compared e.g. to the lowest peak corresponding to case C. There are further differences to be observed regarding the shape of the coarse mode with the most evident one corresponding to the mode width, which is substantially greater for case D than for case C having ranges 0.33-8.65 μm and 0.44-6.64 μm respectively.

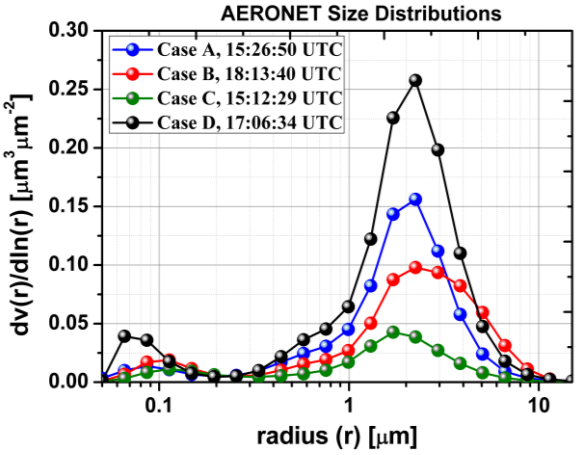

Figure 5.15: AERONET aerosol volume size distributions dV(r)/dln(r) for cases A to D.

Vertically-resolved aerosol properties

- *Aerosol optical properties*

Figure 5.16 (a and b) depicts the vertical profiles of the dust aerosol optical properties of the two independent mineral dust cases A and B. On 11 September 2017 (Fig. 5.16a) a thick, intense and almost uniform dust layer from around ground level up to 4.5 km height (a.s.l.) was detected by EOLE [17:00-18:30 UTC] over Athens (case A). On 16 June 2013 (Fig. 5.16b) there is an almost uniform layer in the atmospheric column above Granada (case B), which, similarly to case A is reaching 4.7 km a.g.l. [22:00-22:30 UTC]. For the aforementioned cases we selected the thin layers at heights 3.5-3.8 and 2.65-3.1 km a.s.l. respectively. The selection of these thin layers inside the dust plumes was based not only on the homogeneity of the optical properties, but also on the backward trajectories in which, at roughly these altitudes, the source region is the same (W. Algeria) as shown in Fig. 5.12. The vertical profiles of the other two cases representing events of more aged and mixed dust layers are also presented in Fig. 5.16 (c and d). At least two decoupled aerosol layers of different intensities are detected over Athens on 19 April 2018 (Fig. 5c) between 1.5 and 4.5 km a.s.l. [17:30-18:50 UTC]. The vertical profiles on 9 June 2016 over Granada (Fig. 5.16d) confirm the decoupled thick mineral dust layer of different intensities, between 2.5 and 5 km a.s.l. Here, we selected the thin layers 2.6-2.8 [17:30-18:50 UTC] and 2.55-2.75 km a.s.l. [01:00-02:00 UTC] respectively, in which there was indication of mixed aerosol layers: polluted dust or even smoke particles for case C, polluted dust for case D (see also Fig. 5.13).

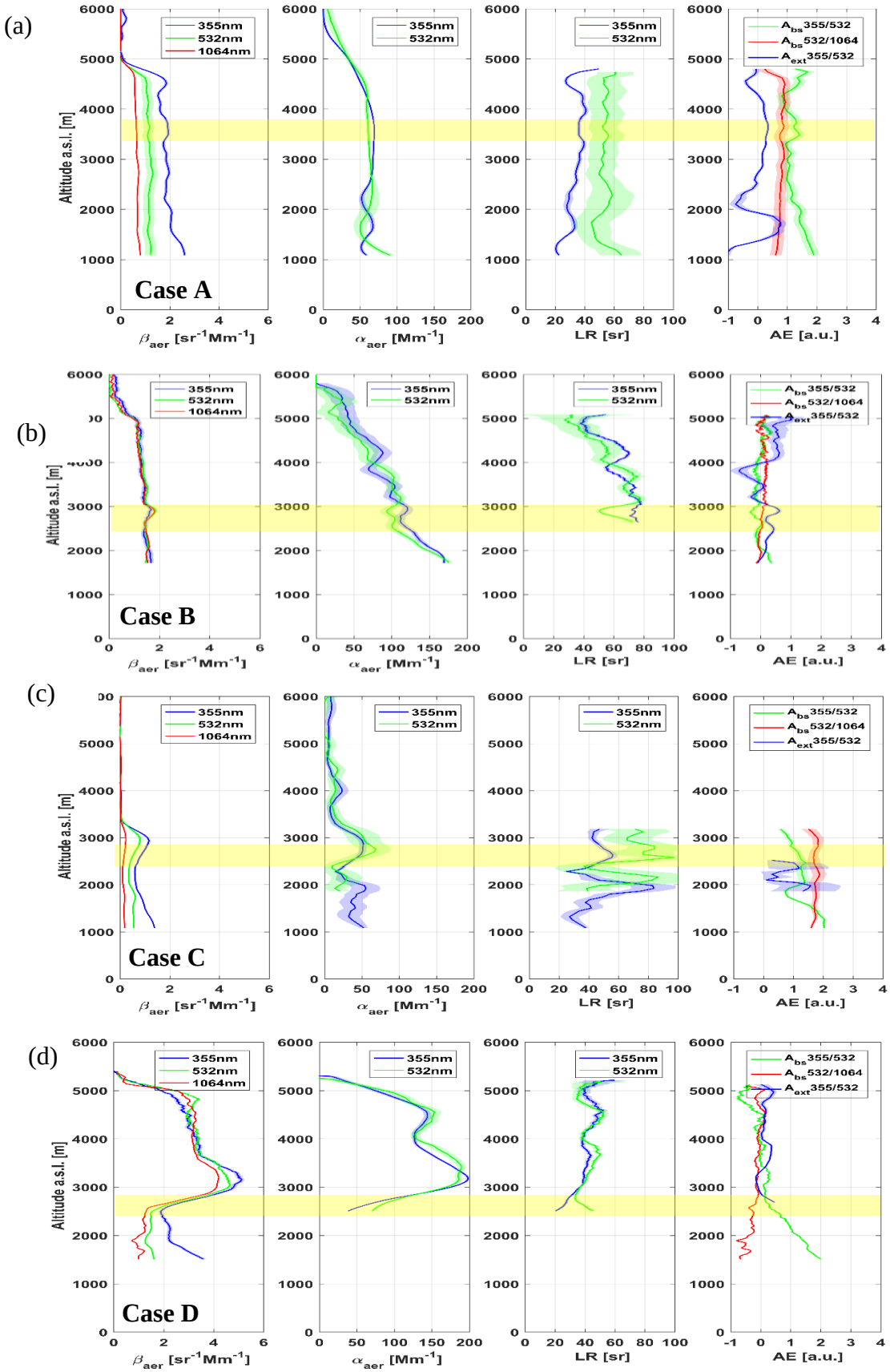

Figure 5.16: Vertical profiles of the aerosol optical properties (βaer, α_{aer}, LR, AE) obtained over a) Athens on 11 September 2017, 17:00-18:30 UTC (Case A), b) Granada on 16 June 2013, 22:00-22:30 UTC (Case B), c) Athens on 19 April 2018, 17:30-18:50 UTC (case C), between and d) Granada on 9 June 2016, 01:00-02:00 UTC (case D) along with their error estimations (horizontal bounds). Yellow layers indicate the regions selected for microphysical analysis.

The mean values of the aerosol optical properties retrieved from the lidar measurements and used for the inversions for the four selected layers are shown in Table 5.4, along with their SD. Their intensive parameters are also mentioned. For the first two cases (A and B) with transport time < 1 day, these values represent the typical optical properties of short-range transported dust plumes. More specifically, in this case, typical LRs were found (54 ± 1 and 64 ± 6 sr at 532 nm respectively) falling within the ranges for Saharan-dust particles found in literature (Müller et al., 2009; Groß et al., 2011). The backscatter-related AE ($AE_{b532/1064}$) values of 0.83 ± 0.04 and 0.03 ± 0.02 respectively, correspond to quite large particles, again, in good agreement with previous findings (Mamouri and Ansmann, 2014; Veselovskii et al., 2016). The small SD values underline that the particles were well mixed in the altitude range of the uniform dust layers.

Concerning the remaining two cases (C and D) we found larger deviations among their intensive optical properties. The quite high mean LR value of 79 ± 5 sr (at 532 nm) for case C corroborates the strong indication that dust particles were mixed with particles of other origins, such as smoke while travelling. Lower LR values of 39 ± 2 sr (at 532 nm) are reported for case D. Contrary to the abovementioned category, here, the decoupled plumes were probably relatively inhomogeneously distributed along the vertical direction and mixed with aerosols from different origins (possible biomass burning mixtures for case C and polluted mixtures for case D) or even different regions in Sahara desert (differences in chemical composition of the mineral dust).

Table 5.4: Average aerosol particle optical properties for the selected layers within the dust zone along with their SD.

Case		**A**	**B**	**C**	**D**
Layer height a.s.l. [km]		**3.50-3.80**	**2.65-3.10**	**2.60-2.80**	**2.55-2.75**
Optical properties	**α_{355} [Mm^{-1}]**	68.62±0.89	115.60 ±6.94	49.11±3.13	62.27 ±1.62
	β_{355} [Mm^{-1} sr^{-1}]	1.89±0.06	1.55±0.11	0.94±0.11	2.39 ±0.43
	α_{532} [Mm^{-1}]	60.69±0.52	100.88±8.35	52.54±9.00	82.67 ±10.06
	β_{532} [Mm^{-1} sr^{-1}]	1.13±0.03	1.67±0.06	0.61±0.10	2.15 ±0.05
	β_{1064}[Mm^{-1} sr^{-1}]	0.63±0.01	1.621±0.001	0.18±0.02	1.83±0.05
	$\delta_{aer\ 355,\ 532}$	0.34±0.02	0.26±0.04	0.11±0.01	0.28±0.01
Intensive properties	**LR_{355} [sr]**	36±1	76±7	51±4	28±4
	LR_{532} [sr]	54±1	64±6	79±5	39±2
	$AE_{\beta\ 532/1064}$	0.83±0.04	0.03±0.02	1.70±0.20	0.25±0.10

Figure 5.17 presents the vertical profiles of δ_{aer} of the four case studies (at 355 nm for Athens and at 532 nm for Granada system). Typical δ_{aer} values of transported mineral dust (Freudenthaler et al., 2009, Groß et al., 2015), were calculated for the cases of the first category, verifying again the dominance of the mineral dust particles. More precisely, mean δ_{aer} values equal to 0.34 ± 0.02 for case A (17:30-18:30 UTC, 3.5-3.8 km) and 0.26 ± 0.04 for case B (22:00-22:30 UTC, 2.65-3.10 km)) provide a clear indication of the non-sphericity of the pure dust particles. For these cases, the particles of mineral dust sources seem to be rather unaffected by anthropogenic or other polluted aerosols. For the cases of the second category, the mean δ_{aer} calculated inside the plumes show marginal values of SD. The value of δ_{aer} was found equal to 0.11±0.01 for case C (17:30-18:30 UTC, 2.6-2.8 km) and 0.28 ± 0.01 for case D (01:00-02:00 UTC, 2.55-2.75 km). The fact that in case D the value of δ_{aer} increases above 2.5 km a.s.l. ($\delta_{aer} = 0.32 \pm 0.01$, 3-4.5 km) confirms the separation between polluted and pure dust layers observed by CALIOP (see Fig. 5.13b). Moreover, the aforementioned influence of mixtures (dust and smoke) can explain the lower δ_{aer} values of around 10% calculated for case C, which are in accordance with previous studies (Ansmann et al., 2011; Groß et al., 2011; Tesche et al., 2011; Wandinger et al., 2016; Giannakaki et al., 2016).

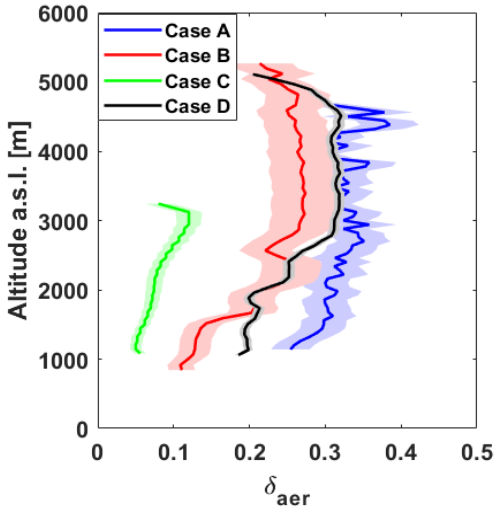

Figure 5.17: Vertical profiles of the δ_{aer} for cases A to D along with their error estimations (horizontal bounds). For Athens and Granada stations depolarization measurements are available at 355 nm and at 532 nm respectively.

- *Aerosol microphysical properties*

For each selected dust layer, the SphInX tool was applied (see Sect. 4.2) using the mean values of our optical datasets presented in Table 5.4 as inputs. Table 5.5 shows the average values of a_t, u_t, r_{eff}, a_{eff} and α_{width}, RRI, IRI and SSA, along with their Var (%) derived by using the 5 best solutions picked by the software according to the algorithm described in Sect. 4.2.

The RI values retrieved by SphInX (Samaras, 2016) for the mineral dust cases of the first category is found equal to 1.4 + 0.004i inside both selected layers and SSA (532 nm) equal to 0.97 for case A and 0.98 for case B, which points to weakly absorbing particles. On the other hand, different values of the CRIs were found for the cases of the second category. More specifically, for case C the CRI was found equal to 1.5+0.002i while for case D it was found equal to 1.5+0.005i.

Table 5.5: Average particle microphysical properties inside the selected layers along with their Variance (Var, %) based on the 5 best solutions picked by the SphInX.

Case		**A**	**B**	**C**	**D**
Layer height a.s.l. [km]		**3.50-3.80**	**2.65-3.10**	**2.60-2.80**	**2.55-2.75**
Lidar-based inversions	**a_t [µm^{2}cm^{-3}]**	152.20±8%	268.30±10%	140.99±3%	228.73±5%
	u_t [µm^{3}cm^{-3}]	16.13±10%	29.42±13%	19.92±8%	36.64±6%
	r_{eff} [µm]	0.32±4%	0.33±3%	0.42±8%	0.48±8%
	α_{eff}	1.18±5%	1.14±5%	1.32±1%	1.32±1%
	α_{width}	0.06±24%	0.06±25%	0.06±15%	0.06±25%
	Distribution uncertainty [%]	48.19	46.31	26.86	23.85
Microphysical properties	**RRI**	1.4±0%	1.4±0%	1.5±0%	1.5±0%
	IRI	0.004±43%	0.004±57%	0.002±50%	0.005±42%
	SSA_{532}	0.97±1%	0.98±2%	0.98±2%	0.96±2%

For the less mixed dust episodes the retrieved 2D shape-size distributions reveal the same three-mode pattern (Figs. 5.18 a and b). Two of the three modes correspond to prolate particles ($a \approx 1.5$), confirming the non-spherical nature of the dust particles. The prolate particle modes can be subdivided into a coarse mode with radii $r \approx 1.7$ µm and a fine mode around 0.5 µm. A third mode centered in $a \approx 1$ and $r \approx 0.3$ µm represents an additional contribution of spherical particles. The effective radius

for the more intense episode of case A is found shifted to larger values (0.57 ± 0.05 μm) as compared to the corresponding case B (0.33 ± 0.02 μm).

In Fig. 5.18c, the dominant mode of the shape-size distribution corresponds to prolate fine particles (up to $\alpha \approx 1.5, r \approx 0.5$ μm) and is extended up to 2.2 μm. Additionally, there is a less prominent but substantially wider mode pertaining to prolate coarse particles (up to $\alpha \approx 1.5, r \approx 1.4$ μm) with a less obvious separation point. Furthermore, the smaller peak indicates a contribution of oblate fine particles ($\alpha \approx 0.7, r \approx 0.3$ μm). However, due to the relatively low magnitude of this peak and the possibility of oversmoothing of the prolate coarse mode, the case that this peak might be either a suppressed larger peak or an artefact, should be considered as well. In Fig. 5.18d, the dominant mode of the shape-size distribution has similar behavior with the one of case C concerning the prolate fine mode (up to $\alpha \approx 1.5, r \approx 0.5$ μm, extended up to 2.2 μm). However, the less prominent mode pertaining again to prolate coarse particles seems to be extended to smaller α values ($\alpha \approx 1.3$, $r \approx 1.5$ μm). Here, there is a more significant coarse mode contribution in accordance with the higher δ_{aer} value compared to case C.

For these four cases the dust particles behave effectively as prolate spheroids as it is further indicated by the values of $\alpha_{\mathbf{eff}}$ ranging between $1.19 - 1.32$ (see Table 3). The value of a_{width} was calculated equal to 0.06 ± 0.01 for all cases. The differences in the shape size distributions for the cases presented in Fig. 5.18, provide an additional indication for differences in aerosol composition occurring due to the different travelled path bound to each case. Since case D owns the most intensive event (see Figure 5.16) it takes the greatest u_t value equal to 37 $\mu m^3 cm^{-3}$, while for the rest cases A, B and C we have 16, 29, and 20 $\mu m^3 cm^{-3}$ respectively (see Table 5.5).

Restricting to a 1-dimensional (1D) aerosol size distribution would offer a short-sighted view. If we picture, for instance, all aspect ratio contributions summed for the distributions in Fig. 5.18 (a,b,c,d) see that there is only radius dependence left, then the figures would appear relatively similar in trend qualitatively. Obviously, even the spheroidal consideration of dust particles does not capture the particle form physically (it is mainly a better fit for the observed optical properties), but with the described approach our analysis can be refined to include possible diversity among cases of interest which is otherwise invisible.

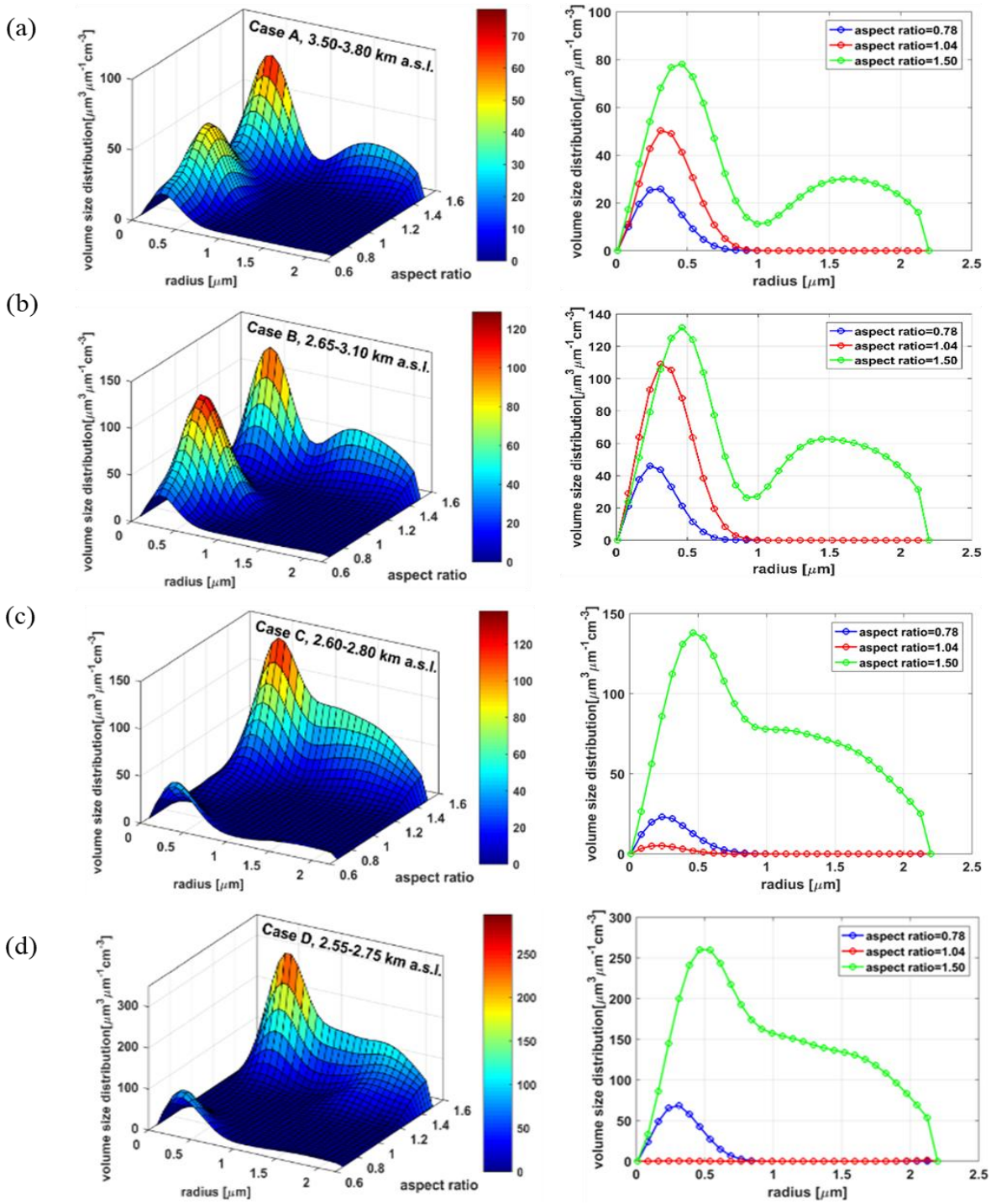

Figure 5.18: The shape-size distribution shown in 3D (left) for the hole aspect ratio range and in 2D (right) for 3selected aspect ratio values (0.78-oblate, 1.04-spherical, 1.50-prolate particles) for a) case A at 3.5–3.8 km a.s.l., b) case B at 2.65-3.10 km a.s.l., c) case C at 2.6–2.8 km a.s.l. and d) case D at 2.55–2.75 km a.s.l. as retrieved by the SphInX software tool.

Although these 2D particle distributions provide more information than a usual size distribution, there are also limitations to this approach which might affect the inversion outcome. Since there are several assumptions pertaining to the whole inversion chain (discretization, regularization, T-matrix theory etc.), a full discussion exceeds the scope of this Thesis and limits itself to some evident remarks. The less pronounced separation between fine and coarse aerosol modes especially for the prolate part in Fig. 5.18 might indicate higher measurement errors which were misidentified by regularization; this is a common encounter also for the usual one-dimensional (size) distributions, (cf. Samaras et al., 2015). The higher aspect ratio end (1.5) might not be sufficient in order to reveal the full extent of the

shape size distribution further along the aspect ratio axis. The same is true for the radius boundary on the right end even though in our cases the distributions are only mildly abrupt in this respect. Finally, the presence of potential small artefacts in the distribution, as for instance in Fig. 5.18 (c and d), has only a small contribution to the derived microphysical parameters since the double integration suppresses further small oscillations in the solution.

5.3 Radiative forcing of dusty layers over the Mediterranean basin

It is well documented that considerable uncertainties in quantifying the global direct radiative effects of aerosols arise from the variability of aerosols' spatial distribution and aging/mixing processes which can affect their optical and microphysical properties. The magnitude and even the sign of the dust aerosol solar radiative forcing are highly uncertain as they strongly depend on their optical properties, their size distribution and their CRI values. Papadimas et al. (2012) reported that the aerosol optical depth seems to be the main parameter for modifying the regional aerosol radiative effects (under cloud-free conditions) and, that on an annual basis, aerosols can induce a significant "planetary" cooling over the broader Mediterranean basin. Other studies (Quijano et al., 2000; Tegen et al., 2010) have shown that the presence of clouds and the surface albedo are also unquestionable parameters affecting the net solar radiative transfer at the top of the atmosphere. However, a comprehensive analysis from ground-based aerosol optical properties to vertical profiles of short- and long-wave radiation estimations in the Mediterranean region has been reported so far only in a few papers (Sicard et al., 2014; Meloni et al., 2003; 2015; Valenzuela et al., 2017; Gkikas et al. 2018).

5.3.1 Dust mass concentration lidar retrievals

To retrieve the aerosol dust mass concentration profiles, we first calculated the vertical profiles of β_{532} and δ_{p532}. Furthermore, by assuming that we have only two aerosol types (dust and non-dust) inside the calculated β_{532} values, we separated the β_{532} profiles in two components: the first arising from the contribution of the weakly depolarizing particles ($\delta_{nd} = 0.05$ for non-dust particles) and the second one from the contribution of strongly depolarizing particles ($\delta_d = 0.31$ for dust particles). Then, the dust-related backscatter coefficient β_d at 532 nm was obtained, following the procedure described by Tesche et al. (2009), according to the equation:

$$\beta_d = \beta_{aer} * {(\delta_p - \delta_{nd})(1 + \delta_d)} \Big/ {(\delta_d - \delta_{nd})(1 + \delta_p)} \quad (5.1)$$

The estimation of the height-resolved mass concentration (in kg m^{-3}) of dust particles was based on the procedure described by Ansmann et al. (2012), using the following equation:

$$mass_d = \rho_d (v_d/\tau_d) \beta_d \, LR_d \quad (5.2)$$

where we assumed the coarse-particle mass density (ρ_d) to be equal to 2.6 gm^{-3}. Furthermore, a mean volume-to-AOD ratio for coarse mode particles, v_d/τ_d was calculated from AERONET measurements (https://aeronet.gsfc.nasa.gov) for each station during the period 2014–2017. We report now, these values in Table 5.6. The mean values of the whole studied period were calculated, since only few of the studied cases were common in EARLINET and AERONET database. For the LR_d, the mean LR values per station, as calculated from the lidar measurements, were also used (cf. Table 5.6; Fig. 5.9c). These values are in good agreement with literature findings for long-range transported Saharan dust events (Tesche et al., 2009; Ansmann et al., 2012; Groß et al., 2011; 2013).

Table 5.6: Assumed (ρ_d) and computed parameters (v_d/τ_d, LR_d) used for the estimation of the height-resolved mass concentration (in kg m^{-3}) of dust particles. The ratio v_d/τ_d is derived from AERONET sun–sky photometer measurements within the period 2014-2017 at Granada, Potenza, Athens and Limassol. The LR_d is calculated from the available lidar measurements per station used in this study.

Station	ρ_d (g m^{-3})	v_d/τ_d (μm) (AERONET)	LR_d (sr)
GRA	2.6	0.80±0.29	52±8
POT	2.6	0.71±0.37	51±9
ATZ	2.6	0.94±0.50	52±9
LIM	2.6	0.87±0.27	49±6

5.3.2 Evaluation of the aerosol mass concentration vertical profiles

Before using the vertical dust mass concentrations profiles retrieved from i) BSC-DREAM8b model simulations (Scheme A) and ii) lidar measurements as calculated from Eq. 5.2 ($mass_d$), (Scheme B, see Sect 4.6.1) as inputs to the LibRadtran model, we performed a day-by-day comparison between them. Due to the different spatial and vertical resolution between the modeled and the lidar profiles, both profiles were degraded to the fixed height levels of the OPAC dataset (0, 1, 2, 3, 4, 5, 6, 7, 8, 9, 10, 11, 12, 35 km).

Figure 5.19 shows the Taylor's diagram of the mass concentration simulated by the BSC-DREAM8b model against the lidar-retrieved ones. The azimuthal angle presents the correlation coefficient, the radial distance presents the normalized SD of each point, the root mean square error (RMSE) is proportional to the distance from the point on the x-axis identified as "Calculated", which, is depicted by a black point at the (1,0) cross section, indicates the lidar retrieved aerosol mass values representing the reference point. The normalization of the SD is performed with respect to the calculated values. In the 66 % of the cases there is a good correlation ($r > 0.6$), and consequently a good prediction of the shape of the vertical distribution is achieved, while in 96 % of the cases the model gives lower concentration values ($normalized\ SD < 1$) revealing an underestimation in the intensity and the mass concentration of the events. Therefore, we report a mean underestimation of the mean mass concentration values of the BSC-DREAM8b of the order of 31%. However, we should take into consideration: i) the spatial resolution, where the lidar observations are considered as point measurements while the simulations represent uniform pixels of 0.3^o resolution and ii) the temporal resolution, where the lidar retrieved profiles are hourly averaged, while the model derived profiles are instantaneous results, saved every 6 hours.

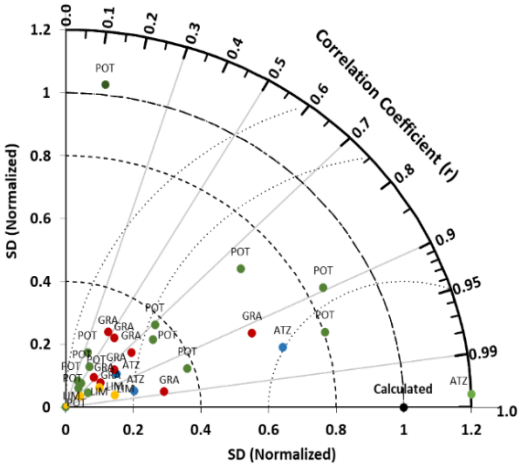

Figure 5.19: Taylor's diagram of the case-by-case vertical mass concentration simulated by BSC-DREAM8b model against the lidar retrieved ones. The black point (1,0) represents the calculated lidar data. The azimuthal angle presents the correlation coefficient (r), the radial distance of any point from the origin (0,0) indicates the normalized SD of the data set. The colored the dots represent each one of the 4 EARLINET stations, namely GRA (red), POT (green), ATZ (blue) and LIM (orange).

By further comparing the modeled mass vertical profiles to the ones calculated by lidar, we report that the mean center of mass (in km) estimated from BSC-DREAM8b profiles is 0.6 km lower than the one calculated from the lidar measurements (2.6 ± 1.0 km and 3.2 ± 1.1 km respectively). The maximum concentration (peak) is usually found in the region 2-3 km, both in the modeled and the observed data. The BSC-DREAM8b, having a significantly lower vertical resolution compared to the lidar, predicts smoother profiles of dust layers by spreading the layer's base to lower altitudes (~1km, in 100% of the cases) and the top at higher altitudes (in 86% of the cases) compared to the observed ones. These remarks are in line with previous studies by Mona et al. (2014) and Binietoglou et al. (2015) where they have reported discrepancies concerning the base, the top layer height and extinction profiles but a good agreement in terms of profile shape, between the BSC-DREAM8b and lidar observations. However, since fixed height levels of the OPAC dataset were finally used in LibRadtran for the ARF simulations of the three Schemes, having significantly lower vertical resolution compared to the intitial lidar profiles, these discrepancies in height were smoothed out.

5.3.3 Evaluation of ground level LibRadtran outputs

The evaluation of the performance of the LibRadtran model was undertaken by statistical means. The relative root mean square error (rRMSE), the relative mean bias error (rMBE) the correlation coefficient (r) and the normalized SD were calculated in order to numerically quantify the performance of the global irradiance calculated from pyranometers and simulated from the three Schemes (cf. Sect. 4.7.1). Table 5.7 shows the statistical results for the modeled global irradiance values versus the reference pyranometer measurements for both locations and the threes schemes. All scheme simulations perform remarkably well, with rRMSE values ranging from 8.3 to 16.2% and rMBE values between 0 and 15.2%. In general, the rRMSE is slightly higher at Granada, mainly for the Scheme A. According to this statistic, the LibRadtran output with the best performance are those obtained with the Scheme C as input followed by Scheme B and A, respectively. This order is the same attending to the rMBE values with the exception of the Scheme A at Athens. The correlation coefficient r depicts the good performance of the radiative transfer model for the three schemes and the two locations models. All simulations present a $r > 0.95$ with minor differences (below a 10%) in the normalized SD values respect to the pyranometer global irradiance values. A slight overestimation is observed for all scheme outputs at Granada (norm $SD > 1$). Conversely, this overestimation is no longer evident in the modeled global irradiance for Athens. It is important to notice the good performance of the Scheme B despite the important calculus involved in it.

Table 5.7: Statistical metrics for the modeled global irradiance values versus the reference pyranometer measurements for Granada and Athens and the threes schemes applied.

Schemes / Metrics	Granada				Athens			
	rRMSE (%)	rMBE (%)	R	SD (norm)	rRMSE (%)	rMBE (%)	R	SD (norm)
Scheme A	16.2	15.2	0.99	1.09	10.8	- 0.2	0.97	0.89
Scheme B	11.9	5.7	0.97	1.10	10.2	8.3	0.99	0.92
Scheme C	8.8	5.9	0.99	1.09	8.3	6.3	0.99	0.96

5.3.4 Regional aerosol radiative forcing (ARF)

As mentioned previously, there is shortage of papers in the literature about the role of dust on the Earth's radiation budget. Since very few *in situ* direct measurements of ARF effects and heat fluxes are available especially in the Mediterranean area (Bauer et al., 2011; Meloni et al., 2018) we are restricted to perform simulations to quantify the role of dust aerosols on the radiative forcing in the studied regions (Soupiona et al., 2020). The mean ARF is calculated during this simulation, calling twice the LibRadtran radiation code: with and without dust aerosols. For all cases the vertical profiles

of ARF starting from ground level/bottom of atmosphere (BOA) up to the top of atmosphere (TOA) in the SW and LW ranges were simulated using the three aforementioned Schemes.

A negative forcing of aerosols both at the BOA and TOA is noted in the SW range, as presented in Fig. 5.20a, which depicts the mean ARF of all cases per scheme. All results within the SW range represent less absorbing aerosols with a cooling behavior. Depending on the dust optical properties and the load relevant intensity, the ARF values at the BOA range from -40 to -13 W m^{-2} at SZA 25º, from -43 to -14 W m^{-2} at SZA 45º and from -44 to -15 W m^{-2} at 65º. At the TOA, the corresponding ranges per SZA are -9.5 to -1.4 W m^{-2} (25º), -16 to -3.3 W m^{-2} (45º) and -24.3 to -6.9 W m^{-2} (65º). Similarly, in the SZA independent LW range (thermal spectral range), the ARF values range from +1.6 to +4.6 W m^{-2} for the BOA and from +0.8 to +3.6 W m^{-2} for the TOA. Our estimations are consistent with results obtained by other literature findings for Saharan dust aerosols over the Mediterranean region. More specifically, Sicard et al. (2014) found that the SW RF at the BOA has always a cooling effect varying from -93.1 to -0.5 W m^{-2}, while the corresponding LW RF has always a heating effect varying from +2.8 to +10.2 W m^{-2}. They also concluded that dust aerosols at the TOA have a cooling effect in the SW spectral range with a RF ranging from -24.6 to -1.3 W m^{-2}, while at the TOA the LW RF varies between +0.6 and +5.8 W m^{-2}. Meloni et al. (2003) found at the island of Lampedusa instantaneous RF of -70.8 W m^{-2} at the BOA and -7.5 W m^{-2} at the TOA within the range 300-800 nm for an event with AOD of 0.51 at 415 nm. For the same location and for another strong Saharan dust outbreak (AOD_{500}=0.59) Meloni et al. (2015) reported a total (SW + LW) radiative forcing of -48.9 W m^{-2} at the BOA, -40.5 W m^{-2} at TOA, and +8.4 W m^{-2} in the atmosphere for SZA=55.1º. A negative radiative effect reaching down to -34.8 W m^{-2} at the surface in the Mediterranean area was also recently reported by Gkikas et al. (2018) for the period March 2000–February 2013.

Variations among the SW and LW values of the ARF are expected since they strongly depend on the different aerosol AODs, mass estimations and extinction values. Mass estimations retrieved from Scheme B are expected to give higher values compared to those given from Scheme A as revealed also by Fig. 5.20. The ARF at the LW spectral region is opposite in sign and significantly lower in absolute values than in the SW region. The difference between the TOA and BOA ARF, with the former to be only weakly perturbed and the latter to be much stronger, can be attributed to the heating within the troposphere, since the presence of the dust mainly leads to a displace of surface's radiative heating into the dust layer. Low reflected solar flux is partially offset by the absorption of upwelling LW radiation. Finally, in the LW spectral region, the mean ARF values at the BOA (Scheme A: +1.6±1.6 W m^{-2}, Scheme B: +4.6±4.7 W m^{-2}, and Scheme C: +2.9±9.4 W m^{-2}) are higher than those at the TOA (Scheme A: +0.8±0.9 W m^{-2}, Scheme B: +3.6±4.4 W m^{-2}, and Scheme C: +1.2±6.2 W m^{-2}) due to the fact that the main source of the LW radiation (Earth's surface) is close to the aerosol layers, mainly observed between 2 and 4 km a.s.l.. As a result, the ARF_{Atm} is positive during the diurnal circle, yielding net radiative heating of the dust layer.

The mean net heating rate within the atmosphere, calculated by adding algebraically both rates in the SW and LW spectral ranges is presented in Fig. 5.20b. Here, the net heating rate is clearly dependent on the available solar radiation, that increases with SZA due to the low incoming solar radiation reaching the BOA at afternoon hours (SZA 65º). Our estimations are in accordance with the fact that as the SZA increases, the optical path of the SW radiation grows significantly, increasing the attenuation of the direct radiation while generating a higher fraction of the diffuse radiation. This effect is more pronounced at the BOA, in which, the intensity of the heating rate is reduced with increasing SZA, since fewer photons are available to heat the dust layers. The net heating rate values for Scheme A are: -0.05±0.04 K day^{-1} (25º), -0.04±0.03 K day^{-1} (45º) and 0.00±0.02 K day^{-1} (65º). Similar to slightly higher values are observed for Scheme B as follow: -0.07±0.06 K day^{-1} (25º), -0.04±0.03 K day^{-1} (45º), and -0.02±0.02 K day^{-1} (65º). For Scheme C, we report higher values of the net ARF during the diurnal circle. More precisely, the net heating rate is almost 1.5 times higher at 25º, 2 times higher

at 45° and around 0.8 times higher at 65°, compared to the aforementioned Schemes. Greater sensitivity in the SZA appears in Scheme B, as it results from the line slope.

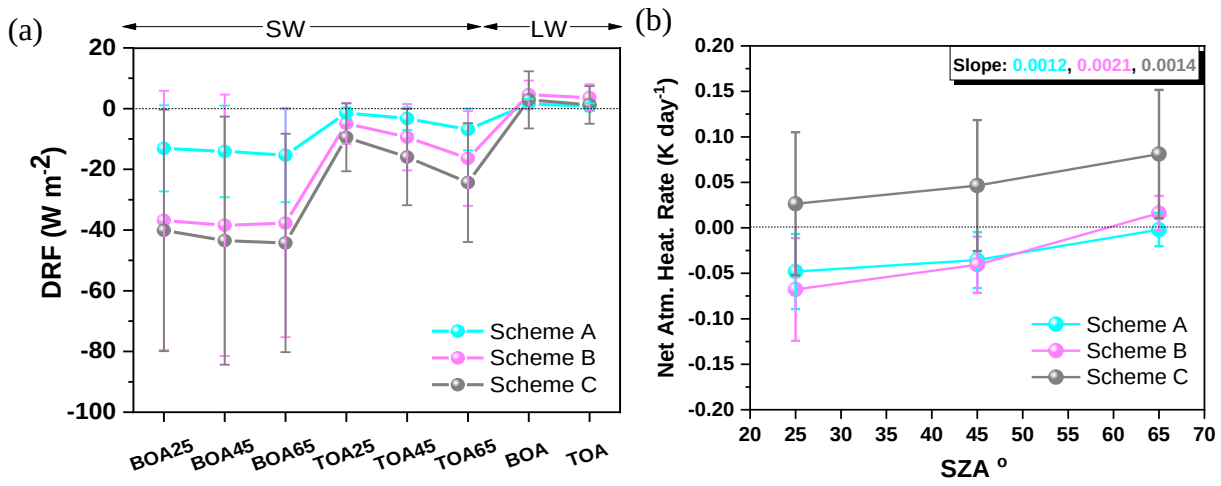

Figure 5.20: Mean values of a) SW and LW ARF at BOA and TOA and b) the net heating rate within the atmosphere, along with their SD for the three Schemes applied in the total set of the studied cases. The inserted box depicts the line slope.

In order to further explain the difference of sign in the net heating rate of Scheme C, compared to the two others presented in Fig. 5.20b, we plotted the aforementioned parameter along with the base layer height, the AOD_{532} and the layer thickness of each case as presented in Fig. 5.21. Taking into account that the effect of net heating rate of the vertical distributions, from negative to positive values, is more pronounced close to surface at small SZA values, the estimations of BOA at 25° SZA were selected to be presented in this graph. It becomes clear that the sign of the net heating rate at BOA depends on the dust vertical structure and the AOD. More precisely, the majority of the cases having low AOD_{532} values (≤ 0.2) and low layer thickness (≤ 2 km) give negative net heating rate values. Additionally, the higher the AOD the higher the absolute value of the net heating rate.

Concerning the base layer height, it plays a key role to the absolute net heating rate of each case, since dust layers close to the ground take higher absolute net heating rate values. For example, let us examine two events which occurred during the same month (August). The first dust event with a layer base at 2.8 km, 0.73 km thickness and AOD_{532} equal to 0.01 has a heating rate of -0.17 K day^{-1}, while the second one, with layer with base at 3.8 km, 0.66 km thickness and AOD_{532} equal to 0.02 has a net heating rate of almost zero (-0.03 K day^{-1}). In another comparison, net heating rate values of -0.02 K day^{-1} versus +0.09 K day^{-1} are reported for two layers, during summer time that have almost the same base (2.6 km and 2.5 km) and thickness (2.3 km and 2.4 km) but different AOD_{532} values (0.08 and 0.34 respectively). Finally, a combination of high AOD_{532} ($0.21 - 0.83$) and high thickness ($2.1 - 5.5$ km), two parameters that are usually directly dependent, along with low base height ($1.0 - 1.5$ km), give high net heating rate values with positive sign ranging from $+0.06$ to $+0.26$ K day^{-1}.

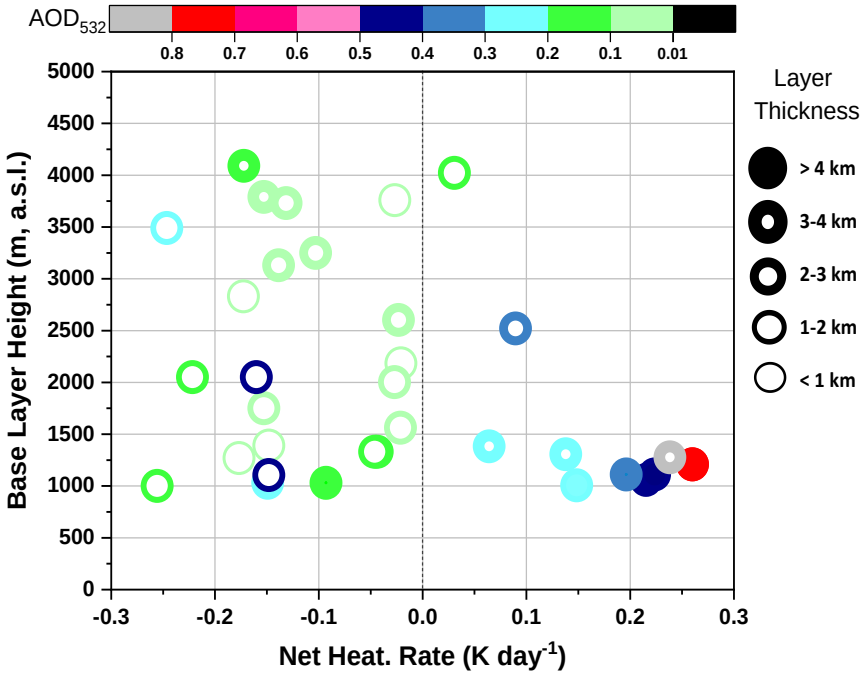

Figure 5.21: Net heating rate values per case of Scheme C estimated at BOA, 25° SZA versus base layer height. The horizontal colorbar indicates the AOD_{532} values and the vertical symbol thickness indicates the layer thickness.

Figure 5.22 (a-c) depicts the same results as in Fig. 5.20a but for each of the three identified clusters: BB and dust, mixed Saharan dust Saharan dust. The ARF in the SW range is negative both in the BOA and TOA for all clusters and is dominated by large dust particles of the Saharan dust episodes (Fig. 9c, Scheme A: -22.5±16.7 W m^{-2}, Scheme B: -34.0±37.0 W m^{-2}, Scheme C: -49.2±50.9 m^{-2} for BOA, and Scheme A: -2.5±2.1 W m^{-2}, Scheme B: -4.4±5.2 W m^{-2}, Scheme C: -12.1±14.4 m^{-2} for TOA, SZA 25°), whereas mixed layer with biomass burning aerosols have significantly lower cooling effect (Fig. 9a, Scheme A: -6.2±4.0 W m^{-2}, Scheme B: -19±9 W m^{-2}, Scheme C: -4.8±3.5 W m^{-2} for BOA, and Scheme A: -0.5±0.4 W m^{-2}, Scheme B: -2.0±1.3 W m^{-2}, Scheme C: -0.7±0.5 m^{-2} for TOA, SZA 25°) for each of the three applied Schemes. ARF seems to be inversely proportional to the mixing ratio, since higher absolute values are estimated for less mixed dust layers. This can be directly linked to the fact that RF values strongly depend on α_{par}, β_{par} and AOD that take much higher values for the Saharan dust cluster as already reported (see Table 5.2).

Focusing now on the SW range, the cooling effect for Scheme A of the Saharan dust cluster is up to 3 times higher compared to the BB and Saharan dust one, whilst the cooling effect for Scheme C of the former cluster is up to 10 times higher compared to the latter one. Also, the cooling effect of Scheme B becomes stronger with the decreasing mixing state but with a lower magnitude (the former cluster is almost 2 times higher compared to the latter). Hence, even though the cases included in the Saharan dust cluster usually take higher mass concentration values than the other cases, as predicted by BSC-DREAM8b (Scheme A), LibRadtran seemingly still underestimates the intensity of strong transported dust episodes over the observation stations. On the contrary, Scheme C is the most sensitive to the mixing state. To explain this result one should consider that on the one hand, spheroidal particles such as dust have larger surface area than spherical ones such as BB aerosols leading to larger AODs (Haapanala et al., 2012) and consequently to increased negative ARF and on the other hand, the Schemes A and B involve greater assumptions concerning dust particles than Scheme C.

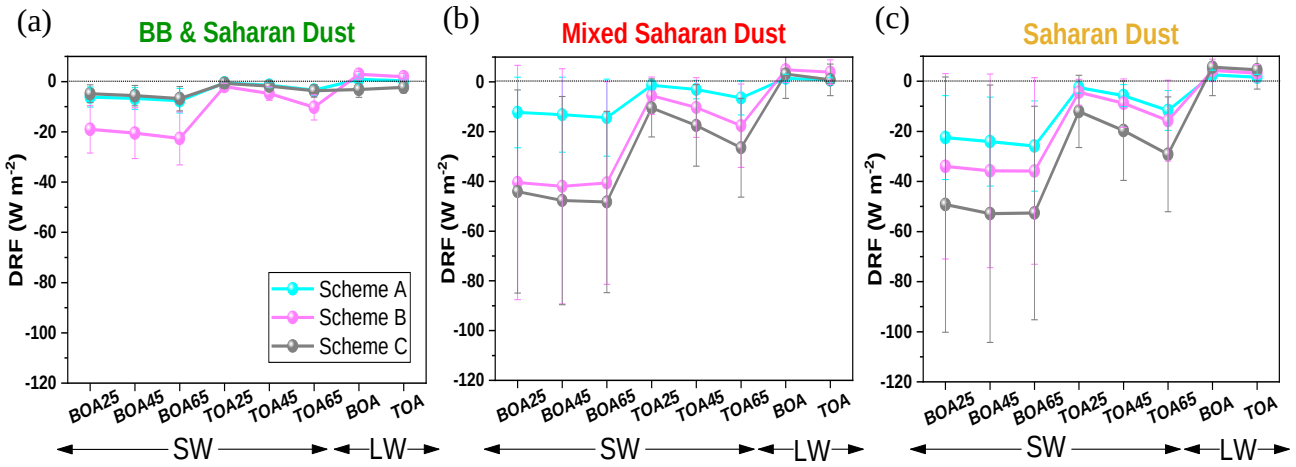

Figure 5.22: Mean values of SW and LW ARF at BOA and TOA and along with their SD for the three Schemes applied regarding the mixing state, namely a) BB & Saharan dust, b) Mixed Saharan dust and c) Saharan Dust. The dotted line represents the ARF zero value.

Finally, our interest is focused on the vertical ARF profiles from the surface (a.s.l.) up to 10000 m height in the free troposphere, where airborne dust is usually found, as estimated by Scheme C at 45° SZA per station. The ARF profiles, in the SW region, presented in Fig. 5.23 (a-d), follow the aerosol extinction vertical structure, with comparable peaks. The ARF values at the BOA are high in absolute values showing a cooling behavior and decrease with increasing height, while their magnitude is proportional to the aerosol load in the whole atmospheric column. Specifically, the ARF ranges from -150.0 to -1.9 W m^{-2} for Granada, from -38.1 to -3.7 W m^{-2} for Potenza, from -64.8 to -13.2 W m^{-2} for Athens and from -90.3 to -28.4 W m^{-2} for Limassol. The corresponding ranges of α_{532} are 0.286–0.029 km^{-1}, 0.268–0.088 km^{-1}, 0.135–0.078 km^{-1} and 0.547–0.214 km^{-1}, respectively. Peaks in α_{532} are observed usually between 2000 and 6000 m a.s.l. indicating the intrusion of dust, which leads to a decrease in the solar radiation reaching the surface.

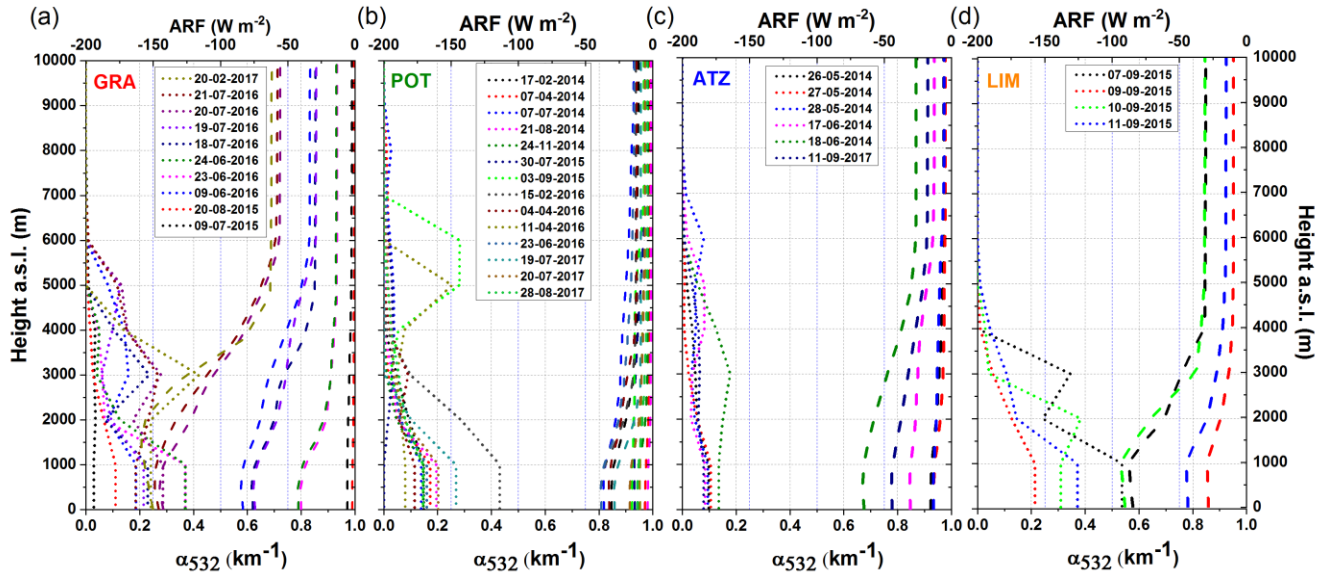

Figure 5.23: Vertical profiles of α_{532} calculated from Raman lidar measurements along with the SW ARF estimated from LibRadtran simulations for the sites of: a) Granada, b) Potenza, c) Athens and d) Limassol, at 45° SZA.

5.4 Aerosol optical and chemical properties of a 3-day lasting dust episode

An intense 3-day lasting Saharan dust episode, that occurred between 26-28 May 2014 over Athens was chosen to be further analyzed not only for the optical but also for the chemical aerosol properties. In this period, according to the FLEXPART model (7-day air mass backward simulations, cf. Sect. 4.4) the air masses sampled over Athens originated from the desert dust regions of Morocco, Algeria and Tunisia (with a total residence time over the Saharan desert of the order of 72 hours per day, cf. Fig.5.24; thus, being enriched with dust particles), pass over the Mediterranean Sea before being detected over Athens between 1000 and 5000 m height.

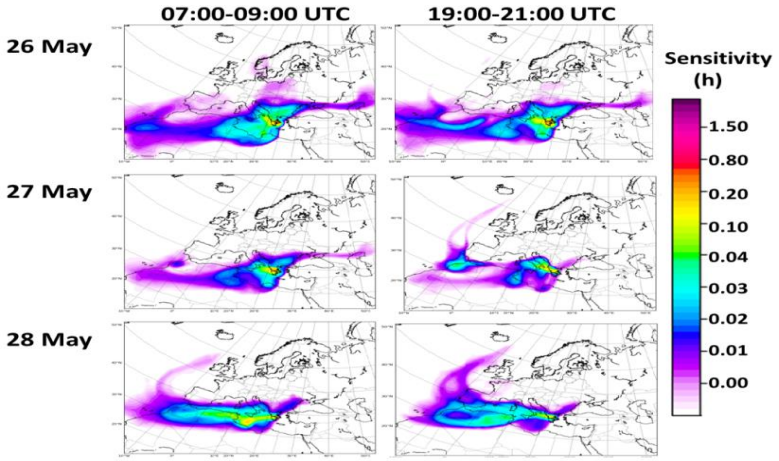

Figure 5.24: 7-day air mass backward FLEXPART simulations for 26-28 May 2014. Particles are released at a uniform rate during a 3-hour interval from 0 to 500 m a.s.l. height, reaching over Athens between 2000-4000 m. The air mass residence time along the trajectory over each site is shown in hours. The chart is plotted with X axis (longitude) and Y axis (latitude).

In Fig. 5.25 we present the range-corrected lidar signal (RCS) observed at 1064 nm over Athens, from 26 May (06:00 UTC) to 28 May (09:00 UTC) 2014. During 26 May (06:00-14:00 UTC) an extremely intense dust layer is detected between 2000 and 4000 m, with less intense dust layers above (up to 5000 m) and below (down to the top of the Planetary Boundary Layer (PBL) at ~ 1100 m). Later the same day (18:00-22:00 UTC) the dust layer becomes less dense, extending from 4000 m height down to the top of the nighttime PBL (~500 m). The following day (27 May) during daytime (06:00-14:00 UTC) the dust layer intensifies around 2500 m height, while continuing its decrease from 3000 m height down to the top of the daytime PBL (~2000 m). Again, during nighttime (18:00-22:00 UTC) the dust layer continues to descent and stays between 2500 and the nighttime PBL (~500 m). The next day (28 May) the dust layer intensifies again after 08:00 UTC and expands in two distinct layers (between 1000 and 2000 m and between 3500 and 4500 m during the nighttime period (18:00-22:00 UTC), where clouds appear over the upper dust layer, between 5000 and 7000 m.

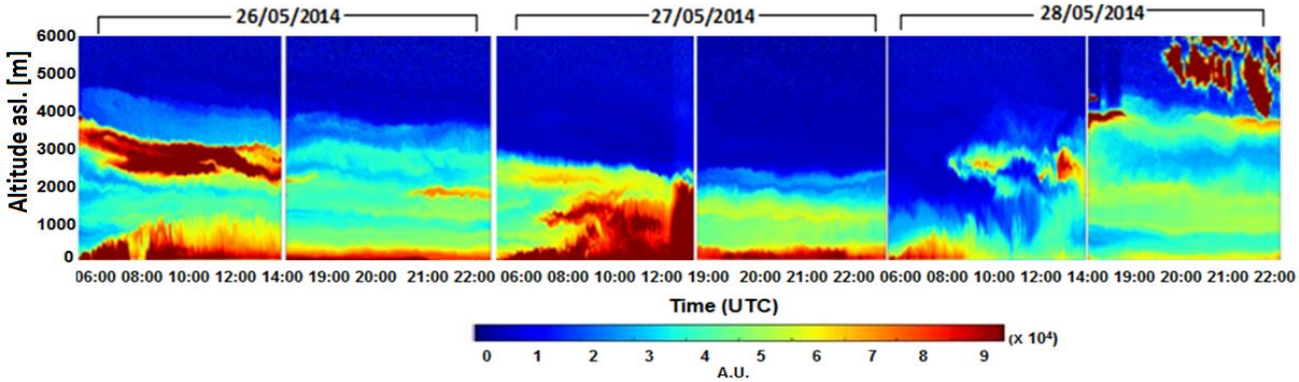

Figure 5.25: Spatio-temporal evolution of the range-corrected lidar signal observed by EOLE at 1064 nm over Athens, from 26 May (06:00 UTC) to 28 May (22:00 UTC) 2014.

In Fig.5.26 we present the spatio-temporal evolution of the vertical profiles of the aerosol optical properties: (a), (b) and (c) β_{aer} at 355, 532 and 1064 nm, respectively; (d) and (e) α_{aer}; (f) and (g) LRs at 355 and 532 nm, respectively; (h) and (i) aerosol Ångström exponent-related to backscatter for the pairs 355/532 nm ($AE_{b355/532}$) and 532/1064 nm ($AE_{b532/1064}$), as well as the AE extinction-related ($AE_{a355/532}$). The LR values range from 35-55 sr (355 nm) and 30-52 sr (532 nm).

The corresponding $AE_{a355/532}$ values (Fig. 5.26j) are below 1 from 2000 to 4500 m height, indicating the presence of large particles (mean value of 0.64±0.18). The strength of the dust event can also be clearly shown by the small values (<1) of $AE_{b355/532}$ during daytime of 26 and 27 May. Moreover, lidar depolarization measurements performed during the same period in the frame of the Hygroscopic Aerosols to Cloud Droplets (HygrA-CD) campaign (http://hygracd.impworks.gr) (Papayannis et al., 2017) at 532 nm (Fig. 5.26k) showed mean δ_{p532} values ranging from 15 to 22% within the dust layer, depending on the intensity of the episode. These values are typical for long-range transported dust particles and/or dust mixtures measured over Greece and the N, NE and central Europe (Papayannis et al., 2014; Groß et al., 2015; Haarig et al., 2017).

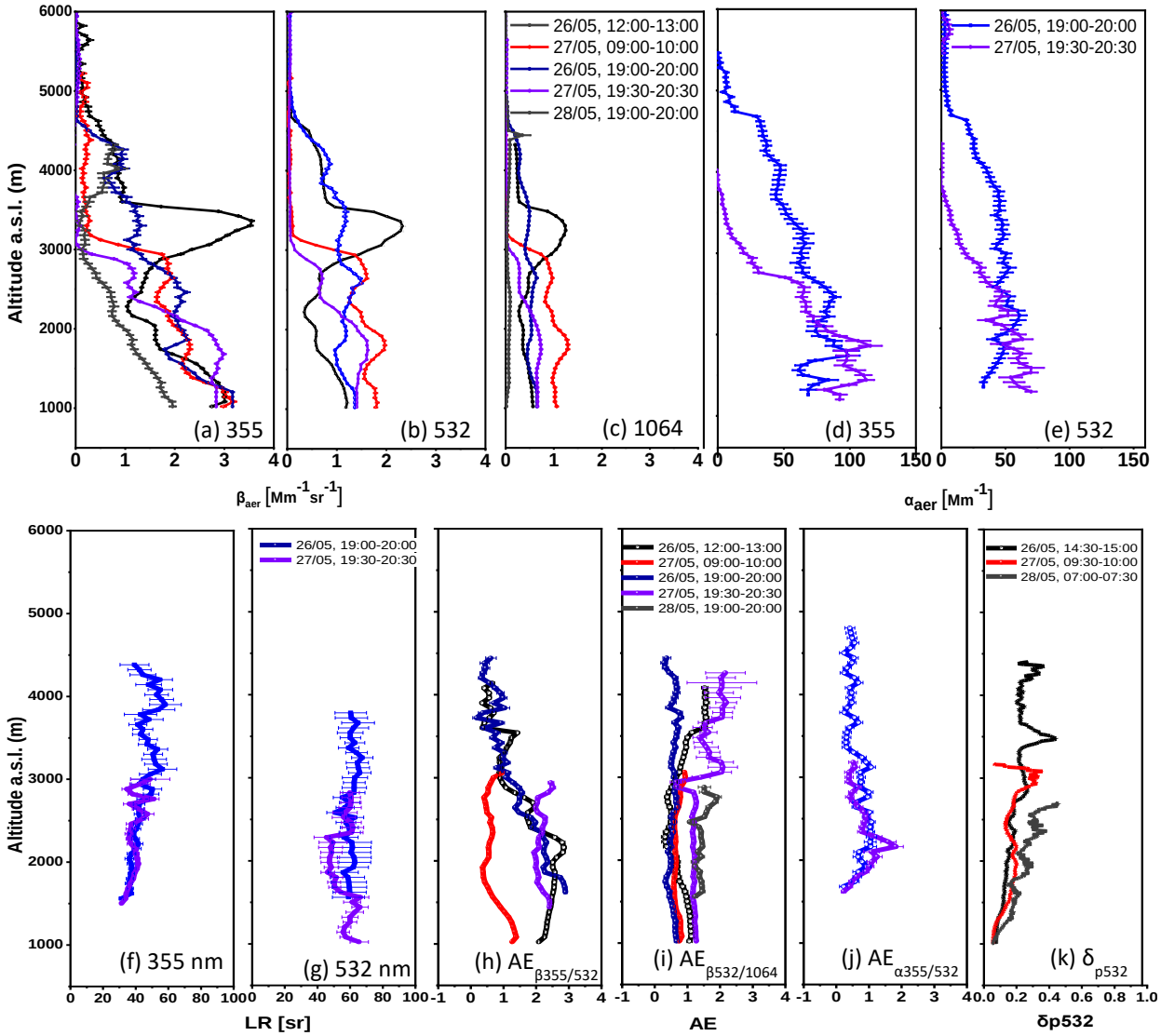

Figure 5.26: Vertical profiles of the aerosol optical properties (26-29 May 2014): (a,b,c) β_{aer} at 355, 532, 1064 nm, respectively; (d,e) α_{aer} coefficient at 355, 532 nm; (f,g) LR at 355 and 532 nm; (h,i,j) $AE_{b(355/532)}$, $AE_{b(532/1064)}$ and $AE_{a(355/532)}$; (k) δ_p at 532 nm. The indicated time of the measurements is given in UTC.

The WRF/Chem model reproduces successfully the spatial distribution and the time evolution of the 3-day episode (Fig. 5.27). The highest dust concentrations (130-350 μg/m^3) are simulated on 26/05, when winds from SW prevail. The layer is simulated between 1.0 and 4.5 km. On 27/5, dust concentrations are lower (up to 150 μg/m^3), especially during the afternoon hours. This day is characterized by western winds and higher wind speeds during the afternoon hours (8-15 m/s up to 4 km). On 28/5, the winds are from the W-NW sectors and more unstable conditions prevail. The PBL reaches its maximum height (~2 km, afternoon, cf. Appendix C). Dust aerosols (50 - 100 μg/m^3) are mainly confined above the PBL while inside the PBL the concentrations are < 100 μg/m^3.

The highest sea salt concentrations (up to 3 μg/m^3) appear on 27/5 when the strongest wind prevails with sea origin. They also reach the NTUA station when the PBL becomes deeper, during late afternoon. The layer of sea salt at higher altitudes that is visible every day, is a result of the intense wind activity in long distance south of the Attica peninsula (over the open sea).

During morning and night hours EC and organics accumulate up to ~500 m due to the calm and stable conditions that prevail at lower altitudes. The highest surface concentrations at NTUA are ~10 μg/m^3 for EC and 6 μg/m^3 for organics (on 27/5). The SO4 concentrations at NTUA are < 10 μg/m^3.

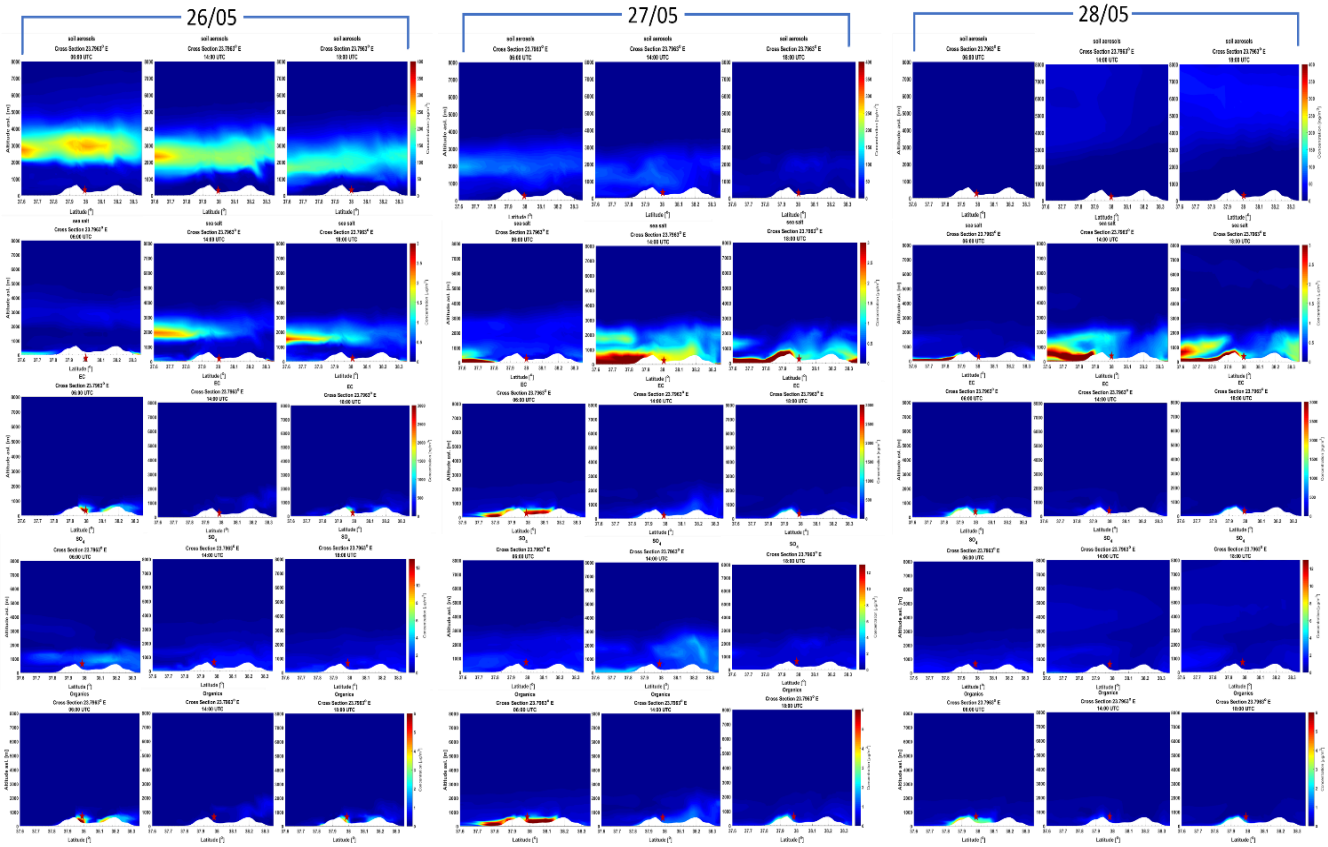

Figure 5.27: Spatial evolution of the cross section 23.7963o E of a) dust b) sea salt, c) Elementary Carbon (EC), d) SO_4 and e) organic concentrations over the Greater area of Athens (37.6-38.3^o N) for 3 selected hours: 06:00, 14:00 and 18:00 UTC. The location of the NTUA station is mentioned with a red star.

5.5 A Special case of a biomass burning (BB) event over Athens- Spherical aerosols

During the period 2014-2017 a few simultaneous measurements were performed by the EOLE lidar and the CIMEL sun photometer within AERONET over Athens, Greece. We selected to analyze a representative Biomass Burning (BB) event occurred on 25 June 2015.

Here, the UP Spherical inversion algorithm was applied to selected layers on the vertical profiles obtained by EOLE, in order to retrieve the aerosol microphysical properties. This method has been developed in the framework of EARLINET (Müller et al., 2016)and is based on explicitly solving the mathematical equations that relate the particle microphysical and optical properties by means of regularization techniques. Forward computations using tables containing microphysical versus optical properties are not carried out, having the advantage that particle size distribution shape is not assumed as input, but approximately calculated as output. Based on the SCC (see Sect. 4.1) calculated aerosol optical properties (a dataset of 3*b* + 2*a* profiles is used as input to this algorithm), the aerosol microphysical properties R_{eff}, SSA, RI and u_t were retrieved by the Spherical Inversion algorithm developed at the University of Potsdam (UP), (Böckmann et al., 2005; Samaras et al., 2015; Müller et al., 2016).

The 5-day air mass backward trajectories arriving over Athens on 25 June 2015, at 19:00 UTC between 1.5-2.6 km, based on the HYSPLIT model, are shown in Fig. 5.28a. The corresponding hot spots of possible fires and thermal anomalies observed by Terra/MODIS (cf. Sect. 4.8) are shown in Fig. 5.28b. Based on the air mass trajectories along Germany-Slovenia-S. Italy, we have strong indications of the existence of BB aerosols mixed with anthropogenic ones, resulting in strong absorbing particles.

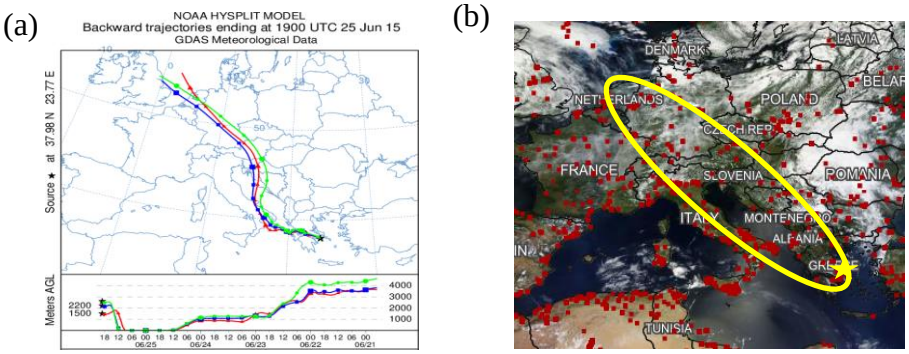

Figure 5.28: a) 5-day air mass backward trajectories arriving over Athens on 25 June 2015 at 19:00 UTC (NOAA HYSPLIT model) and b) Terra/MODIS/ true color image fire map for the period 20/06/2015-25/06/2015 (https://firms.modaps.eosdis.nasa.gov/map).

The nighttime measurements of EOLE detected layers between 1000 and ~3000 m height (Fig. 5.29a). The aerosol profile was separated into four distinct layers based on the relatively stable optical properties (Figs. 5.29b, c, d and e) within each height range, where the values of LR and AE remain nearly constant. To retrieve the aerosol microphysical properties, we used the mean values of the β and α coefficients that are shown in Table 5.8.

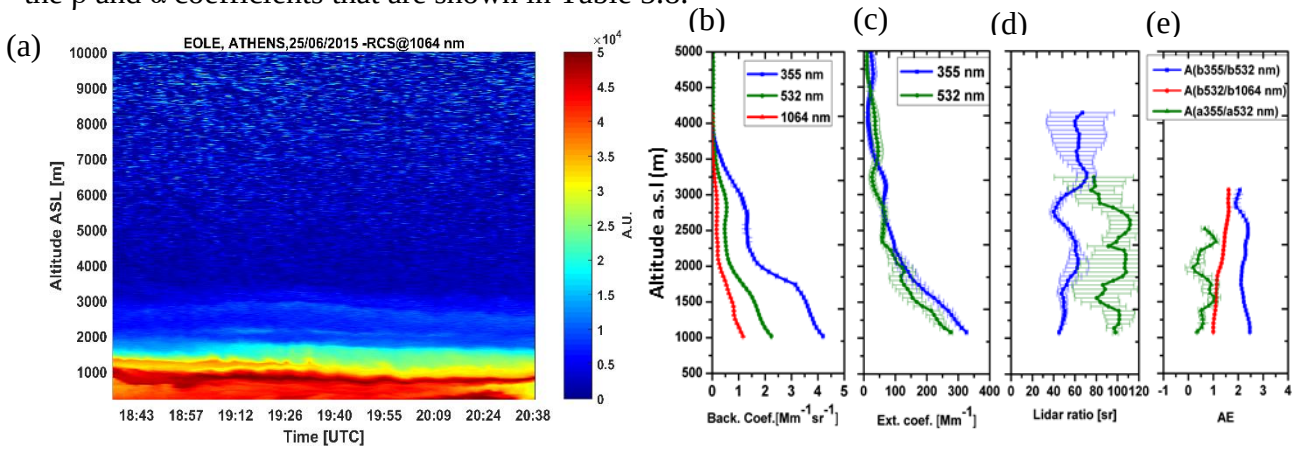

Figure 5.29: a) Temporal evolution of the range-corrected lidar signal (RCS) at 1064 nm observed by EOLE over Athens on 25 June 2015 (18:30-20:30 UTC) (b,c,d,e) vertical profiles of the aerosol optical properties: b_{aer} and a_{aer} coefficients, LR and AEb_{355}/b_{532}, AEb_{532}/b_{1064}, and AEa_{355}/a_{532}, respectively.

Focusing on the fine mode of each layer (particle radius ranging from 0.01 to 1 μm), the mean aerosol microphysical properties (CRI, u_t, R_{eff}, and SSA) along with their SD, derived for 25 June 2015, are presented in Table 5.9. A grid of complex refractive indices was applied (ranging from 1.4–1.6 in real part and 0i–0.02i in imaginary part). High imaginary parts (~0.015i) of CRI indicate the presence of absorbing particles, in accordance with the retrieved SSA values.

Table 5.8: Mean aerosol optical properties at four selected layers with variable thicknesses (25 June 2015). The mean values of *b* and *a* coefficients were used as input to the Spherical Inversion algorithm.

Layers (km)	Thickness (km)	β (355/532/1064 nm) (Mm^{-1} sr^{-1})	α (355/532 nm) (Mm^{-1})	*LR* (355 nm) (sr)	*AE*b_{355}/b_{532} / AE/b_{532}/b_{1064})
A (1.5-1.6)	0.1	3.404 / 1.586 / 0.725	251.053 / 200.216	48±1	2.21±0.02 / 1.12±0.01
B (2.2-2.5)	0.3	1.663 / 0.537 / 0.204	99.652 / 82.302	58±3	2.34±0.05 / 1.45±0.04
C (2.5-3.0)	0.5	1.491 / 0.513 / 0.170	67.512 / 60.795	46±5	2.12±0.18 / 1.58±0.03
D (1.5-3.0)	1.5	2.141 / 0.723 / 0.291	113.190 / 91.522	53±7	2.18±0.14 / 1.39±0.19

Table 5.9: Mean aerosol microphysical properties of the four selected layers with variable thicknesses derived from EOLE lidar data of 25 June 2015.

Layers (km)	CRI	u_t ($\mu m^3/cm^{-3}/\mu m^{-1}$)	R_{eff} (μm)	SSA (355 and 532 nm)
A (1.5-1.6)	1.517±0.008 0.015i±0.002i	24.37±0.27	0.173±0.002	0.914±0.004 0.924±0.003
B (2.2-2.5)	1.500±0.009 0.014i±0.003i	10.23±0.15	0.186±0.002	0.918±0.006 0.928±0.005
C (2.5-3.0)	1.510±0.011 0.015i±0.003i	7.50±0.13	0.217±0.003	0.904±0.017 0.921±0.012
D (1.5-3.0)	1.513±0.008 0.015i±0.002i	11.31±0.13	0.181±0.003	0.912±0.002 0.923±0.002

For a direct comparison of the columnar volume size distribution retrieved from the EOLE lidar data with the one derived from the inversion of the CIMEL sun photometer AERONET data (Sect. 3.6) over Athens on 25 June 2015, we found that the air masses arriving over our site followed the same paths during the time of the closest-in-time sun photometer (15:07 UTC) and lidar (18:30-20:30 UTC) measurements, indicating that the aerosol variability between the two measurements was not significant. The comparison of the results of their mean aerosol optical properties and their size distribution are shown in Figs. 5.30 (a-c), respectively.

(c)

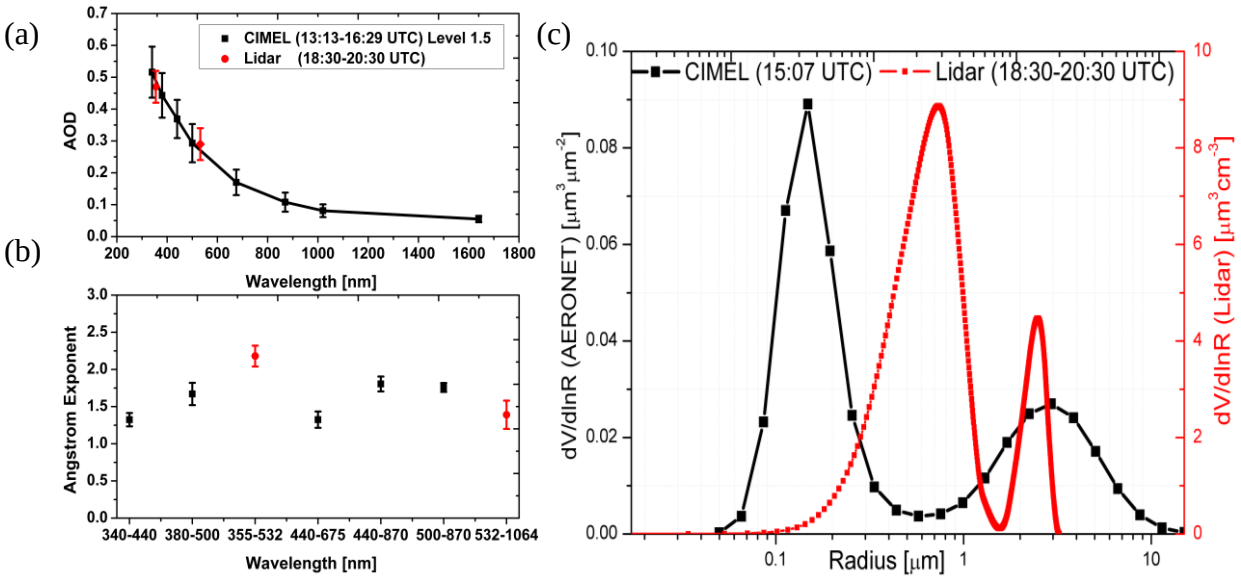

Figure 5.30: Comparison of the mean aerosol optical properties of a) wavelength dependent AOD from CIMEL-AERONET (total mode, level 1.5) and for EOLE lidar, b) mean *AE* values from CIMEL-AERONET and EOLE lidar, along with their standard deviation, and c) aerosol size distribution derived from CIMEL data (radius: 0.05-11 μm) and lidar data (radius: 0.01-3 μm) obtained over Athens (25 June 2015).

Chapter 6: Conclusions

The aim of this Ph.D. Thesis was to study the aerosol optical, geometrical as well as the microphysical properties along with their impact in radiative effect. We especially focus on long-range transported dust events over selected Mediterranean cities (EARLINET stations) and we extensively study the aerosols' aging and mixing properties.

In the first part of this Thesis we presented a comprehensive analysis of the seasonal variability of the vertical profiles of the optical and geometrical properties of Saharan dust aerosols, observed in the height region between 1000 and 6000 m, over the city of Athens, Greece, from February 2000 to December 2017 (18 years of measurements). These observations were performed by a multi-wavelength (355-387-532-1064 nm) Raman lidar system under cloud-free conditions. The statistical analysis (using aerosol monthly mean values) was based on nighttime vertical Raman measurements of range-resolved aerosol optical properties (backscatter and extinction coefficients, lidar ratio, Ångström exponent) at 355 nm (59 dust events during more than 80 measurement hours).

We found that the number of dust events was highest in spring, summer, and early autumn periods and that during spring the dust layers were moved at higher altitudes (~4500 m) than in other seasons. The number of the forecasted dusty days (on monthly basis) by the BSC-DREAM8b model compared to those of the performed lidar measurements were found to have a quite strong correlation (R^2=0.81), with a maximum occurrence predicted for the spring season. In the worst-case scenario, at least 50% of the model-forecasted dust events can be observed by lidar under cloudless skies over Athens. For the sampled dust plumes, we found a mean LR_{355} value of 52±13 sr in the height range 2000-4000 m a.s.l. considering that the dust layers had a mean thickness of 2497±1026 m and a center of mass of 2699±1017 m.

An analysis performed regarding the air mass back-trajectories arriving over Athens revealed two main clusters: one pathway from south-west to north-east, with dust emission areas in Tunisia, Algeria and Libya and a second one from south, across the Mediterranean Sea with emission areas over Libya and the remaining part of Algeria and Tunisia. This clustering enabled us to differentiate between the aerosol optical properties between the two clusters, based on their residence time over the Saharan region, the European continent and the Mediterranean Sea. We finally concluded that even if the dust source regions are about the same, the aging and mixing processes of these air masses, passing over different areas, might have an impact on the aerosol optical properties.

The characteristics of aerosol layers dominated by dust optical, geometrical, and radiative properties over the Mediterranean region were also presented in this study. A total of 51 independent aerosol lidar measurements of Saharan dust events, studied over 4 southern European cities (Granada, Potenza, Athens and Limassol), were carefully selected and analyzed. The dust layers were usually observed between ~1.6 and ~5 km with δ_{p532} and LR_{532} values ranging from 0.16 to 0.35 and from 35 to 73 sr respectively, depending on the air mass mixing state. Significantly high AOT_{532} values (0.40 ± 0.31) were found for Granada indicating that the dust outbreaks occurring over this area were more intense during the studied period. Results of LR_{532} versus δ_{p532} are presented in order to elucidate the difference of pure dust and dust mixtures cases. Layers with lower δ_{p532} (0.17 ± 0.01), AOT_{532} (0.03 ± 0.02) and thicknesses (786 ± 212 m) values have shown high dust mixing ratio, while the properties of the least or no mixed dust layers (δ_{p532}=0.32±0.02, AOT_{532}=0.32±0.23 and thickness=3158±1605 m) are in a good agreement with literature findings for pure Saharan dust cases (Tesche et al., 2009; Papayannis et al., 2009; Ansmann et al., 2012; Mona et al., 2012; Groß et al., 2011; 2013). Lidar stand-alone retrieved aerosol microphysical properties like the R_{eff}, RRI and IRI are also differentiated by the level of mixing.

Despite the numerous individual studies, the uncertainty in estimating the aerosols effect in climate change remains high. Therefore, coordinated and simultaneous studies using data from observation sites operating continuously, such as the EARLINET database are necessary for investigating the climatic effect of aerosols in a larger scale. Three Schemes have been implemented in our study to evaluate the ARF during the selected dust outbreaks: the model mass concentrations by BSC-DREAM8b (Scheme A), the vertical mass concentrations calculated from the dust-only component of the β_{532} (Scheme B) and the α_{532} vertical profiles along with the mean AOT_{532} values (Scheme C).

Lidar derived Schemes B and C are used here as input methods in LibRadtran simulations, since not many techniques have been widely used for retrieving the ARF using lidar vertical measurements as input. Their outputs are compared to the ones retrieved from Scheme A. On the one hand, Scheme B gives the opportunity to calculate only the DRF, even though many assumptions and constants are included in the calculation of the dust mass concentration values. On the other hand, Scheme C is more direct, since the α_{532} profiles are primarily used for retrieving the ARF in the SW range, but without providing a separation of dust and non-dust components. Consequently, the ARF values of Scheme C seem to be overestimated compared to those of Scheme B. These two implemented Schemes can contribute to the characterization of the aerosols' radiative forcing effects over the Mediterranean region, being one of the most sensitive regions to climate forcing (Kim et al., 2019). Scheme A is only recommended for cases were no lidar measurements are available but an estimation of the ARF is required, while one should take into account all the possible underestimations and a model such as BSC-DREAM8b includes.

The ARF variations are strong (of the order of 75%) and result from significant changes in the lidar retrieved optical properties due to the different intensities of the studied cases (α_{532}, β_{532}, AOT_{532}) or the model mass estimations from the BSC-DREAM8b. Additional variations (of the order of 40%) in the SW range are introduced due to the variations in the available solar radiation during day (SZA). The vertical structure of a layer that provides information about the base, the thickness and the intensity (AOT) of a dust layer is critically important, while additional information of its mixing state can be also significant in ARF and net heating rate estimations. Our findings show a much more pronounced ARF at the BOA (ranging from -40 to -13 W m^{-2} at SZA 25º, from -43 to -14 W m^{-2} at SZA 45º and from -44 to -15 W m^{-2} at 65º) compared to the one at the TOA (ranging from -9.5 to -1.4 W m^{-2} at 25º, -16 to -3.3 W m^{-2} at 45º and -24.3 to -6.9 W m^{-2} at 65º) due to the low altitude of the studied layers (usually 2-4 km).

The systematic use of remote sensing vertical profiling measurements as input to radiative transfer models is stressed in this study, creating an essential tool allowing the estimation of the radiative effects produced by different aerosol types such as dust and its mixtures on a regional and a global scale. A further investigation of aerosols' mixing state is needed since, not only their optical but also their microphysical properties and radiative forcing can strongly vary, depending on the mixing types. Furthermore, we recommend that the use of remote and *in situ* measurements in the next generation state-of-the-art dust cycle models for the ARF should be intensified.

Bibliography

Ackermann, I. J., Hass, H., Memmesheimer, M., Ebel, A., Binkowski, F. S. and Shankar, U.: Modal Aerosol Dynamics model for Europe: Development and first applications, Atmos. Environ., 32(17), 2981–2999, doi:10.1016/S1352-2310(98)00006-5, 1998.

Alados-Arboledas, L., Lyamani, H. and Olmo, F. J.: Aerosol size properties at Armilla, Granada (Spain), Q. J. R. Meteorol. Soc., 129(590 PART A), 1395–1413, doi:10.1256/qj.01.207, 2003.

Alados-Arboledas, L., Alcántara, A., Olmo, F. J., Martínez-Lozano, J. A., Estellés, V., Cachorro, V., Silva, A. M., Horvath, H., Gangl, M., Díaz, A., Pujadas, M., Lorente, J., Labajo, A., Sorribas, M. and Pavese, G.: Aerosol columnar properties retrieved from CIMEL radiometers during VELETA 2002, Atmos. Environ., 42(11), 2654–2667, doi:10.1016/j.atmosenv.2007.10.006, 2008.

Aller, J., Kuznetsova, M., Jahns, C. and Kemp, P.: The sea surface microlayer as a source of viral and bacterial enrichment in marine aerosols, J. Aerosol Sci., 36, 801–812, doi:10.1016/j.jaerosci.2004.10.012, 2005.

Amiridis, V., Balis, D. S., Kazadzis, S., Bais, A., Giannakaki, E., Papayannis, A. and Zerefos, C.: Four year aerosol observations with a Raman lidar at Thessaloniki, Greece, in the framework of European Aerosol Research Lidar Network (EARLINET), J. Geophys. Res. Atmos., 110(D21), doi:10.1029/2005JD006190, 2005.

Amodeo, A., D'Amico, G., Giunta, A., Papagiannopoulos, N., Papayannis, A., Argyrouli, A., Mylonaki, M., Tsaknakis, G., Kokkalis, P., Soupiona, O. and Tzanis, C.: ATHLI16: The ATHens Lidar Intercomparison campaign, in EPJ Web of Conferences, vol. 176., 2018.

Ancellet, G., Papayannis, A., Pelon, J. and Mégie, G.: DIAL Tropospheric Ozone Measurement Using a Nd:YAG Laser and the Raman Shifting Technique, J. Atmos. Ocean. Technol., 6(5), 832–839, doi:10.1175/1520-0426(1989)006<0832:DTOMUA>2.0.CO;2, 1989.

Ångström, A.: On the Atmospheric Transmission of Sun Radiation and on Dust in the Air, Geogr. Ann., 11, 156–166, doi:10.2307/519399, 1929.

Ansmann, A., Riebesell, M., Wandinger, U., Weitkamp, C., Voss, E., Lahmann, W. and Michaelis, W.: Combined Raman Elastic-Backscatter LIDAR for Vertical Profiling of Moisture, Aerosol Extinction, Backscatter, and LIDAR Ratio, Appl. Phys. B, 55, 18–28, doi:doi.org/10.1007/BF00348608, 1992.

Ansmann, A., Petzold, A., Kandler, K., Tegen, I., Wendisch, M., Müller, D., Weinzierl, B., Müller, T. and Heintzenberg, J.: Saharan Mineral Dust Experiments SAMUM-1 and SAMUM-2: What have we learned?, Tellus, Ser. B Chem. Phys. Meteorol., 63(4), 403–429, doi:10.1111/j.1600-0889.2011.00555.x, 2011.

Ansmann, A., Seifert, P., Tesche, M. and Wandinger, U.: Profiling of fine and coarse particle mass: Case studies of Saharan dust and Eyjafjallajökull/Grimsvötn volcanic plumes, Atmos. Chem. Phys., 12(20), 9399–9415, doi:10.5194/acp-12-9399-2012, 2012.

Ariya, P. A., Sun, J., Eltouny, N. A., Hudson, E. D., Hayes, C. T. and Kos, G.: Physical and chemical characterization of bioaerosols – Implications for nucleation processes, Int. Rev. Phys. Chem., 28(1), 1–32, doi:10.1080/01442350802597438, 2009.

Arthur, D. and Vassilvitskii, S.: K-means++: The advantages of careful seeding, in SODA '07: Proceedings of the eighteenth annual ACM-SIAM symposium on Discrete algorithms, pp. 1027–1035.

[online] Available from: https://theory.stanford.edu/~sergei/papers/kMeansPP-soda.pdf, 2007.

Baars, H., Ansmann, A., Ohneiser, K., Haarig, M., Engelmann, R., Althausen, D., Hanssen, I., Gausa, M., Pietruczuk, A., Szkop, A., Stachlewska, I. S., Wang, D., Reichardt, J., Skupin, A., Mattis, I., Trickl, T., Vogelmann, H., Navas-Guzmán, F., Haefele, A., Acheson, K., Ruth, A. A., Tatarov, B., Müller, D., Hu, Q., Podvin, T., Goloub, P., Veselovskii, I., Pietras, C., Haeffelin, M., Fréville, P., Sicard, M., Comerón, A., García, A. J. F., Menéndez, F. M., Córdoba-Jabonero, C., Guerrero-Rascado, J. L., Alados-Arboledas, L., Bortoli, D., Costa, M. J., Dionisi, D., Liberti, G. L., Wang, X., Sannino, A., Papagiannopoulos, N., Boselli, A., Mona, L., D'Amico, G., Romano, S., Perrone, M. R., Belegante, L., Nicolae, D., Grigorov, I., Gialitaki, A., Amiridis, V., Soupiona, O., Papayannis, A., Mamouri, R.-E., Nisantzi, A., Heese, B., Hofer, J., Schechner, Y. Y., Wandinger, U. and Pappalardo, G.: The unprecedented 2017-2018 stratospheric smoke event: Decay phase and aerosol properties observed with the EARLINET, Atmos. Chem. Phys., 19(23), doi:10.5194/acp-19-15183-2019, 2019.

Balis, D., Amiridis, V., Kazadzis, S., Papayannis, A., Tsaknakis, G., Tzortzakis, S., Kalivitis, N., Vrekoussis, M., Kanakidou, M., Mihalopoulos, N., Chourdakis, G., Nickovic, S., Pérez, C., Baldasano, J. and Drakakis, M.: Optical characteristics of desert dust over the East Mediterranean during summer: a case study, Ann. Geophys., 24, 807–821, doi:www.ann-geophys.net/24/807/2006/, 2006.

Banks, R. F., Tiana-Alsina, J., Baldasano, J. M., Rocadenbosch, F., Papayannis, A., Solomos, S. and Tzanis, C. G.: Sensitivity of boundary-layer variables to PBL schemes in the WRF model based on surface meteorological observations, lidar, and radiosondes during the HygrA-CD campaign, Atmos. Res., 176–177, 185–201, doi:10.1016/j.atmosres.2016.02.024, 2016.

Barnaba, F. and Gobbi, G. P.: Aerosol seasonal variability over the Mediterranean region and relative impact of maritime, continental and Saharan dust particles over the basin from MODIS data in the year 2001, Atmos. Chem. Phys, 4, 2367–2391, doi:https://doi.org/10.5194/acp-4-2367-2004, 2004.

Basart, S., Pérez, C., Nickovic, S., Cuevas, E. and Baldasano, J.: Development and evaluation of the BSC-DREAM8b dust regional model over Northern Africa, the Mediterranean and the Middle East, Tellus B Chem. Phys. Meteorol., 64(1), 18539, doi:10.3402/tellusb.v64i0.18539, 2012.

Bauer, S., Bierwirth, E., Esselborn, M., Petzold, A., Macke, A., Trautmann, T. and Wendisch, M.: Airborne spectral radiation measurements to derive solar radiative forcing of Saharan dust mixed with biomass burning smoke particles, Tellus B Chem. Phys. Meteorol., 63(4), 742–750, doi:10.1111/j.1600-0889.2011.00567.x, 2011a.

Bauer, S., Bierwirth, E., Esselborn, M., Petzold, A., Macke, A., Trautmann, T. and Wendisch, M.: Airborne spectral radiation measurements to derive solar radiative forcing of Saharan dust mixed with biomass burning smoke particles, Tellus, Ser. B Chem. Phys. Meteorol., 63(4), 742–750, doi:10.1111/j.1600-0889.2011.00567.x, 2011b.

Benavent-Oltra, J. A., Román, R., Granados-Munõz, M. J., Pérez-Ramírez, D., Ortiz-Amezcua, P., Denjean, C., Lopatin, A., Lyamani, H., Torres, B., Guerrero-Rascado, J. L., Fuertes, D., Dubovik, O., Chaikovsky, A., Olmo, F. J., Mallet, M. and Alados-Arboledas, L.: Comparative assessment of GRASP algorithm for a dust event over Granada (Spain) during ChArMEx-ADRIMED 2013 campaign, Atmos. Meas. Tech., 10(11), 4439–4457, doi:10.5194/amt-10-4439-2017, 2017.

Bergstrom, R. W., Pilewskie, P., Russell, P. B., Redemann, J., Bond, T. C., Quinn, P. K. and Sierau, B.: Spectral absorption properties of atmospheric aerosols, Atmos. Chem. Phys., 7(23), 5937–5943, doi:10.5194/acp-7-5937-2007, 2007.

Binietoglou, I., Basart, S., Amiridis, V., Argyrouli, A., Baars, H., Baldasano, J. M. and Balis, D.: A methodology for investigating dust model performance using synergistic EARLINET / AERONET dust concentration retrievals, Atmos. Meas. Tech, 8, 3577–3600, doi:10.5194/amt-8-3577-2015, 2015.

Böckmann, C. and Kirsche, A.: Iterative regularization method for lidar remote sensing, Comput. Phys. Commun., 174(8), 607–615, doi:10.1016/j.cpc.2005.12.019, 2006.

Böckmann, C., Mironova, I., Müller, D., Schneidenbach, L. and Nessler, R.: Microphysical aerosol parameters from multiwavelength lidar, J. Opt. Soc. Am. A, 22(3), 518, doi:10.1364/JOSAA.22.000518, 2005.

Bravo-Aranda, J. A., Titos, G., Granados-Muñoz, M. J., Guerrero-Rascado, J. L., Navas-Guzmán, F., Valenzuela, A., Lyamani, H., Olmo, F. J., Andrey, J. and Alados-Arboledas, L.: Study of mineral dust entrainment in the planetary boundary layer by lidar depolarisation technique, Tellus, Ser. B Chem. Phys. Meteorol., doi:10.3402/tellusb.v67.26180, 2015.

Cachorro, V. E., Toledano, C., Prats, N., Sorribas, M., Mogo, S., Berjón, A., Torres, B., Rodrigo, R., De La Rosa, J. and De Frutos, A. M.: The strongest desert dust intrusion mixed with smoke over the Iberian Peninsula registered with Sun photometry, J. Geophys. Res. Atmos., 113(14), 1–19, doi:10.1029/2007JD009582, 2008.

Cochran, R. E., Ryder, O. S., Grassian, V. H. and Prather, K. A.: Sea spray aerosol: The chemical link between the oceans, atmosphere, and climate, Acc. Chem. Res., 50(3), 599–604, doi:10.1021/acs.accounts.6b00603, 2017.

Córdoba-Jabonero, C., Sorribas, M., Guerrero-Rascado, J. L., Adame, J. A., Hernández, Y., Lyamani, H., Cachorro, V., Gil, M., Alados-Arboledas, L., Cuevas, E. and De La Morena, B.: Synergetic monitoring of Saharan dust plumes and potential impact on surface: A case study of dust transport from Canary Islands to Iberian Peninsula, Atmos. Chem. Phys., doi:10.5194/acp-11-3067-2011, 2011.

Cwiertny, D. M., Young, M. A. and Grassian, V. H.: Chemistry and Photochemistry of Mineral Dust Aerosol, Annu. Rev. Phys. Chem., 59, 27–51, doi:10.1146/annurev.physchem.59.032607.093630, 2008.

D 'amico, G., Amodeo, A., Baars, H., Binietoglou, I., Freudenthaler, V., Mattis, I., Wandinger, U. and Pappalardo, G.: EARLINET Single Calculus Chain – overview on methodology and strategy, Atmos. Meas. Tech, 8, 4891–4916, doi:10.5194/amt-8-4891-2015, 2015.

D 'amico, G., Amodeo, A., Mattis, I., Freudenthaler, V. and Pappalardo, G.: EARLINET Single Calculus Chain – technical – Part 1: Pre-processing of raw lidar data, Atmos. Meas. Tech, 9, 491–507, doi:10.5194/amt-9-491-2016, 2016.

Denjean, C., Cassola, F., Mazzino, A., Triquet, S., Chevaillier, S., Grand, N., Bourrianne, T., Momboisse, G., Sellegri, K., Schwarzenbock, A., Freney, E., Mallet, M. and Formenti, P.: Size distribution and optical properties of mineral dust aerosols transported in the western Mediterranean, Atmos. Chem. Phys., doi:10.5194/acp-16-1081-2016, 2016.

Derimian, Y., Choël, M., Rudich, Y., Deboudt, K., Dubovik, O., Laskin, A., Legrand, M., Damiri, B., Koren, I., Unga, F., Moreau, M., Andreae, M. O. and Karnieli, A.: Effect of sea breeze circulation on aerosol mixing state and radiative properties in a desert setting, Atmos. Chem. Phys. Discuss., 1–37, doi:10.5194/acp-2016-1084, 2017.

Després, V., Huffman, J. A., Burrows, S. M., Hoose, C., Safatov, A., Buryak, G., Fröhlich-Nowoisky, J., Elbert, W., Andreae, M., Pöschl, U. and Jaenicke, R.: Primary biological aerosol particles in the atmosphere: a review, Tellus B Chem. Phys. Meteorol., 64(1), 15598, doi:10.3402/tellusb.v64i0.15598, 2012.

Dorling, S. R.: Cluster analysis: a technique for estimating the synoptic meteorological controls on air a n d precipitation chemistry-method and applications, Atmos. Env., 26A(14), 2575–2581, 1992.

Drummond, A. J.: On the measurement of sky radiation, Arch. Meteorol. Geophys. Bioklimatol., B(7),

413–436, 1956.

Du, B., Pang, C., Wu, D., Li, Z., Peng, H., Tao, Y., Wu, E. and Wu, G.: High-speed photon-counting laser ranging for broad range of distances, Sci. Rep., 8(1), 1–6, doi:10.1038/s41598-018-22675-1, 2018.

Dubovik, O. and King, M. D.: A flexible inversion algorithm for retrieval of aerosol optical properties from Sun and sky radiance measurements, J. Geophys. Res. Atmos., 105(D16), 20673–20696, doi:10.1029/2000JD900282, 2000.

Dubovik, O., Holben, B., Eck, T. F., Smirnov, A., Kaufman, Y. J., King, M. D., Tanré, D. and Slutsker, I.: Variability of Absorption and Optical Properties of Key Aerosol Types Observed in Worldwide Locations, J. Atmos. Sci., 59(3), 590–608, doi:10.1175/1520-0469(2002)059<0590:VOAAOP>2.0.CO;2, 2002.

Dubovik, O., Sinyuk, A., Lapyonok, T., Holben, B. N., Mishchenko, M., Yang, P., Eck, T. F., Volten, H., Muñoz, O., Veihelmann, B., van der Zande, W. J., Leon, J. F., Sorokin, M. and Slutsker, I.: Application of spheroid models to account for aerosol particle nonsphericity in remote sensing of desert dust, J. Geophys. Res. Atmos., 111(11), 1–34, doi:10.1029/2005JD006619, 2006.

Duce, R.: Sources, distributions, and fluxes of mineral aerosols and their relationship to Climate., edited by J. (eds). Charlson, RJ., Heinteznberg, John Wiley & Sons Ltd., 1995.

Emde, C., Buras-Schnell, R., Kylling, A., Mayer, B., Gasteiger, J., Hamann, U., Kylling, J., Richter, B., Pause, C., Dowling, T. and Bugliaro, L.: The libRadtran software package for radiative transfer calculations (version 2.0.1), Geosci. Model Dev., 9(5), 1647–1672, doi:10.5194/gmd-9-1647-2016, 2016.

Fernández, A. J., Sicard, M., Costa, M. J., Guerrero-Rascado, J. L., Gómez-Amo, J. L., Molero, F., Barragán, R., Basart, S., Bortoli, D., Bedoya-Velásquez, A. E., Utrillas, M. P., Salvador, P., Granados-Muñoz, M. J., Potes, M., Ortiz-Amezcua, P., Martínez-Lozano, J. A., Artíñano, B., Muñoz-Porcar, C., Salgado, R., Román, R., Rocadenbosch, F., Salgueiro, V., Benavent-Oltra, J. A., Rodríguez-Gómez, A., Alados-Arboledas, L., Comerón, A. and Pujadas, M.: Extreme, wintertime Saharan dust intrusion in the Iberian Peninsula: Lidar monitoring and evaluation of dust forecast models during the February 2017 event, Atmos. Res., 228, 223–241, doi:10.1016/j.atmosres.2019.06.007, 2019.

Fiocco, G. and Smullin, L. D.: Detection of Scattering Layers in the Upper Atmosphere (60–140 km) by Optical Radar, Nature, 199(4900), 1275–1276, doi:10.1038/1991275a0, 1963.

Flaounas, E., Kotroni, V., Lagouvardos, K., Kazadzis, S., Gkikas, A. and Hatzianastassiou, N.: Cyclone contribution to dust transport over the Mediterranean region, Atmos. Sci. Lett., 16(4), 473–478, doi:10.1002/asl.584, 2015.

Freudenthaler, V., Esselborn, M., Wiegner, M., Heese, B., Tesche, M., Ansmann, A., Müller, D., Althausen, D., Wirth, M., Fix, A., Ehret, G., Knippertz, P., Toledano, C., Gasteiger, J., Garhammer, M. and Seefeldner, M.: Depolarization ratio profiling at several wavelengths in pure Saharan dust during SAMUM 2006, Tellus B Chem. Phys. Meteorol., 61(1), 165–179, doi:10.1111/j.1600-0889.2008.00396.x, 2009.

Fröhlich-Nowoisky, J., Kampf, C. J., Weber, B., Huffman, J. A., Pöhlker, C., Andreae, M. O., Lang-Yona, N., Burrows, S. M., Gunthe, S. S., Elbert, W., Su, H., Hoor, P., Thines, E., Hoffmann, T., Després, V. R. and Pöschl, U.: Bioaerosols in the Earth system: Climate, health, and ecosystem interactions, Atmos. Res., 182, 346–376, doi:https://doi.org/10.1016/j.atmosres.2016.07.018, 2016.

Gerasopoulos, E., Amiridis, V., Kazadzis, S., Kokkalis, P., Eleftheratos, K., Andreae, M. O., Andreae, T. W., El-Askary, H. and Zerefos, C. S.: Three-year ground based measurements of aerosol optical depth over the Eastern Mediterranean: The urban environment of Athens, Atmos. Chem. Phys., 11(5),

2145–2159, doi:10.5194/acp-11-2145-2011, 2011.

Giannakaki, E., Van Zyl, P. G., Müller, D., Balis, D. and Komppula, M.: Optical and microphysical characterization of aerosol layers over South Africa by means of multi-wavelength depolarization and Raman lidar measurements, Atmos. Chem. Phys., 16(13), 8109–8123, doi:10.5194/acp-16-8109-2016, 2016.

Gkikas, A., Obiso, V., García-pando, C. P., Jorba, O. and Hatzianastassiou, N.: Direct radiative effects during intense Mediterranean desert dust outbreaks, Atmos. Chem. Phys., 18, 8757–8787, doi:https://doi.org/10.5194/acp-18-8757-2018, 2018.

Gobbi, G. P., Barnaba, F., Giorgi, R. and Santacasa, A.: Altitude-resolved properties of a Saharan dust event over the Mediterranean, Atmos. Environ., 34, 5119–5127, doi:https://doi.org/10.1016/S1352-2310(00)00194-1, 2000.

Gómez-Amo, J., di Sarra, A. and Meloni, D.: Sensitivity of the atmospheric temperature profile to the aerosol absorption in the presence of dust, Atmos. Environ., 98, doi:10.1016/j.atmosenv.2014.09.008, 2014.

Grell, G. A., Peckham, S. E., Schmitz, R., McKeen, S. A., Frost, G., Skamarock, W. C. and Eder, B.: Fully coupled "online" chemistry within the WRF model, Atmos. Environ., 39(37), 6957–6975, doi:10.1016/j.atmosenv.2005.04.027, 2005.

Groß, S., Freudenthaler, V., Ansmann, A., Baars, H., Haarig, M., Philipp, A., Seibert, P., Toledano, C., Weinzierl, B.: Ground-based polarization sensitive Raman lidar measurements of dust and pollution in the Eastern Mediterranean during the A-LIFE field experiment, in Geophysical Research Abstracts, p. 1. [online] Available from: https://meetingorganizer.copernicus.org/EGU2019/EGU2019-7270.pdf, 2019.

Groß S., Esselborn M., Weinzierl B., Wirth M., Fix A. and Petzold, A.: Aerosol classification by airborne high spectral resolution lidar observations, Atmos. Chem. Phys., 13, 2487–2505, doi:10.5194/acp-13-2487-2013, 2013.

Groß, S., Tesche, M., Freudenthaler, V., Toledano, C., Wiegner, M., Ansmann, A., Althausen, D. and Seefeldner, M.: Characterization of Saharan dust, marine aerosols and mixtures of biomass-burning aerosols and dust by means of multi-wavelength depolarization and Raman lidar measurements during SAMUM 2, Tellus B Chem. Phys. Meteorol., 63(4), 706–724, doi:10.1111/j.1600-0889.2011.00556.x, 2011.

Groß, S., Freudenthaler, V., Schepanski, K., Toledano, C., Schäfler, A., Ansmann, A. and Weinzierl, B.: Optical properties of long-range transported Saharan dust over Barbados as measured by dual-wavelength depolarization Raman lidar measurements, Atmos. Chem. Phys., 15(19), 11067–11080, doi:10.5194/acp-15-11067-2015, 2015.

Guerrero-Rascado, J. L., Ruiz, B. and Alados-Arboledas, L.: Multi-spectral Lidar characterization of the vertical structure of Saharan dust aerosol over southern Spain, Atmos. Environ., 42(11), 2668–2681, doi:10.1016/j.atmosenv.2007.12.062, 2008.

Guerrero-Rascado, J. L., Olmo, F. J., Avilés-Rodríguez, I., Navas-Guzmán, F., Pérez-Ramírez, D., Lyamani, H. and Arboledas, L. A.: Extreme saharan dust event over the southern iberian peninsula in september 2007: Active and passive remote sensing from surface and satellite, Atmos. Chem. Phys., 9(21), 8453–8469, doi:10.5194/acp-9-8453-2009, 2009.

Gustafsson, M. E. R. and Franzén, L. G.: Inland transport of marine aerosols in southern Sweden, Atmos. Environ., 34(2), 313–325, doi:https://doi.org/10.1016/S1352-2310(99)00198-3, 2000.

Haapanala, P., Räisänen, P., Kahnert, M. and Nousiainen, T.: Sensitivity of the shortwave radiative

effect of dust on particle shape: Comparison of spheres and spheroids, J. Geophys. Res. Atmos., 117(8), 1–12, doi:10.1029/2011JD017216, 2012.

Haarig, M., Ansmann, A., Althausen, D., Klepel, A., Groß, S., Freudenthaler, V., Toledano, C., Mamouri, R.-E., Farrell, D. A., Prescod, D. A., Marinou, E., Burton, S. P., Gasteiger, J., Engelmann, R. and Baars, H.: Triple-wavelength depolarization-ratio profiling of Saharan dust over Barbados during SALTRACE in 2013 and 2014, Atmos. Chem. Phys, 175194, 10767–10794, doi:10.5194/acp-17-10767-2017, 2017.

Hansen, C.: Discrete inverse problems: Insight and Algorithms, SIAM., 2010.

Harrison, R.: Key pollutants-airborne particles., Sci Total Env., 334–335, 3–8, doi:10.1016/j.scitotenv.2004.04.059, 2004.

Heller, W. and Nakagaki, M.: Light scattering of spheroids. III. Depolarization of the scattered light, J. Chem. Phys., 61(9), 3619–3625, doi:10.1063/1.1682544, 1974.

Hess, M., Koepke, P. and Schult, I.: Optical Properties of Aerosols and Clouds: The Software Package OPAC, Bull. Am. Meteorol. Soc., 79(5), 831–844, doi:10.1175/1520-0477(1998)079<0831:OPOAAC>2.0.CO;2, 1998.

Hinds, W.: Aerosol Technology: Properties, Behavior, and Measurement of Airborne particles, 2nd ed., John Wiley & Sons., 1998.

Holben, B. N., Eck, T. F., Slutsker, I., Tanré, D., Buis, J. P., Setzer, A., Vermote, E., Reagan, J. A., Kaufman, Y. J., Nakajima, T., Lavenu, F., Jankowiak, I. and Smirnov, A.: AERONET—A Federated Instrument Network and Data Archive for Aerosol Characterization, Remote Sens. Environ., 66(1), 1–16, doi:https://doi.org/10.1016/S0034-4257(98)00031-5, 1998.

Hulburt, E. O.: Observations of a Searchlight Beam to an Altitude of 28 Kilometers, J. Opt. Soc. Am., 27(11), 377–382, doi:10.1364/JOSA.27.000377, 1937.

Immler, F., Engelbart, D. and Schrems, O.: Fluorescence from atmospheric aerosol detected by a lidar indicates biogenic particles in the lowermost stratosphere, Atmos. Chem. Phys., 5(2), 345–355, doi:10.5194/acp-5-345-2005, 2005.

Intergovernmental Panel on Climate Change: Climate Change 2014: Synthesis Report, IPCC, Geneva, Switzerland. [online] Available from: https://www.ipcc.ch/site/assets/uploads/2018/05/SYR_AR5_FINAL_full_wcover.pdf, 2014.

ISO: Solar energy-Specification and classification of instruments for measuring hemispherical solar and direct solar radiation, Int. Organ. Stand., (9060), 11 [online] Available from: https://www.iso.org/standard/16629.html, 1990.

Janssens-Maenhout, G., Crippa, M., Guizzardi, D., Dentener, F., Muntean, M., Pouliot, G., Keating, T., Zhang, Q., Kurokawa, J., Wankmüller, R., Denier van der Gon, H., Kuenen, J. J. P., Klimont, Z., Frost, G., Darras, S., Koffi, B. and Li, M.: HTAP_v2.2: a mosaic of regional and global emission grid maps for 2008 and 2010 to study hemispheric transport of air pollution, Atmos. Chem. Phys., 15(19), 11411–11432, doi:10.5194/acp-15-11411-2015, 2015.

Jiang, J., Zhou, W., Cheng, Z., Wang, S., He, K. and Hao, J.: Particulate matter distributions in China during a winter period with frequent pollution episodes (January 2013), Aerosol Air Qual. Res., 15(2), 494–503, doi:10.4209/aaqr.2014.04.0070, 2015.

Kassomenos P., Kotroni, V., Kallos, G.: Analysis of climatological and air quality observations from Greater Athens area, Atmos. Env., 29B, 3671–3688 [online] Available from: http://forecast.uoa.gr/Publications/25-Kassom_Atm_Env.pdf, 1995.

Kim, G.-U., Seo, K.-H. and Chen, D.: Climate change over the Mediterranean and current destruction

of marine ecosystem, Sci. Rep., 9(1), 1–9, doi:10.1038/s41598-019-55303-7, 2019.

Kim, M., Omar, A. H., Tackett, J. L., Vaughan, M. A., Winker, D. M., Trepte, C. R., Hu, Y., Liu, Z., Poole, L. R., Pitts, M. C., Kar, J. and Magill, B. E.: The CALIPSO version 4 automated aerosol classification and lidar ratio selection algorithm, Atmos. Meas. Tech, 11, 6107–6135, doi:https://doi.org/10.5194/amt-11-6107-2018, 2018.

Kim, M. H., Kim, S. W. and Omar, A. H.: Dust lidar ratios retrieved from the CALIOP measurements using the MODIS AOD as a constraint, Remote Sens., 12(2), doi:10.3390/rs12020251, 2020.

Kipp & Zonen: Instruction Manual CM121 Shadow ring., 2004.

Klett, J. D.: Stable analytical inversion solution for processing lidar returns, Appl. Opt., 20(2), 211, doi:10.1364/ao.20.000211, 1981.

Klüser, L., Kleiber, P., Holzer-Popp, T. and Grassian, V. H.: Desert dust observation from space – Application of measured mineral component infrared extinction spectra, Atmos. Environ., 54, 419–427, doi:https://doi.org/10.1016/j.atmosenv.2012.02.011, 2012.

Koepke, P., Gasteiger, J. and Hess, M.: Technical Note: Optical properties of desert aerosol with non-spherical mineral particles: Data incorporated to OPAC, Atmos. Chem. Phys., 15(10), 5947–5956, doi:10.5194/acp-15-5947-2015, 2015.

Kokkalis, P., Papayannis, A., Mamouri, R. E., Tsaknakis, G. and Amiridis, V.: The EOLE lidar system of the National Technical University of Athens, 26th International Laser Radar Conference, June 25-29, 2012, Porto Heli, Greece., 2012.

Kokkalis, P., Papayannis, A., Amiridis, V., Mamouri, R. E., Veselovskii, I., Kolgotin, A., Tsaknakis, G., Kristiansen, N. I., Stohl, A. and Mona, L.: Optical, microphysical, mass and geometrical properties of aged volcanic particles observed over Athens, Greece, during the Eyjafjallajökull eruption in April 2010 through synergy of Raman lidar and sunphotometer measurements, Atmos. Chem. Phys., 13(18), 9303–9320, doi:10.5194/acp-13-9303-2013, 2013.

Kokkalis, P., Jassar, H. K. Al, Solomos, S., Raptis, P., Hendi, H. Al, Amiridis, V., Papayannis, A., Sarraf, H. Al and Dimashki, M. Al: Long-Term Ground-Based Measurements of Aerosol Optical Depth over Kuwait City, Remote Sens., 10(11), 18, doi:10.3390/rs10111807, 2018.

Kosmopoulos, P. G., Kazadzis, S., Taylor, M., Raptis, P. I., Keramitsoglou, I., Kiranoudis, C. and Bais, A. F.: Assessment of surface solar irradiance derived from real-time modelling techniques and verification with ground-based measurements, Atmos. Meas. Tech., 11(2), 907–924, doi:10.5194/amt-11-907-2018, 2018.

Laakso, L.: Kinetics and dynamics of atmospheric ions, clusters and aerosols., Rep. Ser. aerosol Sci., 70, 5–33, 2004.

Lacis, A.A., and Mishchenko, M. I.: Climate forcing, climate sensitivity, and climate response: A radiative modeling perspective on atmospheric aerosols, in In Aerosol Forcing of Climate: Report of the Dahlem Workshop on Aerosol Forcing of Climate, 24-29 Apr. 1994, Berlin, edited by E. R.J. Charlson and J. Heintzenberg, John Wiley Sons., 1995.

Liou, K. N., Ed.: An Introduction to Atmospheric Radiation, 2nd ed., Elsevier Science, Los Angeles, California., 2002.

Lohmann, U. and Feichter, J.: Global indirect aerosol effects: a review, Atmos. Chem. Phys., 5(3), 715–737, doi:10.5194/acp-5-715-2005, 2005.

Lopatin, A., Dubovik, O., Chaikovsky, A., Goloub, P., Lapyonok, T., Tanre, D. and Litvinov, P.: Enhancement of aerosol characterization using synergy of lidar and sun-photometer coincident observations : the GARRLiC algorithm, Atmos. Meas. Tech., 2065–2088, doi:10.5194/amt-6-2065-

2013, 2013.

Lyamani, H., Olmo, F. J. and Alados-Arboledas, L.: Physical and optical properties of aerosols over an urban location in Spain: Seasonal and diurnal variability, Atmos. Chem. Phys., 10(1), 239–254, doi:10.5194/acp-10-239-2010, 2010.

Madonna F., Amodeo A., Boselli A., Cornacchia C., Cuomo V., D'Amico G., Giunta A., Mona L., and P. G.: CIAO: The CNR-IMAA advanced observatory for atmospheric research, Atmos. Meas. Tech., 4(6), 1191–1208, doi:10.5194/amt-4-1191-2011, 2011.

Maiman, T. H.: Stimulated Optical Radiation in Ruby, Nature, 187(4736), 493–494, doi:10.1038/187493a0, 1960.

Mamouri, R. E., Ansmann, A., Nisantzi, A., Kokkalis, P., Schwarz, A. and Hadjimitsis, D.: Low Arabian dust extinction-to-backscatter ratio, Geophys. Res. Lett., 40(17), 4762–4766, doi:10.1002/grl.50898, 2013.

Mandija, F., Sicard, M., Comerón, A., Alados-Arboledas, L., Guerrero-Rascado, J. L., Bravo-Aranda, J. A., Bravo-Aranda, J. A., Granados-Muñoz, M. J., Lyamani, H., Muñoz Porcar, C., Rocadenbosch, F., Rodríguez, A., Valenzuela, A. and García Vizcaíno, D.: Origin and pathways of the mineral dust transport to two Spanish EARLINET sites: Effect on the observed columnar and range-resolved dust optical properties, Atmos. Res., 187, 69–83, doi:10.1016/j.atmosres.2016.12.002, 2017.

Matthias, V., Balis, D., Bösenberg, J., Eixmann, R., Iarlori, M., Komguem, L., Mattis, I., Papayannis, A., Pappalardo, G., Perrone, M. R. and Wang, X.: Vertical aerosol distribution over Europe: Statistical analysis of Raman lidar data from 10 European Aerosol Research Lidar Network (EARLINET) stations, J. Geophys. Res. Atmos., 109(D18), doi:10.1029/2004JD004638, 2004.

Mattis, I., Ansmann, A., Müller, D., Wandinger, U. and Althausen, D.: Dual-wavelength Raman lidar observations of the extinction-to-backscatter ratio of Saharan dust, Geophys. Res. Lett., 29(9), 1306, doi:10.1029/2002gl014721, 2002.

Mattis, I., Mona, L., Müller, D., Pappalardo, G., Alados-Arboledas, L., D'Amico, G., Amodeo, A., Apituley, A., Baldasano, J. M., Böckmann, C., Bösenberg, J., Chaikovsky, A., Comeron, A., Giannakaki, E., Grigorov, I., Rascado, J. L. G., Gustafsson, O., Iarlori, M., Linne, H., Mitev, V., Menendez, F. M., Nicolae, D., Papayannis, A., Garcia-Pando, C. P., Perrone, M. R., Pietruczuk, A., Putaud, J.-P., Ravetta, F., Rodríguez, A., Seifert, P., Sicard, M., Simeonov, V., Sobolewski, P., Spinelli, N., Stebel, K., Stohl, A., Tesche, M., Trickl, T., Wang, X. and Wiegner, M.: EARLINET correlative measurements for CALIPSO, in Proc.SPIE, vol. 6750., 2007.

Mattis, I., Müller, D., Ansmann, A., Wandinger, U., Preißler, J., Seifert, P. and Tesche, M.: Ten years of multiwavelength Raman lidar observations of free-tropospheric aerosol layers over central Europe: Geometrical properties and annual cycle, J. Geophys. Res. Atmos., 113(D20), doi:10.1029/2007JD009636, 2008.

Mayer, B. and Kylling, A.: Technical note: The libRadtran software package for radiative transfer calculations- description and examples of use, Atmos. Chem. Phys. Discuss., 5(2), 1319–1381, doi:10.5194/acpd-5-1319-2005, 2005.

Mayer, B., Kylling, A., Emde, C., Buras, R., Hamann, U., Gasteiger, J. and Richter, B.: libRadtran User's Guide, Ed. Libr. version 2.0.2, 1–155 [online] Available from: http://www.libradtran.org/doc/libRadtran.pdf, 2017.

McClung, F.J., Hellwarth, R. .: Giant Optical Pulsations from Ruby, J. Appl. Phys., 33, 828, doi:https://doi.org/10.1063/1.1777174, 1962.

Meloni, D., Junkermann, W., di Sarra, A., Cacciani, M. De Silvestri, L., Di Iorio, T. Estellés, V.,

Gómez-Amo, J. L., Pace, G. and Sferlazzo, D. M.: Altitude-resolved shortwave and longwave radiative effects of desert dust in the Mediterranean during the GAMARF campaign: Indications of a net daily cooling in the dust layer, J. Geophys. Res. Atmos., 120, 3386–3407, doi:https://doi.org/10.1002/2014JD022312, 2015.

Meloni, D., di Sarra, A., DeLuisi, J., Di Iorio, T., Fiocco, G., Junkermann, W. and Pace, G.: Tropospheric aerosols in the Mediterranean: 2. Radiative effects through model simulations and measurements, J. Geophys. Res., 108(10), 1–16, doi:10.1029/2002jd002807, 2003.

Meloni, D., Di Sarra, A., Brogniez, G., Denjean, C., De Silvestri, L., Di Iorio, T., Formenti, P., Gómez-Amo, J. L., Gröbner, J., Kouremeti, N., Liuzzi, G., Mallet, M., Pace, G. and Sferlazzo, D. M.: Determining the infrared radiative effects of Saharan dust: A radiative transfer modelling study based on vertically resolved measurements at Lampedusa, Atmos. Chem. Phys., 18(6), 4377–4401, doi:10.5194/acp-18-4377-2018, 2018.

Michaelides, S., Karacostas, T., Sánchez, J. L., Retalis, A., Pytharoulis, I., Homar, V., Romero, R., Zanis, P., Giannakopoulos, C., Bühl, J., Ansmann, A., Merino, A., Melcón, P., Lagouvardos, K., Kotroni, V., Bruggeman, A., López-Moreno, J. I., Berthet, C., Katragkou, E., Tymvios, F., Hadjimitsis, D. G., Mamouri, R. E. and Nisantzi, A.: Reviews and perspectives of high impact atmospheric processes in the Mediterranean, Atmos. Res., 208, 4–44, doi:10.1016/j.atmosres.2017.11.022, 2018.

Miller, R. L. and Tegen, I.: Climate response to soil dust aerosols, J. Clim., 11(12), 3247–3267, doi:10.1175/1520-0442(1998)011<3247:CRTSDA>2.0.CO;2, 1998.

Mishchenko, M. I., Travis, L. D. and Mackowski, D. W.: T-matrix computations of light scattering by nonspherical particles: A review, J. Quant. Spectrosc. Radiat. Transf., 55(5), 535–575, doi:10.1016/0022-4073(96)00002-7, 1996.

Mishra, A. K., Klingmueller, K., Fredj, E., Lelieveld, J., Rudich, Y. and Koren, I.: Radiative signature of absorbing aerosol over the eastern Mediterranean basin, Atmos. Chem. Phys., 14(14), 7213–7231, doi:10.5194/acp-14-7213-2014, 2014.

Mona, L., Papagiannopoulos, N., Basart, S., Baldasano, J., Binietoglou, I., Cornacchia, C. and Pappalardo, G.: EARLINET dust observations vs. BSC-DREAM8b modeled profiles : 12-year-long systematic comparison at Potenza , Italy, Atmos. Chem. Phys., 14, 8781–8793, doi:10.5194/acp-14-8781-2014, 2014.

Mona, L., Amodeo, A., Pandolfi, M. and Pappalardo, G.: Saharan dust intrusions in the Mediterranean area: Three years of Raman lidar measurements, J. Geophys. Res. Atmos., 111(16), 1–13, doi:10.1029/2005JD006569, 2006.

Mona, L., Liu, Z., Müller, D., Omar, A., Papayannis, A., Pappalardo, G., Sugimoto, N. and Vaughan, M.: Lidar measurements for desert dust characterization: An overview, Adv. Meteorol., 2012, doi:10.1155/2012/356265, 2012.

Moulin, C., Lambert, C. E., Dulac, F. and Dayan, U.: Control of atmospheric export of dust from North Africa by the North Atlantic Oscillation, Nature, 387(6634), 691–694, doi:10.1038/42679, 1997.

Müller, D., Ansmann, A., Mattis, I., Tesche, M., Wandinger, U., Althausen, D. and Pisani, G.: Aerosol-type-dependent lidar ratios observed with Raman lidar, J. Geophys. Res. Atmos., 112(D16202), doi:10.1029/2006JD008292, 2007.

Müller, D., Heinold, B., Tesche, M., Tegen, I., Althausen, D., Arboledas, L. A., Amiridis, V., Amodeo, A., Ansmann, A., Balis, D., Comeron, A., D'amico, G., Gerasopoulos, E., Guerrero-rascado, J. L., Freudenthaler, V., Giannakaki, E., Heese, B., Iarlori, M., Knippertz, P., Mamouri, R. E., Mona, L., Papayannis, A., Pappalardo, G., Perrone, R. M., Pisani, G., Rizi, V., Sicard, M., Spinelli, N., Tafuro, A. and Wiegner, M.: EARLINET observations of the 14-22-May long-range dust transport event

during SAMUM 2006: Validation of results from dust transport modelling, Tellus, Ser. B Chem. Phys. Meteorol., 61(1), 325–339, doi:10.1111/j.1600-0889.2008.00400.x, 2009.

Müller, D., Böckmann, C., Kolgotin, A., Schneidenbach, L., Chemyakin, E., Rosemann, J., Znak, P. and Romanov, A.: Microphysical particle properties derived from inversion algorithms developed in the framework of EARLINET, Atmos. Meas. Tech, 9, 5007–5035, doi:10.5194/amt-9-5007-2016, 2016.

Nickovic, S., Kallos, G., Papadopoulos, A. and Kakaliagou, O.: Model for prediction of desert dust cycle in the atmosphere, J. Geophys. Res., 106, 18113–18130, doi:10.1029/2000JD900794, 2001.

Nicolae, D., Nemuc, A., Müller, D., Talianu, C., Vasilescu, J., Belegante, L. and Kolgotin, A.: Characterization of fresh and aged biomass burning events using multiwavelength Raman lidar and mass spectrometry, J. Geophys. Res. Atmos., 118(7), 2956–2965, doi:10.1002/jgrd.50324, 2013.

Nisantzi, A., Mamouri, R. E., Ansmann, A., Schuster, G. L. and Hadjimitsis, D. G.: Middle East versus Saharan dust extinction-to-backscatter ratios, Atmos. Chem. Phys., 15, 7071–7084, doi:10.5194/acp-15-7071-2015, 2015.

Omar, A. H., Winker, D. M., Vaughan, M. A., Hu, Y., Trepte, C. R., Ferrare, R. A., Lee, K.-P., Hostetler, C. A., Kittaka, C., Rogers, R. R., Kuehn, R. E. and Liu, Z.: The CALIPSO Automated Aerosol Classification and Lidar Ratio Selection Algorithm, J. Atmos. Ocean. Technol., 26(10), 1994–2014, doi:10.1175/2009JTECHA1231.1, 2009.

Pan, Y.-L., Pinnick, R. G., Hill, S. C., Rosen, J. M. and Chang, R. K.: Single-particle laser-induced-fluorescence spectra of biological and other organic-carbon aerosols in the atmosphere: Measurements at New Haven, Connecticut, and Las Cruces, New Mexico, J. Geophys. Res. Atmos., 112(D24), doi:10.1029/2007JD008741, 2007.

Papadimas, C. D., Hatzianastassiou, N., Matsoukas, C., Kanakidou, M., Mihalopoulos, N. and Vardavas, I.: The direct effect of aerosols on solar radiation over the broader Mediterranean basin, Atmos. Chem. Phys., 12(15), 7165–7185, doi:10.5194/acp-12-7165-2012, 2012.

Papanikolaou, C., Giannakaki, E., Papayannis, A., Mylonaki, M. and Soupiona, O.: Canadian Biomass Burning Aerosol Properties Modification during a Long-Ranged Event on August 2018, Sensors, 20(5442), doi:10.3390/s20185442, 2020.

Papayannis, A., Ancellet, G., Pelon, J. and Mégie, G.: Multiwavelength lidar for ozone measurements in the troposphere and the lower stratosphere., Appl. Opt., 29(4), 467–76, doi:10.1364/AO.29.000467\r60866, 1990.

Papayannis, A., Balis, D., Amiridis, V., Chourdakis, G., Tsaknakis, G., Zerefos, C., Castanho, A. D. A., Nickovic, S., Kazadzis, S. and Grabowski, J.: Measurements of Saharan dust aerosols over the Eastern Mediterranean using elastic backscatter-Raman lidar, spectrophotometric and satellite observations in the frame of the EARLINET project, Atmos. Chem. Phys, 5, 2065–2079, doi:www.atmos-chem-phys.org/acp/5/2065/, 2005.

Papayannis, A., Mamouri, R. E., Amiridis, V. and Kazadzis, S.: Systematic lidar observations of Saharan dust layers over Athens , Greece in the frame of EARLINET project (2004 – 2006), Ann. Geophys., 27(9), 3611–3620, doi:www.ann-geophys.net/27/3611/2009/, 2009.

Papayannis, A., Mamouri, R. E., Amiridis, V., Giannakaki, E., Veselovskii, I., Kokkalis, P., Tsaknakis, G., Balis, D., Kristiansen, N. I., Stohl, A., Korenskiy, M., Allakhverdiev, K., Huseyinoglu, M. F. and Baykara, T.: Optical properties and vertical extension of aged ash layers over the Eastern Mediterranean as observed by Raman lidars during the Eyjafjallajökull eruption in May 2010, Atmos. Environ., 48, 56–65, doi:10.1016/j.atmosenv.2011.08.037, 2012.

Papayannis, A., Argyrouli, A., Bougiatioti, A., Remoundaki, E., Vratolis, S., Nenes, A., Solomos, S., Komppula, M., Giannakaki, E., Kalogiros, J., Banks, R., Eleftheriadis, K., Mantas, E., Diapouli, E., Tzanis, C. G., Kazadzis, S., Binietoglou, I., Labzovskii, L., Vande Hey, J. and Zerefos, C. S.: From hygroscopic aerosols to cloud droplets: The HygrA-CD campaign in the Athens basin — An overview, Sci. Total Environ., 574, 216–233, doi:10.1016/j.scitotenv.2016.09.054, 2017.

Papayannis, A., Kokkalis, P., Mylonaki, M., Soupiona, R., Papanikolaou, C. A. and Foskinis, R.: Recent upgrades of the EOLE and AIAS lidar systems of the National Technical University of Athens operating since 2000 in Athens, Greece, vol. 237, pp. 4–7., 2020.

Pappalardo, G., Wandinger, U., Lucia, M., Schwarz, A., Mattis, I., Amodeo, A., Ansmann, A., Seifert, P., Linné, H., Apituley, A., Arboledas, L., Balis, D., Chaikovsky, A., De Tomasi, F., Freudenthaler, V., Giannakaki, E., Giunta, A., Grigorov, I., Iarlori, M. and Wiegner, M.: EARLINET correlative measurements for CALIPSO: First intercomparison results, J. Geophys. Res. - Atmos. v.115, 115, doi:10.1029/2009JD012147, 2010.

Pérez, C., Nickovic, S., Pejanovic, G., Baldasano, J. M. and Özsoy, E.: Interactive dust-radiation modeling: A step to improve weather forecasts, J. Geophys. Res. Atmos., 111(16), doi:10.1029/2005JD006717, 2006.

Pérez, C., Haustein, K., Janjic, Z., Jorba, O., Huneeus, N., Baldasano, J. M., Black, T., Basart, S., Nickovic, S., Miller, R. L., Perlwitz, J. P., Schulz, M. and Thomson, M.: Atmospheric dust modeling from meso to global scales with the online NMMB/BSC-Dust model – Part 1: Model description, annual simulations and evaluation, Atmos. Chem. Phys., 11(24), 13001–13027, doi:10.5194/acp-11-13001-2011, 2011.

Petzold, A., Rasp, K., Weinzierl, B., Esselborn, M., Hamburger, T., Dörnbrack, A., Kandler, K., Schütz, L., Knippertz, P., Fiebig, M. and Virkkula, A.: Saharan dust absorption and refractive index from aircraft-based observations during SAMUM 2006, Tellus B Chem. Phys. Meteorol., 61(1), 118–130, doi:10.1111/j.1600-0889.2008.00383.x, 2009.

Petzold, A., Veira, A., Mund, S., Esselborn, M., Kiemle, C., Weinzierl, B., Hamburger, T., Ehret, G., Lieke, K. and Kandler, K.: Mixing of mineral dust with urban pollution aerosol over Dakar (Senegal): Impact on dust physico-chemical and radiative properties, Tellus B Chem. Phys. Meteorol., 63(4), 619–634, doi:10.1111/j.1600-0889.2011.00547.x, 2011.

Pollack, J. B. and Cuzzi, J. N.: Scattering by Nonspherical Particles of Size Comparable to a Wavelength: A New Semi-Empirical Theory and Its Application to Tropospheric Aerosols, J. Atmos. Sci., 37(4), 868–881, doi:10.1175/1520-0469(1980)037<0868:SBNPOS>2.0.CO;2, 1980.

Preißler, J., Wagner, F., Pereira, S. N. and Guerrero-Rascado, J. L.: Multi-instrumental observation of an exceptionally strong Saharan dust outbreak over Portugal, J. Geophys. Res. Atmos., doi:10.1029/2011JD016527, 2011.

Quijano, A. L., Sokolik, I. N. and Toon, O. B.: Radiative heating rates and direct radiative forcing by mineral dust in cloudy atmospheric conditions, J. Geophys. Res. Atmos., 105(D10), 12207–12219, doi:10.1029/2000JD900047, 2000.

Richardson, S. C., Mytilinaios, M., Foskinis, R., Kyrou, C., Papayannis, A., Pyrri, I., Giannoutsou, E. and Adamakis, I. D. S.: Bioaerosol detection over Athens, Greece using the laser induced fluorescence technique, Sci. Total Environ., 696, doi:10.1016/j.scitotenv.2019.133906, 2019.

Rittmeister, F., Ansmann, A., Engelmann, R., Skupin, A., Baars, H., Kanitz, T. and Kinne, S.: Profiling of Saharan dust from the Caribbean to western Africa-Part 1: Layering structures and optical properties from shipborne polarization/Raman lidar observations, Atmos. Chem. Phys., 17(21), 12963–12983, doi:10.5194/acp-17-12963-2017, 2017.

Rother, T. and Kahnert, M.: Electromagnetic Wave Scattering on Nonspherical Particles, Springer Series in Optical Sciences., 2009.

Salvador, P., Alonso-Pérez, S., Pey, J., Artíñano, B., De Bustos, J. J., Alastuey, A. and Querol, X.: African dust outbreaks over the western Mediterranean Basin: 11-year characterization of atmospheric circulation patterns and dust source areas, Atmos. Chem. Phys., 14(13), 6759–6775, doi:10.5194/acp-14-6759-2014, 2014.

Samaras, S.: Microphysical retrieval of non-spherical aerosol particles using regularized inversion of multi-wavelength lidar data, PhD Thesis, Mathematik, Institut f¨ur Probleme, Numerische Mathematik - Inverse, University of Potsdam, Germany., 2016.

Samaras, S., Nicolae, D., Böckmann, C., Vasilescu, J., Binietoglou, I., Labzovskii, L., Toanca, F. and Papayannis, A.: Using Raman-lidar-based regularized microphysical retrievals and Aerosol Mass Spectrometer measurements for the characterization of biomass burning aerosols, J. Comput. Phys., 299, 156–174, doi:10.1016/j.jcp.2015.06.045, 2015.

Schell, B., Ackermann, I. J., Hass, H., Binkowski, F. S. and Ebel, A.: Modeling the formation of secondary organic aerosol within a comprehensive air quality model system, J. Geophys. Res. Atmos., 106(D22), 28275–28293, doi:10.1029/2001JD000384, 2001.

Schladitz, A., Muller, T., Kaaden, N., Massling, A., Kandler, K., Ebert, M., Weinbruch, S., Deutscher, C. and Wiedensohler, A.: In situ measurements of optical properties at Tinfou (Morocco) during the Saharan Mineral Dust Experiment SAMUM 2006, Tellus B, 61, 64–78, doi:10.1111/j.1600-0889.2008.00397.x, 2009.

Schuster, G. L., Dubovik, O. and Arola, A.: Remote sensing of soot carbon – Part 1 : Distinguishing different absorbing aerosol species, Atmos. Chem. Phys., 16, 1565–1585, doi:10.5194/acp-16-1565-2016, 2016.

Seibert, P. and Frank, A.: Source-receptor matrix calculation with a Lagrangian particle dispersion model in backward mode, Atmos. Chem. Phys, 4, 51–63, doi:www.atmos-chem-phys.org/acp/4/51/, 2004.

Seinfeld, J. H. and Pandis, S. N.: Atmospheric Chemistry and Physics: From Air Pollution to Climate Change, Wiley. [online] Available from: https://books.google.gr/books?id=tZEpAQAAMAAJ, 2006.

Seinfeld, J. H., Bretherton, C., Carslaw, K. S., Coe, H., DeMott, P. J., Dunlea, E. J., Feingold, G., Ghan, S., Guenther, A. B., Kahn, R., Kraucunas, I., Kreidenweis, S. M., Molina, M. J., Nenes, A., Penner, J. E., Prather, K. A., Ramanathan, V., Ramaswamy, V., Rasch, P. J., Ravishankara, A. R., Rosenfeld, D., Stephens, G. and Wood, R.: Improving our fundamental understanding of the role of aerosol−cloud interactions in the climate system, Proc. Natl. Acad. Sci., 113(21), 5781–5790, doi:10.1073/pnas.1514043113, 2016.

Shang, X., Xia, H., Dou, X., Shangguan, M., Li, M. and Wang, C.: Adaptive inversion algorithm for 1.5μm visibility lidar incorporating in situ Angstrom wavelength exponent, Opt. Commun., 418, 129–134, doi:10.1016/j.optcom.2018.03.009, 2018.

Sicard, M., Bertolín, S., Mallet, M., Dubuisson, P. and Comerón, A.: Estimation of mineral dust long-wave radiative forcing: Sensitivity study to particle properties and application to real cases in the region of Barcelona, Atmos. Chem. Phys., 14(17), 9213–9231, doi:10.5194/acp-14-9213-2014, 2014.

Solomos, S., Bougiatioti, A., Soupiona, O., Papayannis, A., Mylonaki, M. and Papanikolaou, C.: Effects of regional and local atmospheric dynamics on the aerosol and CCN load over Athens, Atmos. Environ., 197, 53–65, doi:10.1016/j.atmosenv.2018.10.025, 2019.

Soupiona, O., Papayannis, A., Kokkalis, P., Foskinis, R., Sánchez Hernández, G., Ortiz-Amezcua, P.,

Mylonaki, M., Papanikolaou, C.-A., Papagiannopoulos, N., Samaras, S., Groß, S., Mamouri, R.-E., Alados-Arboledas, L., Amodeo, A., and Psiloglou, B.: EARLINET observations of Saharan dust intrusions over the northern Mediterranean region (2014 – 2017): properties and impact on radiative forcing, Atmos. Chem. Phys, 20, 15147–15166, doi:https://doi.org/10.5194/acp-20-15147-2020, 2020.

Soupiona, O., Papayannis, A., Kokkalis, P., Mylonaki, M., Tsaknakis, G., Argyrouli, A. and Vratolis, S.: Long-term systematic profiling of dust aerosol optical properties using the EOLE NTUA lidar system over Athens, Greece (2000–2016), Atmos. Environ., 183, 165–174, doi:10.1016/j.atmosenv.2018.04.011, 2018.

Soupiona, O., Samaras, S., Ortiz-Amezcua, P., Böckmann, C., Papayannis, A., Moreira, G. A., Benavent-Oltra, J. A., Guerrero-Rascado, J. L., Bedoya-Velásquez, A. E., Olmo, F. J., Román, R., Kokkalis, P., Mylonaki, M., Alados-Arboledas, L., Papanikolaou, C. A. and Foskinis, R.: Retrieval of optical and microphysical properties of transported Saharan dust over Athens and Granada based on multi-wavelength Raman lidar measurements: Study of the mixing processes, Atmos. Environ., 214, 116824, doi:10.1016/j.atmosenv.2019.116824, 2019.

Stein, A. F., Draxler, R. R., Rolph, G. D., Stunder, B. J. B., Cohen, M. D. and Ngan, F.: NOAA's hysplit atmospheric transport and dispersion modeling system, Bull. Am. Meteorol. Soc., 96(12), 2059–2077, doi:10.1175/BAMS-D-14-00110.1, 2015.

Stockwell, W. R., Middleton, P., Chang, J. S. and Xiaoyan Tang: The second generation regional acid deposition model chemical mechanism for regional air quality modeling, J. Geophys. Res., 95(D10), doi:10.1029/jd095id10p16343, 1990.

Stohl, A. and Hittenberger, M., and Wotawa, G.: Validation of the lagrangian particle dispersion model FLEXPART against large-scale tracer experiment data, Atmos. Environ., 32(24), 4245–4264, doi:S1352–2310(98)00184–8, 1998.

Stohl, A. and Thomson, D. J.: A density correction for Lagrangian particle dispersion models, Boundary-Layer Meteorol., 90(1), 155–167 [online] Available from: http://citeseerx.ist.psu.edu/viewdoc/download?doi=10.1.1.454.556&rep=rep1&type=pdf, 1998.

Stohl, A., Forster, C., Frank, A., Seibert, P. and Wotawa, G.: Technical note: The Lagrangian particle dispersion model FLEXPART version 6.2, Atmos. Chem. Phys, 5, 2461–2474, doi:www.atmos-chem-phys.org/acp/5/2461/, 2005.

Stull, R. B.: An Introduction to Boundary Layer Meteorology, Springer Netherlands., 1988.

Synge, E. H.: XCI. A method of investigating the higher atmosphere, London, Edinburgh, Dublin Philos. Mag. J. Sci., 9(60), 1014–1020, doi:10.1080/14786443008565070, 1930.

Tegen, I., Lacis, A.A., Fung, I.: The influence of mineral aerosols from disturbed soils on the global radiation budget., Nature, 380, 419–422, doi:10.1038/380419a0, 1996.

Tegen, I., Bierwirth, E., Heinold, B., Helmert, J. and Wendisch, M.: Effect of measured surface albedo on modeled Saharan dust solar radiative forcing, J. Geophys. Res. Atmos., 115(24), 1–15, doi:10.1029/2009JD013764, 2010.

Tesche, M., Groß, S., Ansmann, A., Muller, D., Althausen, D. and Freudenthaler, V., Esselborn, M.: Profiling of Saharan dust and biomass-burning smoke with multiwavelength polarization Raman lidar at Cape Verde, Tellus B, 63, 649–676, doi:10.1111/j.1600-0889.2011.00548.x, 2011.

Tesche, M., Ansmann, A., Müller, D., Althausen, D., Engelmann, R., Freudenthaler, V. and Groß, S.: Vertically resolved separation of dust and smoke over Cape Verde using multiwavelength Raman and polarization lidars during Saharan Mineral Dust Experiment 2008, J. Geophys. Res. Atmos., 114(D13), doi:10.1029/2009JD011862, 2009.

Textor, C., Schulz, M., Guibert, S., Kinne, S., Balkanski, Y., Bauer, S., Berntsen, T., Berglen, T., Boucher, O., Chin, M., Dentener, F., Diehl, T., Easter, R., Feichter, H., Fillmore, D., Ghan, S., Ginoux, P., Gong, S., Grini, A., Hendricks, J., Horowitz, L., Huang, P., Isaksen, I., Iversen, I., Kloster, S., Koch, D., Kirkevåg, A., Kristjansson, J. E., Krol, M., Lauer, A., Lamarque, J. F., Liu, X., Montanaro, V., Myhre, G., Penner, J., Pitari, G., Reddy, S., Seland, Ø., Stier, P., Takemura, T. and Tie, X.: Analysis and quantification of the diversities of aerosol life cycles within AeroCom, Atmos. Chem. Phys., 6(7), 1777–1813, doi:10.5194/acp-6-1777-2006, 2006.

Toledano, C., Cachorro, V. E., De Frutos, A. M., Torres, B., Berjón, A., Sorribas, M. and Stone, R. S.: Airmass classification and analysis of aerosol types at El Arenosillo (Spain), J. Appl. Meteorol. Climatol., 48(5), 962–981, doi:10.1175/2008JAMC2006.1, 2009.

Toledano, C., Wiegner, M., Groß, S., Freudenthaler, V., Gasteiger, J., Müller, D., Schladitz, A., Weinzierl, B., Torres, B., O, N. T., Wiegner, M., Groß, S., Freudenthaler, V., Gasteiger, J., Müller, D., Müller, D., Schladitz, A., Weinzierl, B., Torres, B. and O'Neill, N. T.: Optical properties of aerosol mixtures derived from sun-sky radiometry during SAMUM-2, Tellus B, 63(4), 635–648, doi:10.1111/j.1600-0889.2011.00573.x, 2011.

Tuve, M. A., Johnson, E. A., & Wolf, O. R.: A new experimental method for study of the upper atmosphere., Terr. Mag., 40(452), 1935.

Vainio, M. and Halonen, L.: Mid-infrared optical parametric oscillators and frequency combs for molecular spectroscopy, Phys. Chem. Chem. Phys., 18(6), 4266–4294, doi:10.1039/C5CP07052J, 2016.

Valenzuela, A., Olmo, F. J., Lyamani, H., Antón, M., Quirantes, A. and Alados-Arboledas, L.: Analysis of the columnar radiative properties retrieved during African desert dust events over Granada (2005-2010) using principal plane sky radiances and spheroids retrieval procedure, Atmos. Res., 104–105, 292–301, doi:10.1016/j.atmosres.2011.11.005, 2012.

Valenzuela, A., Olmo, F. J., Lyamani, H., Granados-Muñoz, M. J., Antón, M., Guerrero-Rascado, J. L., Quirantes, A., Toledano, C., Perez-Ramírez, D. and Alados-Arboledas, L.: Aerosol transport over the western mediterranean basin: Evidence of the contribution of fine particles to desert dust plumes over alborán island, J. Geophys. Res., doi:10.1002/2014JD022044, 2014.

Valenzuela, A., Costa, M. J., Guerrero-Rascado, J. L., Bortoli, D. and Olmo, F. J.: Solar and thermal radiative effects during the 2011 extreme desert dust episode over Portugal, Atmos. Environ., 148, 16–29, doi:10.1016/j.atmosenv.2016.10.037, 2017.

Vernier, J.-P., Fairlie, T. D., Deshler, T., Natarajan, M., Knepp, T., Foster, K., Wienhold, F. G., Bedka, K. M., Thomason, L. and Trepte, C.: In situ and space-based observations of the Kelud volcanic plume: The persistence of ash in the lower stratosphere, J. Geophys. Res. Atmos., 121(18), 11,104-111,118, doi:10.1002/2016JD025344, 2016.

Veselovskii, I., Goloub, P., Podvin, T., Bovchaliuk, V., Derimian, Y., Augustin, P., Fourmentin, M., Tanre, D., Korenskiy, M., Whiteman, D. N., Diallo, A., Ndiaye, T., Kolgotin, A. and Dubovik, O.: Retrieval of optical and physical properties of African dust from multiwavelength Raman lidar measurements during the SHADOW campaign in Senegal, Atmos. Chem. Phys, 16, 7013–7028, doi:10.5194/acp-16-7013-2016, 2016.

Veselovskii, I., Hu, Q., Goloub, P., Podvin, T., Korenskiy, M., Derimian, Y., Legrand, M. and Castellanos, P.: Variability in lidar-derived particle properties over West Africa due to changes in absorption: towards an understanding, Atmos. Chem. Phys, 20, 6563–6581, doi:doi.org/10.5194/acp-20-6563-2020, 2020.

Wagner, R., Ajtai, T., Kandler, K., Lieke, K., Linke, C., Muller, T., Schnaiter, M. and Vragel, M.: and

Physics Complex refractive indices of Saharan dust samples at visible and near UV wavelengths: a laboratory study, Atmos. Chem. Phys., 12, 2491–2512, doi:10.5194/acp-12-2491-2012, 2012.

Wandinger, U.: Introduction to Lidar, in Lidar Range-Resolved Optical Remote Sensing of the Atmosphere, edited by C. Weitkamp., 2005.

Wandinger, U., Baars, H., Engelmann, R., Hünerbein, A., Horn, S., Kanitz, T., Donovan, D., van Zadelhoff, G.-J., Daou, D., Fischer, J., von Bismarck, J., Filipitsch, F., Docter, N., Eisinger, M., Lajas, D. and Wehr, T.: HETEAC: The Aerosol Classification Model for EarthCARE, EPJ Web Conf., 119, 01004, doi:10.1051/epjconf/201611901004, 2016.

Weinzierl, B., Sauer, D., Esselborn, M., Petzold, A., Veira, A., Rose, M., Mund, S., Wirth, M., Ansmann, A., Tesche, M., Gross, S. and Freudenthaler, V.: Microphysical and optical properties of dust and tropical biomass burning aerosol layers in the Cape Verde region-an overview of the airborne in situ and lidar measurements during SAMUM-2, Tellus, Ser. B Chem. Phys. Meteorol., 63(4), 589–618, doi:10.1111/j.1600-0889.2011.00566.x, 2011.

Weinzierl, B., Ansmann, A., Prospero, J. M., Althausen, D., Benker, N., Chouza, F., Dollner, M., Farrell, D., Fomba, W. K., Freudenthaler, V., Gasteiger, J., Groß, S., Haarig, M., Heinold, B., Kandler, K., Kristensen, T. B., Mayol-Bracero, O. L., Müller, T., Reitebuch, O., Sauer, D., Schäfler, A., Schepanski, K., Spanu, A., Tegen, I., Toledano, C. and Walser, A.: The Saharan aerosol long-range transport and aerosol-cloud-interaction experiment: Overview and selected highlights, Bull. Am. Meteorol. Soc., 98(7), 1427–1451, doi:10.1175/BAMS-D-15-00142.1, 2017.

Weitkamp, C., Ed.: Lidar Range-Resolved Optical Remote Sensing of the Atmosphere, Springer., 2005.

Whitby, K. T.: The physical characteristics of sulfur aerosols, Atmos. Environ., 12(1), 135–159, doi:https://doi.org/10.1016/0004-6981(78)90196-8, 1978.

Wiegner, M., Groß, S., Freudenthaler, V., Schnell, F. and Gasteiger, J.: The May/June 2008 Saharan dust event over Munich: Intensive aerosol parameters from lidar measurements, J. Geophys. Res. Atmos., 116(23), 1–15, doi:10.1029/2011JD016619, 2011.

Wilson, T. W., Ladino, L. A., Alpert, P. A., Breckels, M. N., Brooks, I. M., Browse, J., Burrows, S. M., Carslaw, K. S., Huffman, J. A., Judd, C., Kilthau, W. P., Mason, R. H., McFiggans, G., Miller, L. A., Nájera, J. J., Polishchuk, E., Rae, S., Schiller, C. L., Si, M., Temprado, J. V., Whale, T. F., Wong, J. P. S., Wurl, O., Yakobi-Hancock, J. D., Abbatt, J. P. D., Aller, J. Y., Bertram, A. K., Knopf, D. A. and Murray, B. J.: A marine biogenic source of atmospheric ice-nucleating particles, Nature, 525(7568), 234–238, doi:10.1038/nature14986, 2015.

Winker, D. M., Vaughan, M. A., Omar, A., Hu, Y., Powell, K. A., Liu, Z., Hunt, W. H. and Young, S. A.: Overview of the CALIPSO mission and CALIOP data processing algorithms, J. Atmos. Ocean. Technol., 26(11), 2310–2323, doi:10.1175/2009JTECHA1281.1, 2009.

World Health Organization: WHO Air quality guidelines for particulate matter, ozone, nitrogen dioxide and sulfur dioxide Global update 2005 Summary of risk assessment., 2005.

World Meteorological Organization: Guide to meteorological instruments and methods of observation., WMO-No.8. [online] Available from: https://library.wmo.int/doc_num.php?explnum_id=10179, 2018.

Zieger, P.: Effects of relative humidity on aerosol light scattering. PhD Thesis Diss., ETH, No 19659, 2011.

List of publications

Journal Publications

1. **Soupiona, O.**, Papayannis, A., Kokkalis, P., Foskinis, R., Sánchez Hernández, G., Ortiz-Amezcua, P., Mylonaki, M., Papanikolaou, C.-A., Papagiannopoulos, N., Samaras, S., Groß, S., Mamouri, R.-E., Alados-Arboledas, L., Amodeo, A., and Psiloglou, B.: EARLINET observations of Saharan dust intrusions over the northern Mediterranean region (2014 – 2017): properties and impact on radiative forcing, Atmos. Chem. Phys, 20, 15147–15166, 2020. https://doi.org/10.5194/acp-20-15147-2020
2. Mylonaki, M., Giannakaki, E., Papayannis, A., Papanikolaou, C.A., Komppula, M., Nicolae, D., Papagiannopoulos, N., Amodeo, A., Baars, H., **Soupiona, O.**, "Aerosol type classification analysis using EARLINET multiwavelength and depolarization lidar observations", Atmos. Chem. Phys. Special issue: EARLINET aerosol profiling: contributions to atmospheric and climate research (under review)
3. Papanikolaou, C., Giannakaki, E., Papayannis, A. and Mylonaki, M., Soupiona, O.: Canadian Biomass Burning Aerosol Properties Modification during a Long-Ranged Event on August 2018, Sensors, 1–19, 2020. https://www.mdpi.com/1424-8220/20/18/5442
4. S. Vratolis, P. Fetfatzis, A. Argyrouli, **O. Soupiona**, M. Mylonaki, J. Maroufidis, A.-C. Kalogridis, M. Manousakas, S. Bezantakos, I. Binietoglou, L.D. Labzovskii, S. Solomos, A. Papayannis, G. Močnik, E. O' Connor, D. Müller, C.G. Tzanis, K. Eleftheriadis, "Comparison and complementary use of in situ and remote sensing aerosol measurements in the Athens Metropolitan Area", Atmospheric Environment, Volume 228, 117439, ISSN 1352-2310, 2020. https://doi.org/10.1016/j.atmosenv.2020.117439
5. Kokkalis, P., Alexiou, D., Papayannis, A. Rocadenbosch F., **Soupiona O.**, Raptis P.I., Mylonaki M., Tzanis C.G. & Christodoulakis J., "Application and Testing of the Extended-Kalman-Filtering Technique for Determining the Planetary Boundary-Layer Height over Athens, Greece", Boundary-Layer Meteorol 176, 125–147, 2020. https://doi.org/10.1007/s10546-020-00514-z
6. H. Baars, A. Ansmann, K. Ohneiser, M. Haarig, R. Engelmann, D. Althausen, I. Hanssen, M. Gausa, A. Pietruczuk, A. Szkop, I. S. Stachlewska, D. Wang, J. Reichhardt, A. Skupin, I. Mattis, T. Trickl, H. Vogelmann, F. Navas-Guzmán, A. Haefele, K. Acheson, A. A. Ruth, B. Tatarov, D. Müller, Q. Hu, T. Podvin, P. Goloub, I. Vesselovski, C. Pietras, M. Haeffelin, P. Fréville, M. Sicard, A. Comerón, A. J. Fernández García, F. M. Menéndez, C. Córdoba-Jabonero, J. L. Guerrero-Rascado, L. Alados-Arboledas, D. Bortoli, M. João Costa, D. Dionisi, G. L. Liberti, X. Wang, A. Sannino, N. Papagiannopoulos, A. Boselli, L. Mona, G. D'Amico, S. Romano, M. R.Perrone, L. Belegante, D. Nicolae, I. Grigorov, A. Gialitaki, V. Amiridis, **O. Soupiona**, A. Papayannis, R.E. Mamouri, A. Nisantzi, B. Heese, J. Hofer, Y. Y. Schechner, U. Wandinger, and G. Pappalardo, "The unprecedented 2017–2018 stratospheric smoke event: Decay phase and aerosol properties observed with EARLINET", Atmos. Chem. Phys., 19, 15183–15198, 2019, https://doi.org/10.5194/acp-19-15183-2019
7. **O. Soupiona**, S. Samaras, P. Ortiz-Amezcua, C. Boeckmann. A. Papayannis, G.A. Moreira, M. Mylonaki, J.A. Benavent-Oltra, A.E. Bedoya-Velasquez, R. Roman, J.L. Guerrero-Rascado, F.J. Olmo, L. Alados-Arboledas, C.A. Papanikolaou, R. Foskinis, "Retrieval of the optical and micro-physical properties of transported Saharan dust over Athens and Granada based on multi-

wavelength Raman lidar measurements: study of mixing processes" Atmospheric Environment, 214, 116824, 2019. https://doi.org/10.1016/j.atmosenv.2019.116824

8. S. Solomos, A. Bougiatioti, **O. Soupiona**, A. Papayannis, M. Mylonaki, C. Papanikolaou, A. Argyrouli, A. Nenes, "Effects of regional and local atmospheric dynamics on the aerosol and CCN load over Athens", Atmospheric Environment, 2018. https://doi.org/10.1016/j.atmosenv.2018.10.025
9. **O. Soupiona**, A. Papayannis, P. Kokkalis, M. Mylonaki, G.Tsaknakis, A. Argyrouli, S. Vratolis, "Long-term systematic profiling of dust aerosol optical properties using the EOLE NTUA lidar system over Athens, Greece (2000-2016)", Atmospheric Environment, 183, 165-174, 2018. https://doi.org/10.1016/j.atmosenv.2018.04.011

Publications in conferences (peer review)

1. **Soupiona O.**, Foskinis R., Papayannis A., Sánchez Hernández G., Ortiz-Amezcua P., Mylonaki M., Papanikolaou C.A., Alados-Arboledas L., Psiloglou B., "Radiative effects of Saharan dust spheroidal aerosols over the Northern Mediterranean using lidar retrieved signals as inputs in LibRadtran model", 2nd European Lidar Conference (web conference), 18-20 November 2020
2. Foskinis R., Papayannis A., Kokkalis P., Komppula M., **Soupiona O.**, Bossioli E., Tombrou M., Mylonaki M., Papanikolaou C.A., Kralli E., "Aerosol effects on Low Cloud formation over the Attica region, Greece", 2nd European Lidar Conference (web conference), 18-20 November 2020
3. Kralli E., Papayannis A., Foskinis R., **Soupiona O.**, de Lastic H.X., Mylonaki M., Papanikolaou C.A., "Systematic water vapour Raman Lidar Measurements over the free troposphere of Athens, Greece using the EOLE Raman lidar system: Implication for Stratospheric-Tropospheric Exchanges", 2nd European Lidar Conference (web conference), 18-20 November 2020
4. **Soupiona O.**, Papayannis A., Mylonaki M., Papagiannopoulos N., Ortiz-Amezcua P., Mamouri R.E., Groß S., Papanikolaou C.A., Kokkalis P., "Saharan dust events over the Northern Mediterranean: 4 years of measurements over 4 EARLINET stations", 29th International Laser Radar Conference, 24-28 June 2019, Hefei, Anhui, China (***Oral presentation***)
5. Papayannis, A., Kokkalis P., Mylonaki M., **Soupiona O.**, Papanikolaou C. A., Foskinis R., Giakoumaki A., "Recent upgrades of the EOLE and AIAS lidar systems of the National Technical University of Athens operating since 2000 in Athens, Greece", Proc. 29th International Laser Radar Conference, 24-28 June 2019, Hefei, China.
6. Papanikolaou C.A, Giannakaki E., Papayannis A., Tombrou M., Mylonaki M., and **Soupiona O.**, "Optical properties of Canadian biomass burning particles over Europe observed with Calipso and ground-based lidar systems", 29th International Laser Radar Conference, 24-28 June 2019, Hefei, Anhui, China.
7. Foskinis R., Papayannis A., **Soupiona O.**, Kokkalis P., Mylonaki M., Papanikolaou C.A., Argyrouli A., Kompulla M., Vratolis S., Eleftheriadis K., "A Case study of interaction between aerosols and clouds based on HYGRA-Capaign measurements", Proc. 29th International Laser Radar Conference, 24-28 June 2019, Hefei, China.
8. Mihalopoulos, N., Amiridis, V., Eleftheriadis, K., Gerasopoulos, G., Kanakidou, M., Kalivitis, N., Kouvarakis, G., Mylonaki, M., Papayannis, A., **Soupiona, O.,** Burrows, J.P. and the EMERGE group, "First results from the EMERGE-Greece campaign by the PANACEA network in April 2018", 14th iCACGP Quadrennial Symposium/15th IGAC Science Conference 25-29 September 2018.

9. **Soupiona O**., Böckman C., Papayannis A., Mylonaki M., Kokkalis P., Papanikolaou C.A., and Foskinis R., Lidar-based Inversions of Aerosol Microphysical Parameters from Long-range Transported Events over Athens", 1st European Lidar Conference, 3-5 July 2018, Thessaloniki, Greece.
10. Papayannis A., Mylonaki M., **Soupiona O.,** Kokkalis P., Tsaknakis G., Papanikolaou C.A., and Foskinis R., Highlights of Biomass Burning Events from 10-year Profiling over Athens, Greece in the Frame of EARLINET (2007-2017), 1st European Lidar Conference, 3-5 July 2018, Thessaloniki, Greece.
11. **Soupiona, O.,** Mylonaki, M., Papayannis, A., Argyrouli, A., Kokkalis, P., Vratolis S., and Tsaknakis, G., Long-term systematic profiling of dust aerosol optical properties using the EOLE NTUA Lidar system over Athens, Greece, (2000-2016), ILRC28, EPJ Web of Conferences 176, 05029 (2018), https://doi.org/10.1051/epjconf/201817605029
12. Amodeo A., D'Amico G., Giunta A., Papagiannopoulos N., Papayannis A., Argyrouli A., Mylonaki M., Tsaknakis G., Kokkalis P., **Soupiona O.,** Tzanis C., "ATHLI16: The Athens LIDAR Intercomparison Campaign, ILRC28, EPJ Web of Conferences 176, 09008, 2018, doi.org/10.1051/epjconf/20181760900
13. D'Amico G., Mattis I., Binietoglou I., Baars H., Mona L., Amato F., Kokkalis P., Rodríguez-Gómez A., **Soupiona O.** and Voudouri K., EARLINET Single Calculus Chain: new products overview, ILRC28, EPJ Web of Conferences 176, 09014, 2018, doi.org/10.1051/epjconf/201817609014
14. Mylonaki M., Papayannis A., Mamouri R., Argyrouli A., Kokkalis P., Tsaknakis G. and **Soupiona O.,** Aerosol optical properties variability during biomass burning events observed by the EOLE-AIAS depolarization lidars over Athens, Greece (2007-2016), EPJ Web of Conferences 176, 05022 (2018) doi.org/10.1051/epjconf/201817605022

PARTICIPATION IN CONFERENCES/MEETINGS/SCHOOLS

- 2nd European Lidar Conference (web conference), 18-20 November 2020
- Sao Paulo School of Advanced Science on Atmospheric Aerosols: Properties, Measurements, Modeling, and Effects on Climate and Health 22 July to 2 August 2019, Sao Paulo, Brazil.
- 29th International Laser Radar Conference, 24-28 June 2019, Hefei, Anhui, China.
- 2nd Cloudnet Training School, 11–15 March 2019, Munich, Germany.
- 1st European Lidar Conference, 3-5 July 2018, Thessaloniki, Greece.
- 4th ACTRIS-2 General Meeting, 17 - 19 April 2018, Nafplio, Greece.
- ACTRIS-2 WP2 Workshop, 13-17 November 2017, Delft, The Netherlands.
- 28th International Laser Radar Conference, 25-30 June 2017, Bucharest, Romania.
- 5th International Conference on Remote Sensing and Geoinformation of the Environment 2017, 20-23 May 2017, Pafos, Cyprus.
- ECARS 2nd Summer School on Atmospheric remote sensing, Pre-TECT campaign, 03-12 April 2017, Finokalia, Greece.
- LICAL 2nd Workshop, 27 February-03 March 2017, Bucharest, Romania.

  ECARS 1st Summer School on Atmospheric remote sensing: challenges and applications, 23-28 May 2016, Bucharest, Romania.

List of Figures

List of Tables

Appendices

Appendix A
Paper I

Atmospheric Environment 183 (2018) 165–174

Contents lists available at ScienceDirect

Atmospheric Environment

journal homepage: www.elsevier.com/locate/atmosenv

Long-term systematic profiling of dust aerosol optical properties using the EOLE NTUA lidar system over Athens, Greece (2000–2016)

O. Soupiona[a,*], A. Papayannis[a], P. Kokkalis[a,b], M. Mylonaki[a], G. Tsaknakis[a], A. Argyrouli[c,d], S. Vratolis[a,e]

[a] Laser Remote Sensing Unit, Physics Department, School of Applied Mathematics and Physical Sciences, National Technical University of Athens, 15780, Zografou, Greece
[b] Remote Sensing Group, Department of Physics, Kuwait University, P.O. Box 5969, Safat, 13060, Kuwait
[c] Technical University of Munich, Department of Civil, Geo and Environmental Engineering, Chair of Remote Sensing Technology, Munich, Germany
[d] German Aerospace Centre (DLR), Remote Sensing Technology Institute, Oberpfaffenhofen, 82234, Wessling, Germany
[e] ERL, Institute of Nuclear & Radiological Sciences & Technology, Energy & Safety, National Centre of Scientific Research Demokritos, 15310, Ag. Paraskevi, Attiki, Greece

GRAPHICAL ABSTRACT

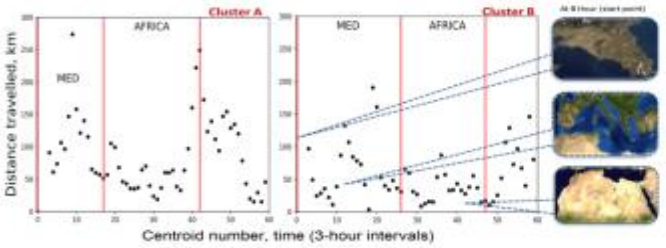

ARTICLE INFO

Keywords:
Aerosols
Dust
Lidar
Aging
Athens
Greece

ABSTRACT

We present a comprehensive analysis of the seasonal variability of the vertical profiles of the optical and geometrical properties of Saharan dust aerosols, observed in the height region between 1000 and 6000 m, over the city of Athens, Greece, from February 2000 to December 2016. These observations were performed by a multi-wavelength (355-387-532-1064 nm) Raman lidar system under cloud-free conditions. The statistical analysis (using aerosol monthly mean values) is based on nighttime vertical Raman measurements of range-resolved aerosol optical properties (backscatter and extinction coefficients, lidar ratio, Ångström exponent) at 355 nm (57 dust events during more than 80 measurement hours). We found that the number of dust events was highest in spring, summer, and early autumn periods and that during spring the dust layers were moved at higher altitudes (~4500 m) than in other seasons. The number of the forecasted dusty days (on monthly basis) by the BSC-DREAM8b model compared to those of the performed lidar measurements were found to have a quite strong correlation ($R^2 = 0.81$), with a maximum occurrence predicted for the spring season. In the worst case scenario, at least 50% of the model-forecasted dust events can be observed by lidar under cloudless skies over Athens. For the sampled dust plumes we found mean lidar ratios of 52 ± 13 sr at 355 nm in the height range 2000–4000 m a.s.l. Moreover, the dust layers had a mean thickness of 2497 ± 1026 m and a center of mass of 2699 ± 1017 m.

An analysis performed regarding the air mass back-trajectories arriving over Athens revealed two main clusters: one pathway from south-west to north-east, with dust emission areas in Tunisia, Algeria and Libya and a second one from south, across the Mediterranean Sea with emission areas over Libya and the remaining part of Algeria and Tunisia. This clustering enabled us to differentiate between the aerosol optical properties between

* Corresponding author.
E-mail address: soupiona.rania@gmail.com (O. Soupiona).

https://doi.org/10.1016/j.atmosenv.2018.04.011
Received 9 October 2017; Received in revised form 5 April 2018; Accepted 8 April 2018
Available online 14 April 2018

Paper II

Atmospheric Environment 214 (2019) 116824

Contents lists available at ScienceDirect

Atmospheric Environment

journal homepage: www.elsevier.com/locate/atmosenv

Retrieval of optical and microphysical properties of transported Saharan dust over Athens and Granada based on multi-wavelength Raman lidar measurements: Study of the mixing processes

O. Soupiona[a,*], S. Samaras[b,e], P. Ortiz-Amezcua[c,d], C. Böckmann[e], A. Papayannis[a], G.A. Moreira[c,d,f], J.A. Benavent-Oltra[c,d], J.L. Guerrero-Rascado[c,d], A.E. Bedoya-Velásquez[c,d,g], F.J. Olmo[c,d], R. Román[c,d,h], P. Kokkalis[i], M. Mylonaki[a], L. Alados-Arboledas[c,d], C.A. Papanikolaou[a], R. Foskinis[a]

[a] Laser Remote Sensing Unit, Physics Department, School of Applied Mathematics and Physical Sciences, National Technical University of Athens, 15780, Zografou, Greece
[b] German Aerospace Center (DLR), German Remote Sensing Datacenter (DFD), Wessling, Germany
[c] Andalusian Institute for Earth System Research (IISTA-CEAMA), 18006, Granada, Spain
[d] Department of Applied Physics, University of Granada, 18071, Granada, Spain
[e] Institute of Mathematics, Potsdam University, 14469, Potsdam, Germany
[f] Institute of Research and Nuclear Energy (IPEN), São Paulo, Brazil
[g] Sciences Faculty, Department of Physics, Universidad Nacional de Colombia, Medellín, Colombia
[h] Grupo de Óptica Atmosférica (GOA), Universidad de Valladolid, Paseo Belén, 7, 47011, Valladolid, Spain
[i] Department of Physics, Kuwait University, P.O. Box 5969, Safat, 13060, Kuwait

ABSTRACT

In this paper we extract the aerosol microphysical properties for a collection of mineral dust cases measured by multi-wavelength depolarization Raman lidar systems located at the National Technical University of Athens (NTUA, Athens, Greece) and the Andalusian Institute for Earth System Research (IISTA-CEAMA, Granada, Spain). The lidar-based retrievals were carried out with the Spheroidal Inversion eXperiments software tool (SphInX) developed at the University of Potsdam (Germany). The software uses regularized inversion of a two-dimensional enhancement of the Mie model based on the spheroid-particle approximation with the aspect ratio determining the particle shape. The selection of the cases was based on the transport time from the source regions to the measuring sites. The aerosol optical depth as measured by AERONET ranged from 0.27 to 0.54 (at 500 nm) depending on the intensity of each event. Our analysis showed the hourly mean particle linear depolarization ratio and particle lidar ratio values at 532 nm ranging from 11 to 34% and from 42 to 79 sr respectively, depending on the mixing status, the corresponding air mass pathways and their transport time. Cases with shorter transport time showed good agreement in terms of the optical and SphInX-retrieved microphysical properties between Athens and Granada providing a complex refractive index value equal to 1.4 + 0.004i. On the other hand, the results for cases with higher transport time deviated from the aforementioned ones as well as from each other, providing, in particular, an imaginary part of the refractive index ranging from 0.002 to 0.005. Reconstructions of two-dimensional shape-size distributions for each selected layer showed that the dominant effective particle shape was prolate with diverse spherical contributions. The retrieved volume concentrations reflect overall the intensity of the episodes.

Paper III

Atmos. Chem. Phys., 20, 15147–15166, 2020
https://doi.org/10.5194/acp-20-15147-2020

Atmospheric Chemistry and Physics
Open Access
EGU

EARLINET observations of Saharan dust intrusions over the northern Mediterranean region (2014–2017): properties and impact on radiative forcing

Ourania Soupiona[1], Alexandros Papayannis[1], Panagiotis Kokkalis[2], Romanos Foskinis[1], Guadalupe Sánchez Hernández[3,4], Pablo Ortiz-Amezcua[3,4], Maria Mylonaki[1], Christina-Anna Papanikolaou[1], Nikolaos Papagiannopoulos[5], Stefanos Samaras[6], Silke Groß[7], Rodanthi-Elisavet Mamouri[8,9], Lucas Alados-Arboledas[3,4], Aldo Amodeo[5], and Basil Psiloglou[10]

[1]School of Applied Mathematics and Physical Sciences, Dept. of Physics, National Technical University of Athens, 15780 Athens, Greece
[2]Department of Physics, Kuwait University, Safat, 13060, Kuwait
[3]Department of Applied Physics, University of Granada, Granada, 18071, Spain
[4]Andalusian Institute for Earth System Research, Granada, 18006, Spain
[5]Consiglio Nazionale delle Ricerche, Istituto di Metodologie per l'Analisi Ambientale, Tito Scalo, 85050, Italy
[6]German Aerospace Center (DLR), German Remote Sensing Data Center (DFD), Wessling, Germany
[7]Institute of Atmospheric Physics, Deutsches Zentrum für Luft- und Raumfahrt (DLR), 82234 Oberpfaffenhofen, Germany
[8]Cyprus University of Technology, Dept. of Civil Engineering and Geomatics, Limassol, Cyprus
[9]ERATOSTHENES Centre of Excellence, Limassol, Cyprus
[10]Institute for Environmental Research and Sustainable Development, National Observatory of Athens, Palaia Penteli, 15236, Athens, Greece

Correspondence: Ourania Soupiona (raniaphd@mail.ntua.gr)

Received: 17 June 2020 – Discussion started: 1 July 2020
Revised: 7 October 2020 – Accepted: 8 October 2020 – Published: 7 December 2020

Appendix B

Table I: Optical and microphysical properties found in the literature about transported Saharan dust events detected in Europe, Morocco and Cape Verde used to compare with our findings.

Reference	Region	Technique	Type	LR (λ)	β-AE (λ)	α-AE (λ)	δp (λ)	RRI (λ)	IRI (λ)	SSA (λ)	r_{eff}
(Mattis et al., 2002)	Leipzig (51.3º N, 12.4º E)	Lidar	Dust	60 – 100 sr (355 nm) 50 – 80 sr (532 nm)			0.15 – 0.25 (532 nm)				
(Papayannis et al., 2005)	Athens (37.9º N, 23.8º E)	Lidar	Dust	53±1 sr (355nm)							
(Guerrero-Rascado et al., 2008)	Granada (37.16º N, 3.61º W)	Lidar	Dust	41 – 45 sr (532 nm)			0.15 – 0.25 (532 nm)				
(Guerrero-Rascado et al., 2009)	Granada (37.16º N, 3.61º W)	Lidar	Dust	50 – 65 sr (532 nm)	-0.4 -0.5 (355/532 nm)						
(Freudenthaler et al., 2009)	Quarzazate, Morocco (30.94º N, 6.91º W)	Lidar	Pure dust				0.26±0.06 (355 nm) 0.30±0.00 (532 nm) 0.28±0.05 (710 nm) 0.27±0.04 (1064 nm)				
(Petzold et al., 2009)	S Morocco (30.93º N, 6.91º W)	In Situ	Dust					1.550 – 1.565 (450 nm) 1.549 – 1.561 (550 nm) 1.546 -1.555 (700 nm)	0.0031 – 0.0052 (450 nm) 0.0016 – 0.0042 (550 nm) 0.0003 – 0.0025 (700 nm)		
(Córdoba-Jabonero et al., 2011)	Santa Cruz de Tenerife (28.5º N, 16.2º W); El Arenosillo (37.1ºN, 6.7º W); Granada (37.16º N, 3.61º W)	Lidar and In situ	Pure dust	45 -70 sr (532 nm)							0.10 -0.15 µm (fine) 1.06 – 1.72 µm (coarse)
(Bauer et al., 2011b)	Praia, Cape Verde (14.95º N, 23.49º W)	In Situ	Pure dust							0.92±0.07 (532 nm)	

(Groß et al., 2011)	Praia, Cape Verde (14.95º N, 23.49º E)	Lidar	Dust	58±7 sr (355 nm) 62±5 sr (532 nm)			0.25±0.03 (355 nm) 0.30±0.01 (532 nm)				
(Tesche et al., 2011)	Praia, Cape Verde (14.95º N, 23.49º E)	Lidar	Dust	53±10 sr (355, 532 nm)	0.2±0.3 (355/532 nm) 0.45±0.16 (532/1064 nm)	0.2±0.3 (355/532 nm)	0.31 – 0.10 (532 nm) 0.37±0.07 (710 nm)				
(Tesche et al., 2011)	Praia, Cape Verde (14.95º N, 23.49º E)	Lidar	Dust/smoke	67±14 sr (355, 532 nm)	0.7±0.3 (355/532 nm, 532/1064 nm)	0.7±0.4 (355/532 nm)	0.15 – 0.05 (532 nm) 0.2±0.1 (710 nm)				
(Weinzierl et al., 2011)	Praia, Cape Verde (14.95º N, 23.49º E)	In situ	Dust					1.550± 0.002 (467 nm) 1.550±0.002 (530 nm) 1.546±0.002 (660 nm)	0.004± 0.002 (467 nm) 0.003±0.002 (530 nm) 0.001 ± 0.001 (660 nm)		1.21±0.32 µm
(Weinzierl et al., 2011)	Praia, Cape Verde (14.95º N, 23.49º E)	Lidar	Dust	42±5 sr (532 nm)			0.22±0.04				
(Toledano et al., 2011)	Praia, Cape Verde (14.95º N, 23.49º E)	Photometry								0.93±0.01 (440 nm) 0.98 – 0.99 (670, 1020 nm)	
(Preißler et al., 2011)	Évora (38.57º N, 7.91º W)	Lidar	Dust	45±11 sr (355 nm) 53±7 (532 nm)	0.4±0.6 (355/532 nm) 0.4±0.2 (532/1064 nm)	0.0±0.2 (355/532 nm)	0.28±0.04 (532 nm)				
(Valenzuela et al., 2014)	Alborán Island (35.95º N, 3.03º W)	Photometry								0.88±0.03 (440 nm) 0.91±0.03 (1020 nm)	
(Bravo-Aranda et al., 2015)	Granada (37.16º N, 3.61º W)	Lidar	Dust		0.8±0.1 (355/532 nm)		0.19±0.03 (532 nm)				

(Denjean et al., 2016)	Western Mediterranean Basin	Airborne In situ	Dust					1.50 – 1.55 (530 nm)	0.000 – 0.005 (530 nm)	0.90 – 1.00 (530 nm)	
(Benavent-Oltra et al., 2017)	Granada (37.16º N, 3.61º W)	Lidar and Photometry	Dust		0.5±0.2 (532/1064 nm)			1.52 – 1.55 [355, 1064 nm]	0.001 – 0.013 (355 nm) 0.002 – 0.004 (640 nm) 0.001 – 0.003 (1064 nm)	0.86 – 0.95 (355 nm) 0.90 – 0.96 (640 nm) 0.96 – 0.99 (1064 nm)	0.10 -0.13 µm (fine) 2.2 – 2.4 µm (coarse)

Table II: Mean optical and microphysical properties of the 51 selected cases of the EARLINET database (Granada, Potenza, Athens and Limassol stations). *The term of mixing refers to the hours the trajectories travelled after leaving African Continent. **The type of mixing was based on the HSRL classification provided by Groβ et al., (2013).

No	Date	Time (UTC)	Station	Mixing* (hours)	Type**	Base (m)	Top (m)	β ($Mm^{-1}sr^{-1}$) [532nm]	α (Mm^{-1}) [532nm]	LR (Sr) [532nm]	δ_p (%) [532nm]	AE_β [532/1064nm]	AOD [532nm]	RRI [532nm]	IRI [532nm]	SSA [532nm]	r_{eff}
1	**17-02-2014**	**19.00**	Potenza	24	Dust Mix.	1030	3130	1.24±0.50	87±27	56±8	0.29±0.04	0.30±0.08	0.16	1.5	0.0022	0.9762	0.44
2	**07-04-2014**	**18.00**	Potenza	108	Dust Mix.	3790	6850	0.53±0.10	11±8	35±10	0.28±0.04	0.78±0.23	0.03	1.4	0.0030	0.9761	0.25
3	**26-05-2014**	**20.00**	Athens	36-42	Dust Mix.	2603	4402	0.73±0.28	42±8	61±10	0.25±0.05	0.72±0.08	0.08	1.4	0.0082	0.9360	0.33
4	**27-05-2014**	**20.00**	Athens	60	Dust Mix.	1562	3127	0.70±0.37	35±23	56±18	0.24±0.06	1.17±0.11	0.07	1.4	0.0080	0.9411	0.25
5	**28-05-2014**	**20.00**	Athens	48-54	Sah. Dust	2003	3578	0.60±0.04	46±17	51±12	0.31±0.08	1.58±0.25	0.07	1.5	0.0082	0.9158	0.49
6	**29-05-2014**	**07.00**	Athens	24	Dust Mix.	1800	2700	1.44±0.21	N/A	N/A	0.29±0.05	N/A	N/A	N/A	N/A	N/A	N/A
7	**17-06-2014**	**21.00**	Athens	18-24	Sah. Dust	4022	5642	0.77±0.55	92±29	46±9	0.34±0.07	N/A	0.16	1.5	0.0032	0.9674	0.39
8	**18-06-2014**	**21.00**	Athens	18-24	Dust Mix.	2520	4913	0.93±0.57	138±46	54±12	0.21±0.03	0.13±0.06	0.34	1.5	0.0032	0.9672	0.40
9	**07-07-2014**	**21.00**	Potenza	16	Sah. Dust	1030	5530	0.63±0.11	45±23	51±13	0.35±0.03	0.26±0.18	0.19	1.5	0.0032	0.9671	0.45
10	**08-07-2014**	**21.00**	Athens	30	Dust Mix.	1382	4382	0.99±0.39	56±20	65±33	N/A	0.77±0.14	0.17	N/A	N/A	N/A	N/A
11	**21-08-2014**	**19.00**	Potenza	30-36	BB & Dust	2830	3490	1.32±0.23	34±18	50±18	0.18±0.01	0.67±0.15	0.02	1.5	0.005	0.9493	0.24
12	**24-11-2014**	**21.00**	Potenza	84-90	BB & Dust	1270	1870	1.00±0.23	89±18	73±7	0.17±0.01	0.52±0.08	0.06	1.5	0.005	0.9497	0.25
13	**06-07-2015**	**21.00**	Granada	72-78	BB & Dust	1411	5581	0.67±0.13	N/A	N/A	0.17±0.01	-0.01±-0.09	N/A	N/A	N/A	N/A	N/A
14	**09-07-2015**	**21.00**	Granada	24-30	BB & Dust	2184	2986	0.99±0.15	33±2	40±9	0.16±0.01	0.29±0.04	0.03	1.5	0.005	0.9661	0.28
15	**30-07-2015**	**22.00**	Potenza	30	Dust Mix.	3730	6550	1.10±0.29	30±6	59±17	0.22±0.03	0.68±0.09	0.07	1.5	0.0042	0.9582	0.36
16	**20-08-2015**	**21.00**	Granada	24-30	BB & Dust	3759	4486	0.44±15	13±6	41±6	0.16±0.01	0.13±0.13	0.01	1.4	0.0032	0.9707	0.39
17	**31-08-2015**	**10.00**	Granada	48-54	Dust Mix.	1306	4471	3.00±1.24	N/A	N/A	0.2±0.01	0.00±0.23	N/A	N/A	N/A	N/A	N/A
18	**03-09-2015**	**21.00**	Potenza	96	Dust Mix.	1390	2170	1.55±0.25	93±16	54±11	0.23±0.04	0.38±0.02	0.08	1.5	0.0022	0.9760	0.36
19	**07-09-2015**	**19.00**	Limassol	108-114	Dust Mix.	2051	3616	6.88±2.21	287±73	40±9	0.28±0.03	N/A	0.45	N/A	N/A	N/A	N/A
20	**09-09-2015**	**20.00**	Limassol	108-114	Dust Mix.	1001	2044	1.87±0.40	141±19	53±7	0.27±0.03	N/A	0.15	N/A	N/A	N/A	N/A
21	**10-09-2015**	**18.00**	Limassol	114-120	Sah. Dust	1106	2381	8.37±2.84	379±112	48±7	0.33±0.03	N/A	0.48	N/A	N/A	N/A	N/A
22	**11-09-2015**	**19.00**	Limassol	108	Dust Mix.	2051	3776	1.90±0.47	101±31	53±10	0.29±0.07	N/A	0.18	N/A	N/A	N/A	N/A
23	**14-09-2015**	**12.00**	Potenza	36-42	Dust Mix.	2410	3310	1.67±0.60	N/A	N/A	0.19±0.02	0.29±0.08	N/A	N/A	N/A	N/A	N/A
24	**15-02-2016**	**18.00**	Potenza	12-18	Sah. Dust	1030	3730	3.81±2.60	122±88	54±18	0.33±0.03	0.77±0.20	0.20	N/A	N/A	N/A	N/A
25	**22-02-2016**	**14.00**	Potenza	30	Dust Mix.	1570	2710	2.36±1.14	N/A	N/A	0.17±0.01	1.26±0.12	N/A	N/A	N/A	N/A	N/A
26	**04-04-2016**	**18.00**	Athens	90-96	Dust Mix.	1022	3242	0.76±0.14	31±13	40±12	N/A	0.85±0.07	0.07	N/A	N/A	N/A	N/A
27	**04-04-2016**	**19.00**	Potenza	60	Dust Mix.	1030	4330	1.26±0.85	58±33	50±15	0.23±0.05	0.80±0.37	0.17	1.5	0.0022	0.9762	0.44

28	**11-04-2016**	**18.00**	Athens	30	Dust Mix.	2027	2755	0.80±0.07	30±12	35±5	N/A	1.34±0.04	0.02	N/A	N/A	N/A	N/A
29	**11-04-2016**	**21.00**	Potenza	30-36	Dust Mix.	1750	2890	1.01±0.37	62±7	53±12	0.28±0.05	0.37±0.09	0.05	1.5	0.0032	0.9640	0.49
30	**09-05-2016**	**19.00**	Athens	54-60	Dust Mix.	1794	3054	0.51±0.16	26±6	62±14	N/A	0.89±0.24	0.04	N/A	N/A	N/A	N/A
31	**26-05-2016**	**19.00**	Potenza	30-36	Dust Mix.	3430	4930	0.60±0.40	N/A	N/A	0.27±0.06	0.4±0.13	N/A	N/A	N/A	N/A	N/A
32	**09-06-2016**	**01.00**	Granada	42	Dust Mix.	1059	5259	2.68±1.10	123±43	50±9	0.27±0.05	0.25±0.28	0.44	1.5	0.020	0.9799	0.38
33	**23-06-2016**	**20.00**	Potenza	48-54	Dust Mix.	3490	5410	2.03±0.8	85±21	47±16	0.36±0.03	0.84±0.33	0.20	1.4	0.0032	0.9665	0.42
34	**23-06-2016**	**21.00**	Granada	126	Dust Mix.	1306	4651	0.82±0.18	65±38	64±10	0.27±0.05	0.18±0.16	0.21	1.5	0.0042	0.9721	0.29
35	**24-06-2016**	**04.00**	Granada	66	Dust Mix.	1006	5371	0.84±0.30	73±55	53±18	0.26±0.05	0.39±0.12	0.22	1.5	0.0022	0.9768	0.42
36	**04-07-2016**	**20.00**	Granada	30	Dust Mix.	2941	4779	0.54±0.30	32±3	44±15	0.21±0.02	0.58±0.17	0.02	N/A	N/A	N/A	N/A
37	**11-07-2016**	**14.00**	Granada	48-54	Dust Mix.	1261	3256	1.81±0.30	N/A	N/A	0.21±0.02	0.66±0.12	N/A	N/A	N/A	N/A	N/A
38	**18-07-2016**	**21.00**	Granada	60	Dust Mix.	1111	5881	1.96±1.49	136±66	57±24	0.28±0.04	0.18±0.18	0.4	1.5	0.0032	0.9798	0.24
39	**19-07-2016**	**22.00**	Granada	24-30	Sah. Dust	1111	6631	1.35±0.33	91±29	60±14	0.30±0.03	-0.07±0.19	0.39	1.4	0.0030	0.9817	0.32
40	**20-07-2016**	**22.00**	Granada	36-42	Sah. Dust	1209	5746	1.44±0.27	96±32	53±11	0.30±0.02	0.06±0.02	0.78	1.4	0.0040	0.9757	0.36
41	**21-07-2016**	**00.00**	Granada	42	Dust Mix.	1209	5709	3.58±1.48	185±60	54±9	0.29±0.02	0.18±0.11	0.80	1.4	0.0030	0.9825	0.27
42	**19-09-2016**	**19.00**	Athens	24	Dust Mix.	1082	2942	1.29±0.32	26±14	50±10	N/A	0.77±0.07	0.05	N/A	N/A	N/A	N/A
43	**20-02-2017**	**20.00**	Granada	18	Dust Mix.	1276	4344	5.71±2.00	290±116	53±5	0.27±0.05	0.11±0.29	0.83	1.4	0.0030	0.9826	0.27
44	**27-04-2017**	**20.00**	Potenza	24	Dust Mix.	1030	3250	1.09±0.15	N/A	N/A	0.35±0.02	1.31±0.12	N/A	N/A	N/A	N/A	N/A
45	**08-06-2017**	**18.00**	Limassol	48-54	Dust Mix.	2051	4668	1.38±0.67	N/A	N/A	0.26±0.07	N/A	N/A	N/A	N/A	N/A	N/A
46	**21-06-2017**	**07.00**	Granada	78-84	Dust Mix.	1359	5244	0.78±0.40	N/A	N/A	0.25±0.03	0.18±0.11	N/A	N/A	N/A	N/A	N/A
47	**26-06-2017**	**20.00**	Limassol	30-36	Dust Mix.	4166	6236	0.17±0.08	N/A	N/A	0.22±0.02	N/A	N/A	N/A	N/A	N/A	N/A
48	**19-07-2017**	**20.00**	Potenza	108	Dust Mix.	4090	7270	0.46±0.22	11±1	48±14	0.28±0.03	1.12±0.30	0.15	N/A	N/A	N/A	N/A
49	**20-07-2017**	**21.00**	Potenza	108	Dust Mix.	3250	5350	0.78±0.33	21±9	40±13	0.23±0.04	0.85±0.16	0.09	1.5	0.0042	0.9592	0.36
50	**28-08-2017**	**19.00**	Potenza	162	Dust Mix.	3130	5410	0.62±0.38	25±14	46±12	0.25±0.05	1.07±0.13	0.06	1.5	0.0032	0.9676	0.39
51	**11-09-2017**	**18.00**	Athens	18-24	Sah. Dust	1382	4920	1.67±0.32	63±9	53±6	0.32±0.03	0.79±0.11	0.23	1.5	0.0032	0.9668	0.41

Appendix C

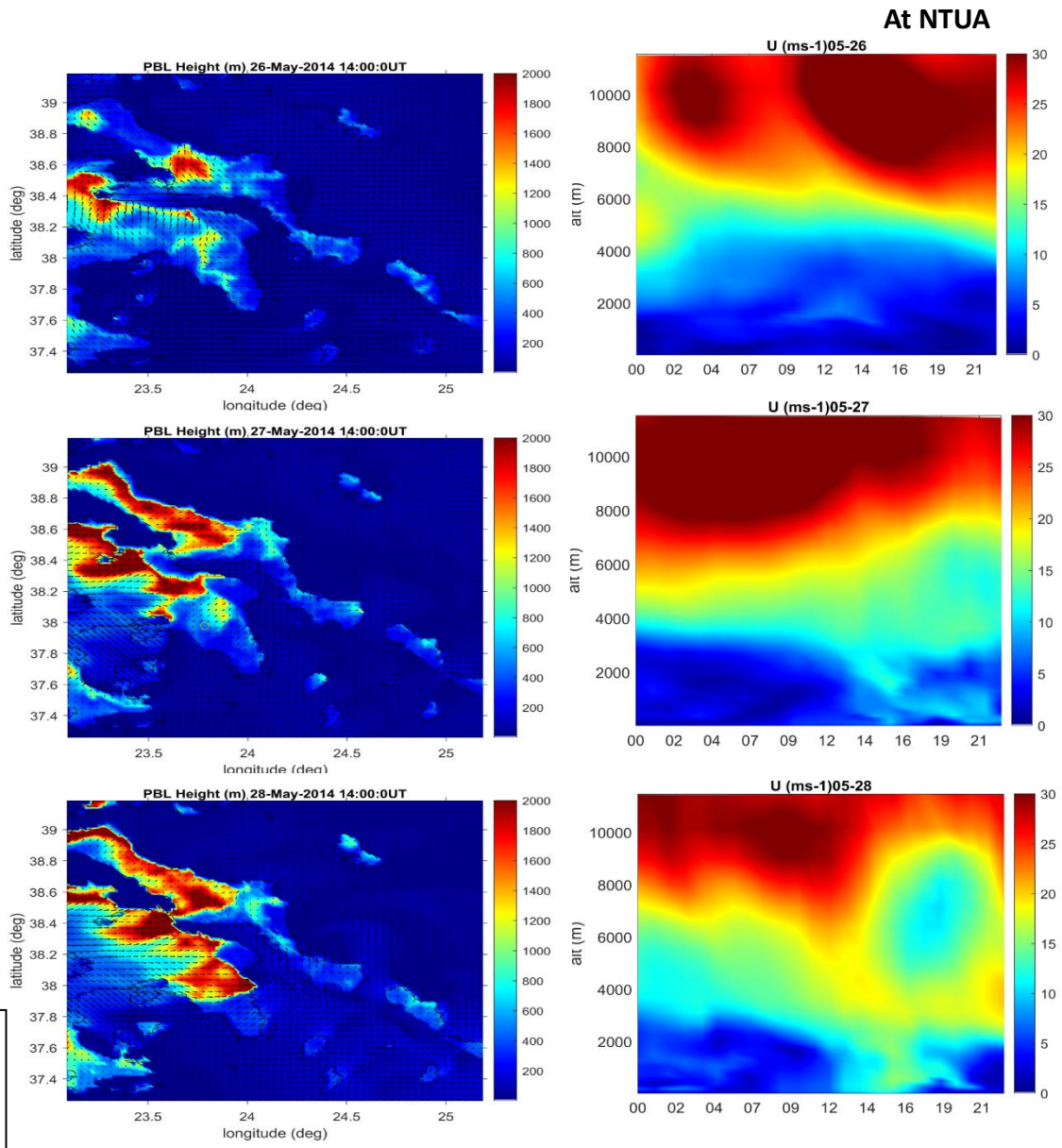

Figure I: Spatial evolution of the PBL height (m) on 26, 27 and 28 May 2014, as simulated by WRF/Chem model.

Figure II: Vertical wind speed (m s^{-1}) at NTUA station, on 26, 27 and 28 May 2014, as simulated by WRF/Chem model.